The University Of Sheffield.

University of Sheffield

Viscosity Measurements Using a Multiple Frequency Matching Layer Viscometer

Tomos Brenchley

A thesis submitted in partial fulfilment of the requirements for the degree of

Doctor of Philosophy

The University of Sheffield

Faculty of Engineering

Department of Mechanical Engineering

Submission Date

April 2021

Abstract

Lubricating oil is used to separate two surfaces in relative motion. To adequately reduce wear and maintain optimum efficiency, it is vital to know the viscosity of the lubricating oil. Most lubricating oils are non-Newtonian, meaning the viscosity is dependent on the shear rate. This thesis develops a tool to carry out viscosity measurements of lubricating oils at varying high shear rates in-situ.

To fully understand how the lubricant will react in-situ it is necessary to subject the oil to the harsh conditions found in an engine. However, this is very challenging to replicate. If viscosity measurements are completed in-situ, it negates the need to replicate the harsh conditions. Due to the many advantages of ultrasound, including low cost, ability to complete measurements in harsh conditions and continuous measurements, the ultrasound method is the most promising technique to complete high shear in-situ measurements. The shear reflection method obtains the lubricating oils viscosity by measuring the returned amplitude of an emitted shear ultrasound wave. When the emitted wave reaches a boundary, a proportion of the wave will be reflected, and a proportion will be transmitted. The proportion reflected is dependent upon the acoustic impedance of the media on either side of the boundary. For lubricating oil, its acoustic impedance is related to its viscosity.

The ultrasonic shear reflection viscometer had to be adapted to measure the viscosity of lubricating oils because the majority of the signal was reflected as the difference in the acoustic impedance of the piezoelectric crystal and oil was too great. This made it impossible to determine the viscosity of lubricating oils. By installing an intermediary layer, known as the matching layer, between the piezoelectric crystal and the lubricating oil, a greater proportion of the signal was transmitted, and the reflection coefficient could be used to determine the viscosity of lubricating oils.

This thesis focuses on understanding the shear rate exerted on the test oil by the ultrasonic shear reflection viscometer, as without this information the viscometer is unable to be used to measure the viscosity of non-Newtonian fluids, such as engine oils.

In this study a mathematical model was developed to determine the viscosity of Newtonian and non-Newtonian fluids from the pressure reflection coefficient for a three-layered system. The model illustrated the advantages of the three-layered system, and a sensitivity analysis was completed to understand the relationship between frequency and reflection coefficient. This model was validated by measuring the viscosity of Newtonian fluids with a viscosity range of $16 - 710cP$, using an ultrasound viscometer over the frequencies $1 - 10MHz$, and comparing with viscosity results from a low shear Couette viscometer. This multiple frequency matching layer viscometer was instrumented with different frequency transducers and different thickness matching layers to obtain maximum sensitivity. Using the multiple frequency matching layer viscometer different input signal settings were altered to find the optimal settings.

A further model was then developed from Stokes' second problem, which is used to describe the flow from an oscillating surface, to understand the shear rate exerted on the lubricating oil from the ultrasound matching layer viscometer. Previous researchers have successfully used the Cox-Merz rule for simple fluids at low shear rates which states that the shear rate for a steady and oscillatory shear can be related by, $\eta(\dot{\gamma}) = \eta(\omega)$, where η is the dynamic viscosity, $\dot{\gamma}$ is the shear rate, and ω is the angular velocity. This thesis argues that for high shear rate measurements, the shear rate from the ultrasonic shear reflection viscometer is dependent on the viscosity and velocity of the fluid and the frequency of the shear wave.

To determine the shear rate exerted on the lubricating oil using the derivation from Stokes' second problem, the velocity of the lubricating oil was required. Due to the non reflective nature of lubricating oil it was indirectly measured using a laser vibrometer, and was found to be dependant on the excitation voltage.

Viscosity measurements of non-Newtonian lubricants were completed on the multiple frequency matching layer viscometer and compared with results obtained on an ultra-shear Couette viscometer. The results were more similar using Stokes' second problem than Cox-Merz, which validated the shear rate model. Finally using this model, a shear rate viscosity plot was created for Newtonian and non-Newtonian oils.

Acknowledgements

I would firstly like to express my deepest thanks to Professor Rob Dwyer-Joyce for all the support and guidance that he has provided throughout this entire process. I would also like to thank him for introducing me to the exciting engineering area of in-situ acoustic tribological sensors and for all the fantastic opportunities he provided.

I would also like to thank the University of Sheffield and CDT for the financial assistance and training to enable this research to be completed, with special thanks to Ms Kim Matthews-Hyde for her support.

I would like to acknowledge all the PhD students and research associates of the CDT and Tribology group who have provided advice and friendship, with a special mention to Dr Xiangwei Li, Dr Georgios Tyreas, Doctor Olivia Manfredi, Dr Michele Schirru, Mr Joe Kanja and Mr David Fort.

Finally and most importantly, I would like to say a huge thank you to my parents and family for their support throughout this entire process – I promise you'll never have to check another equation or proof read a draft chapter again.

Contents

List of Figures

List of Tables

Acronyms

DMA Isodecyl Methacrylate

EAL Environmentally Acceptable Lubricant

FFT Fast Fourier Transform

PAO Polyalphaolefin

QCM Quartz Crystal Microbalance

RC Reflection Coefficient

USV Ultra Shear Viscometer

VII Viscosity Index Improver

ZDDP Zinc Dithiophosphates

Nomenclature

Symbol	Chapter	Description	Units
α	2	Viscosity Pressure Coefficient	$-$
α	2	Angle Between Cone and Plate	rad
α	3	Attenuation Coefficient	$-$
$\bar{U}$	6,8	Maximum Velocity	m/s
δ	2,5	Phase Shift	rad
δ	3	Penetration Depth	m
Δf	2,4	Frequency Shift	Hz
δ_{99}	6	Thickness of Stokes Layer	m
$\dot{\epsilon}$	5	Strain Rate	$1/s$
$\dot{\gamma}$	2, 4, 6, 8	Shear Rate	$1/s$
$\dot{\gamma}_{max}$	6	Maximum Shear Rate	$1/s$
$\dot{\theta}$	5	Stress Rate	N/m^2s
ϵ	5	Strain	$-$
η	2, 3, 4, 5, 6, 8	Dynamic Viscosity	Pas
η_0	2, 8	Dynamic Viscosity at Zero Shear	Pas
η_0	2	Dynamic Viscosity at Atmospheric Pressure	Pas
η_∞	2, 8	Dynamic Viscosity at Infinite Shear	Pas
η_l	4	Dynamic Viscosity of Liquid	Pas
γ	2, 3, 5	Shear Strain	$-$
γ	7	Creep Factor	$-$
λ	2	Relaxation Time	s
λ	3, 5	Wavelength	m
λ	8	Carreau-Yasuda Constant	$-$
μ_q	4	Shear Modulus of Quartz	N/m^2
ν	2, 6, 8	Kinematic Viscosity	m^2/s
ω	2, 3, 4, 5, 6, 8	Angular Velocity	rad/s
ω	6	Velocity Component in z-Plane	m/s
ϕ	4	Angle of Incidence	rad
ρ	2, 3, 5, 6, 8	Density	kg/m^3
ρ_b	2	Density of Ball	kg/m^3
ρ_l	3, 4	Density of Liquid	kg/m^3
ρ_q	2, 4	Density of Quartz	kg/m^3
ρ_s	3	Density of Solid	kg/m^3
ρ_T	8	Density at Temperature, T	kg/m^3
ρ_{T0}	8	Density at Temperature, T0	kg/m^3
$\tilde{U}$	6	Arbitrary Velocity	m/s
τ	2	Shear Stress	N/m^2

Symbol	Chapter	Description	Units
τ	5	Relaxation Time	s
$\tau*$	2	Complex Shear Stress	N/m^2
θ	3, 4	Phase Shift	rad
θ	3, 5	Stress	N/m^2
θ	3	Beam Spread	rad
θ_0	5	Initial Stress Amplitude	N/m^2
A	2	Area	m^2
a	2, 8	Carreau-Yasuda Index	$-$
a	2	Vogel Material Constant	$-$
a	2	Diameter of Capillary	m
A	8	Area	m^2
A_0	3	Initial Amplitude of Wave	m
A_d	3	Amplitude of Wave After Distance, d	m
a_T	8	Reduced Shear Rate	$-$
b	2	Vogel Material Constant	$-$
c	2	Vogel Material Constant	$-$
c	3, 5	Speed of Sound	m/s
c_l	3	Speed of Sound In Liquid	m/s
c_m	7	Speed of Sound In Matching Layer	m/s
c_s	3	Speed of Sound In Solid	m/s
c_t	3	Speed of Sound in Transducer	m/s
d	3	Distance	m
D_T	3	Transducer Diameter	m
E	3	Elastic Modulus	N/m^2
E	5	Stiffness of Spring	N/m^2
F	2, 8	Force	N
f	2, 3, 7, 8	Frequency	Hz
f_0	2, 3, 4	Natural Frequency	Hz
G	2, 3, 5	Shear Modulus	N/m^2
g	2	Acceleration Due to Gravity	m^2/s
G'	2, 5	Storage Modulus	N/m^2
G''	2, 5	Loss Modulus	N/m^2
$G*$	2, 5	Complex Shear Modulus	N/m^2
h	2	Distance Between Plates	m
h	2	Height of Capillary	m
h	2	Height of Spindle	m
H	4	Gap Between Plates	m
h	4	Film Thickness	m
h	4	Distance of Outlet Gap	m
I	6	Intensity of Sound Wave	W/m^2
K	2	Flow Consistency Index	$-$
k	5	Wavenumber	$1/m$
k	8	Material Density Parameter	kg/m^3
k_m	3	Wavenumber of Matching Layer	$1/m$
L	2	Length of Capillary	m
L	7	Creep Displacement	m
L_0	7	Displacement After 0.1s	m

Symbol	Chapter	Description	Units
n	2	Power Law Constant	$-$
N	3	Near Field Distance	m
n	7	Natural Integer	$-$
n	8	Carreau-Yasuda Constant	$-$
P	2, 5, 6, 8	Pressure	N/m^2
p'	4	Pressure Change	N/m^2
p_i	3, 5, 8	Incident Pressure	N/m^2
p_t	3, 5, 8	Transmitted Pressure	N/m^2
r	2	Radius of Capillary	m
R	2, 4	Radius of Plate	m
R	2, 3, 5, 8	Reflection Coefficient	$-$
R	4	Amplitude Difference	$-$
R_1	2	Inside Radius Spindle	m
R_2	2	Outside Radius Spindle	m
R_F	4	Reflection Factor	$-$
R_{res}	5	Reflection Coefficient When Perfectly Matched	$-$
R_z	8	Mechanical Impedance	kgm^2/s^3A^2
SMC	7	Dimensional Parameters Couette Viscometer	$-$
SSI	8	Shear Stability Index	$-$
t	2	Temperature	C
T	2	Torque	N/m
T	3	Transmission Coefficient	$-$
t	3	Thickness	m
t	3, 5, 6, 7	Time	s
T	6	Time Period	s
T	8	Temperature	C
t_m	7	Thickness of Matching Layer	m
T_R	8	Reference Temperature	C
t_t	3	Thickness of Transducer	m
T_0	8	Initial Temperature	C
TK	7	Dimensional Parameters Couette Viscometer	$-$
u	6, 8	Velocity Vector	m/s
U	6	Velocity	m/s
u_{fluid}	6	Velocity of Fluid	m/s
u_i	5, 8	Incident Velocity	m/s
u_q	2	Velocity of Oscillator	m/s
u_r	5	Reflected Velocity	m/s
u_{solid}	6	Velocity of Solid	m/s
u_t	5, 8	Transmitted Velocity	m/s
v	2, 6	Velocity	m/s
V	2	Volume	m^3
v	4	Sliding Speed	m/s
V	6	Velocity Flow Field	m/s
V	8	Applied Voltage	V
Y	4	Amplitude Change of Tuning Fork	m
y	6	Distance from Plate	m
z	5, 6, 8	Acoustic Impedance	kg/m^2s

Symbol	Chapter	Description	Units
z_l	2, 3, 4, 6	Acoustic Impedance of Liquid	kg/m^2s
z_Q	2, 4	Acoustic Impedance of Oscillator	kg/m^2s
z_s	3, 6	Acoustic Impedance of Solid	kg/m^2s

Chapter 1

Introduction

This chapter begins by discussing the motivation for this thesis. It notes how the viscosity of lubricating oil is not one singular value and is dependant on many factors, including the shear rate, and shows how vital it is to complete viscosity measurements at the same shear rate that the lubricants will experience in-situ. This chapter further discusses lubricant depletion, highlighting the need to complete regular, if not continuous measurements. It is suggested that viscosity measurements be completed using the reflectance method from an ultrasonic shear wave. The aims and objectives of this project are then stated, before each chapter in this thesis is briefly outlined.

1.1 Statement of the Problem

To reduce the amount of friction and wear between surfaces in relative motion, a lubricant is used. The most important characteristic of a lubricant is its viscosity, as it determines the distance that the components are separated. When the viscosity is too low, the components will not be adequately separated, and wear will occur. If the viscosity is too great, the components will not experience wear; however, energy will be lost, reducing the efficiency of the system.

Lubricating oils are a combination of a base oil and an additive package. The base oil is used to provide sufficient viscosity to separate the components. The additive package adds further functionality such as reducing corrosion and wear and adding viscosity stability over different temperatures. The base oil is typically Newtonian, whereas the additive package is non-Newtonian, and when combined the mixture is non-Newtonian. As additive technology has advanced, as shown in Figure 1.1, so has the complexity of the lubricating oil. It is therefore extremely difficult to predict the behaviour of the lubricant and experimental measurements are required.

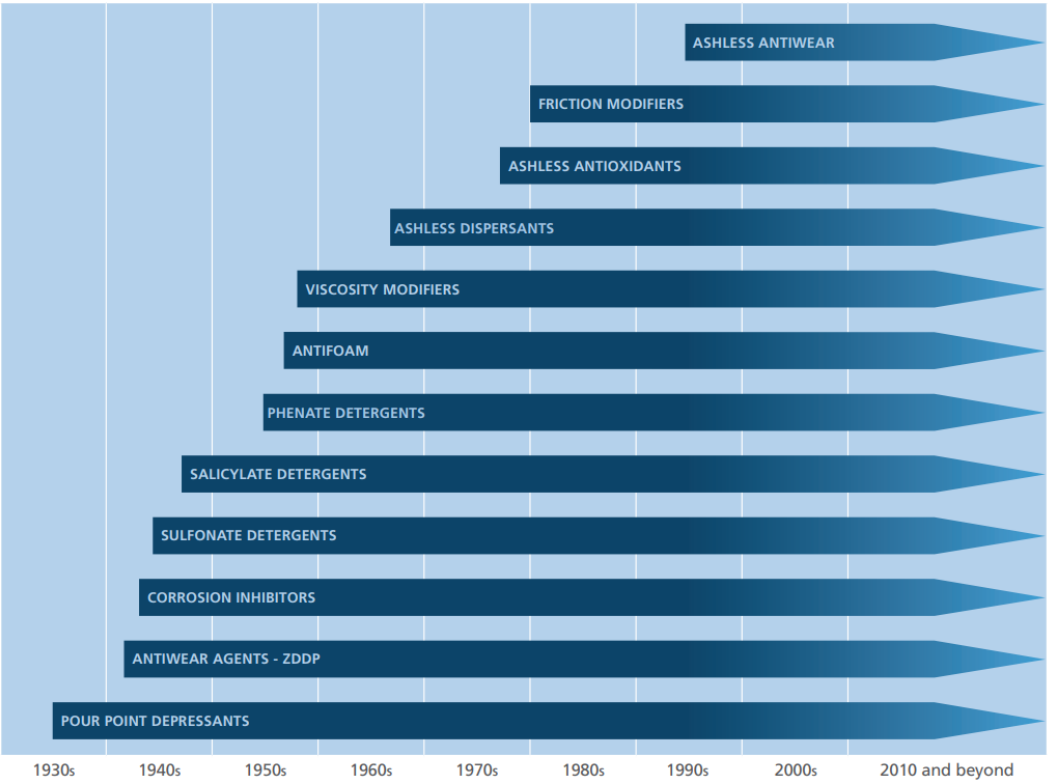

Figure 1.1: Timeline of main lubricant additives. (ATC Europe, 2016)

A non-Newtonian lubricant is a viscoelastic fluid where the viscosity of the fluid is dependent on the shear rate that the fluid experiences. For a typical shear thinning non-Newtonian fluid, the relationship between the shear rate and the viscosity is split into three zones and is shown in Figure 1.2. This diagram shows that at a particular shear rate, the viscosity will reduce.

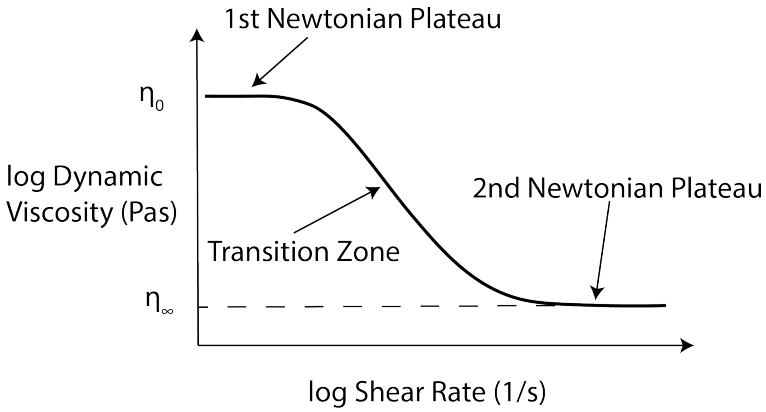

Figure 1.2: Typical viscosity shear rate curve for a shear thinning fluid.

The shear rate when the transition zone begins and ends, and the rate of this reduction of viscosity, is dependant on many factors, including temperature, pressure, and the composition of the lubricating oil. An example of the viscosity measurements completed over a range of shear rates for a diesel engine oil is shown in Figure 1.3.

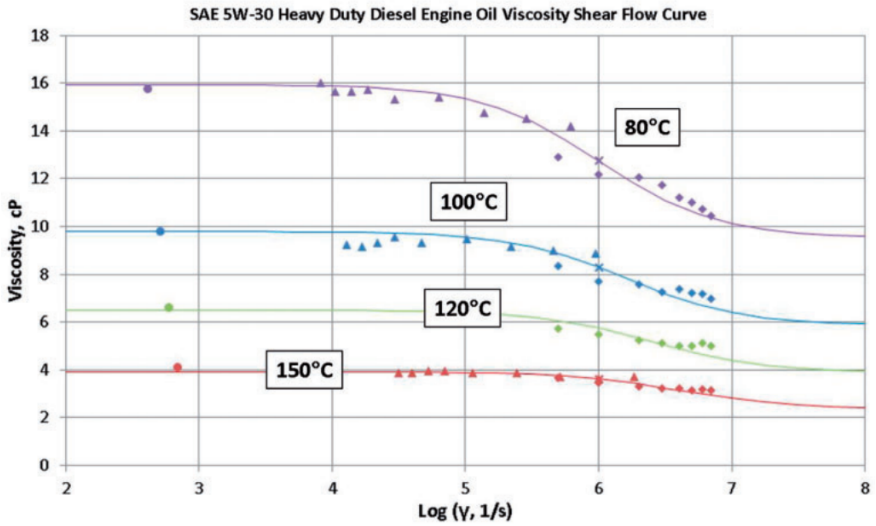

Figure 1.3: Relationship between viscosity and shear rate for SAE 5W-30 heavy duty diesel engine oil at different temperatures.(Taylor et al., 2017)

Taylor et al. (2017) recently produced a study collating investigations into the shear rates in engineering systems, and found that the maximum shear rate experienced in a journal bearing is $5 \times 10^6 s^{-1}$, whilst in a piston ring, is $2 \times 10^7 s^{-1}$, and for a valve train the lubricant can be subjected to shear rates as great as $2 \times 10^8 s^{-1}$. When comparing this information to Figure 1.3, it is shown that the lubricating oil will have experienced a shear rate greater than the first Newtonian plateau, this will lead to a decrease in viscosity. If using a low shear viscometer to complete this measurement, the viscosity measured would not produce an accurate representation of the performance of the viscosity in-situ. This highlights the importance of measuring the viscosity at shear rates comparable to those that the lubricating oil will be subjected.

In addition to this, lubricating oil will deteriorate over time, causing the viscosity to change. The deterioration is created by the stressful environment in which they are operating and will cause the additives to degrade through a series of chemical reactions (Nguele et al., 2014). An example of this viscosity change for an engine oil when in use is shown in Figure 1.4.

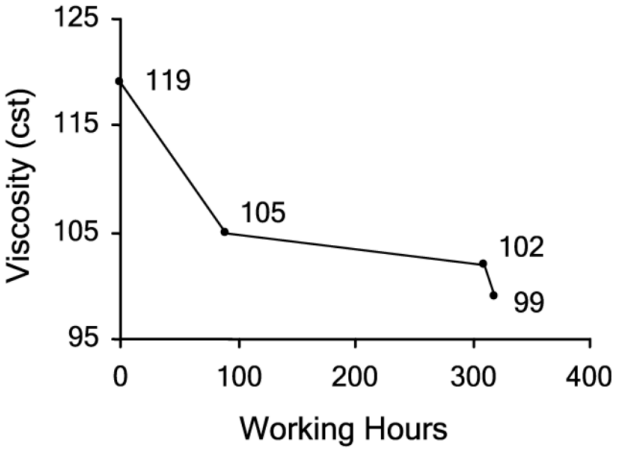

Figure 1.4: Viscosity versus working hours for an engine oil. (Kumar et al., 2005)

As will be further discussed in Chapter 4, there have been developments where conventional viscometers have been adapted for high shear measurements. These viscometers are very expensive and require measurements to be completed ex-situ.

A technology currently available to complete in-situ high shear measurements is the shear reflectance ultrasound technique (Schirru, 2016). This measurement technique has advantages including low cost, intrinsically high shear rates, small installation area and sensitive components being located away from the measurement interface to allow for readings in harsh environments. Current work using this method has produced reliable results for Newtonian fluids; however, further investigation of the shear rate is required to successfully measure the viscosity of non-Newtonian fluids.

1.2 Aim and Objectives

This work aims to develop the core technology for the application of an in-situ viscometer that can perform measurements of Newtonian and non-Newtonian fluids at high shear rates, comparable to the shear rates it will experience in a typical engineering system, and over an extensive shear rate range. This work focuses on measurements completed at a single temperature due to the complexity of measurements over a range of temperatures, including the contraction and expansion of components, and the complex relationship between key ultrasound characteristics and temperature.

The objectives of this thesis are:

1. Develop a mathematical model to enable viscosity information to be retrieved from the shear ultrasound reflection coefficient by combining the three layered and rheological models. This information will then be used to complete a sensitivity analysis at a range of different frequencies.

2. Develop a mathematical model to increase the understanding of the shear rate exerted on the oil from the ultrasound wave by adapting Stokes' Second Problem, which models the velocity profile of a fluid when placed on an oscillating elastic plate. The effect of frequency on the shear rate will then be determined and compared to the Cox-Merz rule.

3. Build a viscometer based on the current ultrasound technology to successfully measure oil viscosity over an extensive shear rate range using shear ultrasound technology. This viscometer should be able to complete measurements over the frequency range 1 - 10 MHz.

4. Validate the viscosity model by comparing oscillatory measurements using the ultrasound viscometer and low shear steady shear measurements from a Couette viscometer, for both Newtonian and non-Newtonian fluids.

5. Evaluate the shear rate model by comparing oscillatory measurements using the ultrasound viscometer and steady shear measurements from an ultra shear Couette viscometer. This will be done by successfully measuring the shear rate exerted on the fluid samples from the matching layer ultrasound viscometer.

1.3 Thesis Layout

This thesis has been sectioned into nine parts, with the theory and introduction sections at the start, leading into the mathematical models, and finally, the experimental measurements and comparison with the mathematical models.

- **Chapter 2: Introduction to Viscosity.** This chapter defines viscosity and how it will change when subjected to certain conditions. The relationship between viscosity and shear modulus is derived and shows how the measurements are related to non-Newtonian fluids. Finally, standard measurement techniques to measure viscosity are described and the relationship between the fluids viscosity and the apparatus parameters are noted.

- **Chapter 3: Ultrasound Wave Theory.** In this chapter, the basics of ultrasound theory is presented, with particular emphasis placed on the reflection coefficient and its relationship with fluids acoustic impedance. Methods for emitting and receiving signals are noted and the important parameters of the received signal are described.

- **Chapter 4: Literature Review.** This chapter reviews previous viscometers. The chapter is split into three main sections; the first is standard conventional viscometers that have been adapted for high shear rate measurements, the second

is in-situ viscometers, and the third is ultrasound viscometers. The chapter finishes by comparing the different viscometers, justifying the direction of this thesis.

- **Chapter 5: A Three Layered Ultrasonic Model for Viscoelastic Fluids.** In this chapter, a novel mathematical model for a two and a three-layered system is developed that allows for a relationship between the pressure reflection coefficient and viscosity for Newtonian and non-Newtonian fluids. A sensitivity study is completed on the models showing how different parameters affect the reflection coefficient.

- **Chapter 6: Determination of Liquid Shear Rate.** This chapter uses Stokes' second problem to develop a mathematical model that defines the shear rate for a Newtonian fluid being subjected to a shearing force from an oscillating wave. A sensitivity analysis is also completed on this model, showing how different parameters affect the shear rate.

- **Chapter 7: Experimental Approach and Viscosity Measurements.** This chapter details the components of a matching layer ultrasound viscometer. Several studies are completed where the signal input parameters are changed, and the reflection coefficient is measured, allowing for optimisation of the viscosity measurements. Finally, measurements are completed on Newtonian and non-Newtonian fluids using the multiple matching layer ultrasound viscometer. The results are compared to low shear rate viscosity measurements completed on a Couette viscometer.

- **Chapter 8: Determination of Ultrasonic Shear Rate.** In this chapter, the mathematical model developed in Chapter 6 is investigated. The input parameters of the shear rate model are measured and varied and the viscosity of lubricating oil is monitored. The shear rate model is used to measure environmentally acceptable lubricants (EALs), and the results are compared to the Cox-Merz model. From this investigation the lubricating oils used in this thesis are plotted on a viscosity shear rate figure.

- **Chapter 9: Conclusions.** In this chapter the results from the previous chapters are collated and summarised, and suggested further work is outlined.

Chapter 2

Introduction to Viscosity

This chapter gives a definition of viscosity, the factors which can change the viscosity, and laboratory tools that can be used to measure this important parameter. This chapter also gives a brief introduction to common additives that make up lubricating oil.

2.1 Viscosity

Viscosity is a measure of the resistance of a fluid to deformation at a given rate. It is caused by the internal friction of the fluid caused by molecules and particles sliding against each other. A common way to define viscosity is by the shear stress, τ, and shear rate, $\dot{\gamma}$, that is exerted on the fluid. Figure 2.1 shows two plates that are separated by a fluid with a distance, h. The bottom plate is fixed and remains stationary, and the top plate, with an area, A, is subject to a force, F, which moves the plate with velocity, V.

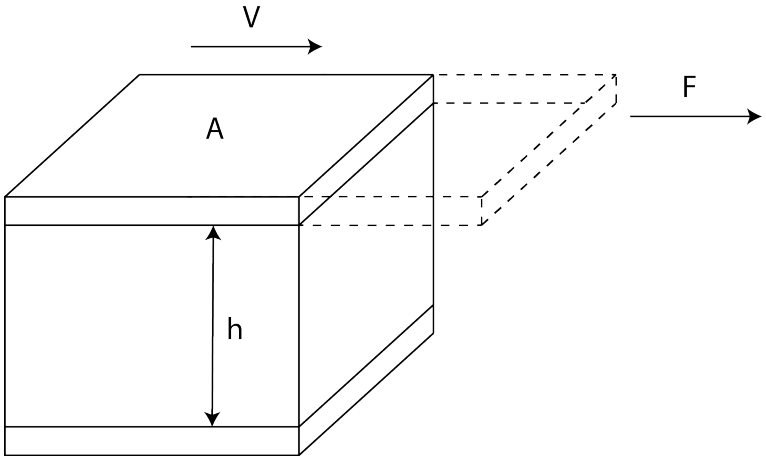

Figure 2.1: Newtonian viscosity model.

Using this analogy to represent a fluid being sheared, the shear stress and shear rate are defined in Equations 2.1 and 2.2, with units N/m^2 and s^{-1} respectively.

$$\tau = \frac{F}{A} \tag{2.1}$$

$$\dot{\gamma} = \frac{V}{h} \tag{2.2}$$

Newton's law of viscosity states that the ratio of shear stress to shear rate is a constant, where the constant is equal to the dynamic viscosity. This law allows for a direct relationship between dynamic viscosity, η, shear stress and shear rate, as shown in Equation 2.3. The unit of dynamic viscosity is Ns/m^2, or more commonly Pas.

$$\tau = \eta\dot{\gamma} \tag{2.3}$$

The kinematic viscosity is also used to describe a fluid's resistance to motion. Kinematic viscosity describes how fast the fluid is moving when a certain force is applied, whereas the dynamic viscosity gives information on the force required to make the fluid flow at a certain rate. The kinematic viscosity, ν, has units, m^2/s, and is related to the dynamic viscosity by the fluid's density, ρ.

$$\nu = \frac{\eta}{\rho} \tag{2.4}$$

The viscosity is an extremely important parameter in engineering systems. The significance can be demonstrated using the Stribeck curve, Figure 2.2, which describes the relationship between friction, load, viscosity and entrainment velocity. One of the main purpose of a lubricating oil is to separate surfaces that are moving relative to each other by stopping the asperities of the surfaces rubbing. When the asperities rub it causes wear, this is called boundary lubrication, and is the regime where the maximum friction coefficient occurs, regime 1. When a lubricating oil with a sufficient viscosity is introduced into the system, mixed lubrication takes place, regime 2. In this regime a much smaller amount of asperity contact occurs because the load is also supported by the lubricating oil. The mixed lubrication regime produces the smallest friction coefficient. As the distance between the surfaces increase, due to an increase in the viscosity or velocity, the asperities on each surface do not touch and a full oil film is formed, regime 3. This is called the hydrodynamic regime and no wear occurs. The unwanted increase in the friction coefficient is caused by viscous drag, and reduces the efficiency of the system.

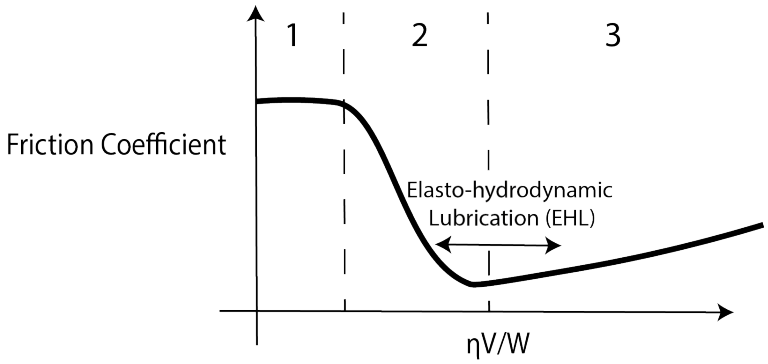

Figure 2.2: Stribeck curve.

2.2 Viscosity and Shear Rate

Newton's equation for viscosity, Equation 2.4, is only true when the viscosity is independent of shear rate. Fluids where this assumption is true are called Newtonian fluids. Examples of Newtonian fluids include water, acetone and standard calibration oils. The majority of fluids that are used in engineering applications are non-Newtonian, and for engineering applications, lubricating oils are subject to shear. As an example, the shear rates in an automotive engine can vary massively, from $10^2 - 10^7 s^{-1}$, as shown by Bartz (1976) in Figure 2.3. It is therefore extremely important to understand the relationship between viscosity and shear rate.

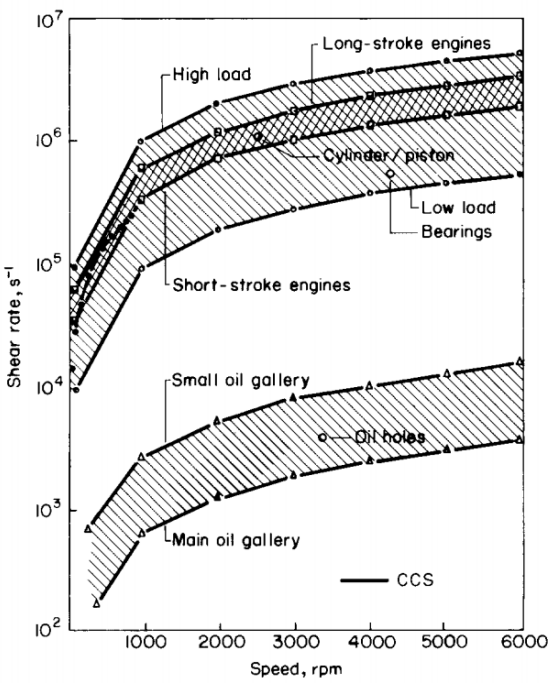

Figure 2.3: Bartz (1976). Shear rates in an internal combustion engines.

The relationship between shear stress and shear rate, and viscosity and shear rate for some common non-Newtonian fluids is shown in Figure 2.4 and Figure 2.5, respectively.

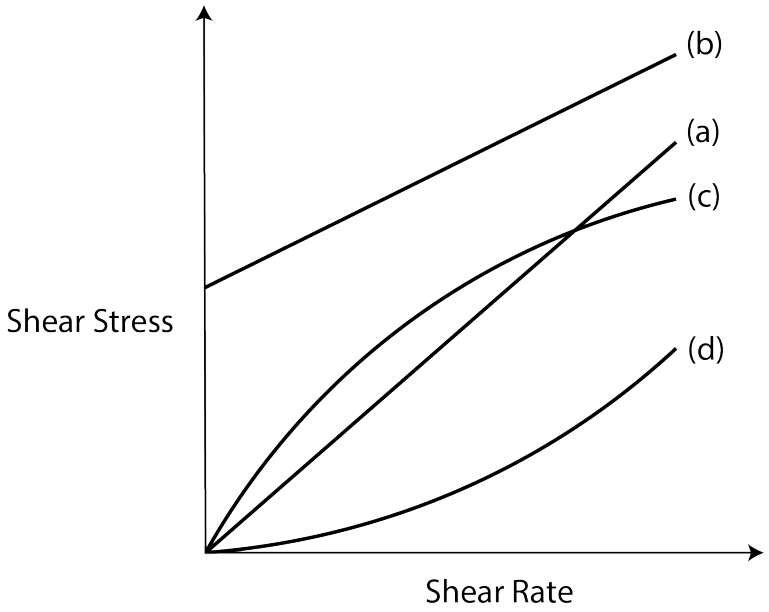

Figure 2.4: Flow curves for model viscous materials. (a) Newtonian fluid; (b) Bingham fluid; (c) Shear thinning fluid; (d) Shear thickening fluid.

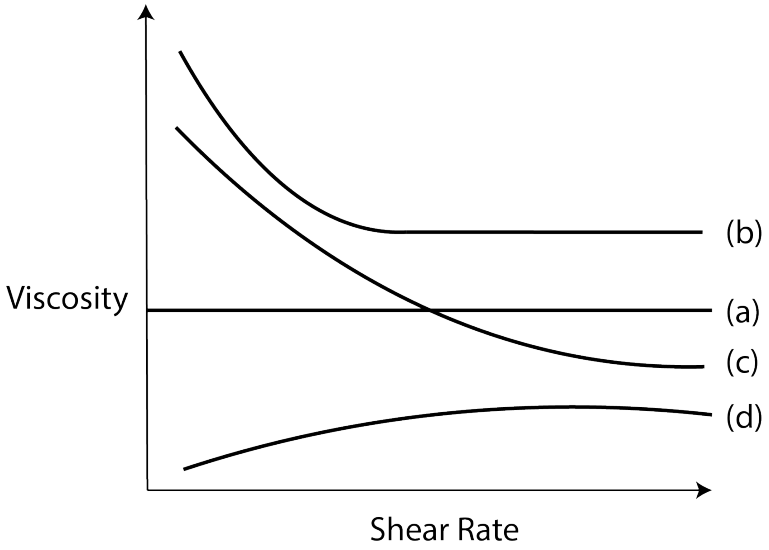

Figure 2.5: Viscosity shear rate curves for model viscous materials. The curves are labelled as in Figure 2.4.

A Bingham fluid is one which behaves as an elastic body when a low amount of stress is applied, but when this stress has been overcome it acts as a Newtonian fluid. An example of an everyday Bingham fluid is toothpaste.

The shear thinning and shear thickening fluids are used to describe a fluid when the relationship between the shear stress and shear rate is non linear, and the viscosity decreases and increases with shear rate, respectively.

Shear thinning behaviour can be explained by looking at the polymer chains or elongated particles. When a shearing force is applied to the fluid the polymer chains

elongate and align, as shown in Figure 2.6. When aligned the particles present a decrease in resistance to motion and therefore the viscosity decreases.

Shear thickening behaviour is far less common than shear thinning, and is mostly undesirable. It often occurs in an aqueous solution where a shear force cause the water to displace and the particles move closer together, increasing the resistance to motion.

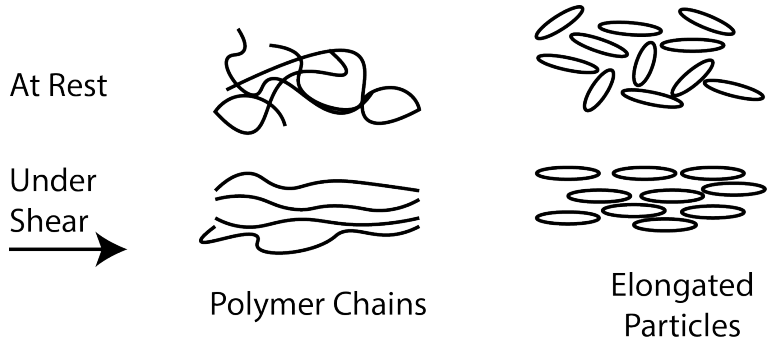

Figure 2.6: Shear thinning behaviour of polymer chains, droplets and particles.

2.2.1 Relationship Between Shear Modulus and non-Newtonian Fluids

Non-Newtonian fluids are also known as viscoelastic fluids as they display a mixture of viscous and elastic behaviour when sheared, whereas Newtonian fluids only present viscous behaviour. The shear modulus, G, describes a fluids viscoelastic behaviour, and shows the relationship between the shear stress, τ, and shear strain, γ.

$$G = \frac{\tau}{\gamma} \tag{2.5}$$

When referring to the two parallel plates analogy as shown in Figure 2.1, the shear strain is equal to the distance moved in the x direction divided by the distance between the plates, h. The relationship between dynamic viscosity and shear modulus can be derived from Equation 2.3 and Equation 2.5, where ω is equal to the angular velocity, $\omega = 2\pi f$.

$$\eta = \frac{G}{\omega} \tag{2.6}$$

The complex shear modulus, G^*, describes the entire viscoelastic behaviour of the sample and is related to the complex shear stress, τ^*, and the shear strain, γ.

$$G^* = \frac{\tau^*}{\gamma} \tag{2.7}$$

The storage modulus, G', represents the elastic portion of the viscoelastic behaviour. The elastic portion is stored in the deformed material and this energy is used to reform the structure to its original shape.

The loss modulus, G'', represents the viscous part of the viscoelastic behaviour. Viscous behaviour is due to the internal friction, which creates heat that is absorbed by the sample.

The phase shift, δ, is used to show the relationship between the viscous and elastic behaviour. The phase shift can be described by again employing the two plate analogy, Figure 2.1. If the top plate is being driven by a force, the bottom plate will have to exert a force in the opposite direction to remain in a fixed position. The phase shift is the time lag between the force applied to the top plate and the force applied to the bottom plate. For an ideally elastic material the phase response will be 0°, and for an ideally viscous material the phase response will be 90°. The loss factor, $\tan\delta$ is often used to describe the relationship between the viscous and elastic behaviour.

$$\tan\delta = \frac{G''}{G'} \tag{2.8}$$

The relationship between the complex shear modulus, loss modulus, storage modulus, and phase shift is shown in Equation 2.9 - 2.11, and presented in Figure 2.7.

$$G^* = G' + iG'' \tag{2.9}$$

$$G' = |\tau^*|cos\delta \tag{2.10}$$

$$G'' = |\tau^*|sin\delta \tag{2.11}$$

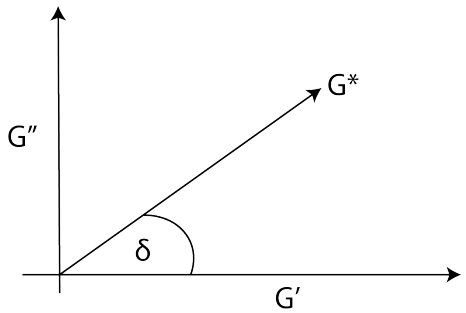

Figure 2.7: Argand diagram of the complex shear modulus.

2.2.2 Engine Oil and Shear Rate

For a fluid such as engine oil, the viscosity-shear rate relationship can be split into three sections as shown in Figure 2.8. There is an initial Newtonian plateau where the viscosity remains constant as the shear rate increases. The viscosity at this first Newtonian plateau is often called zero viscosity, η_0. As the shear rate increases, the viscosity reduces because the shear rate changes the structure of the fluid. The particles

become aligned and the polymers are stretched which leads to a decrease in viscosity. The section where the viscosity is decreasing with an increasing shear rate is called the transition zone. The fluid then reaches a point where an increase in shear rate no longer causes a decrease in viscosity as the fluid particles are fully aligned and the elongated particles are fully stretched, the second Newtonian plateau. The viscosity at this second Newtonian plateau is called the infinite viscosity, η_∞.

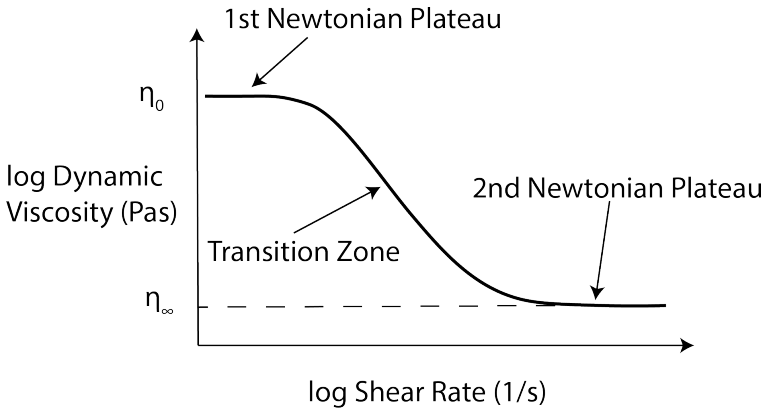

Figure 2.8: Viscosity - shear rate curve for a shear thinning fluid.

There are many mathematical models that relate the shear rate and the viscosity for an engine oil including the Power Law model and the Carreau-Yasuda model (Yasuda et al., 1981). The relationship between these models can be seen in Figure 2.9.

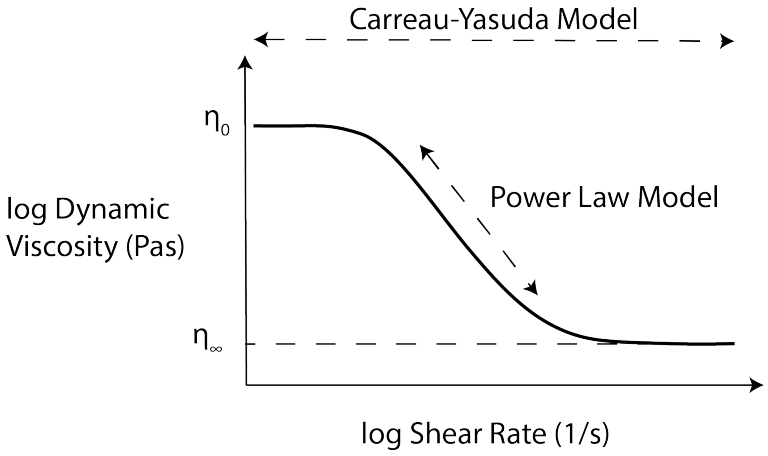

Figure 2.9: Mathematical models for the viscosity - shear rate curve for a shear thinning fluid.

The Power Law model, also known as the Ostwald de Waele relationship, is the simpler of the two models. It is used to model the viscosity of shear-thinning fluids where the fluid does not have a Newtonian plateau region, either at low or high shear rates. The model is related to the viscosity of the fluid, η, the flow consistency index, K, and the power law constant, n, Equation 2.12. If n is less than 1, this indicates a

pseudoplastic fluid, if equal to 1 this indicates a Newtonian fluid, and if greater than 1 this indicates a dilatant fluid. This model is often used to model fluids such as low-viscosity dispersions.

$$\eta = K\dot{\gamma}^{n-1} \tag{2.12}$$

The Carreau-Yasuda model is more complex than the Power Law model and is used to model pseudoplastic flow where there are asymptotic viscosities. This model calculates the viscosity, η, using the viscosity at an infinite shear rate, η_∞, viscosity at zero shear rate, η_0, the relaxation time of the fluid, λ, the shear rate, γ, the power index, n, and the index controlling the transition from the first Newtonian plateau to the power law region, a. It should be noted that the variables are independent of each model. This model is often used to measure fluids that shear thin such as polymer melts and polymeric solutions.

$$\eta = \eta_\infty + \frac{\eta_0 - \eta_\infty}{(1 + (\lambda\dot{\gamma})^a)^{\frac{1-n}{a}}} \tag{2.13}$$

2.2.3 Types of Shear

The two common types of shear are steady and oscillatory shear. Steady shear measurements operate with a continuous rotation and oscillatory shear measurements operate with a sinusiodal displacement, as shown in Figure 2.10. The two measurement types are often related by the Cox-Merz rule (Cox and Merz, 1958) and is shown in the function below, where $\dot{\gamma}$ is the steady shear rate and ω is the angular velocity. This function states that the steady shear viscosity at a given shear rate is equal to the oscillatory viscosity at the same angular frequency.

$$\eta(\dot{\gamma}) = \eta(\omega) \tag{2.14}$$

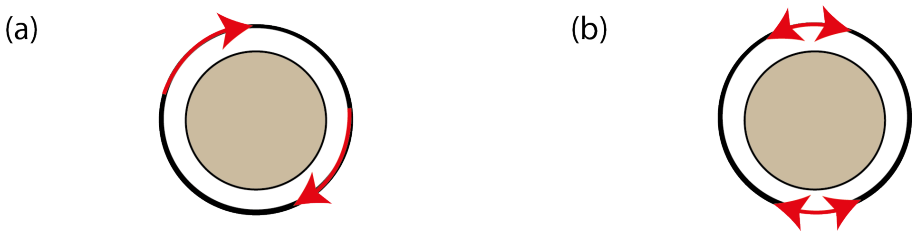

Figure 2.10: *a)* Steady and *b)* oscillatory shear.

2.3 Viscosity and Temperature

An increase in temperature leads to a decrease in viscosity. As the temperature increases the molecules gain energy and the strength of the bonds between these molecules

weaken, reducing the viscosity. The most common method used to find the kinematic viscosity at different temperatures for liquid petroleum products is by using the ASTM standard D341-17 (ASTM, 2017), where a line can be drawn between two points where the kinematic viscosity and temperature is known. This line can then be interpolated or extrapolated to find the viscosity at different temperatures. The dynamic viscosity at different temperatures is often calculated by using the Vogel equation (Vogel, 1921), Equation 2.15, where a, b,and c are material constants.

$$\eta = a \exp^{\frac{b}{t-c}} \tag{2.15}$$

2.4 Viscosity and Pressure

If the pressure increases the viscosity of the fluid will increase. As the pressure increases the molecules of the fluid will compress causing an increase in viscosity. The pressure-viscosity relationship is most often calculated using the Barus equation (Barus, 1893), Equation 2.16. In this equation α is the viscosity-pressure coefficient, η_0 is the dynamic viscosity at atmospheric pressure, and P is the pressure applied to the fluid.

$$\eta = \eta_0 \exp^{\alpha P} \tag{2.16}$$

2.5 Engine Oil

An engine oil is a non-Newtonian fluid which is composed of a base oil and an additive package, and often displays the viscosity shear rate relationship as seen in Figure 2.8 .

A base oil is most often a refined crude oil, but can be manufactured synthetically, and is the main factor in determining the viscosity of an engine oil. Base oils can be classified into five categories using the specifications outlined by the American Petroleum Institute (API), depending on the refining method and the properties of the oil (API, 2015).

An additive package is a group of additives combined, where an additive is a chemical that increases the functionality of the engine oil. Details about additives are provided in Section 2.6.

An engine oil is often classified by its viscosity, as is shown in Table 2.1. Some engine oils are classified as multigrade oils, such as 10W30, which is an oil that meets the specification of a low temperature and high temperature viscosity grade.

SAE Viscosity Grade	Low Temperature Cranking Viscosity (mPas)	Low Temperature Pumping Viscosity (mPas)	Low Shear Rate Kinematic Viscosity at 100(C) Min (cSt)	Low Shear Rate Kinematic Viscosity at 100(C) Max (cSt)	High Shear Rate Viscosity at 150(C) Min (cSt)
0W	6200 at -35	60 000 at -40	3.8	-	-
5W	6600 at -30	60 000 at -35	3.8	-	-
10W	7000 at -25	60 000 at -30	4.1	-	-
15W	7000 at -20	60 000 at -25	5.6	-	-
20W	9500 at -15	60 000 at -20	5.6	-	-
25W	13 000 at -10	60 000 at -15	9.3	-	-
8	-	-	4.0	6.1	1.7
12	-	-	5.0	7.1	2.0
16	-	-	6.1	8.2	2.3
20	-	-	6.9	9.3	2.6
30	-	-	9.3	12.5	2.9
40	-	-	12.5	16.3	3.5/3.7
50	-	-	16.3	21.9	3.7
60	-	-	21.9	26.1	3.7

Table 2.1: SAE engine oil viscosity grades (SAE International, 2015).

To reduce the amount of friction and increase the efficiency of internal combustion engines, lubricants are becoming less viscous. This is shown in Figure 2.11, where it is shown that the trend for passenger car motor oil is decreasing in viscosity, and that this trend is expected to continue. To ensure that the lubricants can function at much lower viscosities and retain their protective properties over ever extending drain intervals the additive packages are becoming increasingly complex.

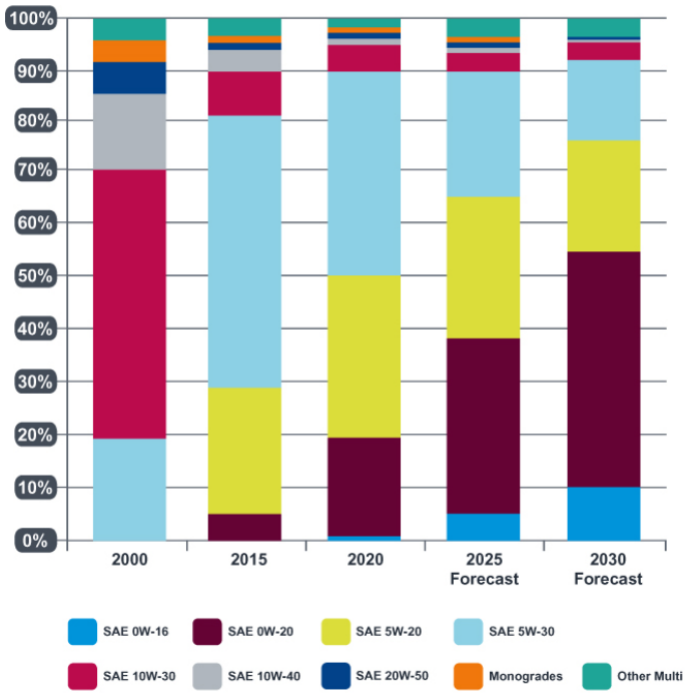

Figure 2.11: Passenger car motor oil viscosity grade trends in North America. (Infineum International Limited, 2009)

2.6 Additive Packages

Additive packages are an extremely important part of lubricating oils as they add greater functionality to the oil. The importance of additive packages to industry can be quantified by viewing the annual turnover of the additive industry. In 2014 the additive industry had a worldwide turnover of approximately €11700 million, with the European market share being approximately €3600 million (ATC Europe, 2016). Unlike most base oils, additive packages are often non-Newtonian, making the lubricating oils non-Newtonian. Below is a brief introduction to some commonly used additives.

2.6.1 Friction Modifiers

There are two main types of friction modifiers; organic friction modifiers (OFMs) and organo-molybdenum friction modifiers (Fujitsu and Griffiths, 2006). Friction modifiers were originally used for limited slip gear oils, automatic transmission fluids, slideway lubricants and multipurpose tractor fluids to meet industry requirements for a smooth transmission from static to dynamic condition, a reduction in noise, frictional heat and start up torque (Rudnick, 2009). Friction modifiers are now used to decrease or increase the viscosity of an oil.

It is widely agreed that OFM's work by absorbing on rubbing metal surfaces to form monolayers (Tang and Li, 2014). The monolayers strength is due to the weak

van der Waal interaction between opposing hydrocarbon chains at the interface. The monolayers make a boundary film which prevents metal on metal contact, reducing friction.

One of the most common types of friction modifiers is organic friction modifiers, such as fatty acids which are often derived from fats and vegetable oils. As the trend is towards a reduction in viscosity of lubricating oils, friction modifiers are increasingly used to retain the required protection of the surfaces in relative motion.

2.6.2 Pour Point Additives

Pour point additives are used to reduce the pour point of an oil. The pour point is the minimum temperature at which an oil will pour. This additive is often used when the oil is subjected to low temperatures.

Examples of a commercially available pour point additive are alkylaromatics and aliphatic polymers. This type of additive is increasingly being used in additive packages as the modification in flow characteristics, that is provided by using pour point additives, allows for a greater choice of base stock selection

2.6.3 Extreme Pressure Additives

Extreme pressure additives are used to reduce metal/metal interaction by creating a thin film. It does this by the polar head from the additives interacting with the metal surface, and the tail interacting with the base oil, creating a boundary. Most of the additives are activated within a certain temperature range.

One of the most common examples of an extreme pressure additive is molybdenum disulfide. The size of these molecules is approximately 1 – 4 nm in length, when made synthetically. Due to the increased pressure in modern engines, this additive is becoming increasingly important

2.6.4 Viscosity Index Improvers

Viscosity index improvers (VIIs) reduce the amount a viscosity varies due to its change in temperature. This is a key factor when a machine starts as it allows for the lubricant to flow freely around the mechanical components and when the machine is at higher temperature it allows for the lubricant to keep its viscosity, providing the minimum film thickness to separate the moving components.

Viscosity modifiers are larger than most other types of lubricant additives, with a size of approximately 30 μm. Modern engines function of an ever-increasing range of shear rates, and to maintain an adequate viscosity, viscosity modifiers are becoming increasingly important.

2.6.5 Antioxidants

When oxidation occurs, organic acids are produced. The organic acids are extremely corrosive and lead to deterioration in the non-ferrous metals in the system. Inhibitors stop the formation of the organic acids by acting as a peroxide or as a free radical trap, disrupting the chain propagating steps of the oxidative process. An example of a widely used antioxidant is aromatic amines or hindered phenols.

2.6.6 Antiwear Additives

Antiwear additives are used when hydrodynamic lubrication is not possible. The additive reduces friction by adhering to the metal surface, creating a layer between the metal/metal contact.

The most common antiwear additive and the most common lubricant additive is zinc dithiophosphates (ZDDP). The approximate size of a ZDDP molecule is 7.2nm. However, ZDDP, is slowly being weened out of, due to its high phosphate content which is harmful to catalytic converters and therefore the maximum concentration of ZDDP has been reduced.

2.6.7 Detergents

Detergents are used to reduce engine deposits and provide anti-corrosion and anti-rust protection. The detergent works by neutralising acids formed in the combustion process which can cause corrosion, wear and polymerisation which leads to a viscosity increase and a resin formation. A common example of a detergent is calcium sulfonate which can range from 15 – 500 nm in length.

2.6.8 Dispersents

Dispersants are used to suspend the soot and sludge, stopping large particles conglomerating. The dispersant can carry out this function as it consists of a polar head which attracts to the soot particle. Due to the aim towards low viscosity lubricating oils, traditional high molecular weight dispersants are no longer suitable. However due to the increasing soot, sludge, and cleanliness requirements they are becoming increasingly important.

2.7 Laboratory Viscometers

For the reasons described earlier in this chapter it has been shown that it is vital to know the viscosity of lubricating fluids. Figure 2.12 shows a classification of laboratory viscometers.

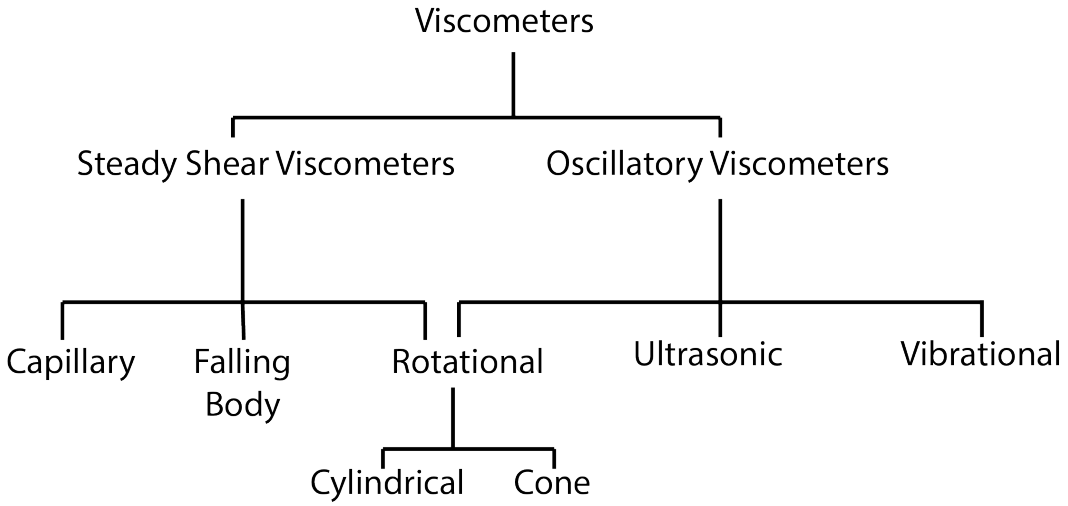

Figure 2.12: Viscometer classification.

In this section the mechanism of these viscometers is described and the relationship between the dimensional parameters of the apparatus and the viscosity is noted. The advantages and disadvantages of these viscometers is highlighted in Chapter 4.

2.7.1 Capillary Viscometer

This viscometer measures viscosity by introducing a fluid in the left tube of the capillary viscometer. Due to the surface tension and adhesive forces between the fluid and the capillary wall, fluid is drawn up through the tube on the right. The time that it takes for the the fluid to flow from A to B is directly related to its kinematic viscosity. This viscometer is sometimes called the U-tube viscometer, due to its shape, or the Ostwald viscometer, after its German inventor. The advantage of this instrument is the lack of moving parts and the simple relationship to the fluid's viscosity. Common sources of error are angular misalignment of the tube, temperature inaccuracy and cross contamination due to the difficulty in the cleaning procedure. The most common and simple equation used to calculate the viscosity from this viscometer is shown in Equation 2.17, where g is the acceleration due to gravity, h is the height of the capillary, a is the diameter of the capillary, l is the length of the capillary and V is the volume of liquid dispensed (Viswanath et al., 2007).

$$\nu = \frac{\pi g h a^4}{8LV} \tag{2.17}$$

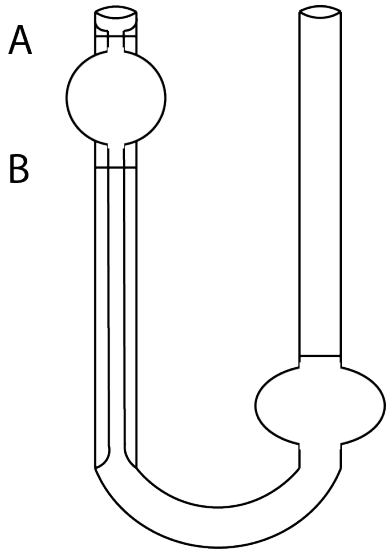

Figure 2.13: Capillary viscometer.

2.7.2 Falling Body Viscometer

A falling body viscometer determines the dynamic viscosity of a fluid by measuring the time that it takes a body to fall through a sample. This time is related to viscosity using the Höppler principle. If a ball is being used as the body which is falling, the equation for this relationship is shown in Equation 2.18, where r is the radius of the ball, v is the velocity of the ball, g is the gravitational acceleration and ρ_b and ρ is related to the density of the ball and the fluid respectively (Viswanath et al., 2007). This instrument allows for quick repeat experiments by being able to be turned on its axis by 180°, and has an accuracy of 2%. Unlike other viscosity measurements described in this section, the fluid sample has to be transparent.

$$\eta = \frac{2gr^2(\rho_b - \rho)}{9v\pi} \tag{2.18}$$

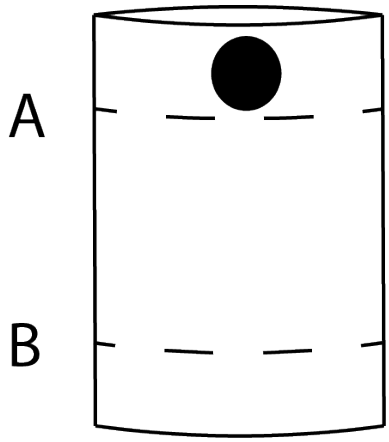

Figure 2.14: Falling body viscometer.

2.7.3 Rotational Viscometer

The rotational viscometer is able to measure the dynamic viscosity of Newtonian and non-Newtonian fluids. It composes of a drive motor - to rotate the spindle, and a force sensor - to measure the torque required to drive the spindle. According to the ASTM standard D2196-10 (ASTM, 2018), a rotational viscometer has 95 percent confidence levels. The two common types of rotational viscometers are the cone on plate and cylindrical viscometers.

2.7.3.1 Cone On Plate Rotational Viscometer

This type of viscometer uses a cone which is placed on a flat plate, as shown in Figure 2.15. The angle between the cone and the flat plate is, α, and is typically very small. Fluid is then introduced between the cone and the plate and the cone is rotated with an angular velocity, ω. The viscosity, η, is then calculated using Equation 2.19, where T is the torque and R is the radius of the plate (Whorlow, 1992).

$$\eta = \frac{3T\alpha}{2\pi R^3\omega} \tag{2.19}$$

The cone on plate rotational viscometer is well suited to measure the viscosity of non-Newtonian fluids as the shear is practically constant throughout the sample.

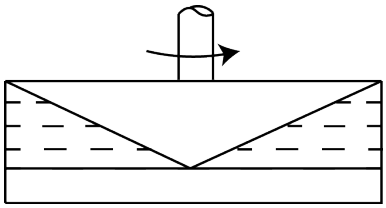

Figure 2.15: Cone on plate rotational viscometer.

2.7.3.2 Cylindrical Rotational Viscometer

The cylindrical rotational viscometer, consists of a spindle and a cup where the test fluid is placed in the cup and the spindle is submerged in the test fluid as shown in Figure 2.16. The torque, T, that is required to drive the spindle is related to the dynamic viscosity, η, by Equation 2.20, where ω is the angular velocity and the dimensional parameters of the spindle, height of the spindle, h, inside radius R_1 and outside radius R_2 (Viswanath et al., 2007). The shear rate can be controlled in multiple ways with the most common by changing the velocity of the motor or the dimension of the spindle.

$$\eta = \frac{T(R_2^2 - R_1^2)}{4\pi R_1^2 R_2^2 h\omega} \tag{2.20}$$

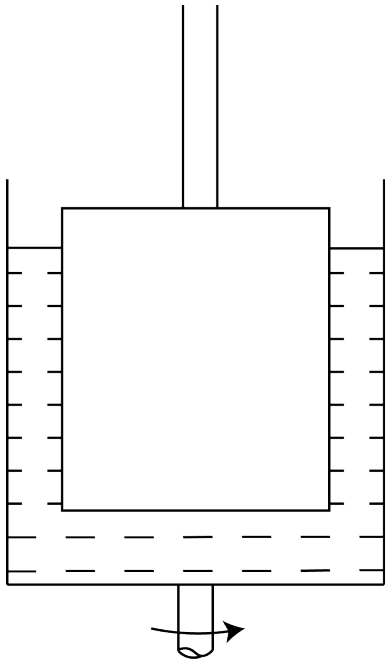

Figure 2.16: Concentric cylinder rotational viscometer.

2.7.4 Vibrational Viscometer

There are many different variants of vibrational viscometers, all of which use dynamic motion to measure the viscosity. The two most common type of vibrational viscometer are the vibrating rod viscometer and the QCM (quartz crystal microbalance). The vibrational viscometer consists of an oscillating component that is in contact with the test sample. Either the displacement of the oscillator is measured, or the change in frequency. The more viscous a sample the greater the change in frequency. This is shown in Equation 2.17, by relating the change in frequency, Δf, to the dynamic viscosity, η, natural frequency of the system, f_0, fluid density, ρ, and density and velocity of the oscillator, ρ_q and u_q, respectively (Keiji Kanazawa and Gordon, 1985).

$$\eta = (\frac{\Delta f}{f_0^{3/2}})^2 \frac{\pi \rho_q u_q}{\rho} \tag{2.21}$$

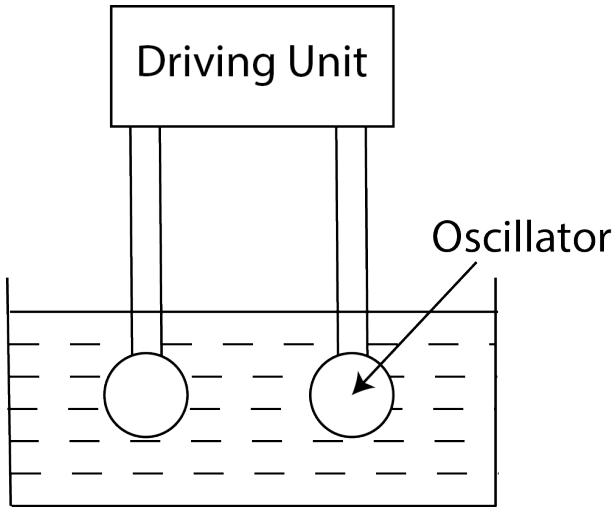

Figure 2.17: Vibrational viscometer.

2.7.5 Ultrasonic Viscometer

Ultrasonic viscometers are a relatively new technology. An ultrasound transducer sends a shear wave into the test fluid where the wave is reflected, Figure 2.18. By dividing the amplitude of the pulsed and received signal, R, this relationship can be related to the acoustic impedance of the liquid, z_l, and acoustic impedance of the quartz, z_Q, Equation 2.22 (Mason and Mcskimin, 1947). As shown in Equation 2.6, the acoustic impedance can be directly related to its dynamic viscosity. For lubricating oils this measurement technique is insensitive and further developments have been suggested by Schirru and Dwyer-Joyce (2016) to increase the sensitivity of the viscometer by introducing an intermediary layer between the elastic plate and the test fluid. Further information about ultrasonic viscometers can be found in Chapter 4.

$$R = \frac{z_Q - z_l}{z_Q + z_l} \tag{2.22}$$

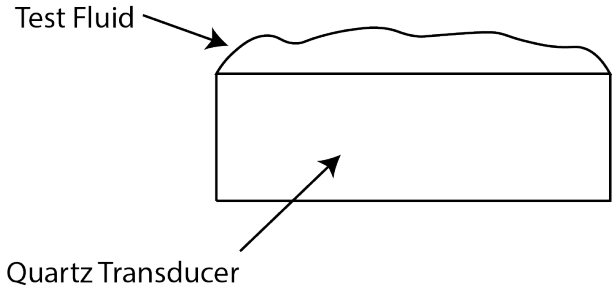

Figure 2.18: Ultrasound viscometer.

2.7.6 Variations of Laboratory Viscometers

Laboratory viscometers have been adapted to complete measurements when subjecting the test fluid to different conditions. Variants of the laboratory viscometers are discussed in greater detail in Chapter 4.

2.7.6.1 High Shear Rate Measurements

One condition that is becoming increasingly important is high shear. The advancement of engines, such as more efficient fuel delivery, higher compression ratios, and onboard computers, has led to engines producing higher output power and speeds, which subjects the lubricating oil to greater shear rates. Lubricating oil has had to develop to stop wear whilst increasing efficiency and functionality at these higher shear rates. This has been done by adding increasingly more additives, the increased use of synthetic oils, and a bias towards low viscosity oils. This means that it is vital to understand the rheological properties for low viscous oils at high shear rates.

An example of this measurement device is the rotational viscometer, where the speed of the rotor has been dramatically increased, such as the Ultra Shear Viscometer (PCS Instruments, 2018), or the capillary viscometer where the fluid is subjected to a greater force, such as the VROC viscometer (RhenSense Inc., 2020).

2.7.6.2 In-situ and Ex-situ Measurements

All the laboratory viscometers listed are ex-situ viscometers. With the advancements of engines, the conditions that the lubricating oil is being subjected to are becoming more extreme, which increasingly affects the viscosity. To complete viscosity measurements using a laboratory viscometer it is necessary to remove the lubricating oil from the application and operating conditions. This reduces the understanding of the rheological properties in-situ due to the difficulty in replicating the harsh operating conditions that the lubricating oil is being subjected to. To overcome this, adaptations have been made to laboratory viscometers to allow them to complete measurements in-situ. This often requires miniaturising the viscometers and increasing the specification.

2.8 Summary

Lubricating oils are extremely effective at reducing the friction in engineering components. They consist of a base oil and an additive package that not only reduces the viscosity but adds many other functions. These lubricating oils are viscoelastic fluids which exhibit non-Newtonian behaviour. As the shear rate changes in each system it is vital to know the viscosity at different shear rates. The shear modulus of a fluid is a useful parameter to show the relationship between the viscous and elastic components

of a non-Newtonian fluid, and this can be directly related to the dynamic viscosity. There are standard laboratory viscometers that can be used to measure the viscosity of lubricating oils to a high degree of accuracy, however these measurements are all taken at a low shear rate. In Chapter 4, variants of the laboratory viscometers will be discussed that allow for measurements in-situ and when exerting the fluid to high shear rates.

2.9 Conclusion

To obtain accurate viscosity information about lubricating oils, the measurements should be completed at conditions that they will experience in-situ, as these conditions will dramatically affect the viscosity of the lubricating oils. This should either be done by replicating the conditions, or completing the viscosity measurements in-situ.

Chapter 3

Ultrasound Wave Theory

In this thesis, an ultrasonic viscometer is used to measure the viscosity of lubricating oil. This chapter presents a general overview of ultrasound theory and gives a brief history of ultrasound developments and applications, before describing their characteristics and means of generation.

3.1 Definition of Ultrasound

Ultrasound is a sound wave that has a frequency between $20kHz - 1GHz$, Figure 3.1. In 1877 the first publication related to ultrasound was released, *The Theory of Sound* by Lord Rayleigh (Strutt, 1877). This publication was closely followed by the development of sonar which led to significant advances in underwater acoustics and transducers (Newman and Rozycki, 1998). In 1937 ultrasound measurements were used in the medical sector; the amplitude of the ultrasound wave was monitored when directed at a brain, measuring bone thickness (White, 1988), and ultrasound waves were used to investigate tissue.

Using ultrasound to detect cracks was first completed in the 1920s. However, it was more widely used in the early 1970s due to the advancements in ultrasound technology and the discipline of fracture mechanics. It is now widely used today to quickly and efficiently detect flaws in materials that the human eye cannot detect. With each previous application, the technology was significantly advanced, enabling there to now be smaller and cheaper probes emitting more stable signals, allowing for more precise measurements.

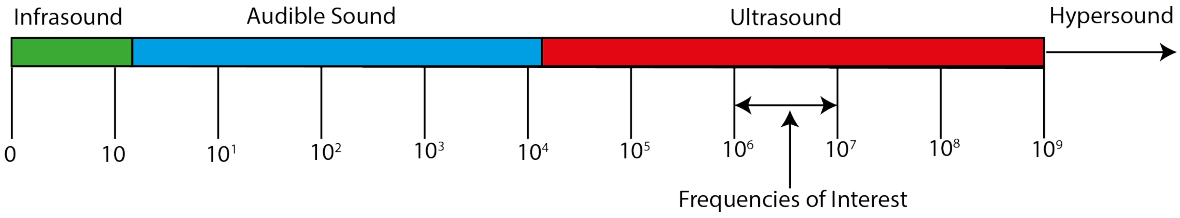

Figure 3.1: Sound waves classified by frequency range.

3.2 Wave Modes

Ultrasound waves propagate the same way as other sound waves: transferring energy to the next particle in the corresponding plane. The amplitude and frequency will remain constant for a perfectly elastic material, and all particles will start to move simultaneously. It should be noted that the particles do not move to the next plane; only the waves characteristics are transferred to corresponding planes.

There are two main modes; longitudinal and shear. The difference between them being their propagation direction. When shear waves travel, they create a perpendicular displacement of the particles to the wave's direction. This means that a shear wave cannot travel very far through liquid or gas as there is little resistance for a driving motion perpendicular to the propagation of the wave. An example of a shear wave is a ripple on the surface of a fluid, or the vibrations in a guitar string when plucked.

Longitudinal waves displace medium parallel to the direction of travel. An example of a longitudinal wave is a sound wave from a conventional sound system. The difference between the wave propagation of a longitudinal and shear wave is illustrated in Figure 3.2, showing the direction of motion in a 2D plane.

Longitudinal and shear are not the only type of wave modes. Other types include Rayleigh, Lamb and Love waves; however, these are outside this thesis's framework.

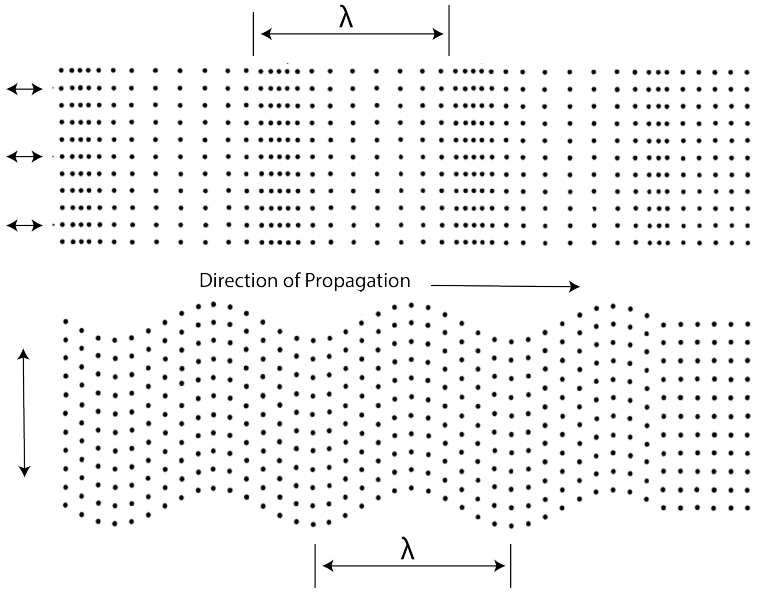

Figure 3.2: Longitudinal (top) and shear (bottom) wave propagation.

3.3 Speed Of Propagation

The speed that a sound wave travels depends on the medium through which it travels and the wave mode. Due to the direction of propagation, a longitudinal wave travels

approximately twice as fast as a shear wave. Table 3.1 shows the propagation speed for shear and longitudinal waves in some typical engineering materials.

Medium	Shear Velocity (km/s)	Longitudinal Velocity (km/s)
Aluminium	3.04	6.42
Nylon, 6/6	1.1	2.6
Mild Steel	3.2	5.9

Table 3.1: Wave velocities in typical engineering components(Cheeke, 2017).

The speed of sound for a shear wave, c_s, is proportional to the shear modulus of the medium, G, and the speed of sound for a longitudinal wave, c_l, is proportional to the elastic modulus of the medium, E.

$$c_s = \sqrt{G/\rho} \tag{3.1}$$

$$c_l = \sqrt{E/\rho} \tag{3.2}$$

3.4 Acoustic Impedance

The acoustic impedance, also known as the characteristic impedance, z, is used to describe the resistance the ultrasound wave undergoes when passing from one medium into another. The acoustic impedance of a solid, z_s, is a real quantity and is related to the density, ρ_s, and the speed of sound in the solid c_s.

$$z_s = \rho_s c_s \tag{3.3}$$

The shear acoustic impedance of a liquid, z_l, is a complex quantity related to the liquid's density, ρ_l and the fluids complex shear modulus, G.

$$z_l = \sqrt{\rho_l G} \tag{3.4}$$

As is shown in Section 3.9, the greater the similarity of the acoustic impedance of two materials, the greater the amount of energy that is transmitted into the second medium, and the less amount of energy will be reflected. It is generally found that the acoustic impedance for a solid is much greater than the impedance for a gas or a liquid. Therefore when an ultrasound wave passes from one a solid to a fluid, there will be a large amount of reflection. It is a critical property to consider when designing a system with multiple material phases, such as a shear ultrasound viscometer measuring the viscosity of oil.

3.5 Attenuation

As all real-world materials are elastic, as a wave travels through a medium, energy is lost, and the amplitude of the wave decreases. The amplitude of a wave, A_d, after travelling a distance, d, after having an initial amplitude of, A_0 can be calculated using Equation 3.5. In this equation, the attenuation coefficient α, depends on the material properties - the greater the attenuation coefficient, the faster the amplitude of the wave decreases.

$$A_d = A_0 e^{-\alpha d} \tag{3.5}$$

3.6 Penetration Depth

The shear penetration depth describes the distance that a shear wave travels through a fluid before the amplitude is attenuated to $1/e$ of its initial value.

$$\delta = \sqrt{\frac{2\eta}{\rho_l \omega}} \tag{3.6}$$

Figure 3.3 is modelled using Equation 3.6 and illustrates the relationship between the penetration depth, frequency and viscosity. It shows the asymptotic function between the penetration depth and the frequency, and it reveals that the more viscous a fluid, the further the shear wave can penetrate.

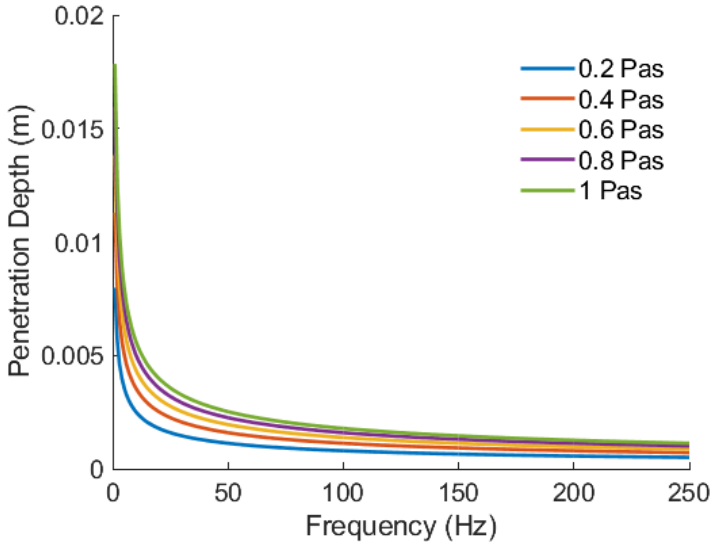

Figure 3.3: The penetration depth of a shear wave for different frequencies and fluid viscosities.

3.7 Phase

The phase of a wave describes the lag of one wave behind the other and is measured in radians. The equation used to measure the phase difference, θ, between two signals, θ_1, and θ_2, is shown in Equation 3.7 and is illustrated in Figure 3.4.

$$\theta = \theta_1 - \theta_2 \tag{3.7}$$

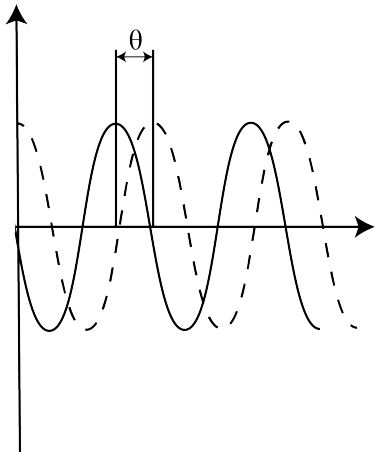

Figure 3.4: Phase.

3.8 Wave Interference

When two waves pass each other, they interact, leading to a change of amplitude. The resultant wave is equal to the sum of the amplitude of the two individual waves.

If two waves are of the same frequency and are in phase, they will constructively interfere. This means that the amplitude of the resultant wave is equal to the maximum of the two waves summed, and is showed graphically in Figure 3.5a. If the two waves are of the same frequency and are $\pi/2$ radians out of the phase, the waves will destructively interfere, and the amplitude of the resultant wave is zero, as shown in Figure 3.5b.

This concept is essential in many applications, such as a modern electronic automobile muffler and non-reflective coatings, and can be used to manipulate signals- often to remove noise. In this thesis, a layer is placed between the metal medium that the transducers are bonded to and the oil, which is exactly one-quarter of a wavelength thick - this layer is referred to as the matching layer. As discussed in later chapters, this layer dramatically increases the sensitivity of viscosity measurements.

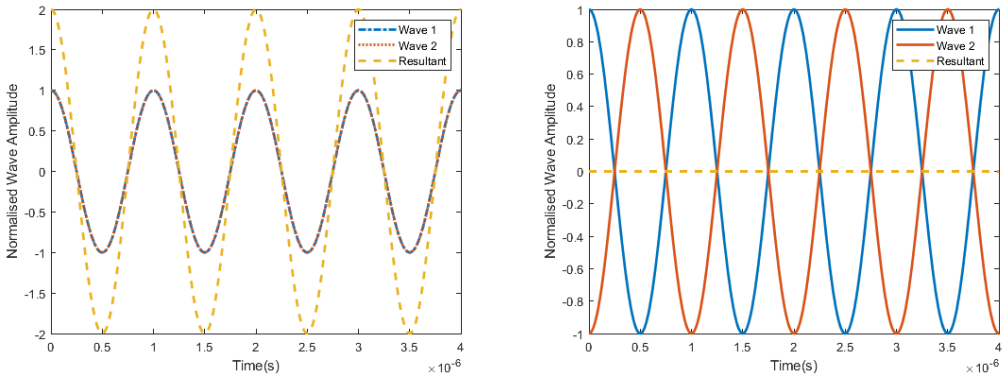

(a) Constructive interference.

(b) Destructive interference.

Figure 3.5: Wave interference.

3.9 Reflections At An Interface

The reflection coefficient describes the proportion of energy reflected as a wave travels from one medium to another. The modulus of the reflection coefficient, R, is unitless and is between 0 and 1. The reflection and transmission coefficients are defined as the ratio of the reflected and transmitted acoustic pressure divided by the incident pressure, respectively.

$$R = \frac{p_r}{p_i} \tag{3.8}$$

$$T = \frac{p_t}{p_i} \tag{3.9}$$

The reflection coefficient and transmission coefficient can be related using Equation 3.10.

$$T = 1 + R \tag{3.10}$$

In the following two subsections the reflection from a two and three layered system are stated. These equations are derived fully in Chapter 5.

3.9.1 2 Layered System

The reflection coefficient of a two-layered system, Equation 3.11, has been derived previously in literature by Brekhovskikh (1980) and Kinsler and Frey (1962). Both show the relationship between the reflection coefficient, R, and the acoustic impedance of materials 1 and 2, z_1 and z_2 respectively, for when two mediums are perfectly bonded. Figure 3.6 illustrates this with an initial pressure wave, p_i, travelling from left to right and reaching the boundary between media 1 and 2. When the boundary is reached, part of the wave is reflected, p_r and part of the wave is transmitted, p_t.

$$R = \frac{z_2 - z_1}{z_2 + z_1} \tag{3.11}$$

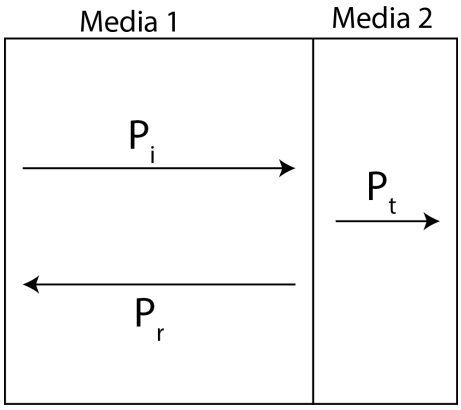

Figure 3.6: Two layered system.

3.9.2 3 Layered System

For an acoustic wave travelling through multiple layers, such as for a metal - matching layer - oil system, the reflection coefficient has again been derived many times before by authors, including Brekhovskikh (1980). Figure 3.7 illustrates the pressure waves in the system. Below is the equation as derived by Kinsler and Frey (1962) where it has been expanded using Euler's identity to show the frequency in terms of sine and cosine.

$$R = 1 - \frac{4}{2 + \frac{Z_3}{Z_1} + \frac{Z_1}{Z_3} cos^2(k_m t_2) + (\frac{Z_3^2}{Z_1 Z_3} + \frac{Z_1 Z_3}{Z_2^2}) sin^2(k_m t_2)} \tag{3.12}$$

The wavenumber, k_2, describes the number of waves per distance, and t_2 is the thickness of the second medium layer.

$$k_2 = \frac{2\pi}{\lambda_2} \tag{3.13}$$

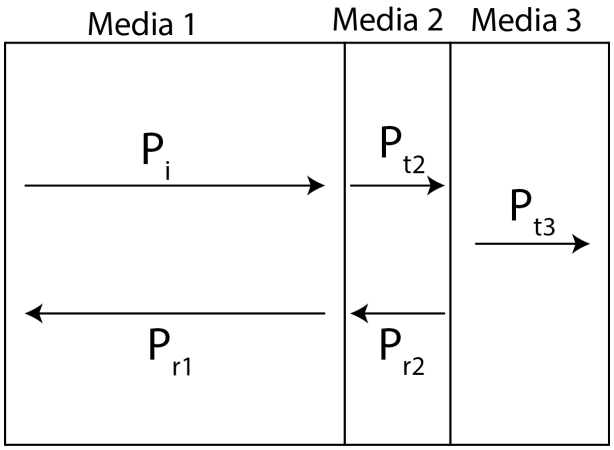

Figure 3.7: Three layered system.

3.9.3 Comparison Between the 2 and 3 Layered System

Figure 3.8 shows the reflection coefficient for a two and three-layered system where medium 2 in the two-layered system, and medium 3 in the three-layered system, is a fluid. As the frequency increases, the reflection coefficient for the three-layered system cyclically drops. This is due to the frequency changing the corresponding wavelength, and as discussed, when it is $\pi/2$ out of phase, destructive interference is caused, reducing the reflection coefficient.

For the two-layered and the three-layered systems, the reflection coefficient decreases as the frequency increases due to the frequency dependency of the acoustic impedance of the fluid, as shown in Equation 3.4.

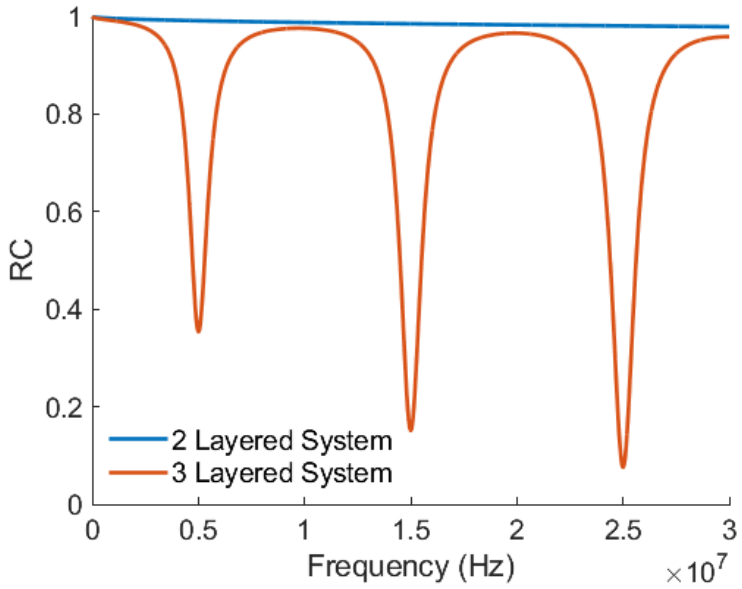

Figure 3.8: Reflection coefficient in the frequency domain.

3.10 Propagation of Shear Waves Through Fluids

Although it is commonly believed that shear waves cannot propagate through fluids, this is untrue. The interaction between a shear wave and fluid has previously been derived by many authors, including Whorlow (1992), and is reproduced again here.

If we assume the simplest case, Figure 3.9, where a viscoelastic plate is oscillating in the x-direction and waves are propagated in the z-axis, the shear strain, γ, can be correlated to its coordinate change.

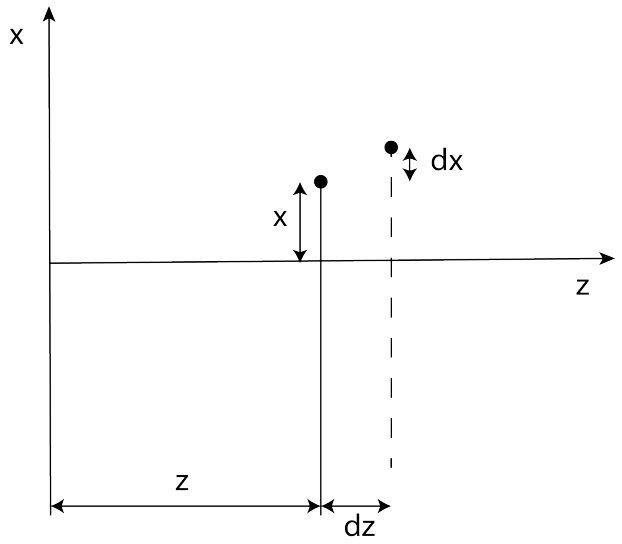

Figure 3.9: Propagation of plane shear wave.

$$\gamma = \frac{\delta x}{\delta z} \tag{3.14}$$

The equation of motion for the plate can be described in terms of stress, σ, with respect to time, t.

$$\rho \frac{\delta^2 x}{\delta t^2} = \frac{\delta \sigma}{\delta z} \tag{3.15}$$

As shown in the previous chapter, it is possible to relate the fluid properties to the stress and strain, $G = \frac{\sigma}{\gamma}$, where $\gamma = \frac{\delta x}{\delta z}$. Using these relationships Equation 3.15, can be written in terms of the fluid properties.

$$\frac{\delta^2 x}{\delta t^2} = \frac{G}{\rho} \frac{\delta^2 x}{\delta z^2} \tag{3.16}$$

When the motion is sinusoidal, as would be for a shear wave that is oscillating with frequency, ω, the solution can be transformed, where $c = \sqrt{\frac{G}{\rho}}$.

$$x = x_0 \exp[i\omega(t - z/c)] \tag{3.17}$$

Although, in theory, the shear modulus can be measured from the velocity and attenuation of the shear wave, it is not very practical due to the high attenuation. Therefore, the shear modulus is derived in terms of acoustic impedance. Acoustic impedance is the ratio of the acoustic load and displacement, and therefore can be written in terms of the shear modulus of the fluid.

$$z_l = -\frac{\sigma}{\frac{\delta x}{\delta t}} \tag{3.18}$$

Using the relationship between shear modulus and stress and strain, and applying a further known definition for the shear modulus, $G = i\omega\eta$, the acoustic impedance can be written in terms of shear modulus.

$$z_l = \sqrt{\rho G i\omega} \tag{3.19}$$

The relationship between shear modulus and viscoelastic behaviour has been discussed in Chapter 2, and is used in Chapter 5 to determine the viscosity from the reflection coefficient.

3.11 Piezoelectricity

The Curie brothers discovered the piezoelectric effect in 1880 and found that applying a stress to specific materials caused an electric charge to be induced (Curie, 1880). In 1881, the reverse was found by Lippmann, where applying a voltage to a material caused a proportional change in shape. The materials which show this effect are known as piezoelectric materials. The most common being single crystals and synthetic material lead zirconate titanate, more commonly known as PZT. The number of applications that this knowledge has brought about is vast and far-reaching, including sonar, analogue watches, loudspeakers and mobile phones.

3.11.1 Piezoelectric Element

A piezoelectric material can be manipulated to produce ultrasound waves by applying an alternating current, which in turn causes rapid fluctuations in its dimensions and an ultrasound wave is produced. The centre frequency, f_0, at which the ultrasound waves are produced is dependent on the thickness of the material, t_t, and speed of sound in the transducer, c_t, as can be seen in Equation 3.20.

$$t_t = \frac{c_t}{2f_0} \tag{3.20}$$

This equation shows that as the central frequency increases, the thickness of the transducer decreases. The thicknesses for a PZT-2 transducer emitting varying ultrasound frequencies are shown in Table 3.2.

Frequency	Thickness (mm)
100 kHz	11.03
1 MHz	1.10
10 MHz	0.11
100 MHz	0.01

Table 3.2: Thickness of a piezoelectric transducer for differing frequencies.

3.11.2 Piezoelectric Transducers

Commercial transducers are often used as they require minimal set-up and produce a superior signal compared to bare elements. This superior signal is produced by manufacturing a sensor made from multiple components, as shown in Figure 3.10. The backing block dampens the piezoelectric transducer transmitting a larger amount of energy to the location of interest. Around the acoustic absorber, backing block and piezoelectric element there is often a metal shield which prevents unwanted electrical signal interfering with the element. A matching layer is placed on the piezoelectric element to allow greater transmission by introducing a layer with an intermediary acoustic impedance between the piezoelectric element and the interface that the element will be in contact with.

Another method to produce ultrasound waves is to bond a bare piezoelectric element straight onto the interface of interest. Although this method will reduce the signal quality compared to the commercial probe, it is much cheaper and smaller, allowing it to be installed in more locations. In this thesis bare element piezoelectric transducers are used.

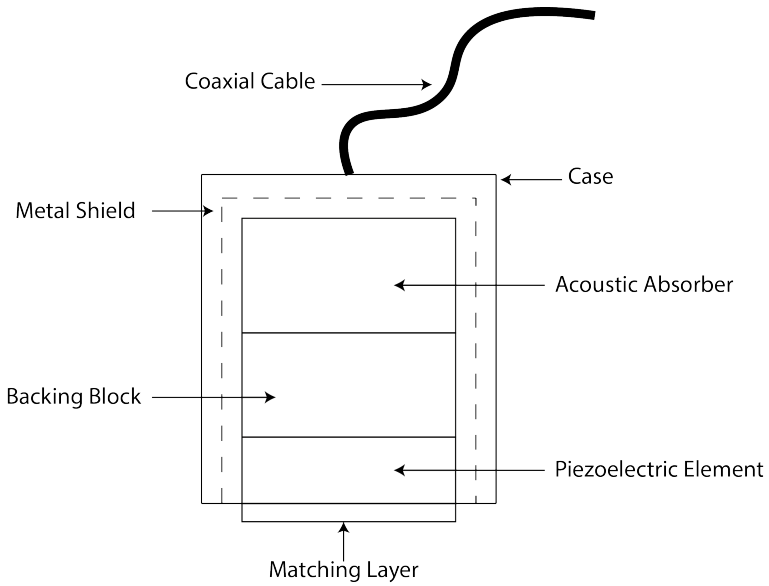

Figure 3.10: Commercial transducer components.

When a transducer is used to acquire a wave's reflection, there are two standard

arrangements used, Figure 3.11. The first is called pulse-echo, where the transducer that emitted the original wave is also used to capture the reflected signal. This arrangement has the advantage that only one transducer is required, reducing the cost and the installation area. The second arrangement is called pitch-catch, where two transducers are placed next to each other, and as one emits the signal, the second captures the reflected pulse. The advantage of this second method is that, unlike the first method, transmission and emission happen simultaneously, allowing it to make continuous measurements.

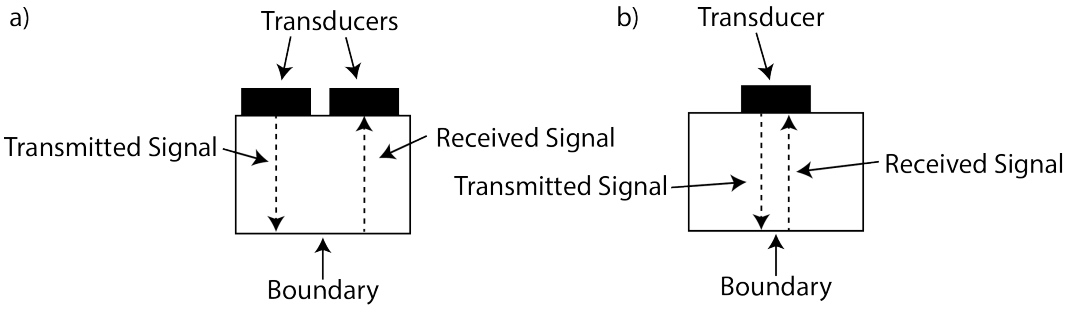

Figure 3.11: The two commonly used transducer set-ups, *a)* pitch- catch and *b)* pulse echo.

3.12 Ultrasound Signal Characteristics

The reflected signal acquired by the transducer is captured in the time domain, 3.12*a*. It is then converted to the frequency domain by using the fast Fourier transform, FFT, which shows how the energy of a signal is distributed over a range of frequencies, 3.12*b*.

The frequency-domain signal has several significant characteristics defined in multiple standards, including ASTM (2014) and ISO (2017). The upper and lower cut-off frequency is defined by a drop from the peak amplitude, typically $-3dB$. The bandwidth is the difference between the upper cut-off frequency and the lower cut-off frequency. It is important to note that the peak frequency is not equal to the centre frequency, although this may be the case.

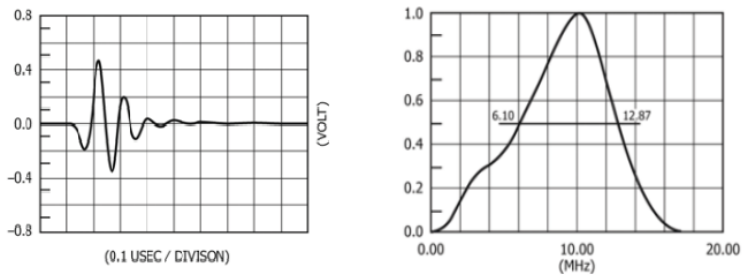

Figure 3.12: *(a)* Time and *(b)* Frequency response from an ultrasound transducer. (ASTM, 2014)

Key	Description
X	Frequency
Y	Amplitude
1	Peak Frequency
2	Upper Cut-Off Frequency
3	Lower Cut-Off Frequency
4	Centre Frequency
5	Bandwidth at Specified Amplitude Drop
6	Peak Amplitude
7	Specified Amplitude Drop

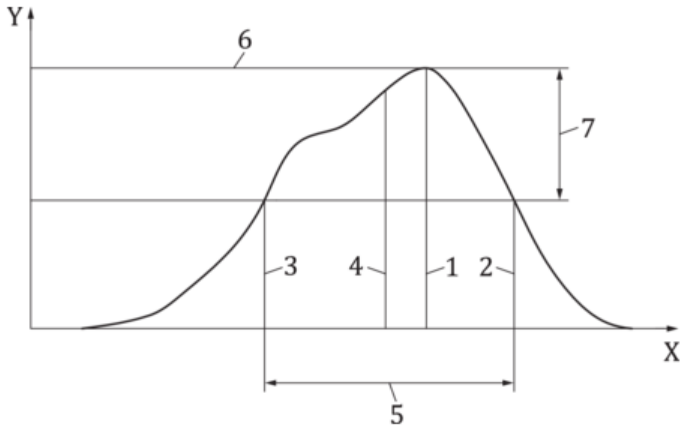

Figure 3.13: Frequency response characteristics.(ISO, 2017)

3.12.1 Near Field

As the ultrasound signal propagates from multiple locations on the transducers face, it produces numerous ultrasound signals. This means the pressure wave that emanates is complicated due to waves interfering with each other. After a certain point, the signal becomes more stable, the end of the near field. Ultrasound measurements should not be completed in the near field due to the fluctuations in pressure. The near field distance, N, can be calculated by knowing the transducer's diameter, D_T, and the speed of sound in the material, c.

$$N = \frac{D_T^2 f}{4c} \tag{3.21}$$

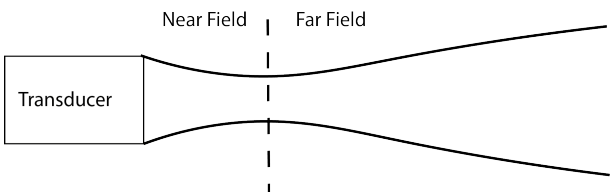

Figure 3.14: Near field.

3.12.2 Beam Spread

As a sound field propagates from the source, it spreads. The beam spread equation can quantify the angle that it deviates from the centre line. This phenomenon occurs as the energy is not fully transferred in the direction of propagation because the particles are not perfectly aligned in the direction of propagation. As the distance away from the transducer increases and the sound field area increases, the intensity will decrease, adversely affecting ultrasound measurements. The beam spread, θ, can be calculated by knowing the speed of sound in the material, c, the diameter of the transducer, D_T, and the frequency, f. In some literature, the term beam divergence is used, which is equal to $\theta/2$.

$$\sin\theta = 1.2\frac{c}{D_T f} \tag{3.22}$$

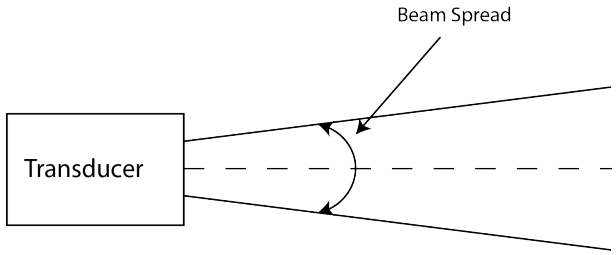

Figure 3.15: Beam spread.

3.13 Summary

This chapter introduces essential ultrasound concepts, including reflection coefficient and acoustic impedance and shows different means of emitting and capturing an ultrasound wave and how the signal can be tuned to increase the sensitivity.

The concepts presented are the basis for developing a matching layer multiple frequency ultrasound viscometer, which uses a shear wave to measure the viscoelastic properties of oil.

3.14 Conclusion

A shear ultrasound wave can be used to measure viscosity of oils by using the relationship between the reflection of a shear wave and the shear modulus of a fluid . This relationship is investigated further in Chapter 5.

Chapter 4

Literature Review

The literature review is split into three sections; conventional viscometers adapted for high shear measurements, conventional in-situ viscometers, and viscosity measurements using the reflection coefficient from an ultrasonic viscometer. The high shear and in-situ viscometer sections are organised by viscometer type: coaxial, parallel plate, capillary and oscillatory. For each viscometer discussed in these two sections, the mechanism of how the viscosity of a fluid is obtained by the laboratory viscometers have been described in Section 2.7. The ultrasonic viscometer section is organised chronologically as the developments of different ultrasonic viscosity measurements are entwined. This chapter concludes by noting the advantages and disadvantages of the different viscometers, which will convince the reader of the rationale of the thesis direction. It may be noted that this chapter does not include literature relating to the direct comparison of shear and steady measurements; this information can be found in Chapter 6, where the author proposes a theory to relate the shear rate of the conventional and ultrasonic systems.

4.1 High Shear Rate Conventional Viscometers

The advancement of engines led to lubricating oils being subjected to ever-increasing shear rates. Conventional viscometers were adapted to produce these high shear rates, mimicking the shear rates produced in engines.

4.1.1 Rotational Viscometers

4.1.1.1 Coaxial Viscometer

The first high shear rate viscometer was designed by Merrill (1954), Figure 4.1, and was based on the coaxial viscometer. The viscometer applied high shear rates to the test fluid by rotating a spindle at very high speeds, which were achieved by connecting the spindle to a drill press. As with the conventional viscometer, the torque exerted by the test sample on the spindle was monitored and manipulated to find the viscosity

of the fluid. Unlike the low shear coaxial viscometer, this viscometer required minimal annular clearances and precise coaxial alignment to produce significant shear rates with small amounts of error. The temperature was monitored by numerous thermocouples installed in multiple locations, and water was circulated around the outside cylinder at 21°C to combat any temperature increase through viscous heating. Despite this, the temperature increased by 2°C after 60 seconds, Table 4.1, significantly reducing the true viscosity value. Using this apparatus, measurements were carried out on a Newtonian fluid with a viscosity of $9000cP$ at a shear rate of $6690s^{-1}$ and good agreement was shown with viscosity measurements using a low shear Interchemical viscometer, despite the temperature change.

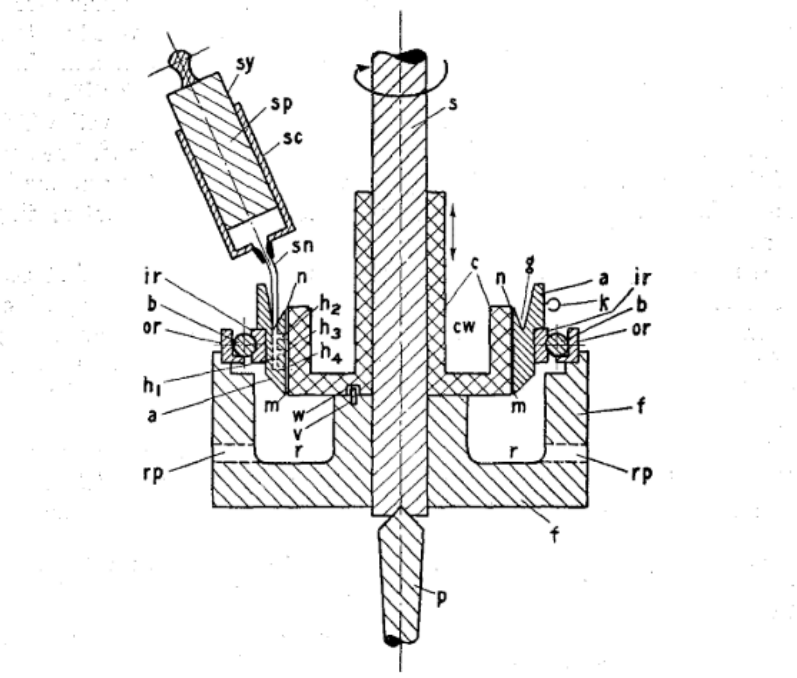

Figure 4.1: Merrill (1954). High shear coaxial viscometer.

Time from Start (sec)	Temperature of Fluid (°C)	Change of Temperature (°C)
5	21.0	0
30	22.2	+1.2
60	23.0	+2.0

Table 4.1: Adapted from (Merrill, 1954). Temperature change of fluid when subjected to high shear rates.

For many years, Merrill and Ram worked together, publishing articles based on Merrill's high shear coaxial viscometer. Ram (1968) increased the maximum shear rate by rotating the shaft at greater speeds. Using this apparatus to complete measurements on a Newtonian fluid, a water-glycerine solution, he concluded that the sample was shear-thinning above $60,000s^{-1}$. This conclusion was disputed by many

authors, including Dontula et al. (1999), which generates uncertainties regarding the accuracy of viscosity measurements when using this apparatus.

A commercial viscometer used for measuring the viscosity up to $10^7 s^{-1}$ was developed by PCS Instruments, known as the USV, Ultra Shear Viscometer, Figure 4.2. The viscometer's main adaptations were to dramatically reduce the shearing time to 30ms, reducing the temperature increase of the fluid due to viscous heating. The installation of an electromagnetic clutch implemented this short shearing time. This instrument has been cited multiple times in publications, including measurements of viscosity modifier polymer solutions at $10^6 s^{-1}$ (Marx et al., 2017), and heavy-duty diesel engine oil measurements over a range of temperatures at $10^6 s^{-1}$, (Taylor et al., 2017).

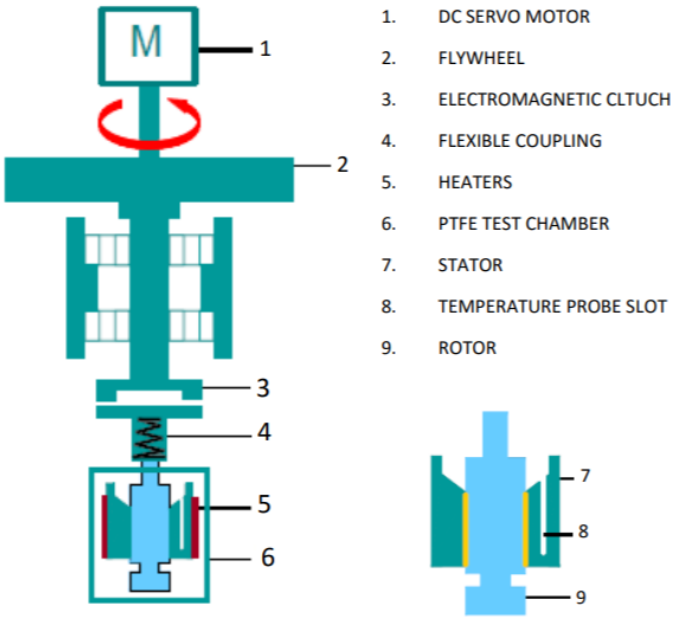

Figure 4.2: PCS Instruments (2018).Schematic of PCS Ultra Shear Viscometer.

The high shear coaxial viscometer is the most commonly used viscometer for high shear rate ex-situ measurements as:

1. Measurement conditions are steady-state.
2. There is a negligible variation of shear rate and shear stress through the sample.
3. Non-Newtonian behaviour can easily be studied and characterised.

Unfortunately, the high shear coaxial viscometer also has notable disadvantages, including the unwanted increase in the fluid temperature when subjected to high shear rates. A further disadvantage is the range of viscosities that can be measured at high shear rates; as the shear rate increases, the amount of torque required increases, limiting the maximum viscosity that can be measured.

4.1.1.2 Parallel Plate Viscometer

Much later in 1985, Connelly and Greener (1985), published a paper that detailed a novel device to measure the viscosity of Newtonian and shear-thinning fluids over high shear rates using a disk-based method, Figure 4.3. The motivation behind this development was that despite current high shear coaxial apparatus 'the behaviour of liquids at high shear rates is fundamentally not well understood' (Connelly and Greener, 1985).

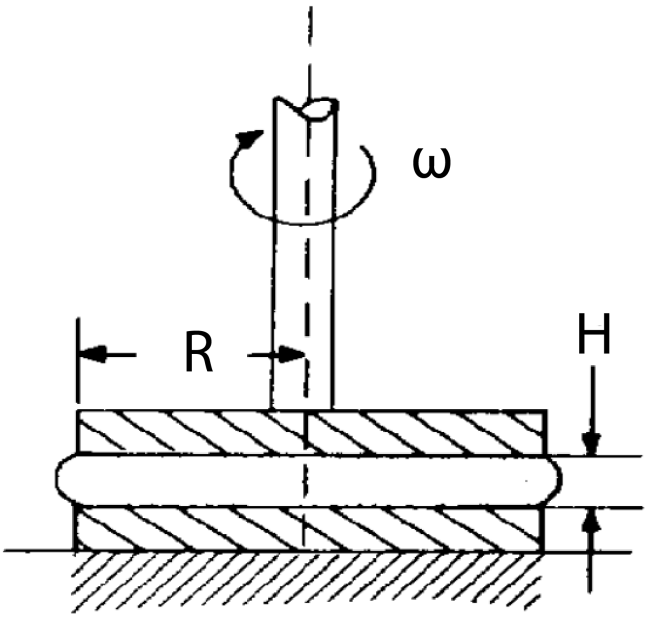

Figure 4.3: Connelly and Greener (1985). High shear parallel disk viscometer.

Previously, the parallel plate method was only able to measure relatively low shear rates, as they were reported to develop flow instabilities above $100s^{-1}$. To overcome this, the gap between the plates was decreased, an idea already proved to work by Walters and Barnes (1980). It was found that decreasing the gap between the plates, H, reduced instabilities and increased the shear rate. The increase in shear rate was also produced by an increase in the rotational speed, ω. This relationship is shown in Equation 4.1 , where R is the radius of the plate.

$$\dot{\gamma} = \frac{\omega R}{H} \tag{4.1}$$

By keeping the gap below $0.1mm$, shear rates of $10^4 s^{-1}$ could be reached. When comparing the high shear rate parallel viscometer results, for both Newtonian and non-Newtonian fluids, with a low shear rate viscometer, a good match was found. There were still areas of uncertainties for the high shear parallel plate viscometer, including radial migration and surface fracture, but concluded that both effects were negligible

for this set-up. As with the coaxial viscometer, viscous heating was the largest area of uncertainty. One of the biggest challenges with viscous heating is detecting it, as it betrays itself as a rheological shear thinning effect. To detect this, a T-loop program was used where a hysteresis response would indicate viscous heating. Using this method, it was found that if the fluid was subjected to high shear for less than 2 seconds, the viscous heating effect would be negligible- this was dependent on the viscosity of the sample and the shear rate, Figure 4.4. However, it was noted that there was a minimum time that the fluid needed to be subjected to for accurate measurements, a loop that was too fast would give rise to disturbances and possibly cause the shear rate to be unsteady.

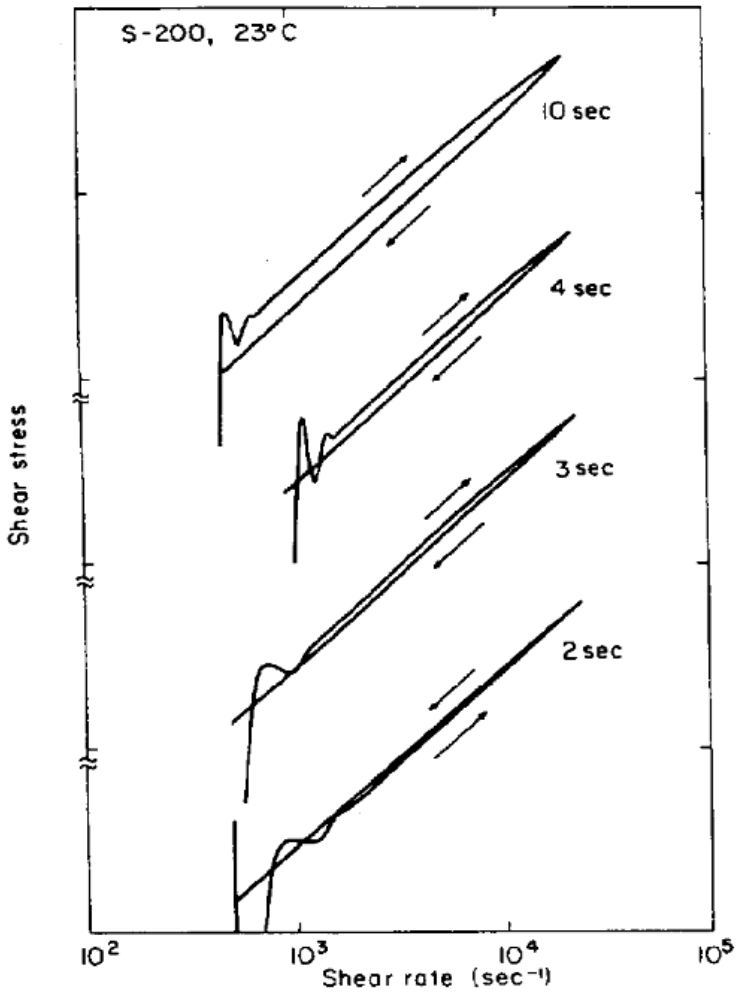

Figure 4.4: Connelly and Greener (1985). Shear stress response from shear rate T-loop.

Two years later, Kramer et al. (1987) used this viscometer with the hysteresis technique to measure the viscosity of guar gum up to $50,000 s^{-1}$. This high shear rate was produced by further reducing the gap between the parallel plates to 50 microns. These results were compared with a high shear capillary viscometer, and the results

were found to be similar. This report argued that the results collected by the parallel disk viscometer were more accurate than the high shear capillary viscometer due to the capillary viscometers high sensitivity to its radial dimensions.

Dontula et al. (1999) used a variant of Connelly's high shear parallel plate viscometer to measure the viscosity of a glycerine-water solution. This test disproved results collected by Ram (1968), showing that up to $90,000s^{-1}$, the viscosity remained constant. This suggests that this measurement technique is superior.

In 2004, Mriziq et al. (2004) adopted the high shear rate parallel plate viscometer to include a capacitance method to measure the sample's thickness. Equation 4.2 was used to calculate the shear rate with respect to the relative sliding speed, v, and the film thickness, h.

$$\dot{\gamma} = \frac{v}{h} \tag{4.2}$$

Non-Newtonian samples were measured over a shear rate of $10^3 - 10^6 s^{-1}$. This viscometer allowed for the thickness and the sliding speed to be varied. Results presented, Figure 4.5, clearly show that the relationship between the shear rate and the viscosity were independent of the film thickness, adding to the reliability of this type of viscometer.

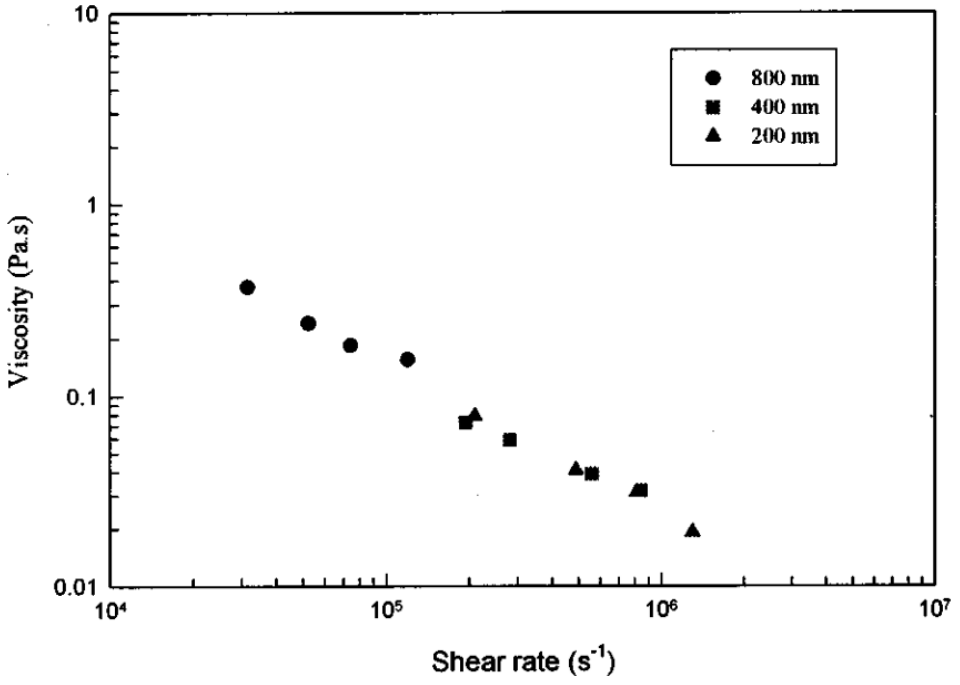

Figure 4.5: Mriziq et al. (2004). Viscosity over a range of shear rates with varying film thicknesses.

More recently, variants of the high shear parallel plate viscometer have been used in many studies, including:

1. Viscosity measurements of shear-thinning motor oil (Bair, 2015).
2. Steady shear rheological measurements of water in oil emulsion (Zahirovic et al., 2009).
3. Viscosity measurements of the shear property of oil film containing additives (Hirayama et al., 2020).

Brookfield has developed a commercial high shear rate cone on plate viscometer. The measurement device only requires small sample quantities, 0.5 – 2 ml and boasts an accuracy of 1% . This viscometer does not reach the high shear rates that have been obtained by other researchers in this section, with the maximum shear rate being $1875s^{-}1$. Further information can be found in the Wells/Brookfield website (Brookfield Engineering, 2019).

The advantages of using the parallel plate viscometer are the extensive range of shear rates that can be exerted on the samples and the small sample size required. Unfortunately, like the high shear coaxial viscometer, the viscous heating of the test sample is still a problem. However, it can be reduced by limiting the amount of time the fluid is subjected to shear. A further disadvantage is that measurements can only be taken at the edge of the plate, the place of maximum shear rate, as the shear rate will change across the radius.

4.1.2 Capillary Viscometer

Talbot (1974) designed a high shear capillary viscometer. The apparatus varied the shear rate by driving the sample through capillaries of different diameters, $0.1 - 1mm$, using nitrogen pressure. The relationship between the capillary diameter, viscosity and shear rate is shown in Table 4.2. It shows that as the capillary diameter increases, the range of viscosity measurements reduces. Using this set-up, polymer solutions in petroleum lubricating oil were measured over a shear rate of $10^2 - 10^6 s^{-1}$. The time that it took for a measured volume of test fluid to pass through the capillary was recorded, which was then converted to viscosity using Equation 2.18. The data was compared with an approximating function based on the probability function, which provided a satisfactory fit. However, some solutions showed unexpected pseudo-plastic flow, which was conjectured to be caused by the disruption of aggregates in the fluid.

Capillary Diameter (mm)	Viscosity (mPas)	Shear Rate ($s^{-}1$)
2.8	600-200,000	10-2,000
2.4	50-100,000	10-4,000
2.1	0.3-60,000	20-6,000
1.59	0.1-20,000	40-13,000
1.05	0.01-4,000	150-50,000

Table 4.2: Adapted from (Pollak et al., 2017). Capillary diameter, viscosity and shear rate relationship.

Galvin et al. (1981) further developed this viscometer by producing higher pressures to $0.2GPa$, through use of a ram, Figure 4.6. This meant that the shear rate was able to be varied without changing the capillary diameter.

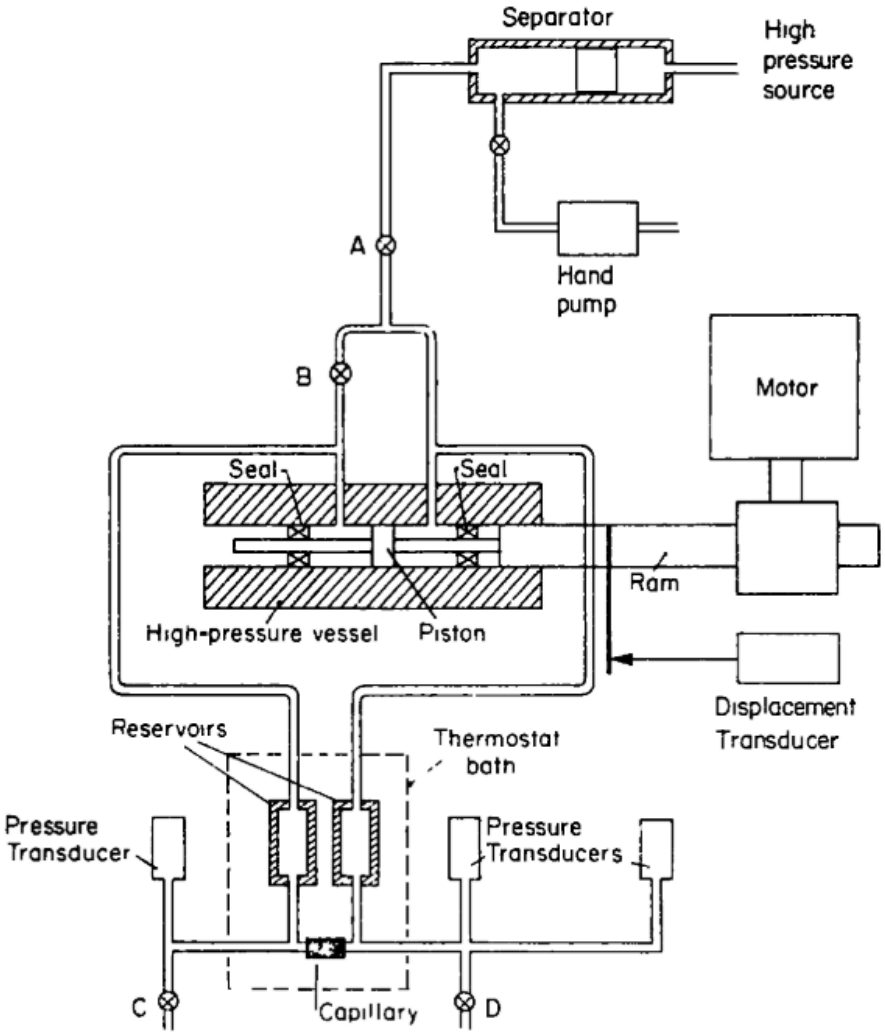

Figure 4.6: Galvin et al. (1981). High shear rate capillary viscometer.

Measurements so far were limited to Newtonian fluids. To overcome this Duda et al. (1988) devised a new mathematical analysis, which was based upon an iterative method of comparing the viscosity with Newtonian fluids and calibrating.

> The pressure drop associated with the kinetic energy is a function of the non-Newtonian characteristics of the fluid, which are unknown when this correction is used in the data analysis procedure. However, a simple iterative procedure can be utilised to facilitate this excess pressure drop correction. (Duda et al., 1988)

Using this iterative method, the viscosity of lubricant containing polymers was successfully measured over the shear rate range, $10^5 - 10^7 s^{-}1$. If the fluid shows significant viscoelastic behaviour, the pressure difference would increase dramatically and reduce the accuracy of the measurements.

RheoSense has developed a commercial benchtop high shear rate capillary viscometer called the m-VROC viscometer. The accuracy is reported to be 2% with a shear rate range of $0.5 - 1.4 \times 10^6 s^{-1}$. Further information can be found in the principle of operation application note (RhenSense Inc., 2020).

One of the main advantages of the high shear capillary viscometer over its rivals is the low cost of the apparatus. A part of this is because it does not require a motor as there are no rotating components. Another advantage is that there is no air-liquid interface, increasing the accuracy of the measurements. The difficulties of using a capillary viscometer at high shear rates are that non-viscometric flow fields exist at the ends of the capillary, meaning viscosity measurements can only occur in the centre. There will be a significant pressure gradient across the capillary at high shear rates, which affects the viscosity. As with the other conventional viscometers, the fluid temperature can be significantly increased by viscous heating.

4.1.2.1 Microviscometers

More recently, advancements are being made to miniaturise the high shear capillary viscometer. The advantage of using a micro viscometer is the low build cost, ease of operation and the small volume of sample required. Disadvantages include significant wall effects; however, correction procedures can remove this.

Kang et al. (2005) recently developed a microchannel viscometer where the channels' dimensions were $150 \times 150 \mu m$, which produced a shear rate of $10^6 s^{-}1$. The maximum viscosity measured was $1 Pas$. Applying the Bagley correction factor removed significant wall effects allowing accurate measurements of non-Newtonian polymers. Erickson et al. (2002) completed a study into the microchannels' dimension sensitivity and found that a change in the channel's dimensions varied the viscosity results significantly. So far, no researcher has been able to provide a sufficient explanation for this. Much work is needed to make these viscometers a viable option, but with so many advantages, this apparatus type will likely be more prevalent in the future.

4.1.3 Falling Body Viscometer

The falling body viscometer has not been applied to high shear viscometry as there are many difficulties which were summarised by Schaschke (2010):

1. The measurement fluid is required to be clear or translucent to allow tracking of the falling body.

2. To acquire accurate measurements, a vessel and a sample with sizeable volume are required.

3. The sinker movements cannot be guaranteed to be vertical, altering the body's time to fall.

4. Other considerations that will affect the body's movement include end effects that propagate in the form of vertices, wake oscillations and shredding.

More importantly than all these reasons, when shearing the test fluid, it will lead to movements that will disrupt the motion of the falling body, altering the time it takes to fall and, therefore, making accurate viscosity measurements unattainable.

4.1.4 Oscillatory/ Vibrational Viscometers

Oscillatory viscometers do not require significant adaptation to conduct high shear viscosity measurements, as their operation depends on transducers that can operate at high frequencies.

Chung (1973) developed the first vibrational viscometer. A steel tuning fork was oscillated using two electromagnetic units, and the damping force was measured. The damping force was calibrated using different viscosity Newtonian fluids, glycerin-water solutions, and an exponential fit was found, where Y is the amplitude change.

$$\eta = 10 \exp 0.086Y \tag{4.3}$$

It was noted that this measurement technique could only complete accurate measurements over a small viscosity range. A further disadvantage was that for the oscillator to remain stable, it required to be warmed up for one hour. Unfortunately, this paper did not mention a shear rate value or frequency at which the tuning fork was oscillating.

Due to the technical advances needed to produce systems that can quickly and accurately create oscillations, the tuning fork viscometer was not advanced until 1998, when Giessibl (1997) developed a tuning fork for atomic force microscopy using a quartz crystal which was chosen due to the stability of the sensor (Eernisse et al., 1988).

Divišová et al. (2012) adapted the tuning fork viscometer to complete measurements of small sample sizes, 300µl, over an extensive temperature range $-120°C$ - $150°C$, Figure 4.7. The fork was oscillated at a frequency of 30kHz and the viscosity of two Newtonian fluids, n-hexane and de-ionised water, were measured. As with the original vibrational viscometer, it was found that the measurements were only able to be completed for low viscosity fluids, such as hexane, and the viscosity of highly viscous fluids was unable to be measured due to the significant damping exerted from a high viscosity fluid. A second limitation of this viscometer was that the fluid had to be non-conductive to stop a short circuit.

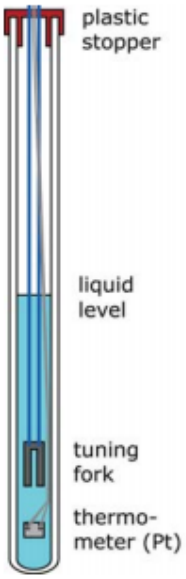

Figure 4.7: Divišová et al. (2012). Sketch of the tuning fork viscometer.

However, due to its accuracy in the measurement of low viscosity fluid, it has been successfully applied in several studies to measure the viscosity of superfluid helium (Clubb et al., 2004) (Blaauwgeers et al., 2007) (Bradley et al., 2008).

The only company that manufactures laboratory-based tuning fork viscometers is A&D Weighing (Gupta, 2014). The frequency that the fork is vibrated is 30Hz (A&D Company, 2009), which will produce a relatively low shear rate.

Another variant of the oscillating viscometer is the oscillating cup. Due to its mechanical simplicity, small sample requirement and stability at high temperatures it is often used to measure the viscosity of molten metals (Ferriss and Quested, 2000). The measurements are completed at low oscillations, with typical frequency sweeps completed over $0.1 - 100 rad/s$ (TA Instruments, 2020), and are therefore not investigated further in this section.

The QCM, quartz crystal microbalance, is an oscillatory measurement device that allows for the measurement of a fluids viscosity and density. The QCM consists of a

shear crystal with two electrodes on opposite sides. When an electric field is applied to this transducer the crystal oscillates at its natural frequency. When a fluid is placed on the QCM the frequency of the system changes. This change in frequency, Δf, is related to viscosity, η_l, by the equation developed by Keiji Kanazawa and Gordon (1985), where f_0 is the resonant frequency, ρ_l is the density of the fluid, and μ_q and ρ_q are the shear modulus and density of the quartz respectively.

$$\Delta f = -f_0^{3/2} \sqrt{\frac{\eta_l \rho_l}{\pi \mu_q \rho_q}} \tag{4.4}$$

This relationship was used by Ash et al. (2003) to complete viscosity measurements of oil at 10MHz. A small sample of oil $0.5mm^3$ was placed on the crystal and the viscosity was measured. It was found that for oils with viscosity below $500cP$, the results were comparable to measurements completed using a conventional viscometer, however viscosity measurements above $500cP$ deviated away from conventional measurements. This deviation was hypothesised to be caused by the long relaxation time of the oils.

4.1.5 Comparison of Adapted Conventional Viscometers for High Shear Rate Measurements

Table 4.3 shows a comparison of the discussed adapted conventional viscometers for high shear rate measurements.

	Advantages	Disadvantages
Coaxial	• Steady-state measurement conditions. • Non-Newtonian behaviour of fluids can be studied. • High shear rates measurements can be completed.	• Requires precise annular clearances. • Significant viscous heating of the sample. • The measurable viscosity range is dependant on the torque measurable.
Parallel Plate	• Small quantity of lubricant required. • Extensive range of shear rates.	• Lower shear rates produced than the coaxial viscometer. • Viscous heating. • Measurement has to be completed at plates edge.
Capillary	• Inexpensive. • No air-liquid interface. • No rotating parts.	• Limited to Newtonian fluids. • Non-viscometric flow fields exist at the capillaries end. • Viscous heating.
Oscillatory	• Easy to adapt for high shear measurements. • Able to measure over a large temperature range. • Small sample size required.	• Small amount of research completed at high frequencies. • Fluid cannot be conductive. • Measurements can only be completed at low viscosities due to damping.

Table 4.3: Comparison of adapted conventional viscometers for high shear rate measurements.

4.2 In-situ Viscometers

In-situ viscometers are used to measure the viscosity of fluids locally. The main advantage of this is the ability to monitor the viscosity of the fluid continuously in conditions that cannot be replicated in the laboratory. In-situ viscometers are often more expensive than their lab-based counterparts due to being designed to a higher specification as they are often subjected to higher temperature and pressures. As with the high shear rate viscometers section, this is also split into measurement type.

4.2.1 Rotational Viscometer

4.2.1.1 Coaxial Viscometer

Cheng and Davis (1969) recognised the importance of continuous viscosity measurements and realised that by measuring the viscosity in-situ, the flow properties could be constantly identified. An in-situ viscometer was designed, based upon the rotational viscometer, and was able to measure the viscosity over a range of shear rates, Figure 4.8. A conventional rotational viscometer was modified by replacing the manual speed selection switch with a programmable switch that could be programmed using a cam timer and a pair of solenoids. This set-up allowed for switching through all the rotational speeds, 6 – 352 rpm, in approximately 6 minutes. The viscometer collected the fluid sample by injecting it into the cup via a fluid sample inlet from the process stream. Unfortunately, continuous flow disrupted measurements, and therefore injections were completed periodically. Tests were completed using aqueous solutions, and the results showed a good correlation to the expected results; these results, however, were carried out in a laboratory setting. This was the first in-situ viscosity measurement technique that allowed the measurement of non-Newtonian fluids. Areas of concern were noted when applying this technology in-line, including:

1. Oscillations occurred at the bob when rotating at high speeds, leading to uncertainties in results.

2. The results were unreliable for certain configurations.

3. The results of the viscosity were time-consuming as the data and processing tasks were completed by the tape punch and the off-line computer.

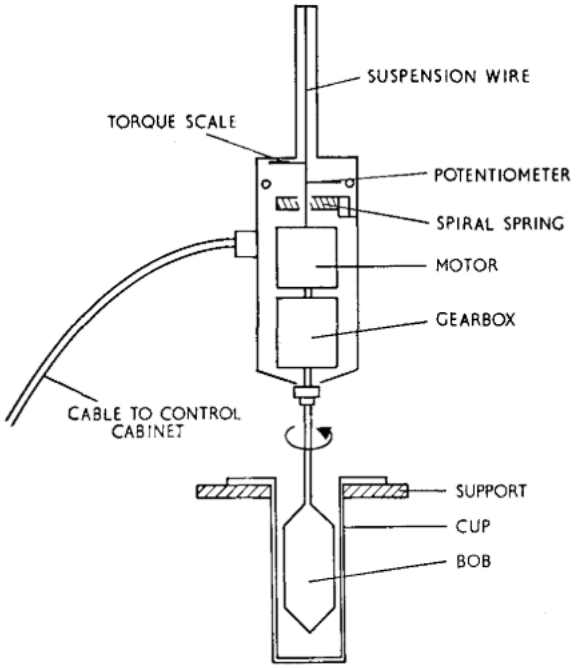

Figure 4.8: Cheng and Davis (1969). In-line rotational viscometer.

Kawatra and Bakshi (1998) applied this in-situ rotational viscometer in-line, sampling the fluid, and successfully measured the viscosity of slurries up to $3500s^{-}1$. This result proved that this device could complete viscosity measurements of non-Newtonian fluids.

Although it is shown that this method can successfully measure the viscosity, this viscometer has no advantage over periodically sampling the test fluid and analysing using an ex-situ conventional rotational viscometer.

4.2.1.2 Deflection Viscometer

A different type of rotational in-situ viscometer was suggested by Steiner et al. (2010). This viscometer drew fluid by rotating a shaft driven by a motor. As the fluid was pulled through, the tube deflected, which was a function of viscosity, Figure 4.9.

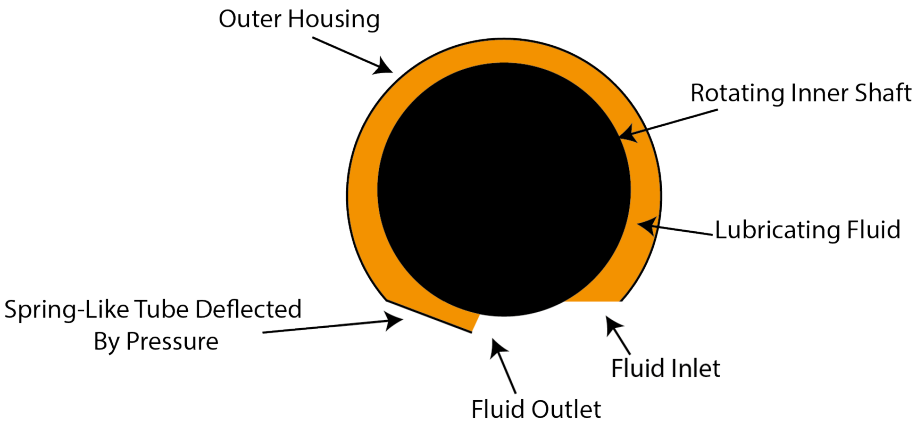

Figure 4.9: Dynamic in-line viscometer principle.

This viscometer had the advantage of monitoring the deflection using a contactless transducer which allowed the viscometer to be installed in locations that are subjected to harsh conditions. This advantage of this viscometer over previous in-situ rotational viscometers was that it could be installed without a by-line. Završnik and Joseph-Strasser (2013) adapted this viscometer to allow for the inlet deflection to vary, Figure 4.10.

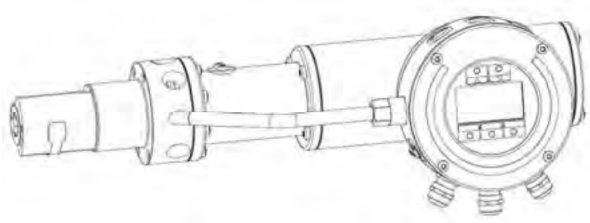

Figure 4.10: Završnik and Joseph-Strasser (2013). Dynamic in line viscometer.

This change in inlet changed the shear rate and therefore pressure, p', allowing the sample to measured over a range of shear rates. This change in pressure was a function of the samples dynamic viscosity, η, the rotational speed of the bob, ω, and the distance of the outlet gap, h.

$$p' = \frac{dp}{dx} = f\{\eta, \omega, (\frac{1}{h})^2\} \tag{4.5}$$

Comparisons of the low shear rate conventional viscometer and the in-situ dynamic viscosity for Newtonian samples showed a good correlation, but the non-Newtonian viscosity measurements were lower than expected. This work was carried forward by Anton Paar to manufacture a commercial in-situ rotational viscometer, L-Vis 510. It has been reported that this viscometer can complete measurements in the viscosity range $1mPas - 50,000mPas$ to an accuracy of 1%. The viscometer is made from stainless steel and can operate in the temperature range $-5°C - 200°C$ up to a maximum

pressure of 25 bar. There are limitations to this viscometer, including interrupting the flow, which could potentially be detrimental to the engineering system. The maximum shear rate exerted on the fluid for viscosity measurements was $352s^{-1}$, much lower than the shear rate of many processes. Another disadvantage is the large installation area, $130mm \times 100mm$, reducing the number of applications where this viscometer can be used.

4.2.1.3 Parallel Plate Viscometer

The parallel plate rotational viscometer has never been developed into an in-situ viscometer. This is likely due to the relatively large size required for operation, and the challenge of containing the fluid.

4.2.2 Capillary Viscometer

There is very little research on the development of a capillary viscometer to be used in-situ. This is likely due to the capillary viscometer's limitations, of the inability to measure the viscosity of non-Newtonian fluids. Despite this, Kalotay (1999), developed an in-situ capillary viscometer which was composed of a flow meter to measure the volumetric flow. A pair of pressure sensors were installed at either end of the flow meter allowing for the pressure change to be measured. It was found that by using a calibration process, the ratio between the volumetric flow and change in pressure was equal to the apparent viscosity of the sample. The author had reservations about the design of the viscometer, noting that the flow had to be laminar, and as discussed above, the fluid had to be Newtonian.

4.2.3 Falling Body Viscometer

The falling body viscometer cannot be used for in-situ measurements due to the high sensitivity of the measurement apparatus.

4.2.4 Oscillatory Viscometers

Due to the relatively new development of vibrational tuning fork viscometers, there has been little work in adapting this measurement technique for in-situ measurements.

Belmiloud et al. (2008) developed microcantilever devices, and the viscosity of Newtonian fluids was measured over the frequency range $100Hz$ – $600Hz$. It was found that the upper limit of viscosity measurements was $100cP$ due to excessive damping at higher viscosities.

Jakoby et al. (2010) completed an extensive study on multiple configurations of miniaturised vibrational in-situ viscosity sensors and found that the results produced by all measurements did not equal the measurement completed by standard laboratory

viscometers. This inequality was hypothesised to be caused by the increased complexity of the measurement.

MicroMotion has developed an aluminium in-situ commercial fork viscometer. It can be installed by insertion into pipelines, bypass loops and tank installation. The literature claims to measure the viscosity of fluids from $0.5cP$ - $12500cP$ and can be installed into locations with harsh operating conditions, $-40C°C$ - $65°C$, due to the sensitive components being separated from the fork (Emerson, 2020). Unfortunately, the frequency at which the fork oscillates is not provided in any literature.

The author can find no commercial in-situ oscillating cup viscometer which is not surprising as this viscometer type requires the fluid to the contained in a closed cup which is impractical for in-situ measurements.

The QCM is unable to be used to measure the viscosity of oils in-situ due to its sensitive components, making it impractical to be installed in harsh environments.

4.2.5 Comparison of Adapted Conventional Viscometers for In-situ Measurements

Table 4.4 shows a comparison of the discussed adapted conventional viscometers for in-situ measurements.

	Advantages	Disadvantages
Coaxial	• Can be installed in-line. • Large temperature range and pressure -5 - $200°C$, $25bar$.	• Non-Newtonian measurements did not align with expected results. • Low shear rate $352s^{-1}$. • Large installation area.
Parallel Plate	NA	NA
Capillary	• Inexpensive.	• Limited to Newtonian fluids. • Flow has to be laminar. • Not widely investigated.
Oscillatory	• Can be installed in harsh operating conditions.	• Measurements can only be completed at low viscosities due to damping. • Experimental viscosity results do no equal theoretical results. • Measurements completed at relatively low shear rates.

Table 4.4: Comparison of adapted conventional viscometers for in-situ measurements.

4.3 Ultrasonic Shear Waves Used To Measure Viscosity Using Reflection Coefficient

Mason et al. (1949) published the first paper detailing a method to measure the viscosity of liquids using ultrasonic shear waves. The motivation behind this investigation was to discover whether liquids exhibited a shear elastic effect as well as a viscous effect when exerted to rapid shearing, as had been hypothesised by Maxwell (1865). Mason et al. had completed previous investigations using a torsional crystal but found that it was limited to $500kC$ due to the small size. The new ultrasonic viscometer consisted of a crystal bonded to a quartz rod using silver paste. This technology had previously been developed a year earlier, where it was used to measure the attenuation of high-frequency sound waves in metal and glass (Mason and Mcskimin, 1947). By monitoring the reflected signal when the free end of the quartz rod had a liquid load applied, the reflection coefficient and the phase was calculated by comparing the signal when loaded and unloaded, Figure 4.11.

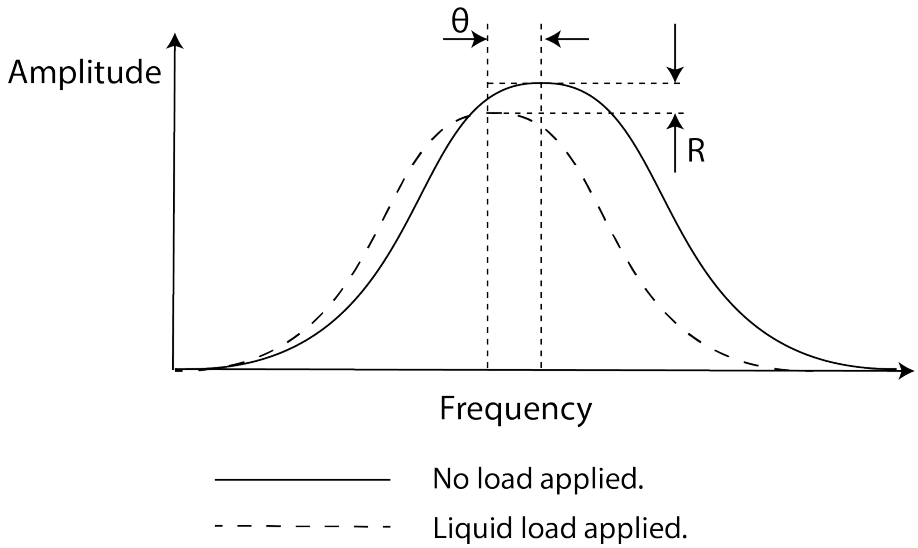

Figure 4.11: Mason ultrasonic viscometer signal analysis.

Using this information the reflection factor, R_F, was calculated using Equation 4.6.

$$R_F = Re^{-i\theta} \tag{4.6}$$

The reflection factor was then directly related to the acoustic impedance of the fluid, z_l, and quartz, z_Q.

$$R_F = \frac{z_Q - z_l}{z_Q + z_l} \tag{4.7}$$

Mason et al. (1949) found at normal incidence, the limiting factor of the viscometer was the relationship between the acoustic impedance of the liquid and the fused quartz.

In this joint publication, McSkimin proposed that pulsing a shear wave at an angle would increase the system's sensitivity. For all the samples in this study, the acoustic impedance of the liquid was a function of the angle of incidence from the normal.

$$z_l = cos(\phi) z_Q \frac{1 - R^2 + 2jR\sin\theta}{1 + R^2 + 2R\cos\theta} \tag{4.8}$$

This method increased the shear impedance transformation ratio of the liquid by a factor of $1/cos(\phi)$, where ϕ is the angle of incidence from the normal. An angle of 79°was chosen, which gave an impedance transformation ratio of 5.25 to 1. The set-up can be seen in Figure 4.12. A series of shear waves was pulsed at $4.5MHz$, $14MHz$ and $24MHz$ and the resistance and reactance of different samples over a range of temperatures of 10°C- 50°C was measured. The acoustic impedance was then related to the shear modulus. It was presumed that the fluid was Newtonian and therefore the elastic portion was discarded.

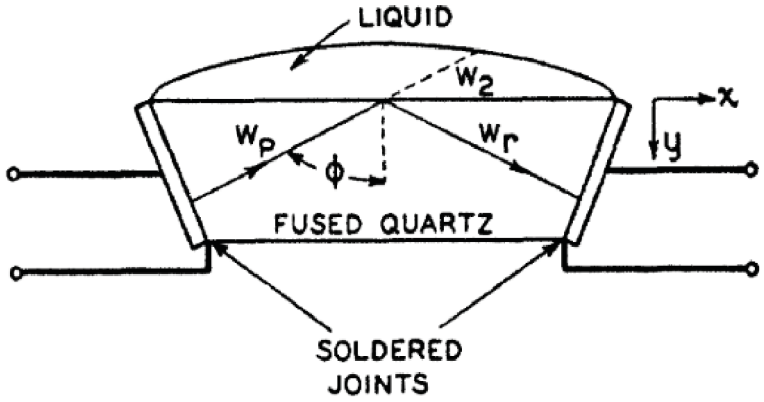

Figure 4.12: Mason et al. (1949). The first ultrasonic viscometer.

Roth and Rich (1953) further developed the ultrasonic viscometer in the paper 'A New Method for Continuous Viscosity Measurement. General Theory of the Ultra-Viscoson'. The motivation for this was not as before, to increase the shear rate, but rather to overcome previous limitations of viscometers not being suitable for in-situ measurements. This lack of viscosity monitoring meant that a temperature-time basis, rather than viscosity, controlled many fluid processes. This was detrimental to operations as most had to be completed by batch processing rather than a continuous process. The Ultra-Viscoson differed from Mason's ultrasonic viscometer by implementing a magnetostrictive transducer which was bonded to a magnetostrictive alloy. A shear wave was produced at the transducer and propagated along the alloy. The magnetostrictive alloy was submerged in the test fluid, and the amount that the shear vibrations in the strip were damped was related to the viscous properties. Using this set-up, Roth measured samples at 30kHz with an accuracy of ±5%.

The next significant advancement was completed by Barlow and Lamb (1959) where measurements of the viscoelastic behaviour of lubricating oil at high shear rates were successfully measured. By using Mason's viscometer an investigation was completed into the influence of the relaxation behaviour of lubricants over the extensive range of $6 - 78Mc$, Figure 4.13. Barlow increased the range and magnitude by improving the electrical apparatus, allowing for greater stability and sensitivity. The extensive range of frequencies was obtained by driving at the transducers resonant frequency, 6Mc, and then driving at odd harmonics up to 78Mc. This is the first paper where ultrasonic spectroscopy was completed, measuring a sample's viscosity at different frequencies.

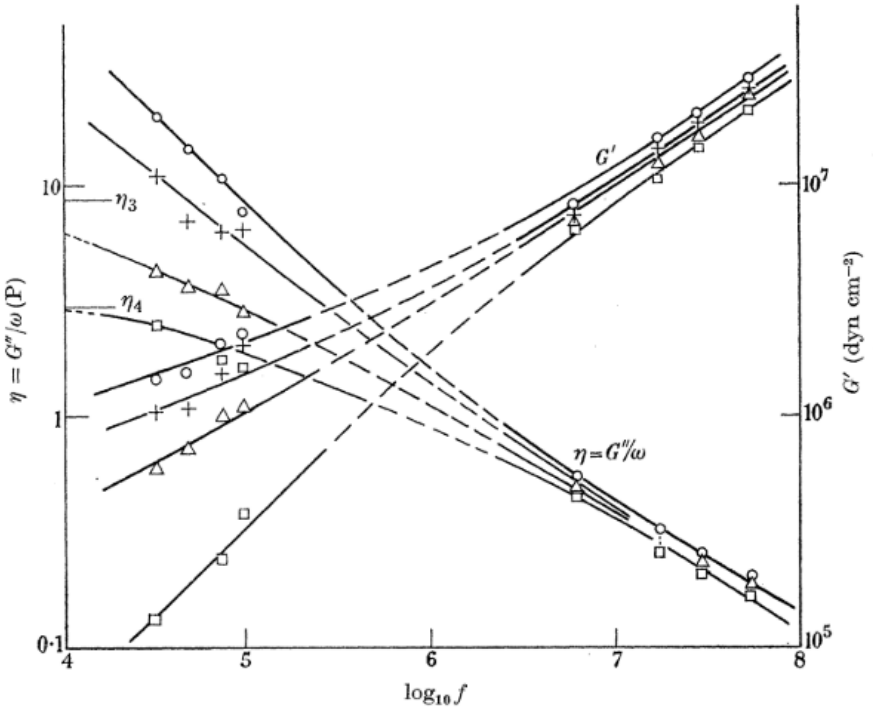

Figure 4.13: Barlow and Lamb (1959). The first ultrasonic spectroscopy results.

The first time viscosity measurements were completed using the reflectance methodology where the transducer was not in contact with the test fluid, was when Cohen-Tenoudji et al. (1987) adapted Mason's ultrasonic apparatus to obtain measurements at high temperatures. The transducer was bonded to a 'buffer system' to distance the transducer from the test fluid, Figure 4.14. The set-up produced two echos, one at the copper-aluminium boundary and a second at the aluminium-fluid boundary. This first echo was monitored and used to calibrate the second reflection when there was a temperature change. This system was used to monitor the viscosity of epoxy over a range of temperatures. The curve was comparable to measurements taken using a torque rheometer at 10Hz, but the absolute value of the ultrasonic viscosity measurements was much lower.

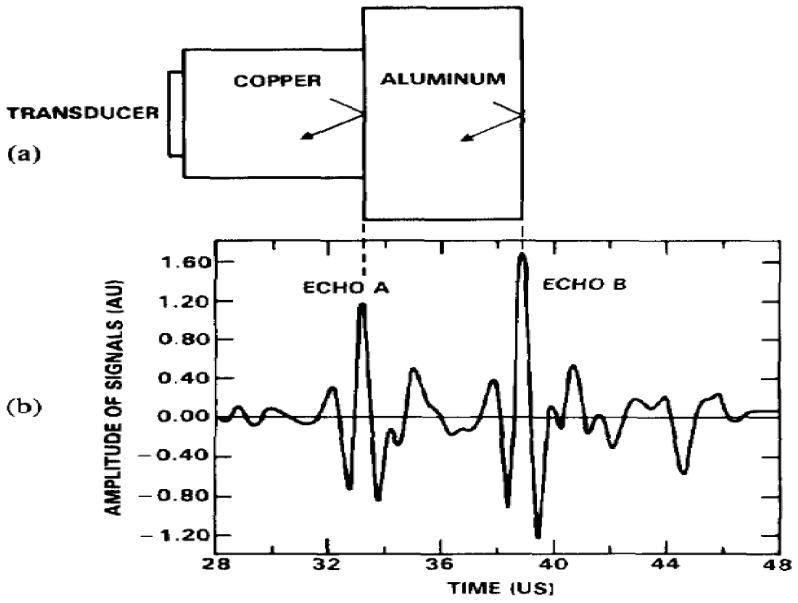

Figure 4.14: Cohen-Tenoudji et al. (1987). Ultrasonic viscometer with a buffer system.

The next considerable advancement came with digitisation. In previous ultrasonic viscometers, the reflected ultrasound signal analysis was time-consuming—the signal needed to be manipulated by hand to transform from the time domain to the Fourier domain. Alig et al. (1997) first utilised digitisation where he used Mason's ultrasonic viscometer set-up and completed viscosity measurements of polymer films. Through digitisation, experiments were conducted using a single frequency pulse technique and an ultrasonic spectroscopy technique. The spectroscopy approach employed a broad-band acoustic pulse and Fourier analysis technique to measure the sample's response over a broad frequency range. The results of this ultrasonic spectroscopy technique are shown in Figure 4.15, illustrating that the storage and loss modulus are frequency-dependent, as did Barlow and Subramaniam (1966). The maximum frequency was limited by the sampling rate of the digitising plug-in card. The frequencies were chosen based on the odd harmonics of the resonant frequency of the crystal because all other frequencies had low signal-to-noise ratios. The digitisation of signal analysis allowed for close to instantaneous viscosity measurements, and equally importantly, ultrasonic spectroscopy to become a viable method.

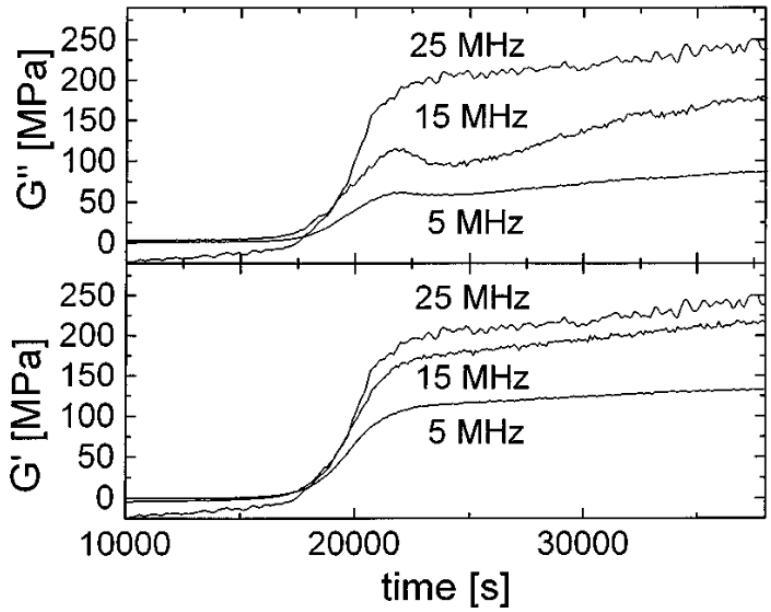

Figure 4.15: Alig et al. (1997). Ultrasonic storage and loss results using digitisation.

These developments allowed for many investigations using ultrasonic viscometers including:

1. Sensor fusion of a longitudinal and a shear wave to measure the viscosity and the density (Greenwood and Bamberger, 2002).

2. The viscosity measurements of foodstuffs (Kulmyrzaev and Mcclements, 2000) (Saggin and Coupland, 2004).

3. Sensor adaption to use a longitudinal wave for wave conversion (Buiochi et al., 2006).

4. Further experiments to measure the viscosity of oils (Saggin and Coupland, 2001).

As shown by results from Saggin and Coupland (2001), Figure 4.16, the reflection coefficient is above 0.94 for an oil with viscosity of 100 Pas. This shows that the ultrasonic system is very insensitive to low viscosity fluids.

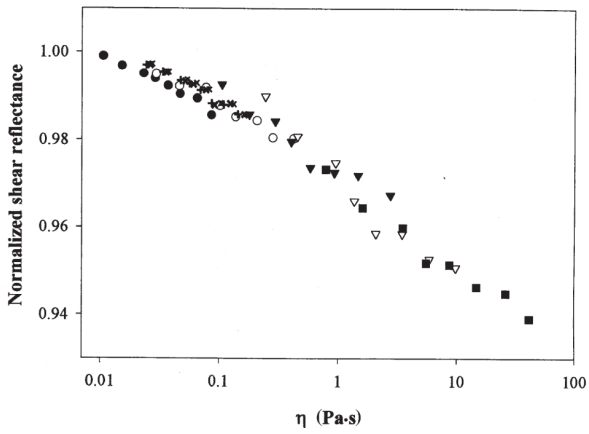

Figure 4.16: Saggin and Coupland (2001). Reflection coefficient versus viscosity for an ultrasonic viscometer.

To overcome this Schirru (2016) developed an ultrasonic viscometer that massively increased the sensitivity, making viscosity measurements of low viscosity oils viable. He did this by employing a matching layer to the interface between the metal and oil, increasing the sound to noise ratio, and reducing the reflection coefficient, Figure 4.17.

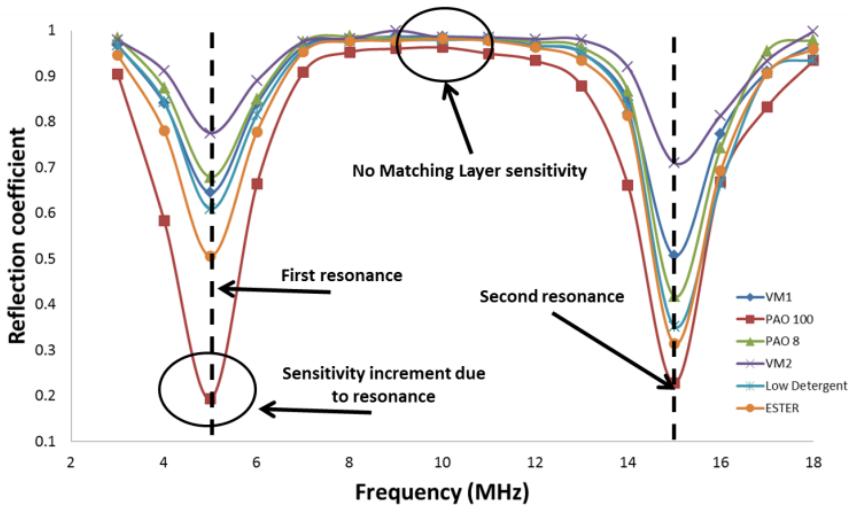

Figure 4.17: Schirru (2016). Reflection coefficient over a range of frequencies for a three layered system.

The matching layer method has been used in ultrasonic development since the late 1970s, where Desilets et al. (1978) applied the quarter wavelength theory established in electronics to ultrasonics, showing that by varying the acoustic impedance of the matching layer the transmission increased. This research laid the foundations for quarter wavelength technology in acoustics and it is why all commercial transducers include a matching layer.

Schirru (2016) successfully installed this on a journal bearing with a 5MHz shear transducer and a 50µm matching layer, Figure 4.18. This allowed for viscosity measure-

ments over a range of temperatures and pressures. The results were analysed using a calibration curve, which is a plot of the reflection coefficient versus the known viscosity of non-Newtonian samples.

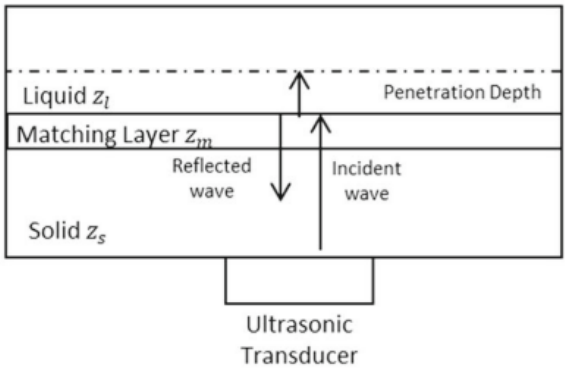

Figure 4.18: Schirru (2016). Schematic of ultrasonic viscometer with a matching layer.

Measurements were also completed at three frequencies using two transducers, a 1MHz transducer and a 4.5MHz transducer excited at its next odd harmonic. The results presented for Newtonian fluids, PAO 100, PAO 40, Figure 4.19, show significant differences between the different frequencies and also theoretical measurements (Liu et al., 2017) . This shows that further development is required when using this method for spectroscopy viscosity measurements.

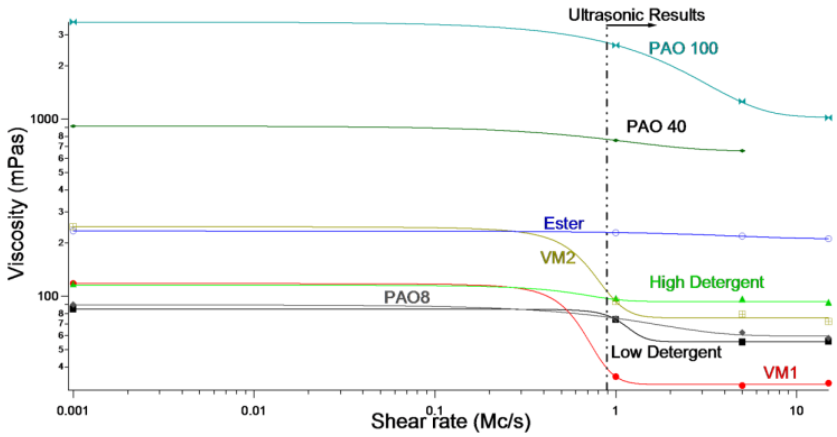

Figure 4.19: Schirru (2016). Ultrasonic spectroscopy using a matching layer viscometer.

4.3.1 Advantages and Disadvantages of Shear Ultrasound Viscometers

Table 4.4 shows a comparison of the discussed shear ultrasound viscometers.

	Advantages	Disadvantages
Shear Ultrasound	• Does not disrupt flow. • Can measure the viscosity of Newtonian and non-Newtonian fluids. • Relatively inexpensive. • Small installation area. • High shear rates. • Large range of viscosities measurable. • Continuous measurements.	• Further work is required to understand the measurements of non-Newtonian fluids.

Table 4.5: Advantages and disadvantages of shear ultrasound viscometers.

4.4 Summary

By studying the conventional viscometers adapted for high shear rates, it has been shown that it is possible to measure the viscosity of Newtonian and non-Newtonian oil. With the adaptions, measurements are more complex and greater considerations are required, such as a more significant influence from shear heating and wall effects.

When examining the conventional viscometers adapted for in-situ measurements, the first viscometers were unable to be used in-line. Instead, they required the oil to be periodically removed from the system. The in-situ viscometers were also very expensive due to modifications having to be made to allow them to be installed in a harsh environment. All the in-situ viscometers reviewed were required to be either installed on a separate line or installed directly in the lubricant, which affected the flow.

Using ultrasonic shear waves to measure viscosity has been shown to have many advantages over the more conventional methods. It shears fluid at extremely high rates due to the operating frequency of the transducers. From the advancements, it is also exceptionally well suited to carry out in-situ measurements due to removing the sensitive components from harsh operating conditions, increasing the sensitivity of measurements, allowing for low viscosity lubricants to be measured, no moving parts, and the small installation area required. However, there are discrepancies when using ultrasound and comparing it to the theoretical values. This deviation may be caused by the lack of understanding of the shear rate applied on the test fluid by the ultrasonic viscometer.

To meet the objectives of this thesis, this literature survey has shown that further development is required to obtain the viscosity from the mathematical model, specifically adapting current models to introduce the pressure reflection coefficient term. This survey has also shown that current ultrasound technology can be adapted to allow for building a highly sensitive viscometer by implementing a three-layered system with multiple thickness matching layers.

Chapter 5

A Three Layered Ultrasonic Model for Viscoelastic Fluids

In this chapter, rheological models are combined with the reflection coefficient model for both a two and three-layered system, simulating the response from a matching layer ultrasonic viscometer, and a novel relationship is presented.

The first section of the chapter derives the pressure reflection coefficient for a two and three-layered system, where all layers are fully elastic. Rheological models for a Newtonian and non-Newtonian fluid are then presented using mechanical analogies. Finally, the pressure reflection coefficient and rheological models are combined, producing a model which is subjected to a sensitivity analysis.

5.1 Introduction

Previous publications have aimed to link the reflection coefficient to the viscosity of the test sample. Schirru et al. (2015) presented a model that correlated the viscosity of a Newtonian fluid and reflection coefficient for a two-layer system. This model presumed that the relaxation time of the fluid is very short, and therefore this variable was negated when calculating the viscosity.

In studies where a three-layered system is employed for a Newtonian fluid (Schirru, 2016), the reflection coefficient has been calculated using the intensity reflection coefficient rather than the pressure reflection coefficient, requiring further information about the ultrasound signal.

Other publications where the viscosity has been correlated to the reflection coefficient of a three-layered system and a non-Newtonian fluid (Schirru et al., 2018) cannot be used due to mathematical errors.

Therefore a new equation is required to link the viscosity and the reflection coefficient for Newtonian and non-Newtonian fluids in a two and three-layer system. This chapter focuses on a change in viscosity with the frequency of the system, as future

matching layer ultrasonic viscometers discussed in later chapters will be manufactured with a range of different frequency transducers.

5.2 Reflection Coefficient in Multiple Layers

As a wave travels through a system consisting of multiple mediums with differing acoustic impedances, upon reaching a boundary part of the wave will be reflected, and part of the wave will be transmitted. This is quantitatively measured in terms of reflection coefficient.

5.2.1 Two Layered Model

For a system that consists of two media with different acoustic impedances, when the incident wave reaches the boundary between different media 1 and 2, a portion of the incident wave, P_i, is reflected, P_r, and a portion of the wave is transmitted, P_t. This interaction is shown in Figure 5.1 and can be mathematically modelled with respect to acoustic impedance.

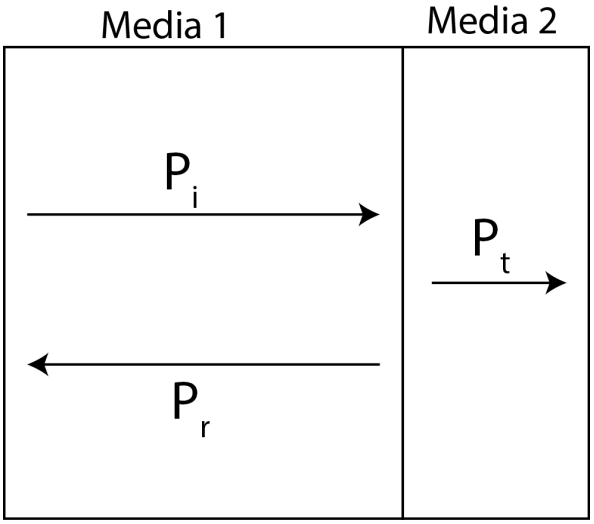

Figure 5.1: Diagram showing the incident, reflection and transmitted wave for a two-layered system.

The model is initialised using the conservation of pressure, p, and velocity, u, at the boundary, Equation 5.1 and Equation 5.2, where i, t and r denote the incident, transmitted and reflected waves respectively.

$$p_i + p_r = p_t \tag{5.1}$$

$$u_i + u_r = u_t \tag{5.2}$$

Dividing these equations, the continuity of acoustic impedance at the boundary is maintained.

$$\frac{p_i + p_r}{u_i + u_r} = \frac{p_t}{u_t} \tag{5.3}$$

Using the relationship between the acoustic impedance, z, and the pressure and velocity, $z = p/u$, the equation is manipulated to incorporate acoustic impedance.

$$z_1 \frac{p_i + p_r}{p_i - p_r} = z_2 \tag{5.4}$$

The reflection coefficient is determined by using the relationship between the reflection coefficient and pressure, Equation 3.8.

$$R = \frac{z_2 - z_1}{z_2 + z_1} \tag{5.5}$$

The relationship between reflection coefficient and frequency is plotted, Figure 5.2. In this simulation, the acoustic impedance of the first medium remains at a constant value of $8.37 \times 10^6 Rayl$, the acoustic impedance of aluminium, and the acoustic impedance of the second layer is varied from 1×10^3 to $1 \times 10^5 Rayl$, the acoustic impedance of lubricating oils. The plot shows that as the acoustic impedance of the second medium increases, the reflection coefficient decreases. This decrease is caused by the acoustic impedance of the mediums becoming increasingly similar in value, allowing for a more significant proportion of the wave to be transmitted, and less reflected. The plot shows that the reflection coefficient has no frequency dependency when the two mediums are fully elastic. It is important to note that the reflection coefficient values are nearing unity, representing almost complete reflection.

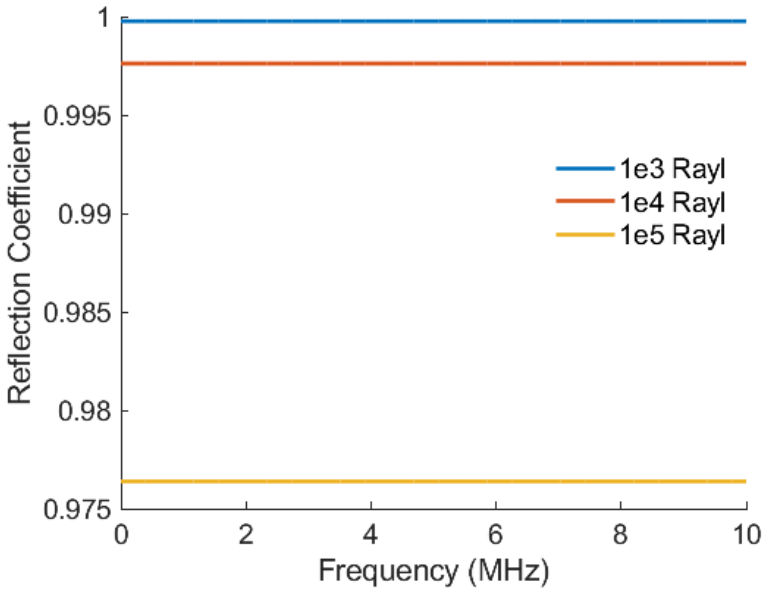

Figure 5.2: Reflection coefficient with respect to frequency for a two-layer system, for different acoustic impedance of the second medium.

5.2.2 Three Layered Model

As with the two-layered system, part of the wave will be reflected when the wave reaches a boundary, and part will be transmitted. For a three-layered system, there are two boundaries, and this is shown in Figure 5.3, with the subscripts denoting the incident, i, transmitted, t and reflected, r, waves, and the number noting the layer that the wave has had its last interaction.

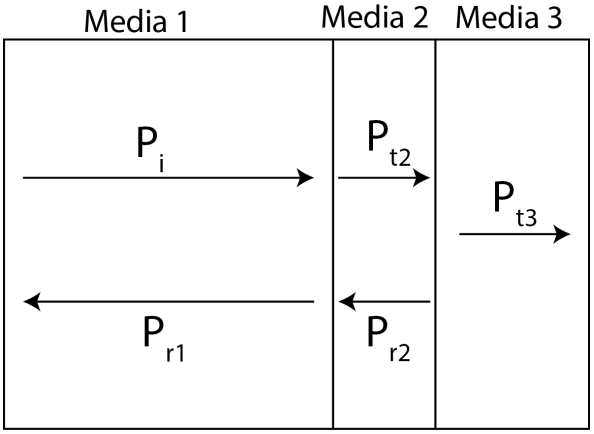

Figure 5.3: Diagram showing the incident, reflection and transmitted wave for a three-layered system.

Unlike the two-layered system, the complex pressure, p, is used as the amplitude and phase both have to be considered. The wavenumber, k_2, describes the number of waves per distance in the intermediate media, $k_2 = \frac{2\pi}{\lambda_2}$. The relationship between the pressure and the complex pressure is shown in the two equations below.

$$p_{t2} = P_{t2} \exp^{j(\omega t - k_2 x)} \tag{5.6}$$

$$p_{r2} = P_{r2} \exp^{j(\omega t + k_2 x)} \tag{5.7}$$

Using the same methodology for the two-layered system applied for the three-layered system - continuity of acoustic impedance- the system is initialised at the two boundaries.

$$\frac{P_i + P_{r1}}{P_i - P_{r1}} = \frac{z_2}{z_1}\left(\frac{P_{t2} + P_{r2}}{P_{t2} - P_{r2}}\right) \tag{5.8}$$

$$\frac{P_{t2} \exp^{-jk_2 t_2} + P_{r2} \exp^{jk_2 t_2}}{P_{t2} \exp^{-jk_2 t_2} - P_{r2} \exp^{jk_2 t_2}} = \frac{z_3}{z_2} \tag{5.9}$$

Rearranging and using Euler's formula, the pressure reflection coefficient, R is determined.

$$R = \frac{(1 - z_1/z_3)\cos k_2 t_2 + j(z_2/z_3 - z_1/z_2)\sin k_2 t_2}{(1 + z_1/z_3)\cos k_2 t_2 + j(z_2/z_3 + z_1/z_2)\sin k_2 t_2} \tag{5.10}$$

Acoustic Impedance	
Media 1	$8.37 \times 10^6 Rayl$
Media 2	$1.1 \times 10^6 Rayl$
Media 3	$0.01 \times 10^6 Rayl$
Media 2 Thickness	$3.9 \times 10^{-5} m$

Table 5.1: Inputs for the three layered model simulations.

Using Equation 5.10 the relationship between reflection coefficient and frequency is plotted. Figure 5.4 shows how this relationship varies when the acoustic impedance of the third layer varies. As with the two-layered system, an increase in the acoustic impedance reduces the mismatch between layers leading to greater transmission and a lower reflection coefficient value.

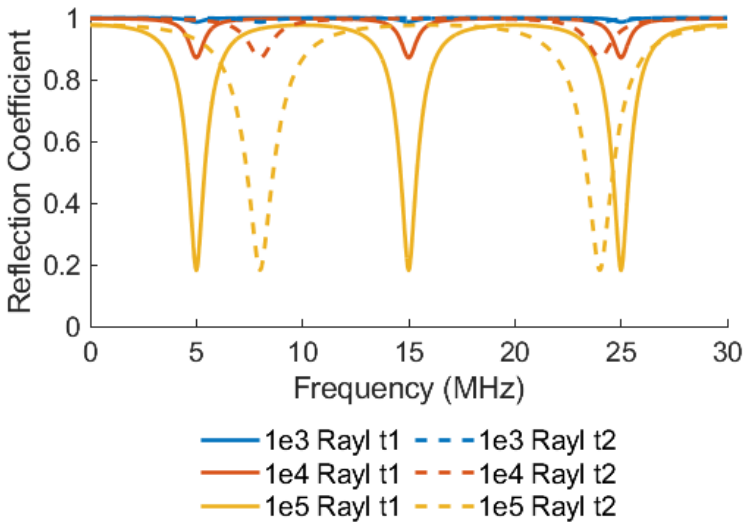

Figure 5.4: Reflection coefficient with respect to frequency for a three-layer system, for different acoustic impedances and thickness of the intermediate medium, where t1 and t2 relate to different thickness intermediary layers.

The plot shows periodic drops in the reflection coefficient as the frequency increases, which occurs when the wavelength is equal to four times the thickness of the intermediate medium. When this happens Equation 5.10 can be reduced to Equation 5.11.

$$R_{res} = \frac{z_2^2 - z_3 z_1}{z_2^2 + z_3 z_1} \tag{5.11}$$

When the quarter wavelength is equal to the thickness of the intermediate medium, the reflection from the intermediate interface will be twice a quarter wavelength, π, out of phase with the reflection from the first interface. These two waves will subsequently destructively interfere, reducing the reflected amplitude from the first boundary.

For destructive interference to occur, as stated, the phase difference has to equal π, meaning the dips in the reflection coefficient will occur at odd modes. The plot further illustrates that unlike the two-layered models, Figure 5.2, the reflection coefficient depends on the frequency, although the reflection coefficient value for each dip remains constant. The plot further shows that as the acoustic impedance becomes more similar, the 'reflection coefficient bandwidth' increases. This is due to the reduction in acoustic mismatch, which reduces the reflection coefficient over all frequencies. This means the more dissimilar the acoustic mismatch becomes, it will be increasingly important to use the specific frequency associated with the minimum reflection coefficient.

Figure 5.4 shows how the thickness of the intermediate medium shifts the frequency at which minimum reflection occurs. This shifting of frequencies allows for adjusting of the system whereby altering the thickness of the intermediate layer, the minimum

reflection can be obtained at different frequencies. This is extremely important as it allows for sensitive measurements at different frequencies.

In future sections, it will be assumed that the thickness of the intermediate layer is always a quarter of a wavelength of the corresponding frequency, showing the minimum theoretical sensitivity if the system was optimised, as shown in Figure 5.5.

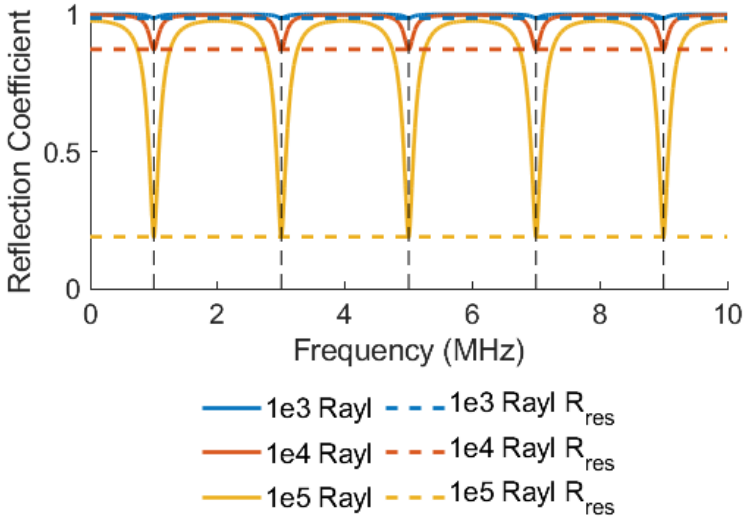

Figure 5.5: A comparison of the reflection coefficient with respect to frequency for a three-layer system when the thickness of the intermediate layer is constant at $\lambda/2$, Equation 5.11.

5.2.3 Two Layer and Three Layer Comparison

One of the main differences between the two and three-layer system is the frequency dependence of the three-layer system. It has been shown that the sensitivity of the system can be manipulated by changing the thickness of the intermediate layer, whereas changing the thickness of the layers in a two-layer system does not affect the reflection coefficient.

A further difference is that the three-layered system has a lower reflection coefficient value for all frequencies than the two-layered system. This can be explained by looking at the mismatch in the acoustic impedance between the layers. It has been shown that the more significant the difference in acoustic impedance, the greater the amount of reflected signal is returned. Therefore by adding an extra layer with an intermediary acoustic impedance, more signal can be transmitted into the fluid layer, reducing the reflection coefficient and allowing sensitive viscosity measurements, Figure 5.6.

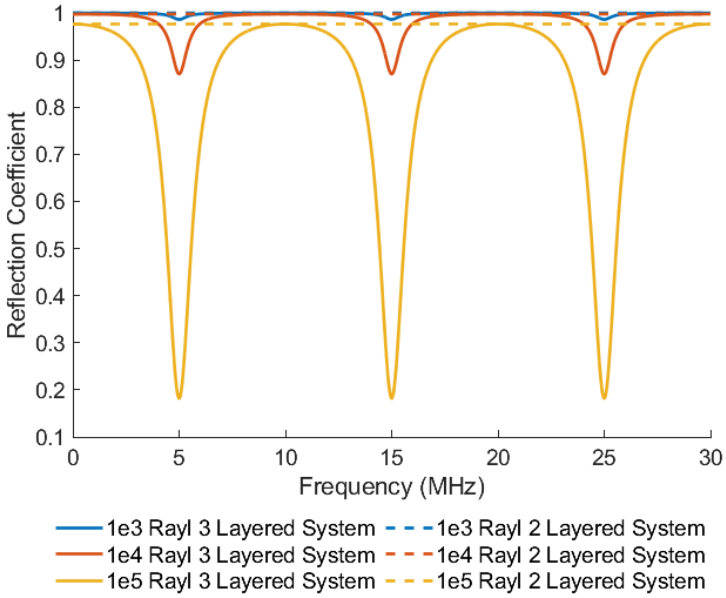

Figure 5.6: A comparison of the reflection coefficient with respect to frequency for a two and three-layer system, for different acoustic impedances of the intermediate medium.

5.3 Rheological Models

Rheological models are used to describe the characteristics of a fluid. They are commonly presented mechanically in terms of a linear elastic spring and a linear viscous dashpot to represent the elastic and viscous elements of a fluid. The linear elastic spring, Figure 5.7*a*, represents a spring with stiffness, E. When the spring is subjected to stress, σ, it experiences an instantaneous elastic strain, with the elastic strain remaining as long as the stress is applied. When the stress on the spring is removed, it instantaneously undergoes a de-straining. The linear elastic spring is modelled using Equation 5.12.

$$\epsilon = \frac{1}{E}\sigma \tag{5.12}$$

The linear viscous dashpot is representative of a dashpot piston-cylinder arrangement that is filled with viscous fluid, Figure 5.7*b*. When stress, σ, is applied, the piston is pulled through a fluid with viscosity, η. When the stress is removed, there is no force to move the piston, so the strain on the piston is permanent. The strain increases linearly and without bounds, with the strain increasing gradually. Using this analogy the strain rate, $\dot{\epsilon}$, can be modelled using Equation 5.13. Integrating the strain rate with time outputs the applied strain when stress is suddenly applied, σ_0, and it is assumed there is zero initial strain, Equation 5.14.

$$\dot{\epsilon} = \frac{1}{\eta}\sigma \tag{5.13}$$

$$\epsilon = \frac{\sigma_0}{\eta}t \tag{5.14}$$

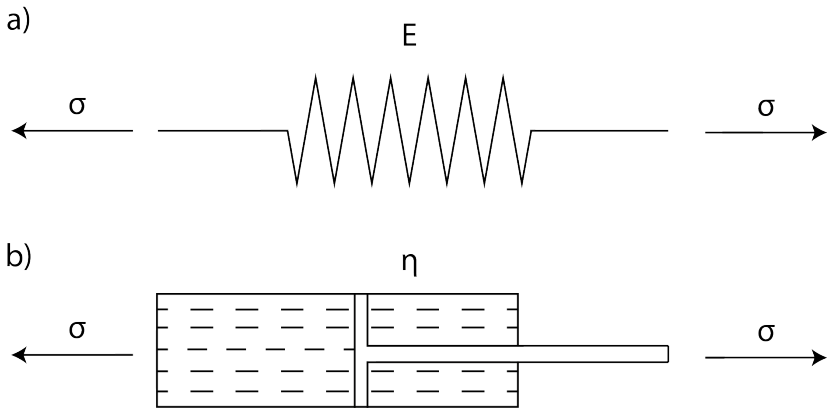

Figure 5.7: Schematic of a *a)* linear viscous spring and *b)* linear viscous dashpot, that are subject to stress.

The shear modulus can be obtained by combining these models with the shear stress and shear strain relationship. The shear modulus is composed of a storage modulus and a loss modulus. The relationship between these parameters is displayed in Figure 5.8. The phase angle dictates if the material is elastic or viscous - if the phase angle is 0°, the material has no loss modulus component and can be considered entirely viscous - a fluid. As the phase angle tends to 90°, the phase angle increases as does the elastic component and represents the fluid becoming more elastic.

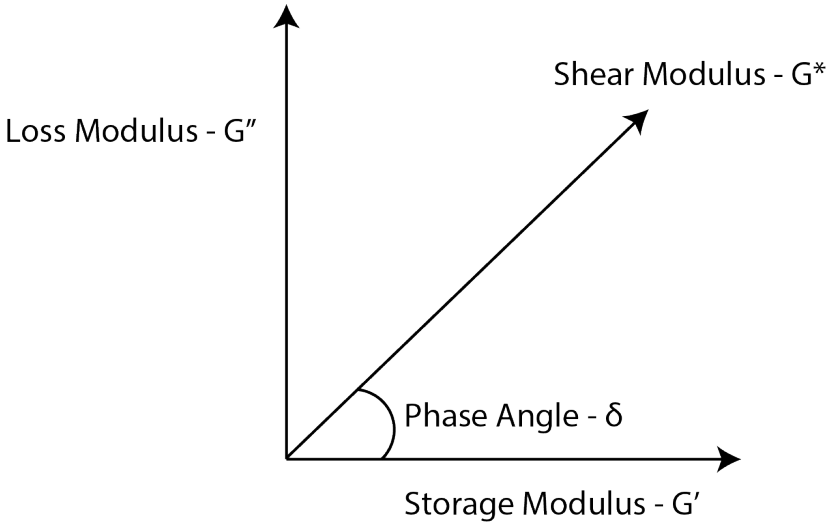

Figure 5.8: The relationship between the storage modulus, loss modulus, phase angle and shear modulus.

5.3.1 Newtonian Model

As stated in earlier chapters, the viscosity of a Newtonian fluid does not alter when varying amounts of shear are applied. For a Newtonian fluid, it is assumed that the fluid is incompressible, and this is presented using Figure 5.9.

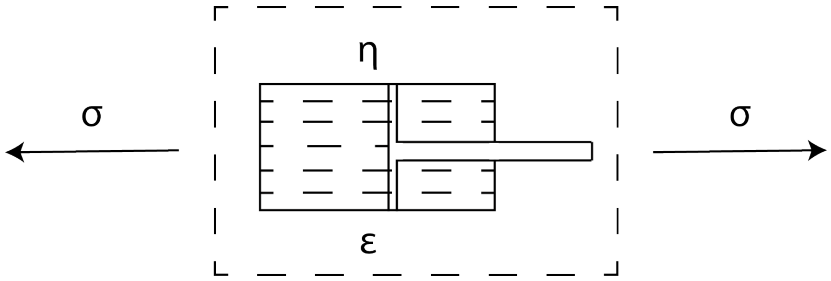

Figure 5.9: Schematic of a Newtonian fluid model using standard mechanical analogies.

By combining the viscous dashpot stress model, Equation 5.14, with the shear stress and shear strain relationship, Equation 2.5, the shear modulus can be obtained.

$$G'' = i\eta\omega \tag{5.15}$$

A Newtonian fluid does not have a storage component, $G' = 0$, the loss component is equal to the shear modulus.

$$G = G' + G'' = i\eta\omega \tag{5.16}$$

5.3.2 Maxwell Model

A model commonly used to describe a viscoelastic fluid under stress is the Maxwell model (Maxwell, 1865). It has been chosen over other viscoelastic models as it considers the relaxation effects of a fluid - the time it takes for the particles in a fluid to return to their natural position, and is also the most simple with the fewest number of variables. Unlike the Newtonian model, the elastic portion of the fluid is also of interest. Therefore, it is modelled using the linear viscous dashpot, which represents the base oil, and the linear elastic spring, which represents the non-Newtonian additive package of the lubricating oil, Figure 5.10.

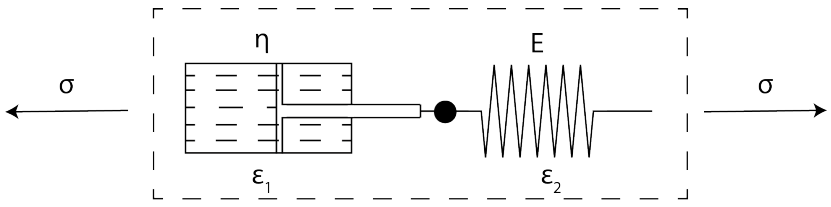

Figure 5.10: Schematic of a Maxwell fluid model using standard mechanical analogies.

The derivation of the model begins with abiding by the equilibrium requirements; the stress must be the same in both the spring and the dashpot elements.

$$\epsilon_1 = \frac{1}{E}\sigma, \dot{\epsilon}_2 = \frac{1}{\eta}\sigma, \epsilon = \epsilon_1 + \epsilon_2 \tag{5.17}$$

By differentiating, ϵ_1 and ϵ_2, and substituting, the standard Maxwell model equation is derived.

$$\sigma + \frac{\eta}{E}\dot{\sigma} = \eta\dot{\epsilon} \tag{5.18}$$

The Maxwell model is rearranged to make the strain rate the subject.

$$\dot{\epsilon} = \frac{\sigma}{\eta} + \frac{\dot{\sigma}}{E\eta} \tag{5.19}$$

For the Maxwell model, the creep compliance function, J, is equal to $1/E$. Using work of Barlow and Lamb (1959), the relaxation time, τ, is equal to the creep compliance function.

$$\dot{\epsilon} = \frac{\sigma}{\eta} + \frac{\dot{\sigma}\tau}{\eta} \tag{5.20}$$

The stress and the strain are sinusoidal due to the harmonic motion of the shear wave and, therefore, Equation 5.20, transforms to Equation 5.22.

$$\sigma = \sigma e^{i\omega t}, \gamma = \gamma e^{i\omega t} \tag{5.21}$$

$$\gamma e^{i\omega t} = \frac{\dot{\sigma} e^{i\omega t}\tau}{\eta} + \frac{\sigma e^{i\omega t}}{\eta} \tag{5.22}$$

Using the relationship between the shear and strain, Equation 2.5, the shear modulus can be found.

$$G = \frac{\eta(i\omega\tau)}{\tau(1 + i\omega\tau)} \tag{5.23}$$

Rearranging Equation 5.23, and grouping the real and imaginary parts allows for the determination of the storage and the loss modulus.

$$G = \frac{\omega^2\eta\tau}{1 + \omega^2\tau^2} + i\frac{\omega\eta}{1 + \omega^2\tau^2} \tag{5.24}$$

$$G' = \frac{\omega^2\eta\tau}{1 + \omega^2\tau^2} \tag{5.25}$$

$$G'' = \frac{\omega\eta}{1 + \omega^2\tau^2} \tag{5.26}$$

5.4 Reflection Coefficient From A Fluid Layer

Combining the reflection coefficient models and the shear modulus derived in the previous sections makes it possible to find a relationship between reflection coefficient and viscosity. The input parameters for this section are shown in Table 5.2, unless otherwise stated. Due to the complex nature of the shear modulus, the reflection coefficient is a complex value. For all future plots, the reflection coefficient refers to the modulus of the reflection coefficient.

Parameter	Layer	
Density	1	$2700 kg/m^3$
	2	$1400 kg/m^3$
	3	$832 kg/m^3$
Speed of Sound	1	$3100 m/s$
	2	$780 m/s$
Viscosity	3	$0.1 Pas$
Relaxation Time	3	$10^{-8} s$

Table 5.2: Input variables for the rheological model simulations.

5.4.1 Newtonian Fluid

5.4.1.1 Two Layered System

For a Newtonian fluid in a two-layered system, the relationship between the reflection coefficient and viscosity is calculated by combining Equation 5.5 and Equation 5.15.

$$R = \frac{\sqrt{i\rho_2\omega\eta} - \rho_1 c_1}{\sqrt{i\rho_2\omega\eta} + \rho_1 c_1} \tag{5.27}$$

Using Equation 5.27, the reflection coefficient can be plotted against frequency for various viscosities, Figure 5.11.

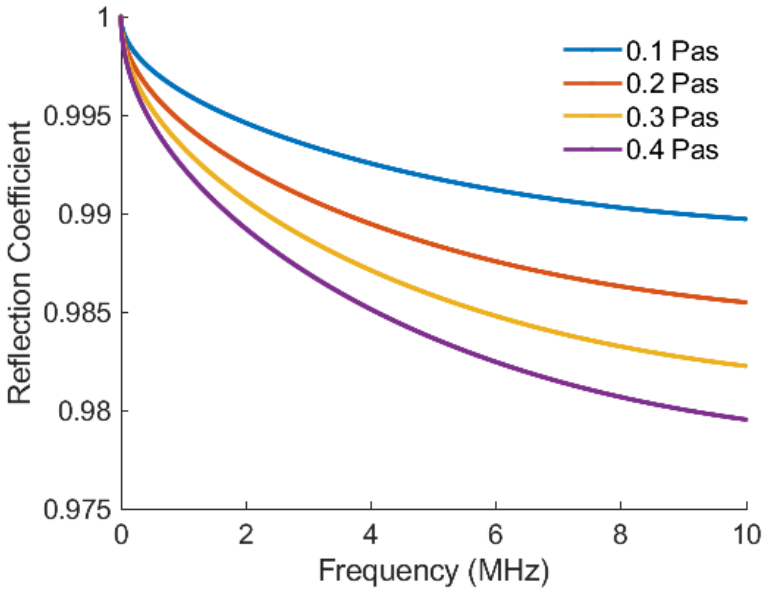

Figure 5.11: A comparison of the reflection coefficient with respect to frequency for a Newtonian two-layer system, for different viscosity fluids.

Compared to Figure 5.2, this plot shows a dependency upon frequency for an elastic two-layered system, where a fluid with a viscosity of 0.4Pas, the reflection coefficient decreases from 0.99 to 0.98 from 2MHz to 10MHz. It should be noted that both these values are close to unity and therefore it is unsuitable to obtain an accurate value of viscosity from the reflection coefficient of a two-layered system. This reflection coefficient decrease is explained by the frequency dependence of the acoustic impedance of the fluid. This relationship can increase the accuracy of viscosity measurements; the greater the frequency, the larger the reflection coefficient value for the same viscosity fluids. Conversely, it also indicates difficulties in low frequencies measurements - the reflection coefficient reaching unity and total reflection.

5.4.1.2 Three Layered System

Manipulating Equation 5.15 to find the acoustic impedance of the fluid, and combining with the three-layered model, Equation 5.11, the relationship between the reflection coefficient and viscosity can be determined for a Newtonian fluid in a three-layered system.

Figure 5.12 has been plotted to further illustrate the difference between the reflection coefficient and the reflection coefficient at resonance, where the viscosity of the fluid is 0.4Pas and the other input parameters are detailed in Table 5.2 .The reflection coefficient has been plotted using the three-layered equation, Equation 5.10, and the reflection coefficient at resonance has been plotted using the perfectly matched three-layered equation, Equation 5.11.

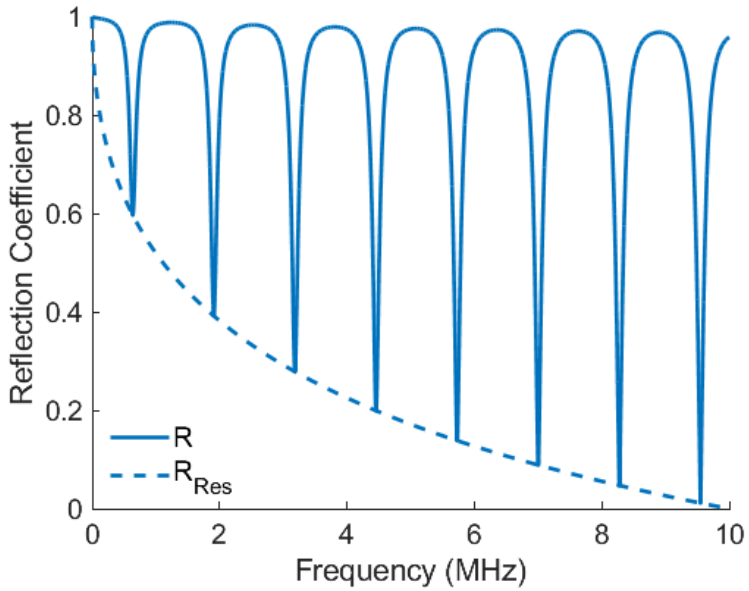

Figure 5.12: A comparison of the reflection coefficient with respect to frequency for a Newtonian three-layer system, for the reflection coefficient and the reflection coefficient at resonance.

$$R_{Res} = \frac{(\rho_2 c_2)^2 - \sqrt{i\rho_2\omega\eta}\rho_1 c_1}{(\rho_2 c_2)^2 + \sqrt{i\rho_2\omega\eta}\rho_1 c_1} \tag{5.28}$$

Figure 5.13 shows that similarly to the two-layered system, as the frequency increases, the reflection coefficient decreases. This reduction is again caused by the frequency dependency of the acoustic impedance of the fluid.

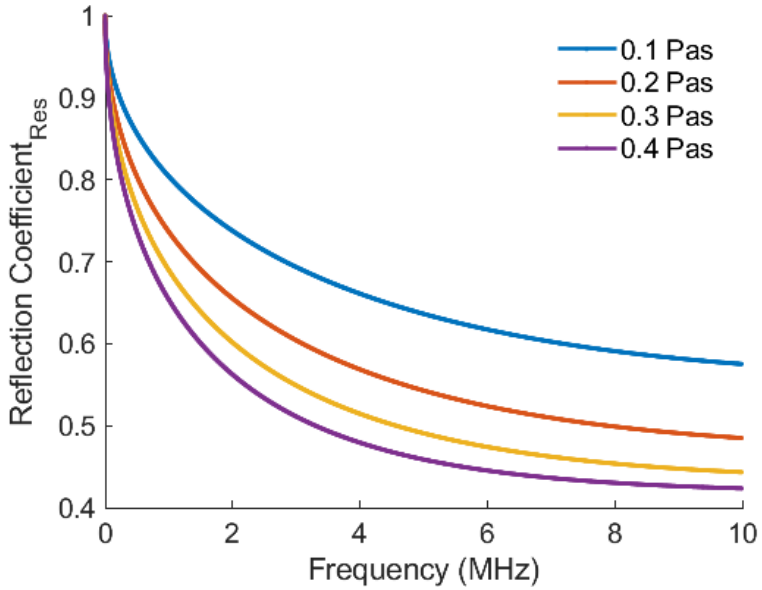

Figure 5.13: A comparison of the minimum reflection coefficient at resonance with respect to frequency for a Newtonian three-layer system, for different viscosity fluids.

Although the trend is the same for the two and three-layered system, the absolute values of the reflection coefficient are much lower for the three-layered system; the difference in reflection coefficient values between 0.1Pas and 0.4Pas at 10 MHz for a two-layered system is approximately 0.015, whereas for a three-layered system this is equal to 0.22. This increase in the difference in reflection coefficient values allows for more accurate viscosity measurements for a three-layer system.

5.4.2 Non-Newtonian Fluid

5.4.2.1 Two Layered System

By manipulating the two-layered model, Equation 5.5, and the Maxwell model, Equation 5.23, the relationship between the reflection coefficient and the viscosity can be found.

$$R = \frac{\sqrt{\rho(\frac{\omega^2\eta\tau}{1+\omega^2\tau^2} + \frac{i\omega\eta}{1+\omega^2\tau^2})} - \rho_1 c_1}{\sqrt{\rho(\frac{\omega^2\eta\tau}{1+\omega^2\tau^2} + \frac{i\omega\eta}{1+\omega^2\tau^2})} + \rho_1 c_1} \tag{5.29}$$

Using this relationship, two figures are created showing the relationship between reflection coefficient and frequency for varying viscosities and relaxation times.

When the viscosity is changed, Figure 5.14a, the trend is similar to the two-layered Newtonian model; an increase in viscosity leads to a decrease in reflection coefficient, and the difference in reflection coefficient values is minimal.

Figure 5.14b provides an insight into the importance of the relaxation time. At shorter relaxation times the reflection coefficient returns a similar value, however as the relaxation time increases the reflection coefficient for the relaxation times diverges.

The figure further shows that above a certain frequency, the reflection coefficient remains constant with increasing frequency. This limit is reached at a lower frequency when the relaxation time is larger; for example, a fluid with a relaxation time of $10^{-7}s$; the reflection coefficient remains constant after 0.4MHz. This limits the reflection coefficient technique when measuring fluids with large relaxation times.

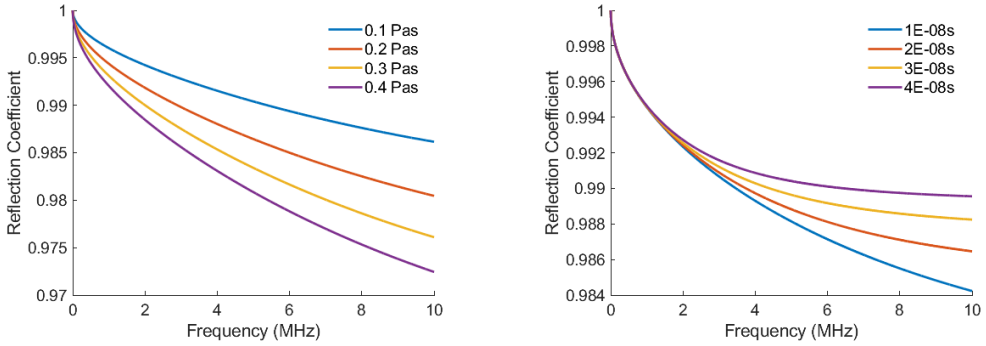

(a) Varying viscosities. (b) Varying relaxation times.

Figure 5.14: A comparison of the reflection coefficient with respect to frequency for a Maxwell two-layer system, for different property fluids.

5.4.2.2 Three Layered System

Again, by using the Maxwell model, Equation 5.23 and inserting into the three-layered model, Equation 5.11, leads to the development of an equation describing the relationship between the reflection coefficient and viscosity for a non-Newtonian fluid in a three-layered model.

$$R_{Res} = \frac{(\rho_2 c_2)^2 - \sqrt{\rho(\frac{\omega^2\eta\tau}{1+\omega^2\tau^2} + \frac{i\omega\eta}{1+\omega^2\tau^2})}\rho_1 c_1}{(\rho_2 c_2)^2 + \sqrt{\rho(\frac{\omega^2\eta\tau}{1+\omega^2\tau^2} + \frac{i\omega\eta}{1+\omega^2\tau^2})}\rho_1 c_1} \tag{5.30}$$

Using this equation the reflection coefficient is plotted for different frequencies in Figure 5.15a and Figure 5.15b for different viscosities and relaxation times respectively. The figures show an identical trend to the two-layered non-Newtonian model, but the reflection coefficient values are much lower, as expected.

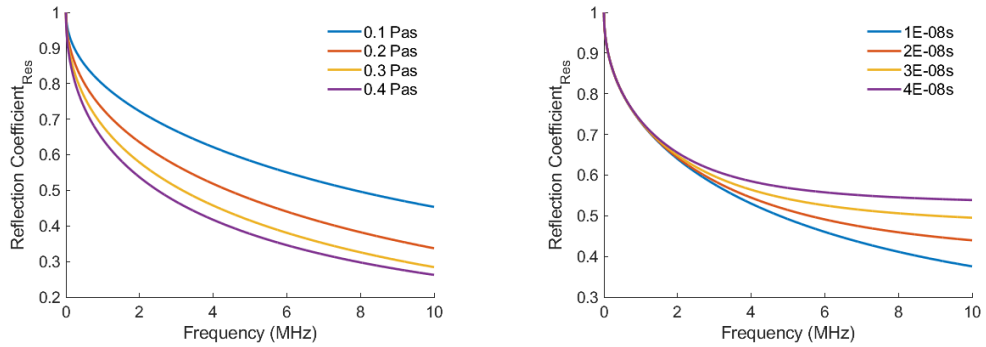

(a) Varying viscosities. (b) Varying relaxation times.

Figure 5.15: A comparison of the minimum reflection coefficient at resonance with respect to frequency for a Maxwell three-layer system, for different property fluids.

5.4.3 Comparison of Newtonian and non-Newtonian Fluid

By combining the Figure 5.14b with Figure 5.11, and Figure 5.15b with Figure 5.13, it is possible to compare the Newtonian and non-Newtonian models at a single viscosity over a range of relaxation times, Figure 5.16a and Figure 5.16b.

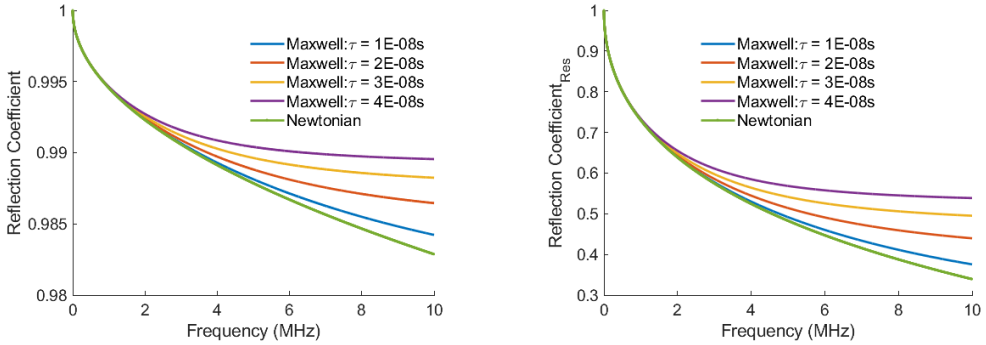

(a) Two-layered model.

(b) Three-layered model.

Figure 5.16: Comparing the reflection coefficient for a two-layered model and the minimum reflection coefficient at resonance for a three-layered model with respect to frequency for Newtonian and Maxwell rheological models.

The plots show that for the Maxwell model, when the product of the relaxation time and frequency reduces, the reflection coefficient values become similar. As the relaxation time decreases, the linear viscous spring has less influence on the fluid properties, reducing to the Newtonian model. This can be explained mathematically as when $\omega^2\tau^2 << 1$, the shear modulus of the Maxwell model is reduced to Equation 5.31, the same as the Newtonian model.

$$G = i\omega\eta \tag{5.31}$$

When the relaxation time increases, as it will for more viscoelastic fluids, the reflection coefficient maintains its value at a greater rate, showing slightly larger reflection coefficient values. The difference between the rheological models increase with increasing frequency, highlighting the need for the knowledge of the relaxation times at high frequencies.

5.5 Conclusion

This chapter develops novel models to correlate the reflection coefficient and viscosity of Newtonian and non-Newtonian fluids on a two and three-layered system. The process of developing these equations has been simplified to Figure 5.16b, and the models have been summarised in Table 5.3.

Rheological Model	Number Of Layers In System	Ultrasound Model: $R = f\{\eta\}$
Newtonian	2	$R = \frac{\sqrt{i\rho_2\omega\eta}-\rho_1 c_1}{\sqrt{i\rho_2\omega\eta}+\rho_1 c_1}$
Newtonian	3	$R_{Res} = \frac{(\rho_2 c_2)^2-\sqrt{i\rho_2\omega\eta}\rho_1 c_1}{(\rho_2 c_2)^2+\sqrt{i\rho_2\omega\eta}\rho_1 c_1}$
Maxwell	2	$R = \frac{\sqrt{\rho(\frac{\omega^2\eta\tau}{1+\omega^2\tau^2}+\frac{i\omega\eta}{1+\omega^2\tau^2})}-\rho_1 c_1}{\sqrt{\rho(\frac{\omega^2\eta\tau}{1+\omega^2\tau^2}+\frac{i\omega\eta}{1+\omega^2\tau^2})}+\rho_1 c_1}$
Maxwell	3	$R_{Res} = \frac{(\rho_2 c_2)^2-\sqrt{\rho(\frac{\omega^2\eta\tau}{1+\omega^2\tau^2}+\frac{i\omega\eta}{1+\omega^2\tau^2})}\rho_1 c_1}{(\rho_2 c_2)^2+\sqrt{\rho(\frac{\omega^2\eta\tau}{1+\omega^2\tau^2}+\frac{i\omega\eta}{1+\omega^2\tau^2})}\rho_1 c_1}$

Table 5.3: A summary of the two and three-layer rheological reflectance models.

Using these models, the reflection coefficient is always close to unity for a two-layered system, but this can be changed by implementing a three-layered system where the acoustic impedance of the second layer is intermediary to the first and third layer.

It was further shown that the sensitivity of a three-layer system was dependant upon the thickness of the intermediate layer and could be manipulated to complete sensitive viscosity measurements at different frequencies.

The models show that a higher frequency would produce a lower reflection coefficient value to obtain highly sensitive results, allowing for more accurate measurements. Concurrently it showed the difficulties in viscosity measurements using the reflection coefficient at low viscosities.

When comparing models, both models returned similar results at low frequencies. However, as the frequency increased, the divergence between the models increased, further increasing as the relaxation time of the fluid increased.

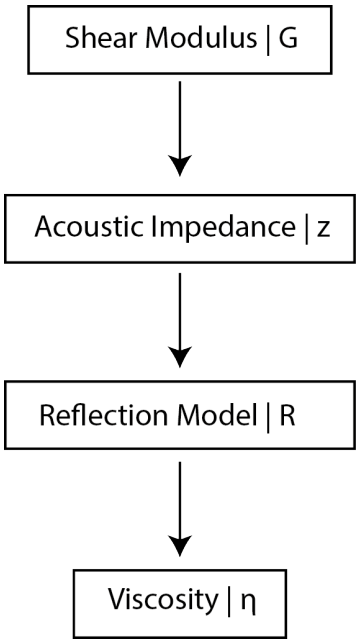

Figure 5.17: A flow chart showing the approach to determine the viscosity from the fluids shear modulus.

Chapter 6

Determination of Liquid Shear Rate

An important aspect of any viscometer is to understand the shear rate at which the fluid is subjected. This chapter begins with discussing current models used to relate oscillatory and steady shear and an alternative to the widely used Cox-Merz rule is presented. A full mathematical derivation is completed to obtain the relationship between the shear rate and the frequency using a variation of Stokes' second problem. The theory is then adapted for a shear ultrasonic viscometer that is used in future investigations in this thesis. For both theories, a sensitivity analysis is completed, and the applicability of the models discussed.

6.1 Oscillatory and Steady Shear

Oscillatory and steady shear measurements can be differentiated by the direction of stress applied to the test sample. For oscillatory measurements, harmonic forces are applied to a material, and its response is measured, whereas steady shear measurements apply a force at a constant rate (Whorlow, 1992). An example of a viscometer where an oscillatory shear is applied is measurements where an ultrasonic transducer is used to stress a rod in contact with a fluid harmonically, and the response is measured. Examples of steady shear measurements are the rotational and capillary viscometers. This difference is illustrated in Figure 6.1. It is important to understand the shear rate from oscillatory measurements to compare against steady shear measurements.

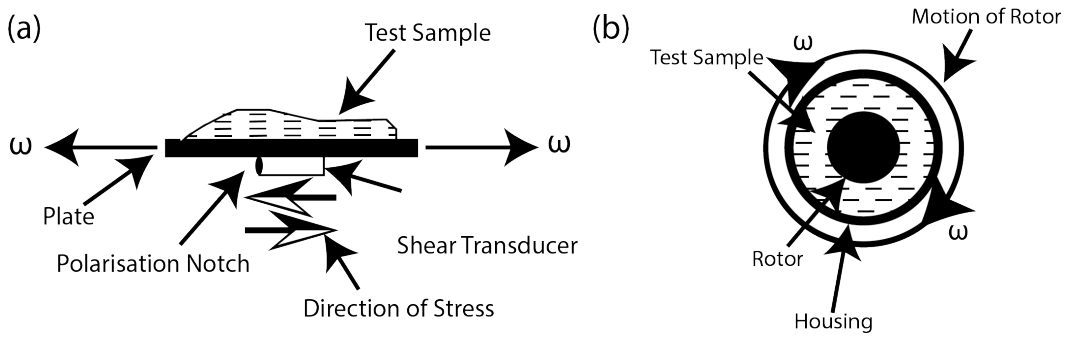

Figure 6.1: *(a)* A plate oscillating from a harmonic force produced by a shear transducer demonstrating oscillatory shear viscometer measurements. *(b)* Top down view of a rotational viscometer that shows the rotor turning with a constant stress, demonstrating steady shear viscosity measurements.

6.2 The Cox-Merz Rule

The most commonly used relationship to correlate oscillatory and steady shear measurements is the Cox-Merz rule (Cox and Merz, 1958). This relationship was established by measuring the viscosity of two polymer solutions using a capillary extrusion viscometer and a concentric cylinder elastoviscometer to obtain steady flow viscosity measurements and dynamic viscosity measurements, respectively. Measurements were all carried out at low shear rates, $25 - 2200\, s^{-}1$, and the dynamic measurements were completed over the frequency range $0.1 - 20\, rad/s$. When plotting these measurements against the natural logarithm of the shear rate and angular velocity, and extrapolating, a good fit between the measurement techniques was found, Figure 6.2, leading to the Cox-Merz rule, Equation 6.1.

$$\eta(\dot{\gamma}) = \eta(\omega). \tag{6.1}$$

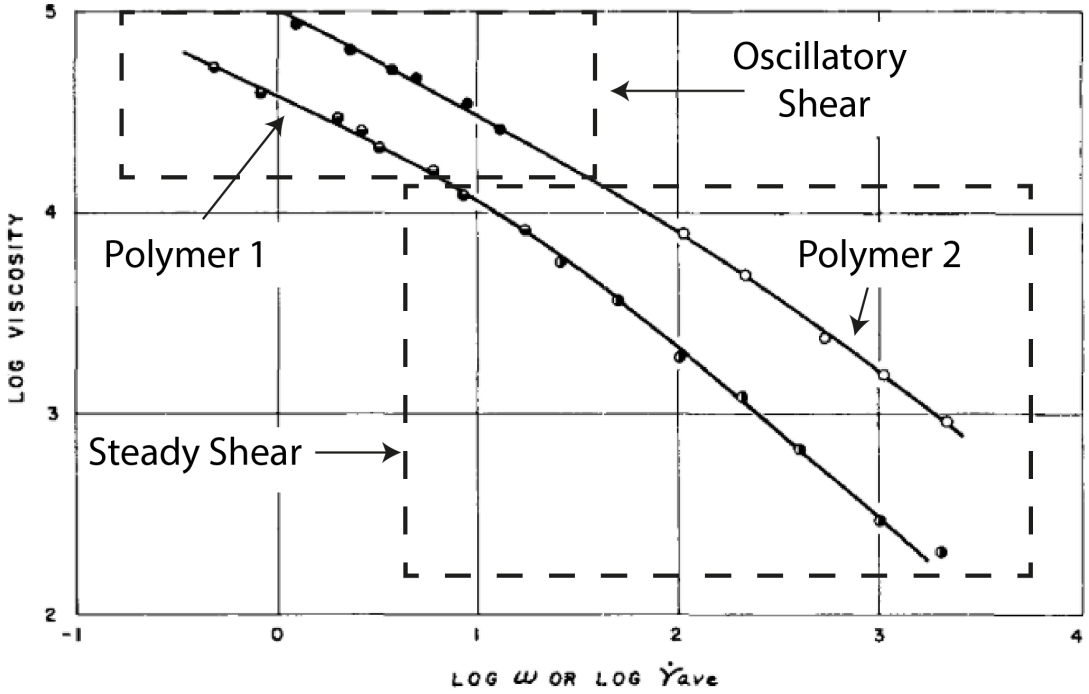

Figure 6.2: Cox and Merz (1958). Viscosity for oscillatory shear rate and steady shear measurements for two different polymers.

In this widely cited paper, no mathematical proof was presented, and the relationship was found by visually comparing the data. The viscosities were measured across a limited range of shear rates, and the two sets of measurements diverged as the shear rate increased.

Numerous investigations have been carried out to determine the Cox-Merz rule's applicability for different fluids when subjected to varying test conditions. Some studies found a positive correlation for the Cox-Merz rule (Kim and Bau, 1989) (Costley et al., 1998). However, many others have found that the Cox-Merz rule cannot be applied, and some of these investigations have been summarised in Table 6.1. These investigations often conclude that the rule reduces its applicability as the frequency increases, and finds other factors, including molecular structure, need to be considered when correlating oscillatory and steady shear measurements.

Authors	Aim of Study	Test Sample	Maximum Shear Rates		Conclusions
			Steady State (s^{-1})	Oscillatory (Hz)	
Yasuda et al. (1981)	To determine the suitability of the Cox-Merz rule for different polystyrene formulations.	Linear and star branched polystyrene.	NA	NA	The Cox-Merz was successfully applied to the majority of the monodisperse samples but was not able to be applied for the broad molecular weight distribution polystyrene solutions.
Doraiswamy et al. (1991)	To develop the Cox-Merz rule to account for the applied strain/oscillation amplitude.	Highly concentrated ceramic solutions.	0.01	100	The Cox-Merz rule did not hold as the complex viscosity was found to be a function of the strain and the frequency.
Al-Hadithi et al. (1992)	Testing the applicability of the Cox-Merz rule for a range of polymeric and colloidal systems.	Polymeric and colloidal systems.	500	40	The Cox-Merz relationship held for the polymeric fluids. Still, it was found that the steady-state viscosity for the colloidal systems was consistently lower than the oscillatory measurements.
Gleissle and Hochstein (2003)	Validating the Cox-Merz rule for concentrated suspensions.	Glass bead, limestone and powdered quartz suspensions.	1000	1000	The Cox-Merz rule did not fit, and the shear modulus was found to be a function of the frequency and the strain amplitude.
Wen et al. (2004)	Testing the Cox-Merz rule for blended mixtures.	Monodisperse and bidisperse entangled polymer solutions.	300	80	The monodisperse entangled polystyrene solutions showed excellent agreement for the Cox-Merz rule. The bidisperse solutions exhibited deviations at high shear rates that increased as the long-chain became markedly dilute.

Table 6.1: A selection of studies where the Cox-Merz relationship does not hold true.

A study that discusses the use of the Cox-Merz rule at shear rates that are more comparable to the viscosity measurements carried out in this thesis, was completed by Bair et al. (2014). In this paper, measurements from a pressurised thin-film Couette viscometer and a torsionally vibrating quartz crystal viscometer were compared. The experimental configuration allowed for dynamic measurements to be compared to oscillatory measurements at much greater frequencies and over a broader range than previous investigations, 5 - 205 MHz. The viscosity of three organic samples, having similar dynamic properties to lubricants, were measured. The Cox-Merz rule was successfully applied for one of the samples, squalane, and only at the transition zone. For the other two samples, the Cox-Merz rule did not provide a suitable correlation at any shear rate, Figure 6.3.

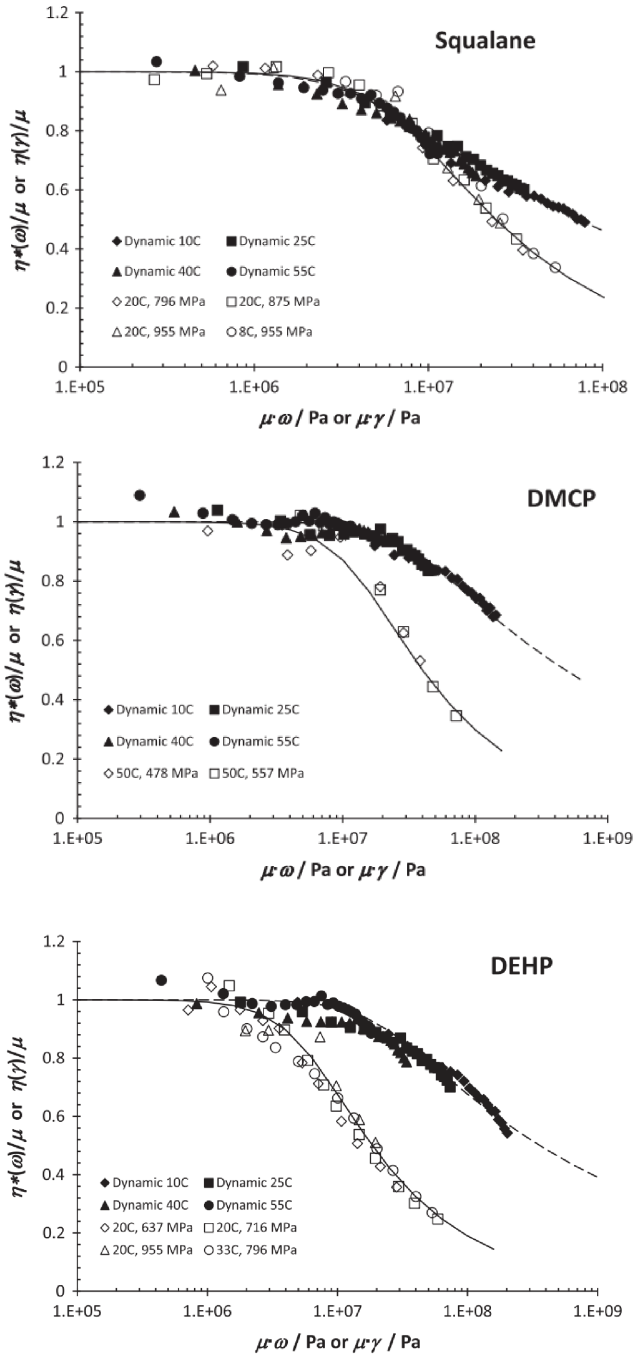

Figure 6.3: Bair et al. (2014). Viscosity measurements comparison for steady shear rate and oscillatory measurements using the Cox-Merz Rule.

From previous investigations, it is clear that there needs to be an alternative to the Cox-Merz rule.

6.3 Mathematical Derivation of Shear Rate For an Ultrasonic Viscometer

In this section, the shear rate is derived by analysing the particle velocity using the Navier-Stokes equation.

6.3.1 Stokes' Second Problem

The Navier-Stokes equation, Equation 6.2, is an adaptation of Euler's equation and is used to describe the flow of incompressible liquids in terms of the fluid velocity vector, u, fluid pressure, P, density, ρ, and kinematic viscosity, ν, where ∇^2 is the Laplacian operator.

$$\frac{\partial u}{\partial t} + u \cdot \nabla u = -\frac{\nabla P}{\rho} + \nu \nabla^2 u. \tag{6.2}$$

Stokes' second problem is a 2D problem, based upon the Navier-Stokes equation, that is used to model the flow in a fluid when subjected to oscillations from a solid surface. This model is widely used and has been verified experimentally using a Laser Doppler Velocimeter (Peng and Hsu, 2008). Figure 6.4 represents the Stokes' second problem - a flat smooth wall bounded on one side, oscillating in-plane sinusoidally.

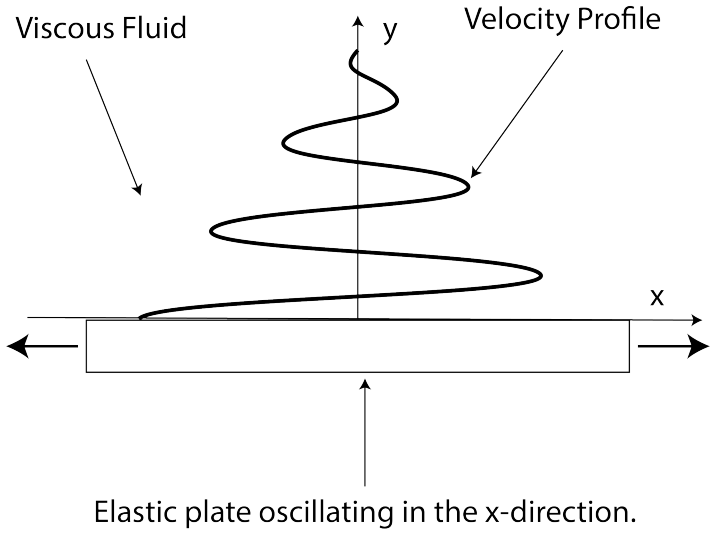

Figure 6.4: A diagram representing Stokes' second problem.

The wall is oscillating with a sinusoidal motion meaning that the velocity, U, is a function of the maximum wave velocity, $\bar{U}$, the angular frequency, ω, the perpendicular distance from the plate, y, and time, t. It is assumed that the velocity profile has no dependency on the x or z axis. When the distance in the y-axis is equal to zero, the velocity is:

$$U(y = 0, t) = \bar{U}\cos(\omega t). \tag{6.3}$$

When there is no wall penetration; when $y = 0$, the velocity field (distribution of velocity), V, is equal to zero.

6.3.2 Continuity Equation

The continuity equation is the conservation of mass in differential form for a 2D incompressible flow. It treats the fluid as a continuum by assuming that any small fluid element is composed of many smaller fluid elements. As the mass is conserved, the continuity equation can be applied by observing the mass fluxes entering and leaving an element; this relationship is shown in Figure 6.5. It is expressed in its standard form below.

$$\frac{\delta\rho}{\delta t} + \nabla(\rho v) = 0 \tag{6.4}$$

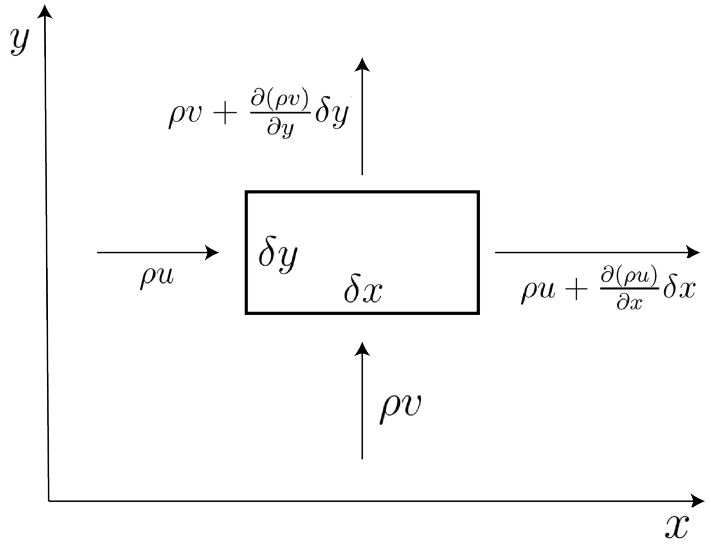

Figure 6.5: Continuity Model.

Assuming that the fluid is incompressible, the density is independent of space and time; the equation can further be reduced to the velocity gradient.

$$\nabla v = 0. \tag{6.5}$$

Expressing in Cartesian form allows it to be more easily applied to Stokes' second problem where u, v and ω are the velocity components in separate planes.

$$\frac{\delta u}{\delta x} + \frac{\delta v}{\delta y} + \frac{\delta \omega}{\delta z} = 0 \tag{6.6}$$

Applying the no-slip boundary condition assumes that the fluid particles' attraction and solid particles are greater than those between the fluid particles. It has been proven to be true for some configurations of multi-layered reflection systems(Nayfeh, 1988). The normal flow field component is equal to zero. Therefore the flow field is a function of x, z and t.

$$\frac{\delta v}{\delta y} = 0 \rightarrow V = V(x, z, t) \tag{6.7}$$

As discussed when initialising the Stokes' second problem, the flow does not depend upon x and z, which when combined with the above relationship implies that the velocity flow field is equal to zero in every plane.

$$V = 0 \tag{6.8}$$

6.3.3 X-Momentum Equation

The momentum equations are a variant of Newton's Second Law where the force is equal to the rate of change of momentum. For a Newtonian incompressible fluid, the X - momentum equation in its Cartesian form is shown in the form presented by Rao (2018):

$$\frac{\delta U}{\delta t} + U\frac{\delta U}{\delta x} + V\frac{\delta U}{\delta y} = -\frac{1}{\rho}\frac{\delta P}{\delta x} + \nu\frac{\delta^2 U}{\delta x^2} + \nu\frac{\delta^2 U}{\delta y^2} \tag{6.9}$$

By making the following assumptions, the momentum equation can be reduced to a much simpler form.

- The penetration depth is equal to zero in all but the y-direction. This assumption can be made if the direction of the shear wave is at a normal angle to the solid-fluid interface. In all future experimental investigations, the transducer is bonded flat to the bottom of the plate, and therefore this assumption can be made.
- The velocity field is equal to zero everywhere, as shown above in the continuity equation. This assumption can be made when the flow is incompressible. For future experiments the amount of pressure that the fluid is subjected to is very small and therefore the density remains constant and can be considered incompressible. It also assumes that the small fluid element is composed of many smaller fluid elements. For a Newtonian calibration sample this is true as the fluid elements are much smaller when compared to the displacement of the ultrasound wave. However, as seen in later chapters, the displacement from the ultrasound shear waves is very small, and in some cases comparable to the size of the additive polymers, meaning that this assumption may not be used for non-Newtonian fluids.

- The pressure gradient is equal to zero. This assumes that the pressure within the fluid is constant. This can be assumed as in future investigations the amount of fluid placed on the elastic plate is relatively small and therefore any change in pressure is negligible.
- The velocity only has a dependence on the y plane. This is true for a semi-infinite problem, which can be assumed to be true if the ultrasonic wave occupies an area that is much smaller that the total surface of the area of the fluid on the plate. For future investigations this can be assumed to be true due to the small size of the piezoelectric element.

By applying these assumptions, the momentum equation is reduced to:

$$\frac{\delta U}{\delta t} = \nu \frac{\delta^2 U}{\delta y^2}. \tag{6.10}$$

To analyse this equation further, two boundary conditions are assumed.

1. At $y = 0$, the velocity is a function of the maximum amplitude.

$$U(y = 0) = \bar{U} \cos(\frac{2\pi t}{T}) \tag{6.11}$$

2. As y tends to infinity; the velocity is equal to zero as the wave has fully decayed.

$$U(y \to \infty) = 0 \tag{6.12}$$

Applying the boundary conditions and Euler's identity, Equation 6.10 is converted to standard form.

$$U(y = 0) = \bar{U}\mathbf{R}[e^{i\omega t}] \tag{6.13}$$

The solution for the velocity at a distance, y, can now be found by substituting the maximum velocity with an arbitrary velocity, $\tilde{U}$.

$$U(y, t) = \mathbf{R}\tilde{U}(y)e^{i\omega t} \tag{6.14}$$

As the equation is linear and the coefficients do not depend upon time, the equation can be substituted into the simplified x-momentum equation, Equation 6.10.

$$i\omega\tilde{U}e^{i\omega t} = \nu \frac{d^2\tilde{U}}{d\tilde{y}^2} e^{i\omega t} \tag{6.15}$$

Rearranging the above equation and substituting $\frac{i\omega}{\nu}$ for λ^2, the equation is presented in standard form for a second-order differential equation, allowing for a solution to be obtained for the velocity, $\tilde{U}$.

$$\frac{d^2\tilde{U}}{d\tilde{y}^2} - \frac{i\omega}{\nu}\tilde{U} = 0 \tag{6.16}$$

$$\frac{d^2\tilde{U}}{d\tilde{y}^2} - \lambda^2\tilde{U} = 0 \tag{6.17}$$

$$\tilde{U}(y) = Ae^{-\lambda y} + Be^{+\lambda y} \tag{6.18}$$

By manipulating λ and making the substitution, $C = \sqrt{\frac{\omega}{2\nu}}$, the velocity can be expressed in the form:

$$\lambda = \sqrt{i\frac{\omega}{\nu}} == \sqrt{\frac{\omega}{\nu}}[\frac{\sqrt{2}}{2} + i\frac{\sqrt{2}}{2}], \tag{6.19}$$

$$\lambda = \frac{\omega}{2\nu}[1+i] = C[1+i],\ where\, C > 0, \tag{6.20}$$

$$\tilde{U}(y) = Ae^{-C[1+i]y} + Be^{+C[1+i]y}. \tag{6.21}$$

To continue to manipulate this relationship, a further pair of boundary conditions are applied.

1. The first boundary condition prohibits exponential growth.

$$lim_{y\to\infty}\tilde{U} = 0, \tag{6.22}$$

$$\implies B = 0. \tag{6.23}$$

2. The second boundary condition equates A to the maximum velocity by taking measurements at the boundary, where $y = 0$.

$$\tilde{U}(y=0) = A, \tag{6.24}$$

$$\tilde{U}(y=0) = \tilde{U}e^{i\omega t} = \bar{U}e^{i\omega t}, \tag{6.25}$$

$$\implies A = \bar{U}. \tag{6.26}$$

The solution can now be determined by substituting the above relationship with Equation 6.14.

$$U(y,t) = \bar{U}Re[e^{-c(1+i)y}e^{i\omega t}] \tag{6.27}$$

Rearranging this, applying Euler's identity and substituting C from Equation 6.20 gives the solution to Stokes' second problem.

$$U(y,t) = \bar{U}e^{-\sqrt{\frac{\omega}{2\nu}}y}\cos[\omega t - \sqrt{\frac{\omega}{2\nu}}y] \tag{6.28}$$

Using Equation 6.28, the velocity profile can be plotted at different times, Figure 6.6. In this figure the values for $\pi/4$, $\pi/2$,π and 2π are identical as for all these values $cos(\omega t) = 1$. When plotting figure for the remainder of this chapter it will be completed when $t = 2\pi$, which represents maximum amplitude.

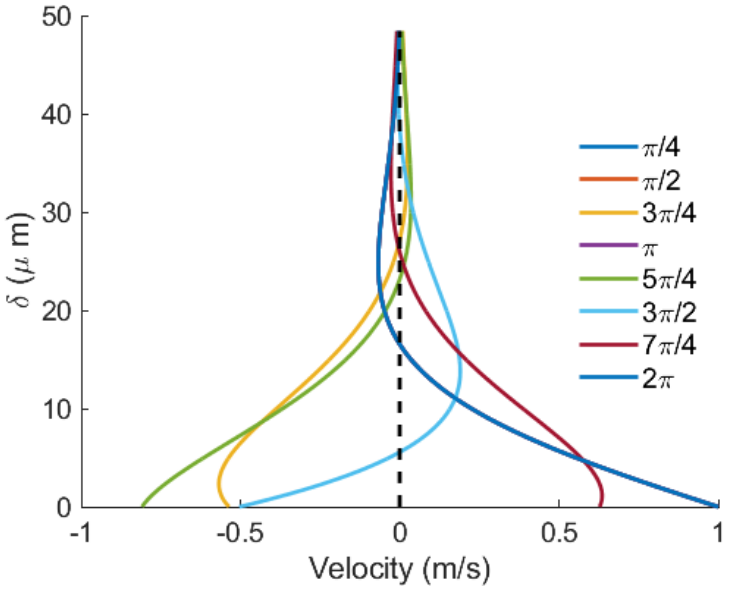

Figure 6.6: The velocity profile of a fluid modelled using Stokes' second problem, shown at different times.

Figure 6.7 and 6.8 show the velocity profile for different excitation frequencies and viscosities, respectively. Both profiles are modelled using the parameters for the Cannon viscosity standard, S20 at 25°C, Table 6.2.

Parameter	
Initial Velocity	$10m/s$
Frequency	$1MHz$
Dynamic Viscosity	$29mPas$
Density	$860kg^3/s$

Table 6.2: Boundary layer modelling input paramaters, based on Cannon Viscosity Standard, S20 at 25°.

Figure 6.7 illustrates that the oscillation frequency will alter the velocity profile. At $y = 0$, the plate's initial amplitude is independent of frequency; however, as the distance away from the plate increases, the velocity profile is dependent on frequency. This is attributed to higher frequency waves being unable to travel as far in a fluid as their low-frequency counterparts.

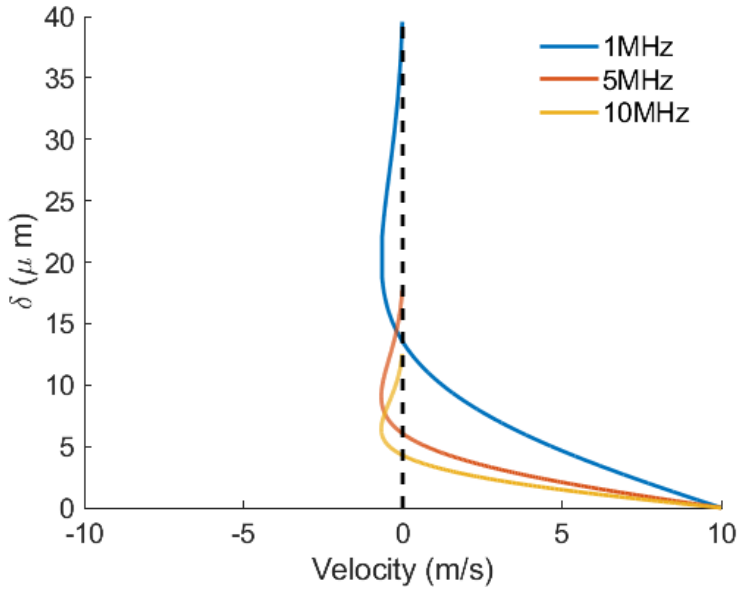

Figure 6.7: The velocity profiles for a fluid with constant viscosity that is on top of a flat plate that is oscillating at a different frequencies, and modelled using Stokes' Second Problem.

Figure 6.8 shows the velocity profiles dependence on the viscosity of the fluid; a lower viscosity fluid causes the velocity to decay at an increased rate. This result is expected as a fluid with greater viscosity can more easily support a shear wave.

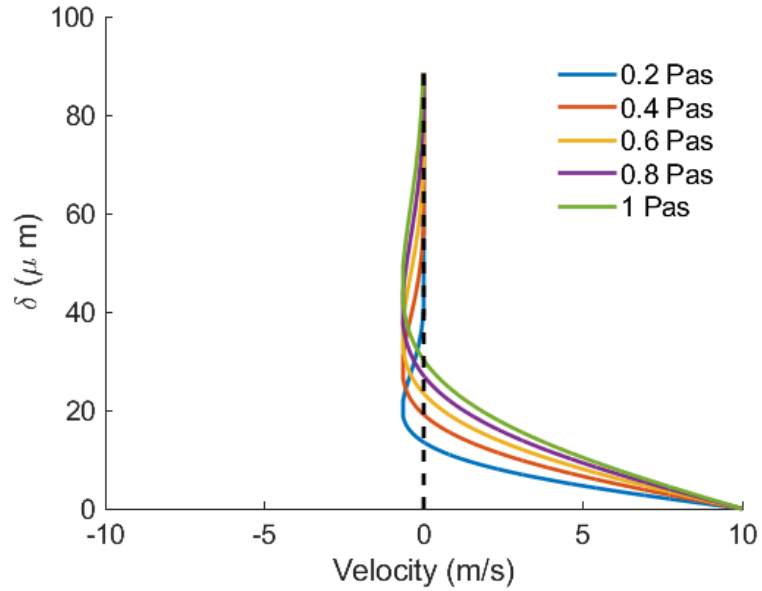

Figure 6.8: The velocity profile for fluids with different viscosities that are on top of a flat plate that is oscillating at a constant frequency, and modelled using Stokes' Second Problem.

6.3.4 The Thickness of Stokes' Layer

The Stokes' layer's thickness is the distance from the wall at which the maximum velocity decays to 1% and is commonly denoted by δ_{99}. It is derived from Stokes' second problem, Equation 6.28.

$$0.01\bar{U} = \bar{U}\exp\sqrt{\frac{\pi}{T\nu}}\times\delta_{99} \tag{6.29}$$

Solving this leads to Stokes' Layer's thickness, which gives further information about the velocity profile.

$$\delta_{99} = 4.6\sqrt{\frac{2\nu}{\omega}} \tag{6.30}$$

The thickness of Stokes' layer with changing frequency is provided by Equation 6.30 and is plotted in Figure 6.9, with the input parameters shown in Table 6.2.

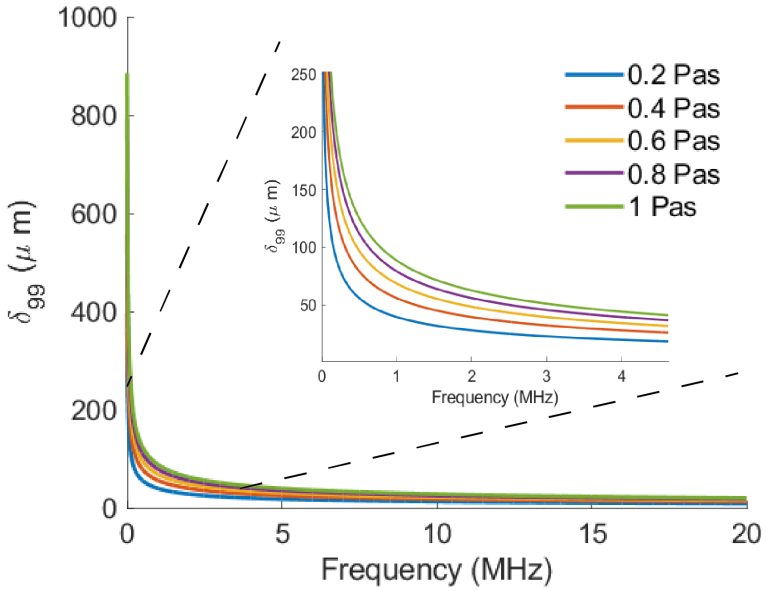

Figure 6.9: The thickness of Stokes' layer with respect to frequency and viscosity.

The figure shows an asymptotic relationship between the frequency and the thickness of the Stokes' layer, where the thickness tends to infinity below a sufficiently low frequency. Above a sufficiently large frequency, Stokes' layer thickness tends to zero. As expected, this plot is extremely similar to the penetration depth plot for varying frequency, Figure 3.3.

Figure 6.9 also shows the relationship between the viscosity and Stokes' layer; an increase in viscosity leads to an increase in Stokes' layer thickness noted in the velocity profile plots and explained by a more viscous fluid more easily carrying a shear wave.

For a homogeneous fluid, such as a laboratory calibration oil, the thickness of Stokes layer will not affect the acoustic impedance of the fluid. For a non-homogeneous fluid, the thickness of the Stokes layer will determine which particles are subjected to pressure from the shear wave. An illustration of a non-homogeneous fluid where the constituent elements are not evenly distributed is shown in Figure 6.10. This fluid is composed of emulsion droplets, polymer chains and elongated particles, commonly found for a fluid that is subjected to shear. If the thickness of Stokes' layer is at δ_1, only the elongated particles will be sheared; if the thickness of the Stokes layer is at δ_2, the elongated particles, polymer chains and emulsion droplets will all be sheared leading to a very different viscosity measurement.

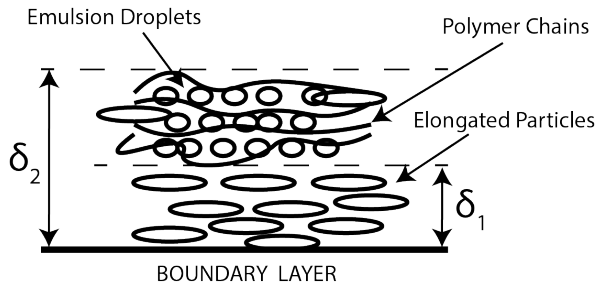

Figure 6.10: Sketch demonstrating the importance of Stokes' layer for a non-homogeneous fluid.

6.3.5 Shear Rate Derivation

The shear rate can be considered as the rate at which layers move past each other, as defined in Equation 2.2. The maximum shear rate will be located at the place where there is maximum velocity, at the wall. By developing the velocity profile relationship, the shear rate profile is found. Completing a further differentiation of the velocity concerning Stokes' layer thickness gives the shear rate relationship. The differentiation is completed when the shear rate is maximum, which occurs when the velocity amplitude is at its maximum, $y = 0$.

$$\frac{\delta U}{\delta y}|_{Wall} = \bar{U} Re[-c(1+i)e^{-c(1+i)y}e^{i\omega t}] \tag{6.31}$$

As the distance where the maximum shear rate occurs will be at the wall, $y = 0$, the equation can be simplified in the knowledge that, $e^{-c(1+i)y} = 1$.

$$\frac{\delta U}{\delta y}|_{Wall} = \bar{U}\sqrt{\frac{\pi}{T\nu}}\dot{(-)}Re[(1+i)e^{i\omega t}] \tag{6.32}$$

Using the relationship, $1 + i = \sqrt{2}\exp^{i\frac{\pi}{4}}$, and Euler's relationship, further simplification can be made.

$$\frac{\delta U}{\delta y}|_{Wall} = -\bar{U}\sqrt{\frac{2\pi}{T\nu}}\cos[\omega t + \frac{\pi}{4}] \tag{6.33}$$

Figure 6.11 shows the two-dimensional velocity and the shear rate profile for the laboratory calibration oil.

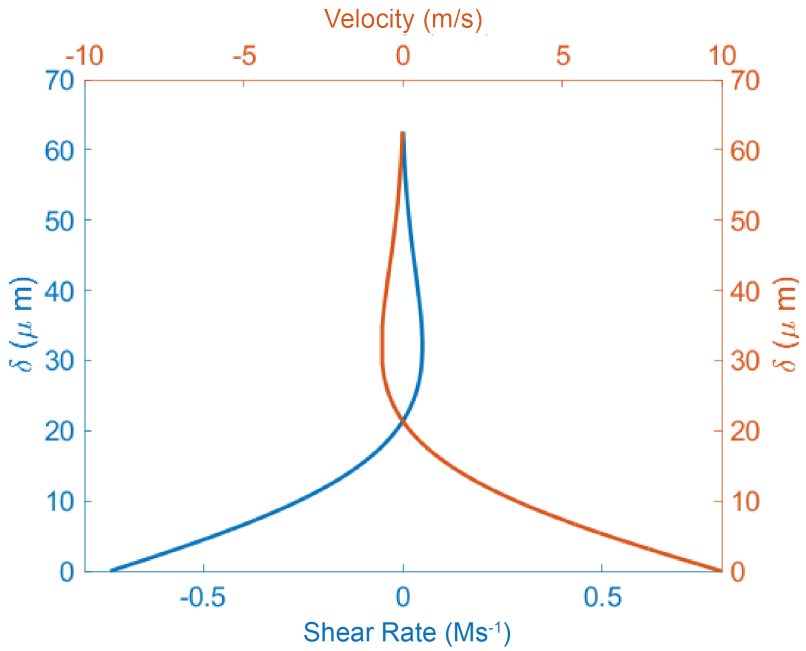

Figure 6.11: The shear rate and velocity profile of a fluid that is on an oscillating elastic plate, modelled using Stokes' second problem.

This figure was produced by overlaying the velocity profile, Figure 6.7, and the shear rate profile. This plot shows that the shear rate and velocity are mirrored in the y-axis. This is expected as the shear rate is the rate of change in shear, which is dependent on velocity. However, the amplitude of the two parameters varies, in this case by orders of magnitude.

The shear rate profile is plotted for changing frequency and viscosity, Figure 6.12 and Figure 6.13 respectively. Unlike the velocity profile, the frequency alters the shear rate's amplitude; the lower the frequency, the lower the shear rate amplitude, which is also the case for the Cox-Merz rule.

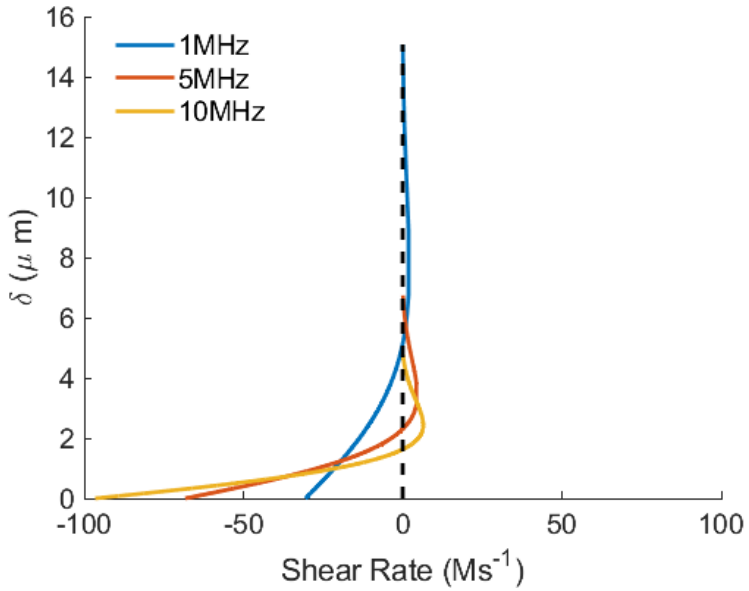

Figure 6.12: The shear rate profile for fluids on a plate that is oscillating with various frequencies, modelled using Stokes' second problem.

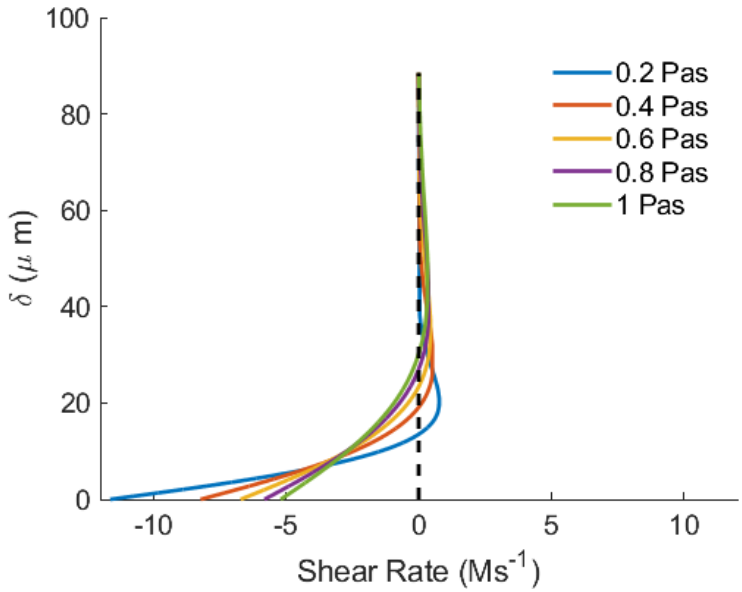

Figure 6.13: The shear rate profile for multiple fluids of varying viscosities, modelled using Stokes' second problem.

6.3.6 Maximum Shear Rate

The location of interest is at the wall as this is where the shear wave will be reflected when using a shear ultrasound viscometer. As shown in the previous shear rate plots, this location corresponds to the maximum shear rate.

The maximum shear rate will occur when $\cos(\omega t + \frac{\pi}{4}) = 1$, allowing for the removal of the harmonic function.

$$Maximum \frac{\delta U}{\delta y}|_{Wall} = -\bar{U}\sqrt{\frac{2\pi}{T\nu}} = \bar{U}\sqrt{\frac{\omega}{\nu}} \tag{6.34}$$

This relationship has also been proposed by Rabani et al. (2016), where the shear rate of an oscillating rod viscosity probe was investigated. The rod was made from carbon steel and was oscillated using a piezoelectric transducer. The velocity of the rod in air was measured using a laser vibrometer, and using this measurement the hypothetical shear rate was predicted for different viscosity fluids. Unfortunately, no viscosity measurements have been completed to verify this relationship, and no literature has used this relationship to compare oscillatory shear and steady shear.

Figure 6.14 shows the relationship for the maximum shear rate against a number of parameters. It shows that the maximum shear rate is a function of the velocity of the fluid, viscosity and frequency, whereas the Cox-Merz rule states that shear rate is only a function of frequency (Cox and Merz, 1958). The plots show that a viscosity increase leads to a decrease in the shear rate, which is due to an increase in the resistance of the fluid to deformation. The figures further show that a greater velocity corresponds to a greater shear rate. This has significant consequences when using ultrasound to measure the viscosity, as each transducer outputs a different amplitude, making the fluid particles move with different velocities.

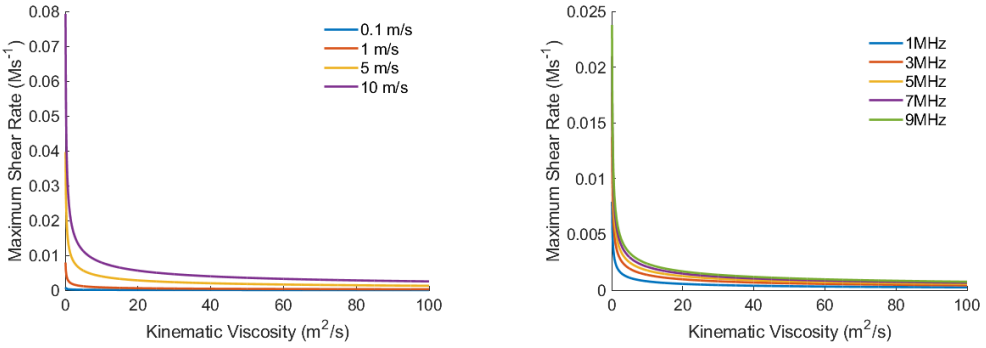

Figure 6.14: The relationship between the maximum shear rate, viscosity and frequency, derived using Stokes' second problem.

6.4 Maximum Shear Rate For an Ultrasonic Shear Rate Viscometer

In the previous section, it was assumed that the fluid was being acted upon only by the elastic plate, Figure 6.15, for many other viscometers, such as the viscometer developed by Schirru (2016), the fluid will also experience a shearing force from the sound pressure field exerted by the shear transducer, Figure 6.16. To account for this extra shearing stress, Equation 6.34 is modified, by considering the velocity of the fluid.

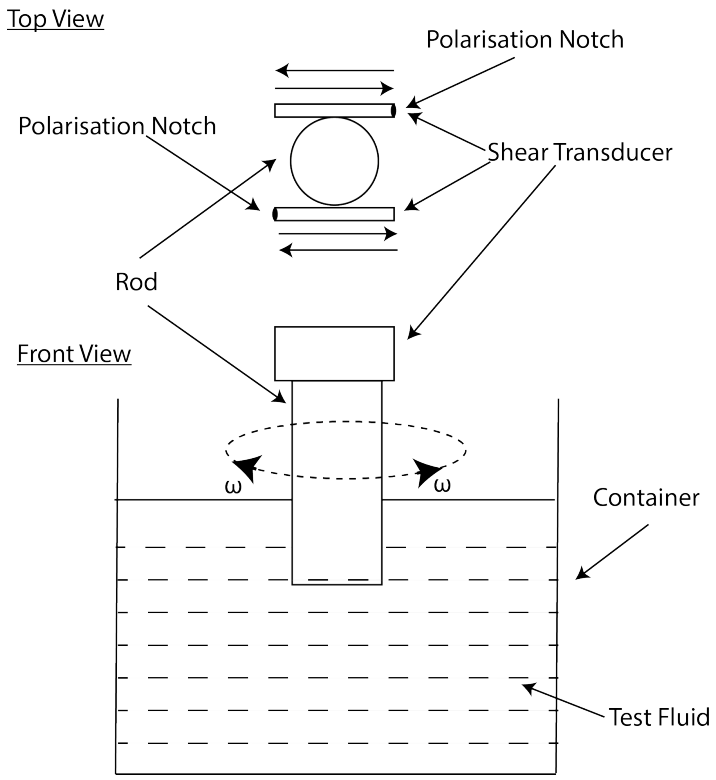

Figure 6.15: A sketch of an oscillating rod viscometer, where the rod is oscillating with an angular velocity, ω.

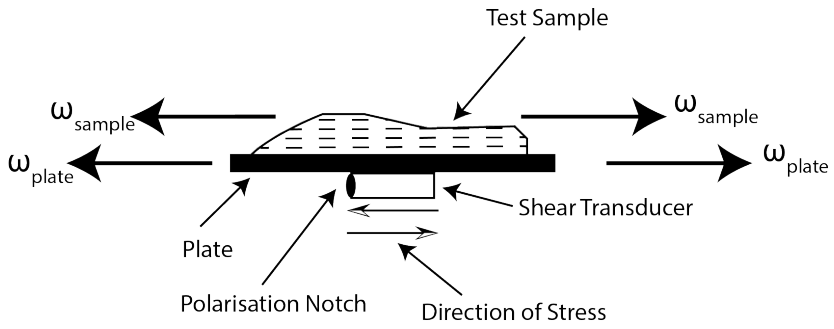

Figure 6.16: A sketch showing the fluid and plate motion due to the stress exerted from the shear transducer.

As stated in the previous section, the maximum shear rate will occur when the velocity is largest, which occurs when $y = 0$. Changes to Equation 6.34 can be made to include the velocity of the test sample, as shown in Equation 6.35.

$$\dot{\gamma}_{max} = (\bar{u}_{fluid} + \bar{u}_{solid})\sqrt{\frac{\omega}{\nu}} \tag{6.35}$$

6.4.1 Comparison Between Models

Figures 6.17 and 6.18 show the comparison between the Cox-Merz rule, Stokes' second problem, and the modified Stokes' second problem, for different frequencies, viscosities

and velocities. The initial values of the frequency, viscosity and velocities are arbitrary values and should only be used to compare and view trends between the models. In both figures, it is evident that the amplitude of the shear rate for Stokes' second problem is much lower than the modified Stokes' second problem, but the gradient is the same. This is expected when comparing the two models, and it is only the initial amplitude that varies. For both models, the Cox-Merz relationship differs greatly compared to the other two models; all show that an increase in frequency relates to increased shear rate.

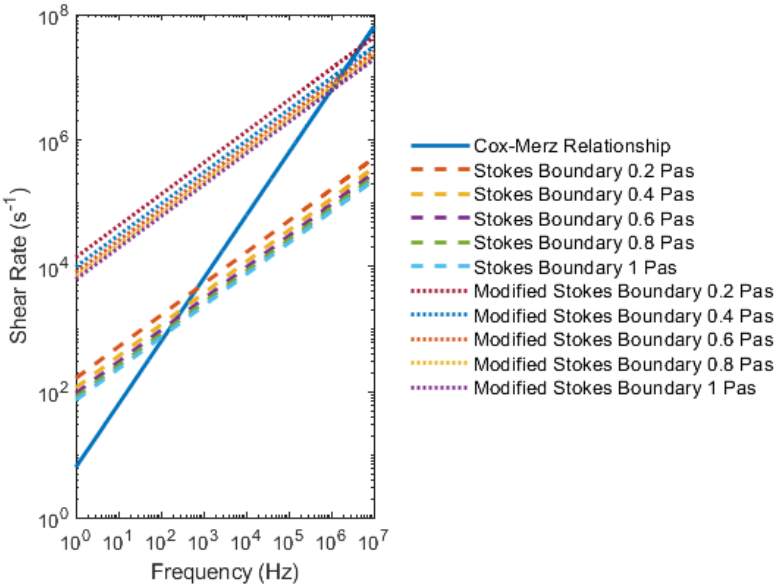

Figure 6.17: A comparison of the different shear rate models to correlate the frequency for different viscosity fluids.

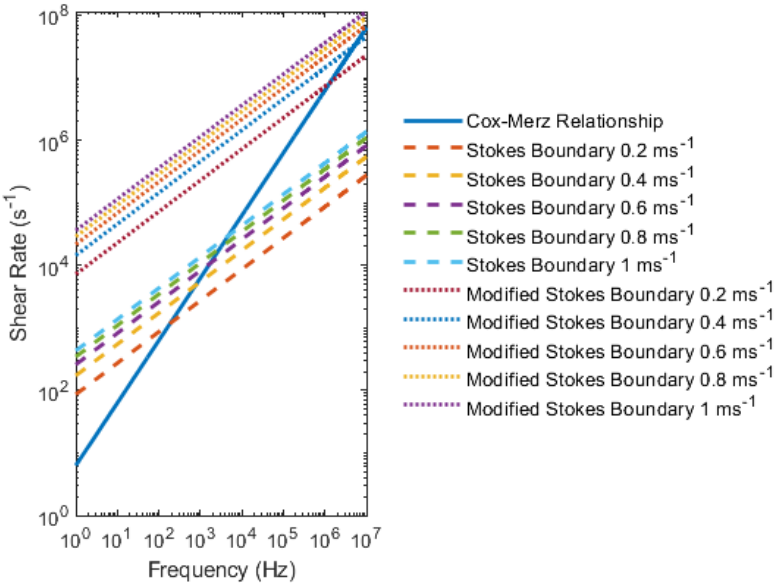

Figure 6.18: A comparison of the different shear rate models to correlate the frequency for different velocities of the elastic plate.

6.5 Conclusions

A literature review has been compiled which focused on viscosity measurements completed by oscillatory viscometers. It was found that for complex fluids or fluids that were exerted to a high shear rate, the Cox Merz could not correlate the steady shear and oscillatory measurements.

An alternative to the Cox-Merz rule was found by development of Stokes' second problem. Using this equation, the relationships between velocity, shear rate and Stokes' layer was found for different viscosity fluids and excitation frequencies.

This relationship was further modified to find the shear rate of a matching layer ultrasonic viscometer where the ultrasound exerted pressure on the test fluid.

The three relationships have been summarised in Table 6.3.

Model	Pressure from ultrasound?	Shear Rate Model: $\dot{\gamma} = f\{\omega\}$
Cox-Merz	No	$\dot{\gamma} = \omega$
Stokes' second problem	No	$\dot{\gamma} = \bar{u}_{solid}\sqrt{\frac{\omega}{\nu}}$
Modified Stokes' second problem	Yes	$\dot{\gamma}_{Max} = (\frac{\bar{u}_{solid} z_{solid}}{z_{fluid}} + \bar{u}_{solid})\sqrt{\frac{\omega}{\nu}}$

Table 6.3: A summary of the shear rate models.

Plots were produced that showed how the shear rate varied for different viscosities, frequencies and velocities and models the models were compared. It was found that the

models disagreed, and the models derived from Stokes' second problem was dependant upon the velocity and viscosity, not just frequency.

The models will be compared using experimental results obtained by using a matching layer ultrasonic viscometer over a range of frequencies in future chapters.

Chapter 7

Experimental Approach and Viscosity Measurements

This chapter describes the apparatus, methodology and signal processing procedure used to obtain viscosity measurements of lubricating oil using a multiple frequency ultrasonic matching layer viscometer. Different signal input parameters are varied and tested to optimise the measurement technique, and a calibration method is used to remove any effect from the instrumentation process. This viscometer is verified by measuring the viscosity of Newtonian and non-Newtonian fluids and comparing to low shear viscosity measurements and the rheological models derived in Chapter 5.

7.1 Experimental Hardware

In the following section, the hardware used to measure the viscosity of fluids using a multiple frequency matching layer viscometer is discussed. A general description of the operation is presented before each component is reported in greater detail.

7.1.1 Overview

To obtain viscosity measurements, several apparatus are required. Here, it is briefly described how the hardware interacts and is shown in Figure 7.1.

1. The signal settings are programmed on a computer, which are sent to a waveform generator via a USB cable.
2. The waveform generator uses this information to induce a pulse with the settings specified.
3. The electrical signal travels along a coaxial cable to a piezoelectric transducer, where it is transformed into a shear ultrasound wave.
4. The shear ultrasound wave travels through the solid and matching layer to the fluid, where it is encoded with viscosity information and is reflected.

5. When the ultrasonic signal returns to the transducer, is is converted back to an electrical signal.

6. The electrical signal travels to an oscilloscope where it is digitised.

7. The signal is transferred to a computer, where it is processed to obtain the viscosity.

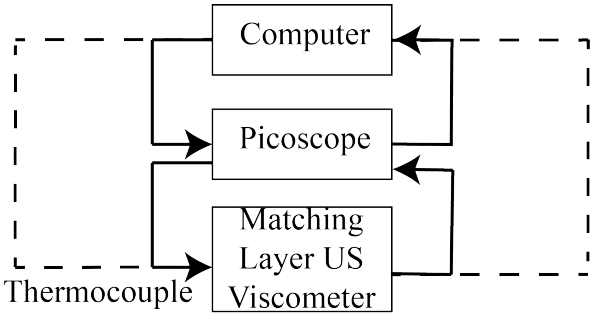

Figure 7.1: Pulse and capture schematic.

7.1.2 The Multiple Frequency Matching Layer Ultrasonic Viscometer

The multiple frequency matching layer viscometer is made up of several different components as is shown by the schematic diagram for a single frequency matching layer viscometer, Figure 7.2, and a photo of a multiple frequency matching layer viscometer, Figure 7.3.

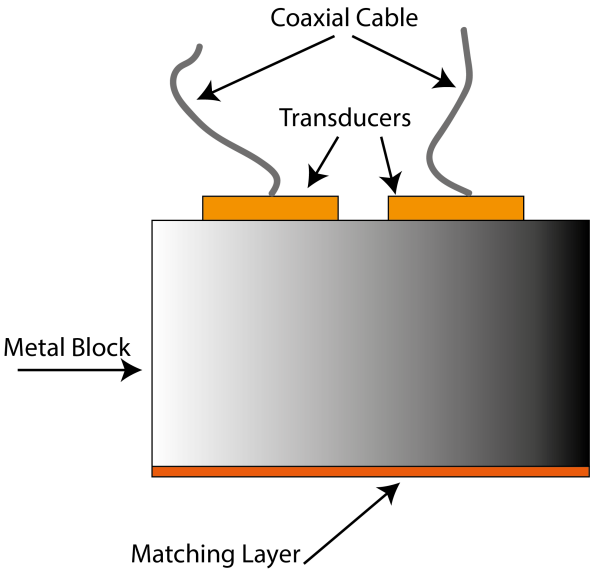

Figure 7.2: Schematic of a single frequency matching layer ultrasonic viscometer.

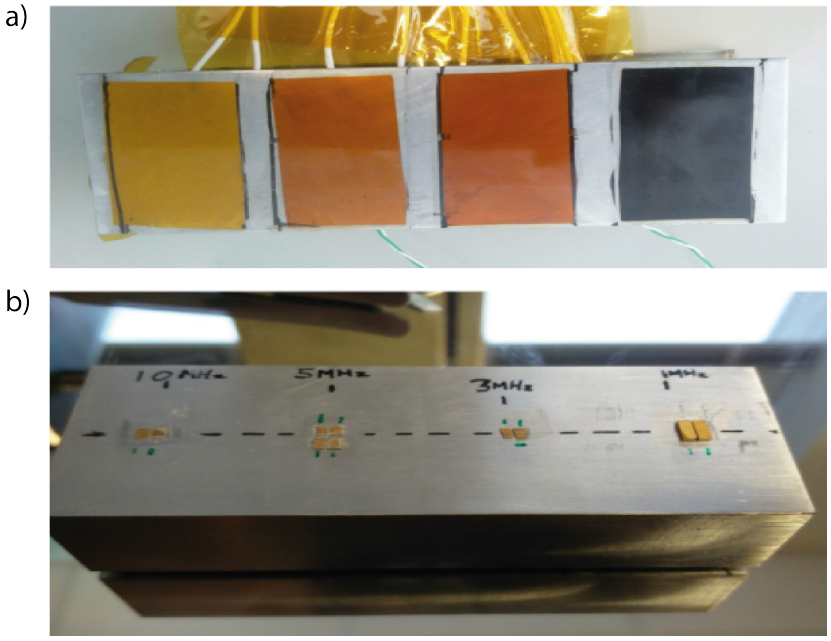

Figure 7.3: *(a)* Top view and *(b)* bottom view photo of multiple frequency matching layer viscometer.

7.1.2.1 Transducers

It has been shown in Chapter 6 that the shear rate is dependant on the frequency of the input signal. By exciting the test fluid with different frequencies, the viscosity of the fluid can be measured over a range of shear rates.

To pulse at different frequencies, two experimental configurations can be employed, as is shown in Figure 7.4. The first is to pulse a single transducer at its resonances. This method has the advantage that it requires only a single transducer but is limited by the bandwidth of the transducer.

The second method requires multiple transducers with different central frequencies. This method allows for a greater frequency resolution but requires more transducers and different thickness matching layers.

In this study, the second method was chosen due to the limited bandwidth of a single transducer.

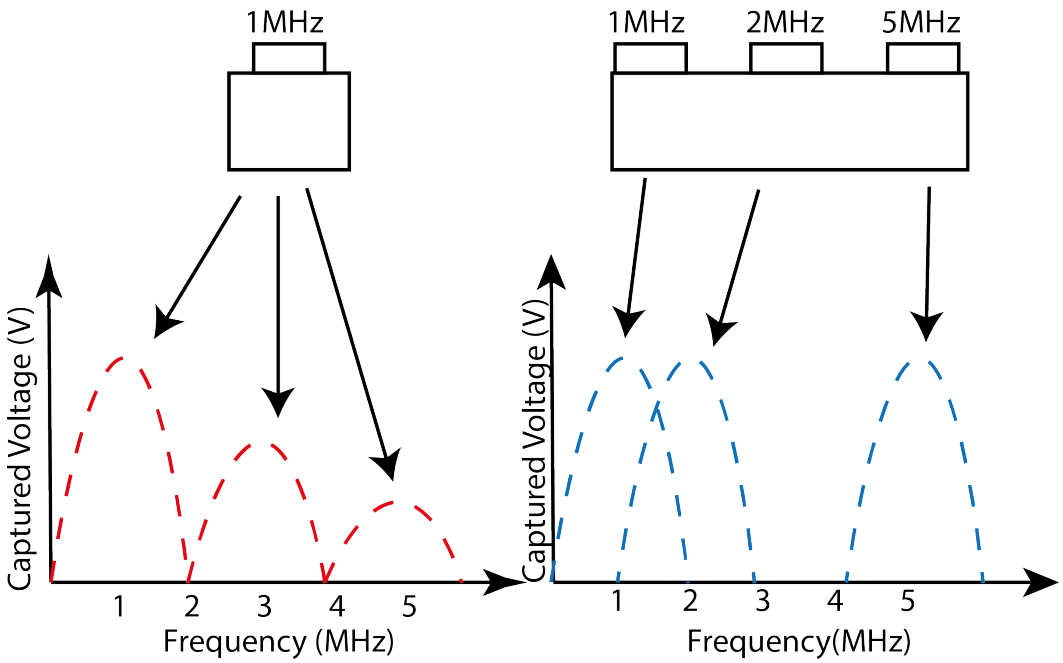

Figure 7.4: Frequency response of a matching layer viscometer with *(a)* single frequency transducer excited at its resonances and *(b)* multiple frequency transducers excited at their single resonance.

The transducers used for all experiments are piezoelectric shear wave transducers. The dimensions of the transducers depend on their application and the transducer's frequency; the lower the frequency, the thicker the transducer. The disadvantage of commercial transducers is the larger size and cost. In this thesis, the experiments require many different frequency transducers, and to reduce the cost, bare crystal elements are used and are bonded to the metal using strain gauge adhesive. Figure 7.5 shows a commercial transducer photo and a bare piezoelectric crystal.

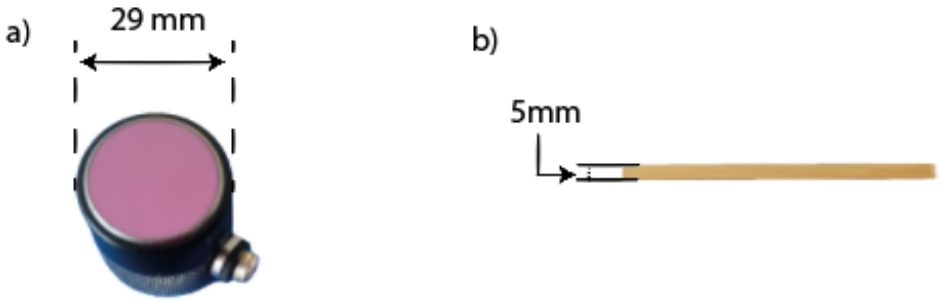

Figure 7.5: Photo of *(a)* commercial transducer and *(b)* bare piezoelectric element.

The dimensions of the bare piezoelectric crystals are $2 \times 5\,mm$, and was chosen because it is small enough to be installed on most engineering components, whilst being large enough to be easily manipulated. Using the transducer dimensions and frequency, the near field zone and beam spread can be calculated using Equation 3.21

and Equation 3.22 respectively. This calculation for the extreme frequencies used in this thesis, 1 - 10MHz, is shown in Table 7.1. The near field results show that the thickness of the aluminium block has to be a minimum of 132mm (for all experiments, it is therefore set at 250mm), and the beam spread shows that when the shear wave reaches the test sample, it will be focused over a small area.

Frequency (MHz)	Near Field (mm)	Beam Spread (°)	Beam Divergence (°)
1	13.2	0.52	1.04
10	131.6	0.05	0.09

Table 7.1: The near field distance and beam spread for different frequencies.

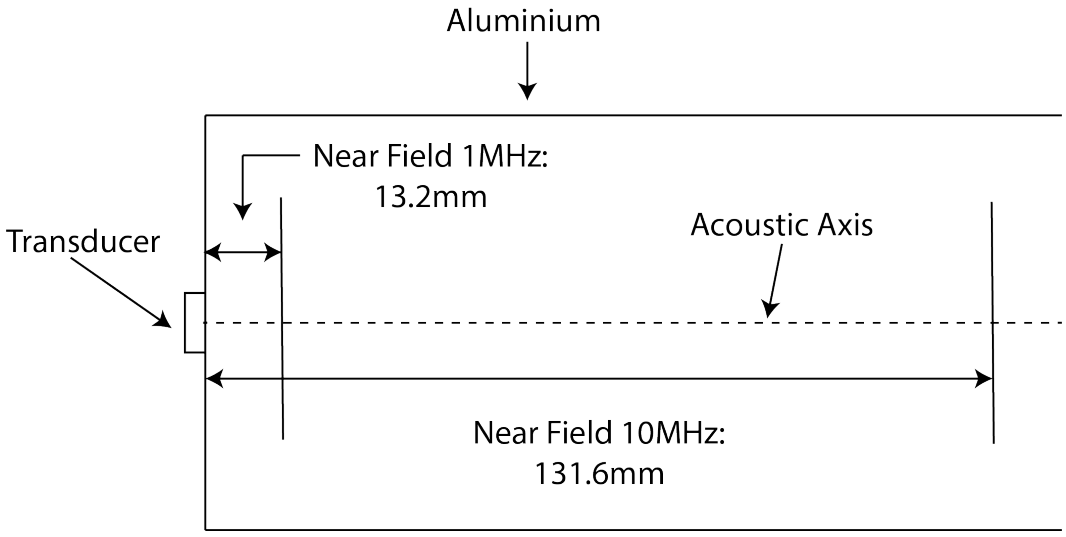

Figure 7.6: Near field distance for a 1MHz and 10MHz transducer bonded to an aluminium block.

7.1.2.2 Matching Layer

The matching layer is a critical part of the ultrasonic viscometer, enabling high sensitivity measurements, as shown in Figure 5.6. Using the reflection coefficient equation for a three-layered model where the third layer is perfectly matched, Equation 5.11, a plot can be produced showing the reflection coefficient for different acoustic impedance matching layers, Figure 7.7.

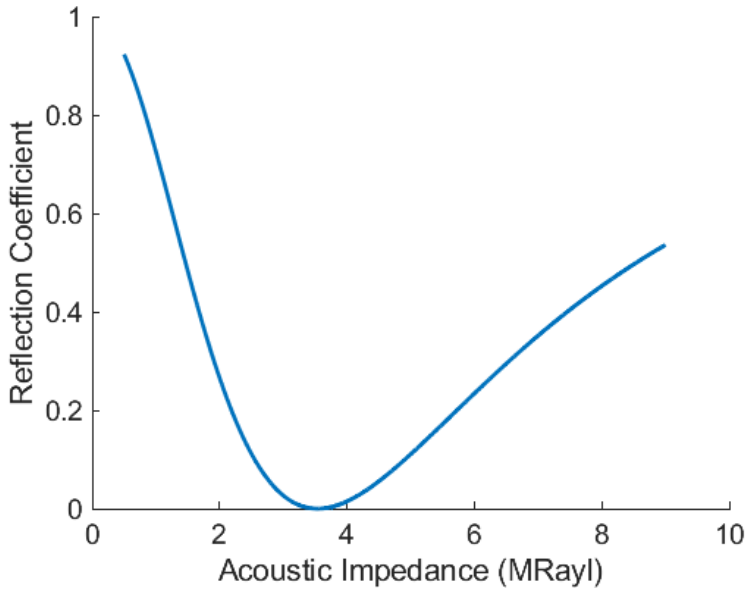

Figure 7.7: Reflection coefficient response for different acoustic impedance matching layer materials.

Using this plot, a database with acoustic impedance's for common materials was filtered to return materials that would produce a suitable reflection coefficient. Some of the more common materials returned are shown in Table 7.2.

Material	Acoustic Impedance (MRayl)	Classification
Mylar	3.00	Plastics
Acrylic, Plexiglas MI-7	3.08	Plastics
Nylon, Black, 6/6	3.15	Plastics
Polyimide	3.16	Plastic
Acrylic, Clear, Plexiglas G Safety Glazing	3.26	Plastics
PVC, Grey	3.27	Plastics
Delrin	3.45	Plastics
Bakelite	3.63	Plastics
Scotchcast XR5235	3.70	Solid
Graphite	4.1	Solid

Table 7.2: Matching layer materials with suitable acoustic impedance's.

Using this information, Polyimide was chosen as the matching layer - a high-performance polymer developed by the DuPont Company. Polyimide has an optimal acoustic impedance for an aluminium - oil configuration of 3.16 $MRayl$. This material has further advantages; it is manufactured in many thicknesses, has high chemical resistance, is stable at high temperatures, is inexpensive- due to the small quantity required, and can be easily bonded to aluminium using strain gauge epoxy. It has also previously been used successfully as a matching layer in ultrasonic transducers (Thompson, 2009)(Haller and Khuri-Yakub, 1992)(Hadimioglu and Khuri-Yakub, 1990).

As discussed in the Literature Review, for the maximum sensitivity of viscosity measurements, the matching layer's thickness should correspond to a quarter of the input frequency wavelength.

$$t_m = \frac{c_m}{4f} \tag{7.1}$$

Using this equation, the optimal thickness of the matching layer for different frequencies is shown in Table 7.3, where the shear speed of sound in Polyimide is $780 m/s$. This table shows that for each frequency transducer, a different thickness matching layer is required. It should be noted that a single thickness matching layer will obtain sensitivity at several other frequencies, and Equation 7.1 is often written as Equation 7.2 , where n is a natural integer.

$$t_m = \frac{nc_m}{4f} \tag{7.2}$$

Frequency (MHz)	Thickness (μm)
1	195
2	97.5
3	65
5	39
10	19.5

Table 7.3: Optimal matching layer thickness for different frequencies.

7.1.3 PicoScope

The PicoScope is produced by Pico Technology, and has dual functionality as a waveform generator and oscilloscope. Compared to more conventional oscilloscopes, the main advantages of a PicoScope are the low cost, size, and portability. A photo is shown in Figure 7.8. The hardware is coupled with in house software developed at the University of Sheffield that allows for the output signal and data acquisition settings to be easily adjusted.

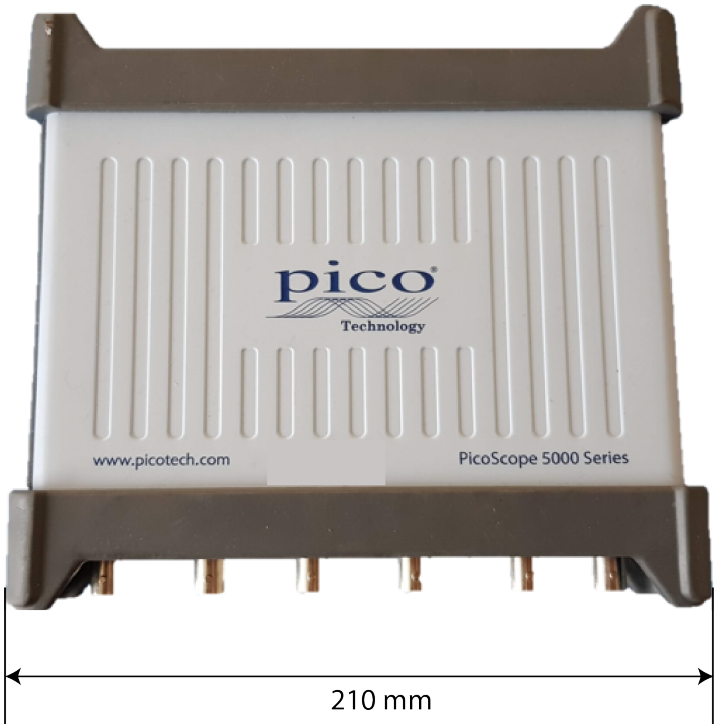

Figure 7.8: Photo of Picoscope.

7.1.4 Multiplexer

A multiplexer, Figure 7.9, is sometimes used in conjunction with the Picoscope and allows for programmable switching of a large number of channels. For a multiple frequency matching layer viscometer, a large number of measurements can be captured across multiple transducers.

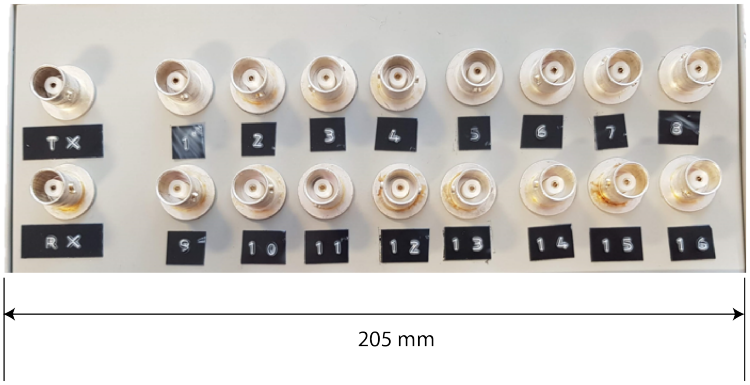

Figure 7.9: Photo of multiplexer.

7.1.5 Cables

BNC connectors and coaxial cable are used to connect the transducers to the PicoScope, allowing for the pulsed voltage to travel to the transducer from the PicoScope, and the received voltage to the PicoScope from the transducer. The cable consists of an outer jacket, a shield, dielectric insulation and a conductor, Figure 7.10.

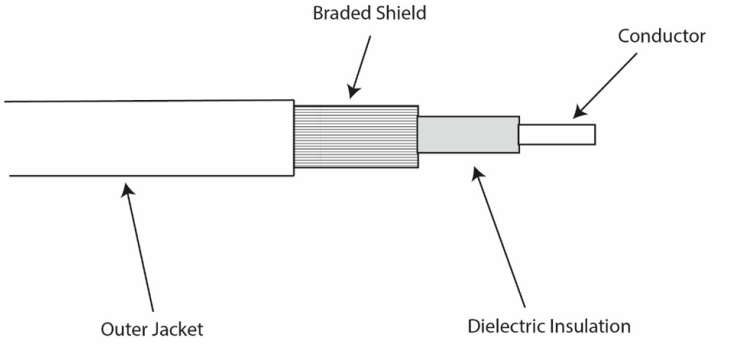

Figure 7.10: Schematic of a coaxial cable.

7.2 Signal Processing

To obtain the reflection coefficient from the returned ultrasound signal, a series of steps are followed, which are detailed in Table 7.4 . In this work, the algorithm is completed using the software package MATLAB, as it allows for storing and manipulating large amounts of numeric arrays whilst also containing a large variety of inbuilt functions and toolboxes that aid in signal manipulation.

Once the reflection coefficient is obtained, it is inputted into the equations developed in Chapter 5, converting from reflection coefficient to viscosity.

Function	Description	Figure
Read Signal	The reflected signal captured using the hardware described above is opened ready for manipulation.	7.11 *(a)*
Average Signal	The initial reflected ultrasound signal is averaged to reduce noise. One hundred captures is more than is necessary, but is chosen due to the low memory requirement of the ultrasound signals and fast processing times.	7.11 *(b)*
Trim Signal	This averaged signal is trimmed to focus on a single echo. If this step is not completed, the FFT shows frequency components from parts of the signal where there is no interest which increases the processing time and adds no benefit.	7.11 *(c)*
Zero Pad Signal	Zero padding adds zero elements to the trimmed signal, increasing its length. This method has been used widely in signal processing. It allows for speeding up the processing time if the number of points of the time domain is made equal to the power of 2 and increases the resolution of the FFT by reducing the spacing of the FFT bins.	7.11 *(d)*
FFT	By completing a Fast Fourier Transform the time domain signal is converted into the frequency domain which allows for frequency analysis to be completed on the signal.	7.11 *(e)*
RC	The reflection coefficient is found by dividing the sample FFT signal by the air FFT signal.	7.11 *(f)*

Table 7.4: Signal processing functions.

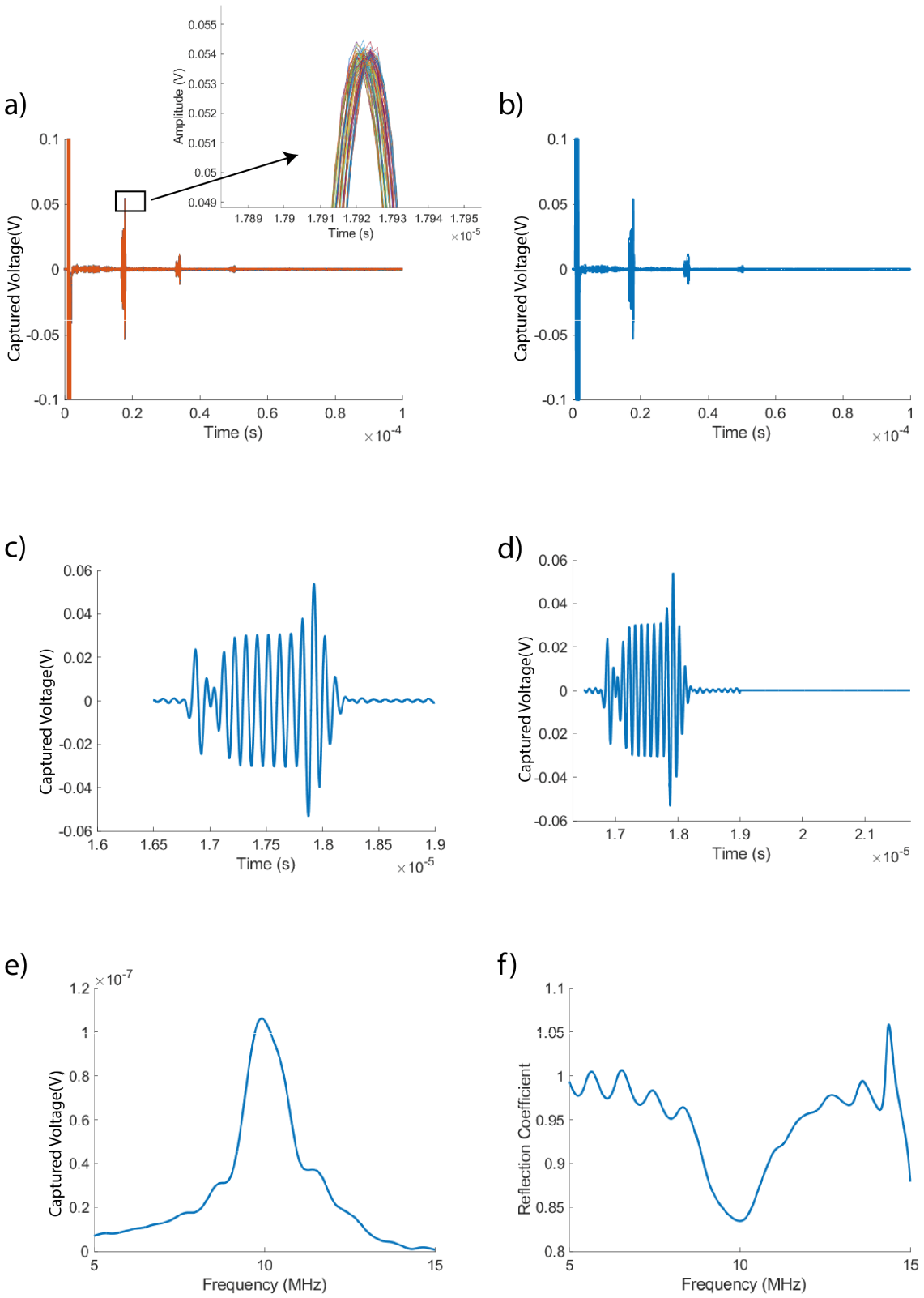

Figure 7.11: Signal processing algorithm corresponding plots.

7.2.1 Calculating Reflection Coefficient

The reflection coefficient and the frequency at which to index the reflection coefficient has been debated by Franco and Buiochi (2019). Three different methods were suggested to negate for oscillating values of viscosity that were displayed across a 3dB band.

1. Obtaining measurements at the central frequency.
2. Averaging over a frequency band.
3. Integral ratio in a frequency band.

It was found that as the sound to noise ratio was improved, the variation in reflection coefficient values reduced (Franco and Buiochi, 2019).

In this thesis, the reflection coefficient was obtained by inspection of the central frequency. This was chosen as the sensor has a high sound to noise ratio and has previously been successfully used to complete viscosity measurements (Schirru, 2016).

7.3 Signal Excitation Settings

When measuring the viscosity using ultrasound, there are an array of pulsing settings that can be changed. Some of these settings are investigated.

For the investigations, a range of Newtonian calibration oils are used, and details are provided in Table 7.5.

Base Oil Category	Oil Sample	Viscosity ($mPas$)	Density (kg/m^3)
Avantor Mineral Oil	85070	16	831.9
Avantor Mineral Oil	85082	66	856.5
Avantor Mineral Oil	85098	120	868.5
Avantor Mineral Oil	85093	420	836.2
Avantor Mineral Oil	85083	710	839.6
Avantor Mineral Oil	85099	1300	842.9
Cannon Mineral Oil	N10	16	881
Cannon Mineral Oil	S20	29	860

Table 7.5: Newtonian samples and their corresponding dynamic viscosity and density at $25°C$.

7.3.1 Number of Cycles

The number of cycles of a sine wave is the number of periods of that wave. The number of cycles is not often considered for ultrasound viscosity measurements as used

is either a single cycle wave (Schirru, 2016), or a continuous wave where a standing wave is formed (Manfredi et al., 2019).

In this study, the number of cycles was increased from 1 to 12 for a 1MHz, 2MHz, 5MHz and 10MHz transducer, and the reflection coefficient was measured using the algorithm described in the previous section. The returned signal in the time domain is shown in Figure 7.12.

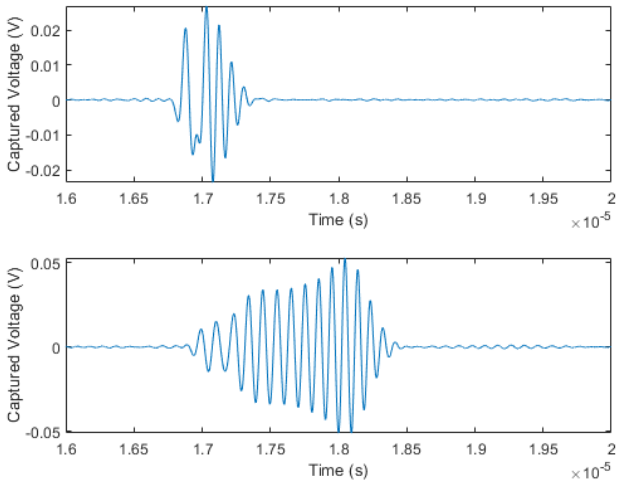

Figure 7.12: Response in the time domain for changing cycle numbers, for a 1 and 12 cycle excitation signal.

As expected, the larger the cycle number, the longer the received pulse. The pulsed signal is limited in length, as the reflected signal should not interact with the transmitted signal.

The reflection coefficient obtained from this returned signal, Figure 7.13, shows that the reflection coefficient remains constant independent of number of cycles. However, analysing the signal further shows that the greater the number of cycles, the smaller the measurement error, Figure 7.14.

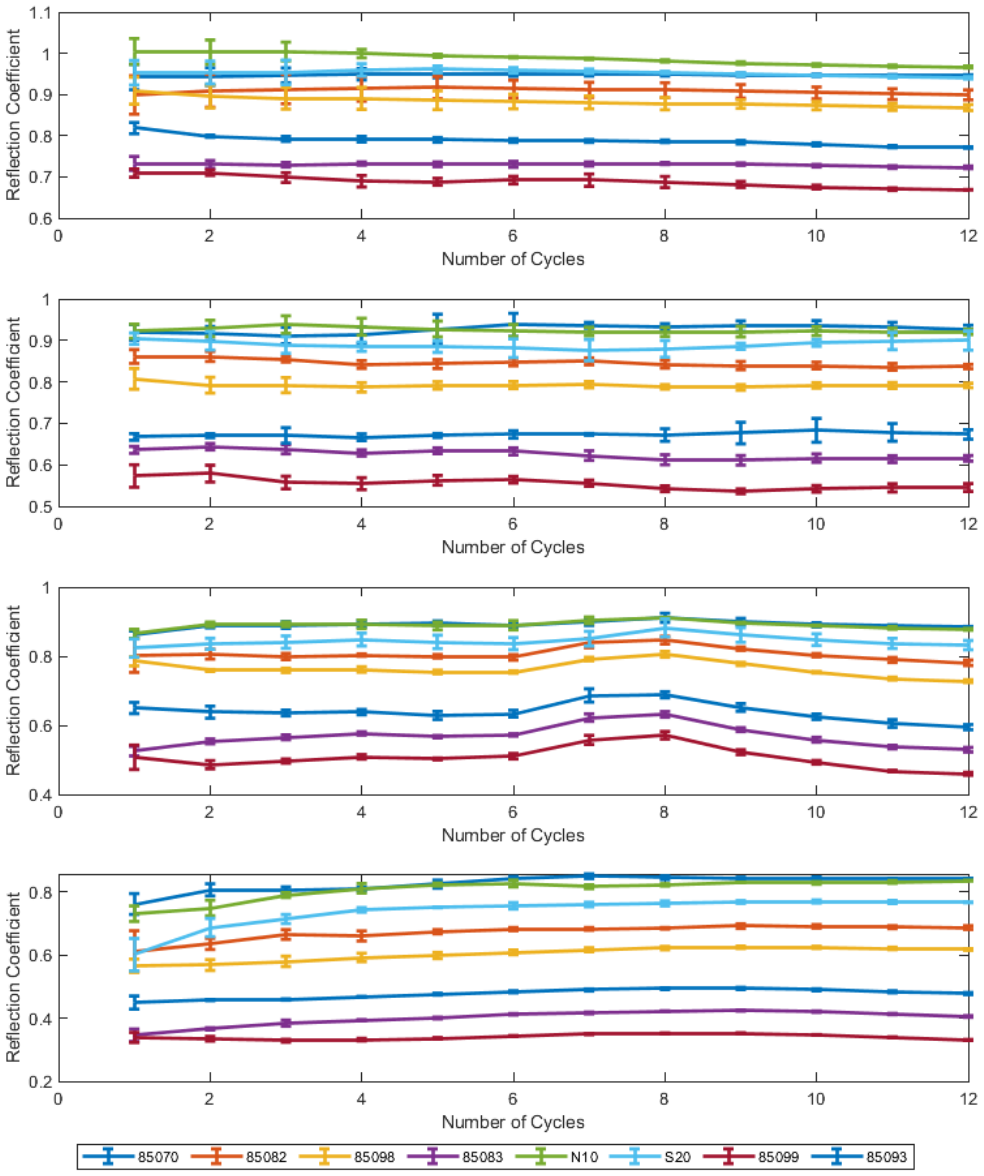

Figure 7.13: Reflection coefficient response for a pulsed wave with different cycle numbers at four different frequency sensors for different calibration oils.

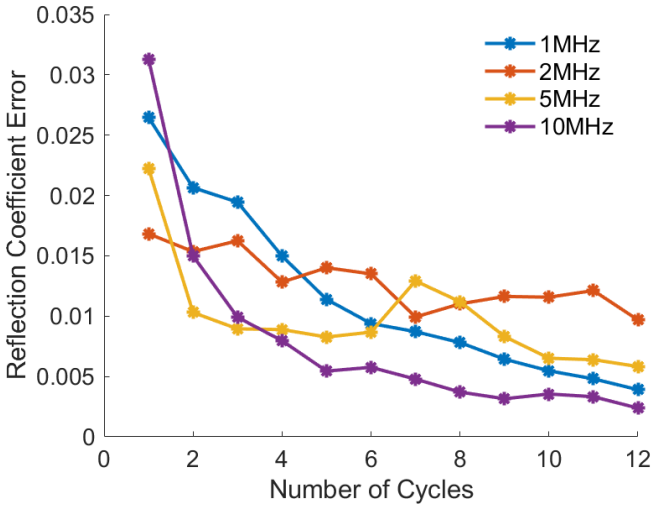

Figure 7.14: Standard deviation for increasing cycle numbers for four different frequency sensors.

The non-linearity of the piezoelectric transducer may explain this correlation, especially creep, explored in previous investigations, (Schitter et al., 2002). The creep can be modelled using Equation 7.3 (Vieira, 1986), where $L(t)$ is the displacement for any fixed input voltage, L_0 is a constant displacement value which is the displacement after $0.1s$ after applying the input voltage, and γ is a creep factor that determines the rate of the logarithm.

$$L(t) = L_0[1 + \gamma \log_{10}(\frac{t}{0.1})], \tag{7.3}$$

It shows that the longer the piezoelectric transducer is subjected to the input voltage, the greater the transducer's displacement. In addition to the creep response region, which can be negated when using the reflection coefficient, piezoelectric transducers have a dynamic response region, as shown in Figure 7.15, where the response from the piezoelectric transducer is harder to predict and leads to errors. This dynamic response region can be overcome when pulsing for a longer time.

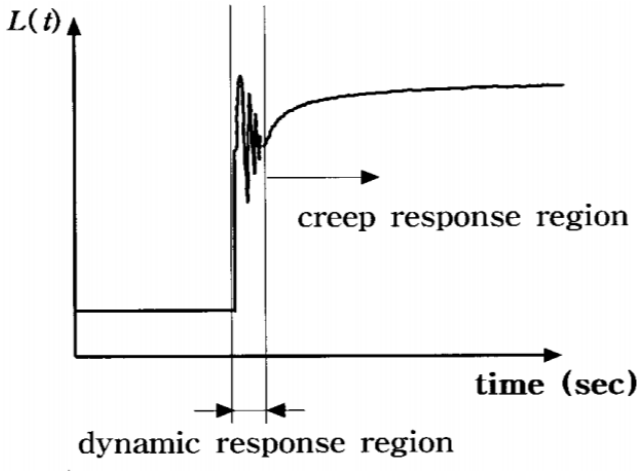

Figure 7.15: Jung and Gweon (2000). A piezoelectric transducer actuator's creep pattern over time.

From these findings, all experiments are pulsed at the largest number of cycles possible, which does not create interference between the transmitted and returning signal.

7.3.2 Waveform

In previous investigations where ultrasonic viscosity measurements have been completed using a matching layer viscometer, it has been suggested that the waveform should be a chirp wave. A chirp wave is a signal where the frequency increases or decreases with time. It was suggested as "The chirp ensures that the matching layer resonance frequency is found precisely" Schirru (2016). The disadvantage of exciting with a chirp wave is that it is more challenging to produce than a sine wave and requires more expensive hardware.

The reflection coefficient was measured for a range of Newtonian calibration oils, using a chirp and a sine wave. The findings are plotted in Figure 7.16, showing that the reflection coefficient measurements for both waveforms are similar.

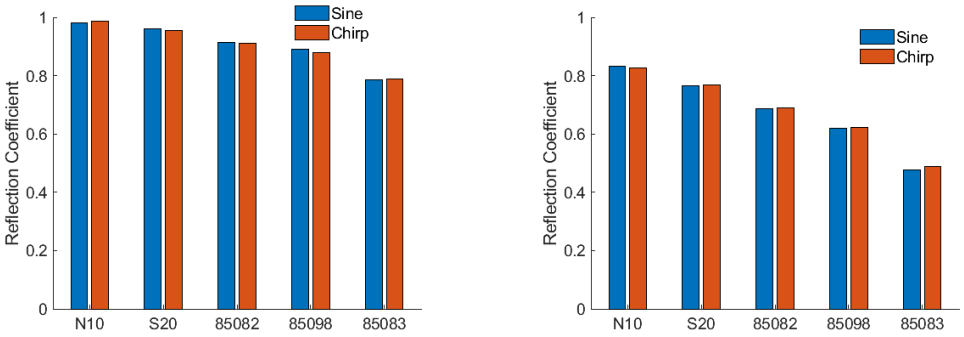

(a) 1MHz Measurements

(b) 10MHz Measurements

Figure 7.16: Reflection coefficient comparison for chirp and sine waves at two frequencies and for multiple oils.

Both waveform shapes produce the same reflection coefficient value because the reflection coefficient is a ratio, meaning that if the amplitude of the signal is different for the chirp and the sine wave, the reflection coefficient will return the same value.

Therefore for all future investigations, a sine wave is chosen over the more complex chirp wave.

7.3.3 Input Frequency

It is usual to pulse at the transducer's central frequency, as this will output a signal with the largest amplitude. However, to obtain maximum sensitivity, it has been shown that the frequency should be a function of the thickness of the matching layer.

A study was completed to determine whether the input frequency of the sine wave affects the reflection coefficient. A selection of laboratory calibration oils from Table 7.5 was tested, and the reflection coefficient was obtained for different input frequencies, Figure 7.17.

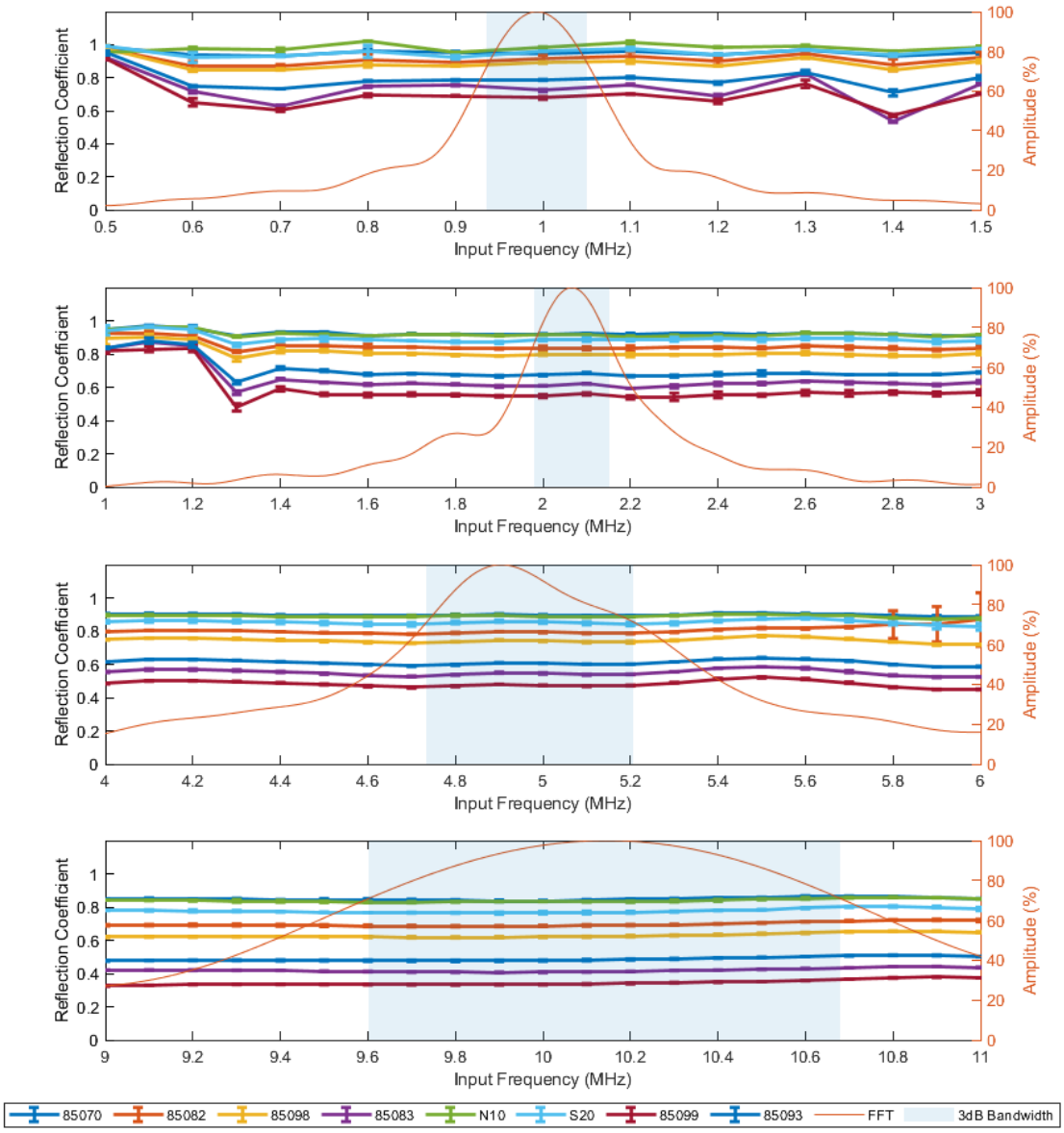

Figure 7.17: Reflection coefficient for changing input frequency sine waves at four different frequency sensors for different calibration oils.

The figure shows that when pulsed with a frequency around the central frequency of the transducer, the reflection coefficient remains steady, but as the excitation frequency tends away from the central frequency, the greater the deviation in the reflection coefficient.

The alteration in the reflection coefficient as the excited frequency is moved away from the central frequency can be explained by viewing the bandwidth of each transducer, which is also plotted on Figure 7.17. As the signal is excited outside the bandwidth, the signal's amplitude reduces and becomes more susceptible to noise, reducing

the accuracy of the results. However, this plot shows that viscosity measurements can successfully be completed outside of the bandwidth of the transducer.

This finding is beneficial for in-situ measurements as it shows that there is no requirement to find the specific frequency, allowing for a faster installation process.

7.4 Comparison of a Low Shear Couette Viscometer and Ultrasonic Matching Layer Viscometer

Using the apparatus and methodology described in this chapter, the viscosity of a Newtonian oil sample, PAO 8, and non-Newtonian oil sample, PAO - DMA blends, was measured at room temperature, $25°C$, at the frequencies 1MHz, 2MHz, 5MHz and 10MHz.

The oil samples were also measured at low shear rates using a Brookfield Couette viscometer. A sample of the oil was placed into the sample holder, which was mounted onto the body of the viscometer, and the spindle was rotated at various speeds to produce different shear rates.

The viscosity results for the low-speed rotational viscometer and results obtained using the multiple frequency matching layer viscometer for a Newtonian sample are presented in Figure 7.18. The error bars for the rotational viscometer were calculated using Equation 7.4, where TK and SMC are constants that are dependant upon the dimensions of the apparatus, and RPM is the number of revolutions per minute.

$$Error = 0.01 \times TK \times SMC \times \frac{10,000}{RPM} \tag{7.4}$$

The error bars for the matching layer ultrasonic viscometer measurements were found by completing five measurements and finding the standard deviation.

Figure 7.18 shows that for both viscometers, the viscosity returned is independent of rotational speed and frequency. This result is expected as PAO 8 is a Newtonian fluid - the viscosity remains constant regardless of the shear rate being applied. As the viscosity is the same for both viscometers, this shows that the multiple frequency matching layer viscometer is able to measure the viscosity of Newtonian fluids at room temperature at $80cP$.

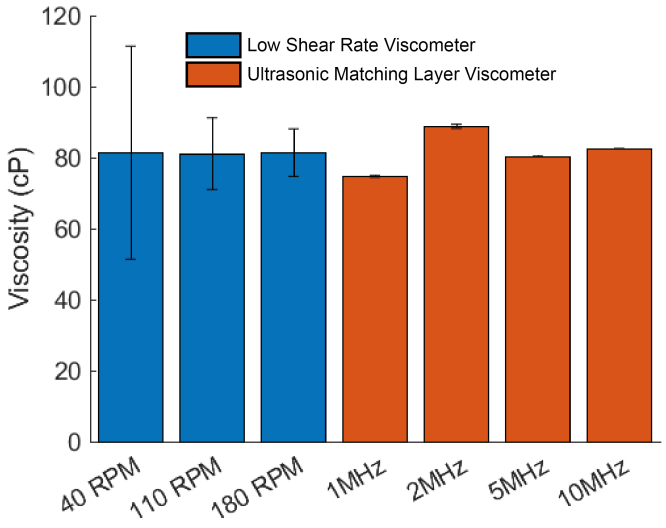

Figure 7.18: Comparison of Couette viscometer results and shear ultrasound viscometer results for Newtonian oil sample, PAO 8.

The non-Newtonian solutions consisted of different proportions of an engine oil additive, DMA (Isodecyl methacrylate), and synthetic base oils, PAO 40 and PAO 100, and are detailed in Table 7.6. The viscosity measurements are shown in Figure 7.19.

Non-Newtonian Solution ID	Base Oil	Base Oil (%)	DMA (%)
#1	PAO40	70	30
#2	PAO40	50	50
#3	PAO40	30	70
#4	PAO100	50	50

Table 7.6: Non-Newtonian oil sample solutions details.

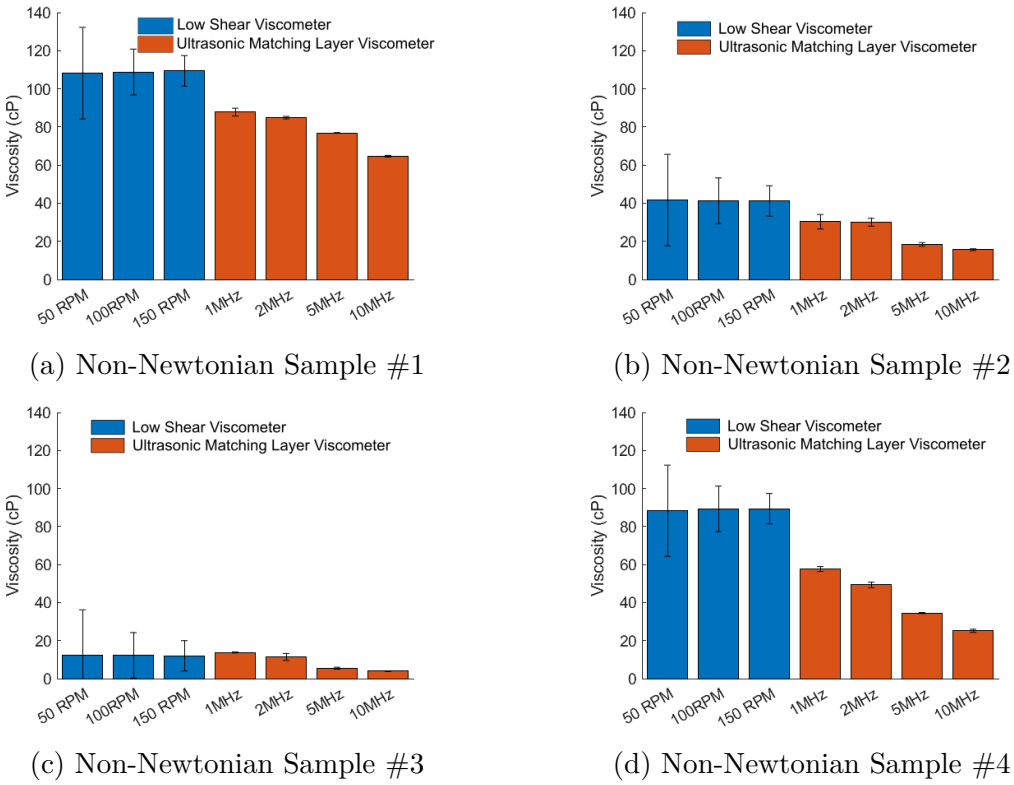

(a) Non-Newtonian Sample #1

(b) Non-Newtonian Sample #2

(c) Non-Newtonian Sample #3

(d) Non-Newtonian Sample #4

Figure 7.19: Comparison of Couette viscometer results and shear ultrasound viscometer results for non-Newtonian oil samples.

The viscosity measurements completed at low shear rates show consistently larger values for all the solutions than the viscosity measurements completed by the multiple frequency matching layer viscometer. This result is expected as the oil solutions are non-Newtonian, the viscosity measurements show a shear rate dependence.

The viscosity measurements completed by the Brookfield viscometer show a constant viscosity when the shear rate is increased. This constant viscosity implies that the viscosity is measured in the oil samples first Newtonian plateau. When the measurements are completed using the matching layer viscometer, the viscosity decreases as the frequency increases. However, it does not plateau, implying that the viscosity measurements are completed in the oils transition zones.

It is impossible to plot the viscosity with respect to shear rates as the shear rate of the multiple frequency matching layer viscometer requires further investigation.

The plots show that a change in base oil and a change in concentrations can be detected by the multiple frequency matching layer viscometer across all frequencies and over a range of viscosities, 10cP - 90cP.

7.5 Evaluation of Rheological Models

To further validate the multiple frequency matching layer viscometer, the viscosities of calibration oils were measured. The reflection coefficient was found, which was then fed into the models derived in Chapter 5, Equation 5.28 and Equation 5.30, to find the viscosity of a Newtonian and non-Newtonian oil respectively. These models were compared to the viscosity measurements provided by the manufacturer.

The first set of results shows the Newtonian model versus experimental measurements, Figure 7.20.

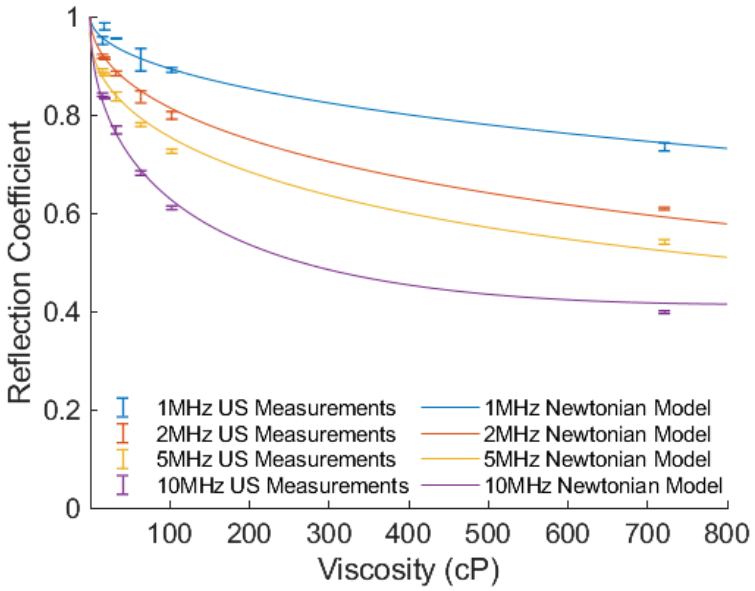

Figure 7.20: A comparison of viscometer results for the Newtonian model, Equation 5.28, using a matching layer ultrasonic viscometer and a Couette low shear viscometer.

A good correlation is shown between the Newtonian model and experimental data, which is confirmed by the R^2 value, Table 7.7. The material parameters were obtained from data sheets and are kept constant for all frequencies and both the Newtonian and non-Newtonian models, listed in Table 7.8.

The second set of results shows the measurements plotted with the non-Newtonian model, Figure 7.21.

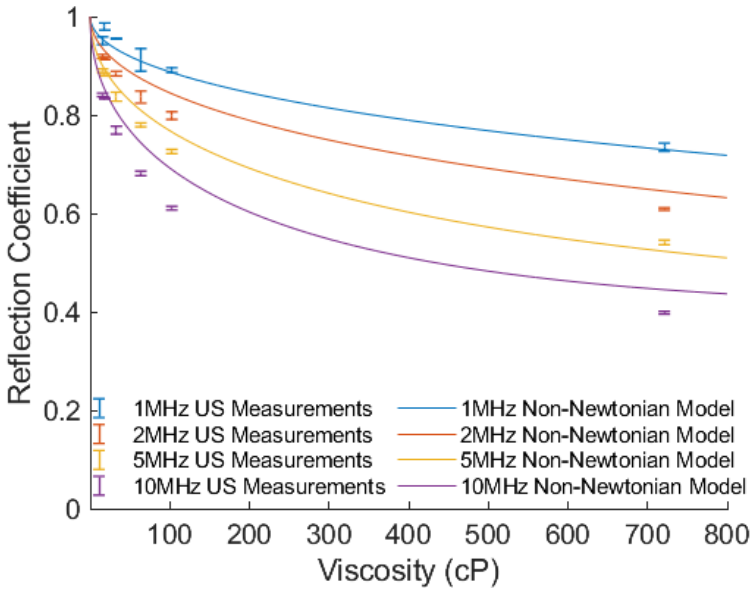

Figure 7.21: A comparison of viscometer results for the non-Newtonian model, Equation 5.30, using a matching layer ultrasonic viscometer and a Couette low shear viscometer.

The figure shows a good agreement between the non-Newtonian model and experimental data. This is expected as it was shown that the Newtonian and non-Newtonian model reduces to the same equation for a short relaxation time.

For simplicity, both Newtonian and non-Newtonian models assumes the density is constant for all the fluids. This is not true, but the model cannot be adapted easily as there is no relationship between viscosity and density.

Another assumption is the relaxation time, as it will be a different value for each oil. It has been set at a short value in this report because of previous measurements (Schirru, 2016).

7.5.1 Model Tuning

Where there is a disparity between the experimental and theoretical results, a trend is seen for results completed at the same frequency. This implies that the sensor causes the disparity. This error may arise from instrumentation, such as using an excessive amount of adhesive to bond the matching layer, or may be caused by inconsistencies in material properties. This leads to an argument for tuning where the material parameters are found by matching the mathematical model with experimental results.

To tune the model, a single oil was selected, and the mathematical model and the low shear Couette viscosity measurement was made equal by selecting the acoustic impedance of the solid and matching layer. The acoustic impedance value for each frequency is noted in Table 7.8. The acoustic impedance values were then used for all future viscosity measurements. As shown in Table 7.7, this produced a better fit across

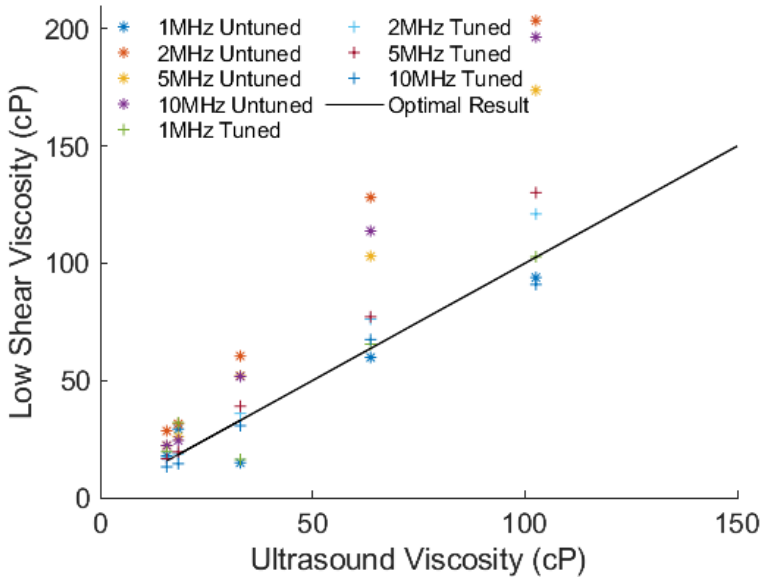

Figure 7.22: A comparison of viscosity results completed using a matching layer ultrasonic viscometer for untuned and tuned measurements, and a low shear Couette viscometer.

the range of viscosities. To further illustrate this increase in correlation, the viscosity values from the tuned model were plotted alongside the results for the untuned model, Figure 7.22. For each frequency sensor and across the viscosity range, the results produced by the tuned model are more closely correlated to the low shear viscosity measurements provided by the manufacturer.

Frequency (MHz)	R^2	
	Untuned	Tuned
1	0.97	0.97
2	0.92	0.99
5	0.97	0.97
10	0.92	0.99

Table 7.7: Fitting result between Newtonian and non-Newtonian model with viscosity measured at low shear rates.

Material Parameters	Untuned	Tuned			
		1MHz	2MHz	5MHz	10MHz
Acoustic Impedance Polyimide (MRayl)	2.75	2.48	2.38	2.35	2.41
Acoustic Impedance Aluminium (MRayl)	8.50	8.52	8.62	8.65	8.59
Density of Oil (kg/m^3)	900	900	900	900	900
Relaxation Time Oil* (ns)	1	1	1	1	1

Table 7.8: Material parameters for reflection coefficient Newtonian and non-Newtonian model.

7.6 Conclusion

The experimental hardware used to take viscosity measurements has been described, and the selection criteria for all the components have been stated. The signal processing technique has been detailed and broken down into functions, and for each of these functions, the transformation of the signal has been shown.

Viscosity measurements were completed with varied signal excitation settings, which allowed for optimisation of the signal.

Finally, two different sets of viscosity measurements were completed. The first compared the viscosity measured using a multiple frequency matching layer viscometer to the viscosity measured using a Couette viscometer at low shear rates. For a Newtonian fluid, the viscosity measurements were constant for both measurement techniques. For a shear-thinning fluid, the viscosity decreased as the frequency increased. Both of these results were as expected and validates the high shear measurement technique.

The second set of experiments compared viscosity measurements obtained by the ultrasonic viscometer with low shear viscosity measurements from a Couette viscometer. Models for both the Newtonian and modified non-Newtonian fluids, derived in Chapter 5, were compared to the experimental results. Both models showed a good correlation, above 92% for all fits, justifying the mathematical models.

A tuning for each of the sensors was completed to remove any variation from the instrumentation process, which increased the correlation between the theoretical and measured results. A summary of the entire signal processing procedure, including tuning the sensors is shown in Figure 7.23.

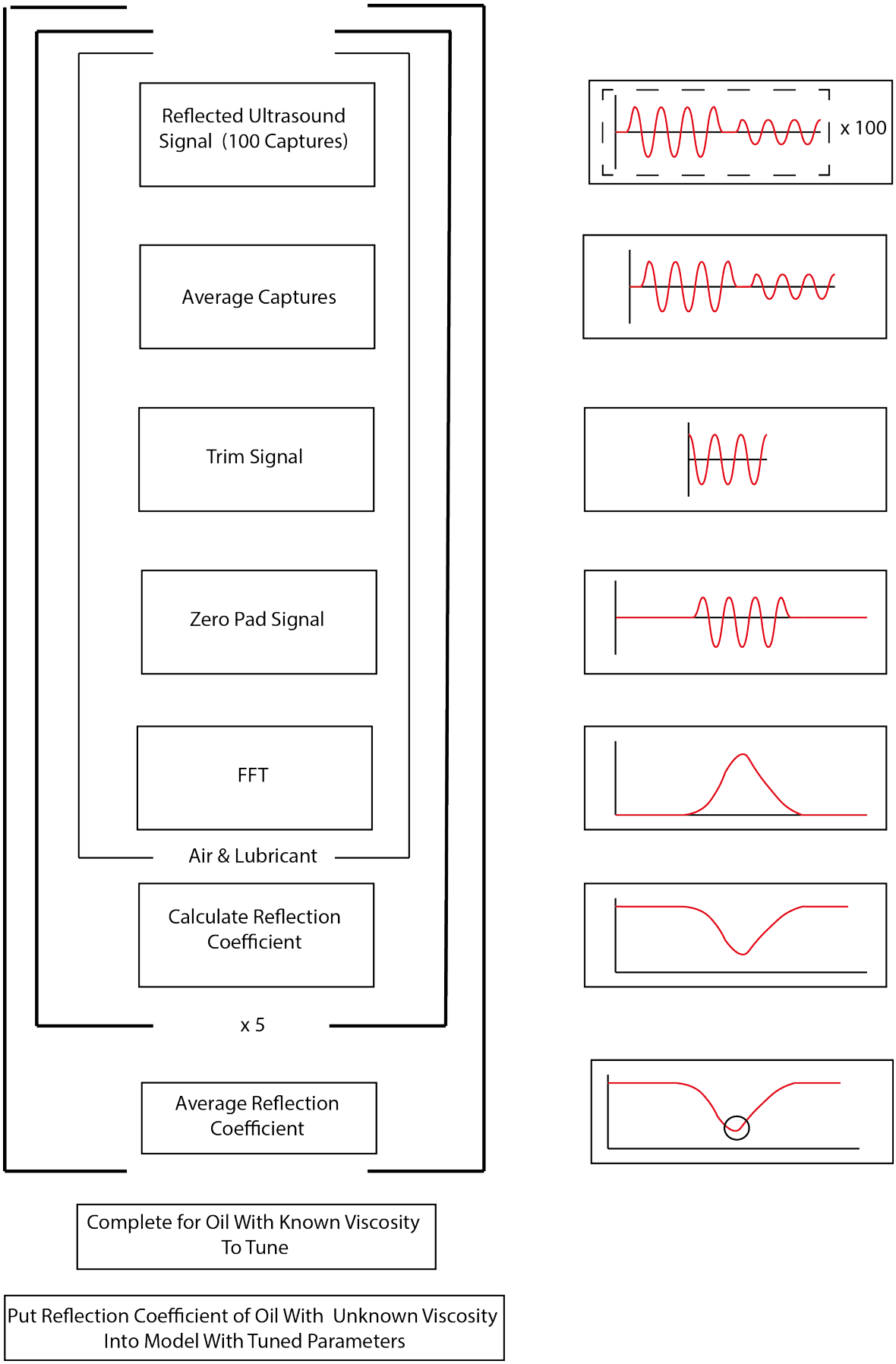

Figure 7.23: Signal processing algorithm summary including tuning.

Chapter 8

Determination of Ultrasonic Shear Rate

In Chapter 6, the model for the shear rate of a multiple frequency matching layer viscometer was derived. This chapter experimentally determines the input parameters to find the shear rate. The viscosity measurements from a multiple frequency matching layer viscometer are then compared with measurements from a steady shear Couette viscometer. Finally, using the information gained in this chapter, the viscosity measurements completed in the Chapter 7 are re-plotted with a common x-axis.

8.1 Introduction

As discussed previously in Chapter 6, it is of paramount importance to understand the shear rate exerted on an oil from the matching layer viscometer to allow for greater understanding of how it will behave in-situ. A model was developed from Stokes' second problem that showed that the shear rate exerted on a fluid using ultrasound was dependent on more than just the frequency, as is implied by the Cox-Merz rule, and an alternative model, Equation 6.34 was developed.

$$\dot{\gamma} = \bar{U}\sqrt{\frac{\omega}{\nu}} \tag{8.1}$$

To obtain the shear rate using this equation, knowledge of the kinematic viscosity of the test oil is required along with the frequency of the ultrasonic shear wave and velocity at which the oil is oscillating. In this chapter, these parameters are experimentally obtained.

8.2 Experimental Determination of Velocity

A laser vibrometer can be used to measure the velocity of particles at high frequencies. The velocity is obtained by focusing laser light at the area of interest and inspecting

the scattered light particles. By using the Doppler effect, the frequency shift is related to the velocity. The typical operation of a laser vibrometer is illustrated in Figure 8.1.

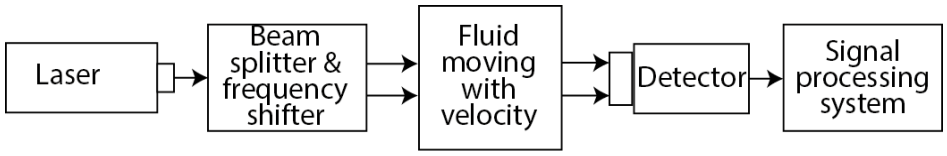

Figure 8.1: Flow chart describing the operation of the laser vibrometer.

For many laser vibrometers, the light signal source and receiver are positioned in the same location. For measurements to be completed the emitted signal is required to be reflected back from the location of interest. The laser vibrometer has been selected as the device to measure the velocity produced by the ultrasonic transducer as it has previously been shown to successfully measure the velocity of an elastic plate that has been excited by sound waves (Li, 2018).

8.2.1 Alternative Method To Measure the Velocity of a Fluid

As mentioned, for a laser vibrometer where the emitter and detector are built into the same unit, to measure the velocity of a fluid, it is required that the light is reflected from the location of interest to the detector. As most fluids are not reflective, it is impossible to measure the fluids velocity directly. A new method is proposed that calculates the velocity of the fluid from the velocity of the plate upon which it in is contact with and the pressure reflection coefficient.

By combining the pressure reflection coefficient equation, Equation 5.5, and the acoustic impedance equation, Equation 3.4, the velocity of the fluid at the boundary can be determined.

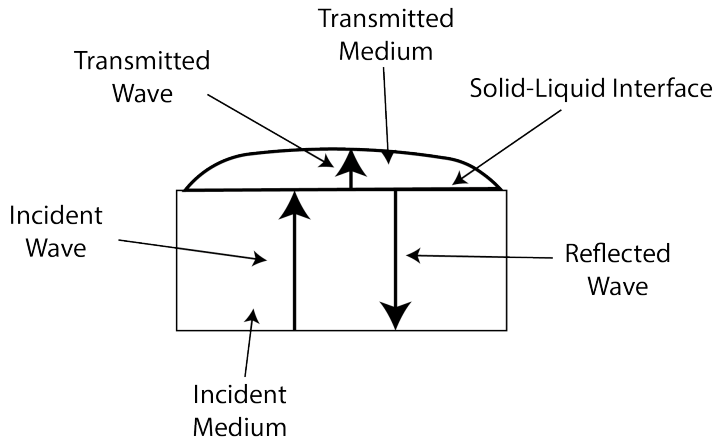

Figure 8.2: Diagram showing the wave interaction in a system with an elastic and fluid layer.

For a two-layered system, Figure 8.2, the relationship between the transmission coefficient, T, and the transmitted and incident pressure, p_t and p_i, are related by Equation 8.2.

$$T = \frac{p_t}{p_i} \tag{8.2}$$

The pressure transmission coefficient and reflection coefficient, R, are related simply by Equation 8.3.

$$T = R + 1 \tag{8.3}$$

Using the relationship between the pressure and acoustic impedance, z, the velocity, u, can be calculated.

$$u = \frac{p}{z} \tag{8.4}$$

By manipulating the above three equations, it is possible to find the velocity of the fluid sample from the velocity of the elastic layer, the reflection coefficient, and the acoustic impedance of both media where z_1 is the acoustic impedance of the elastic layer, and z_2 is the acoustic impedance of the fluid layer.

$$u_t = \frac{p_t}{z_2} = \frac{p_i(R+1)}{z_2} = \frac{z_1}{z_2}u_i(R+1) \tag{8.5}$$

For a three-layered system this can simply be adapted to calculate the velocity in the third medium, u_{t2}, by replacing the acoustic impedance of the second medium with the third medium, z_3. In this equation the velocity of the incident wave in the initial media, u_i can continue to be used as the reflection coefficient considers the intermediary layer.

$$u_{t2} = \frac{z_1}{z_3}u_i(R+1) \tag{8.6}$$

8.2.2 Apparatus and Method

Two ultrasonic shear transducers of central frequencies 1MHz and 2MHz were bonded to an aluminium block with a thickness of 20mm. Unlike previous ultrasonic viscometer configurations, no matching layer was bonded to the surface of the aluminium block to allow for the maximum amount of laser light to be reflected from the surface. The transducer was connected to an amplifier, RITEC RAM 5000, and the applied voltage was varied between $9V - 320V$.

A laser vibrometer head, OFV 354, was directed at the free surface of the aluminium block, directly opposite the transducer. The signal sent from the vibrometer head was

manipulated using the vibrometer controller, OFV 2500. The velocity decoder limited the maximum frequency measurable in the laser vibrometer hardware to 3MHz.

The laser light could not be directly reflected from the aluminium surface because the shear transducers produce an in-plane displacement that the laser vibrometer cannot detect. The aluminium block was positioned at an angle of 45° to the laser vibrometer head to measure the in-plane displacement as has been successfully demonstrated by Li (2018). This positioning caused the light reflected from the aluminium surface to travel at an angle perpendicular to the laser vibrometer head. The light was redirected by positioning a mirror perpendicular to the aluminium block, directly next to the laser light reflecting from the aluminium surface. When the laser sensor head received the reflected laser light, the built-in decoder outputted the time - velocity signal, which was captured on a Picoscope.

The laser vibrometer head, mirror, and ultrasonic viscometer were all mounted on optical rails, which increased the measurements' stability and accuracy.

One thousand captures were made for each measurement and averaged to reduce a large amount of noise, as was completed in previous successful studies (Nishizawa et al., 1998).

The schematic of this experiment can be seen in Figure 8.3, and photos of the laser vibrometer are shown in Figure 8.4.

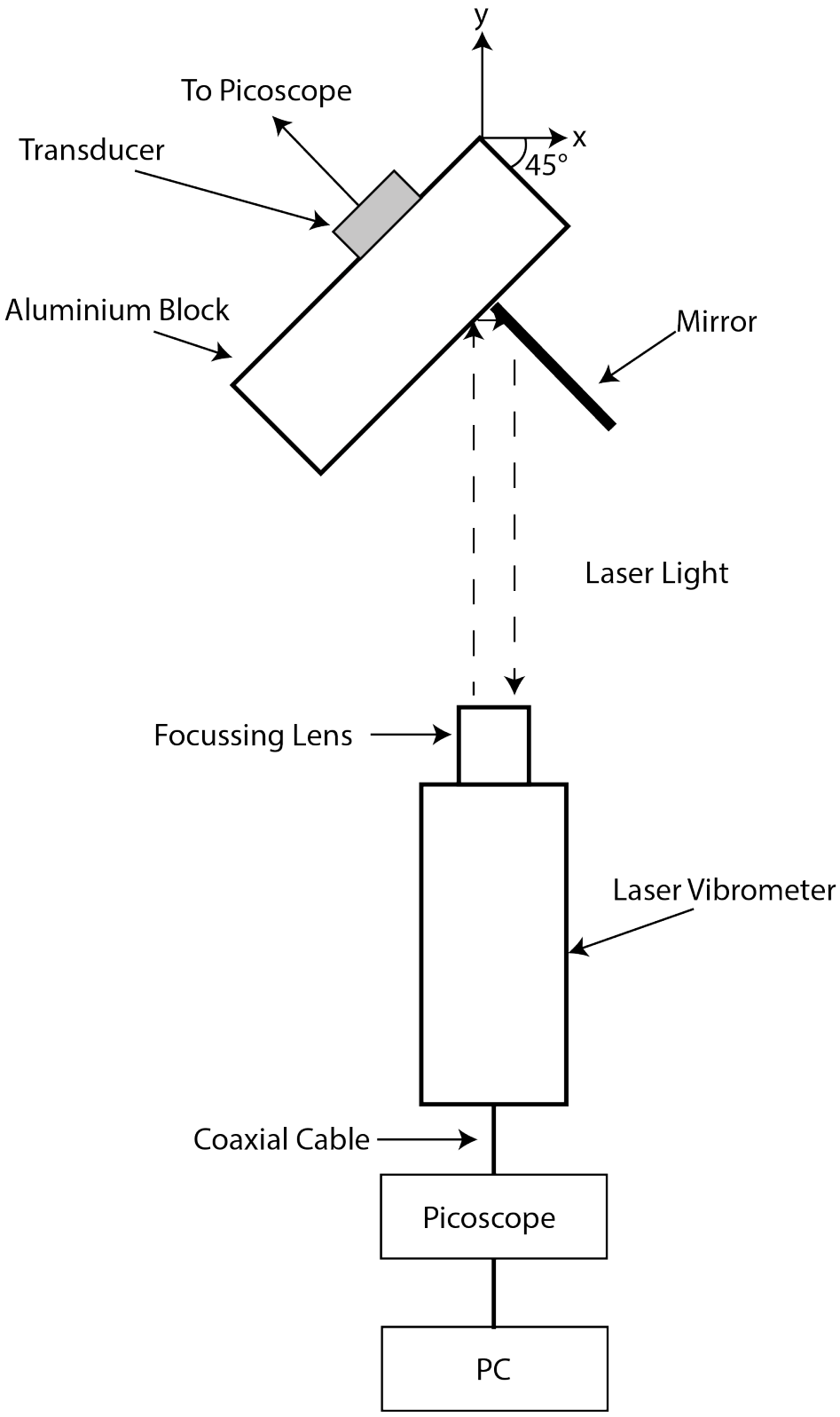

Figure 8.3: Diagram of the hardware used to complete velocity measurements.

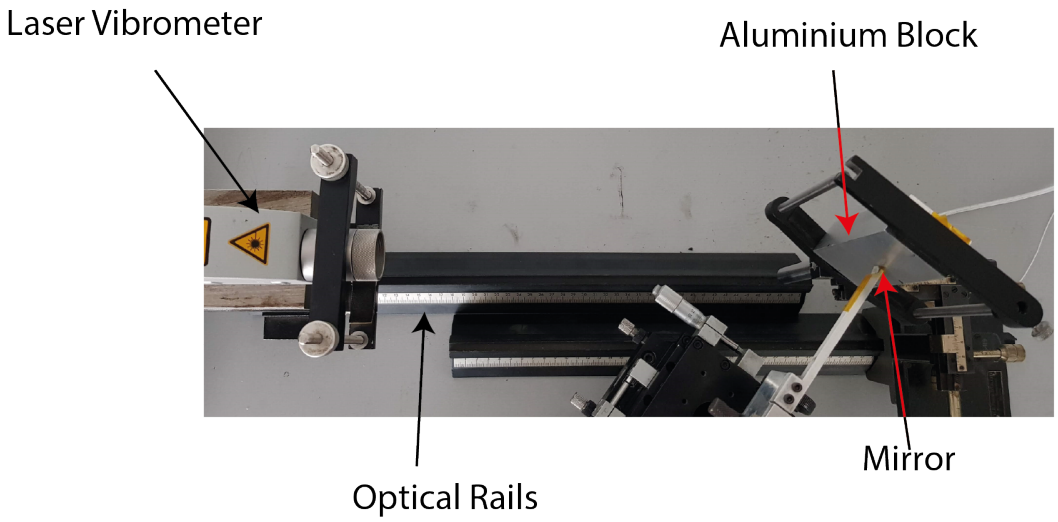

(a) Top down view.

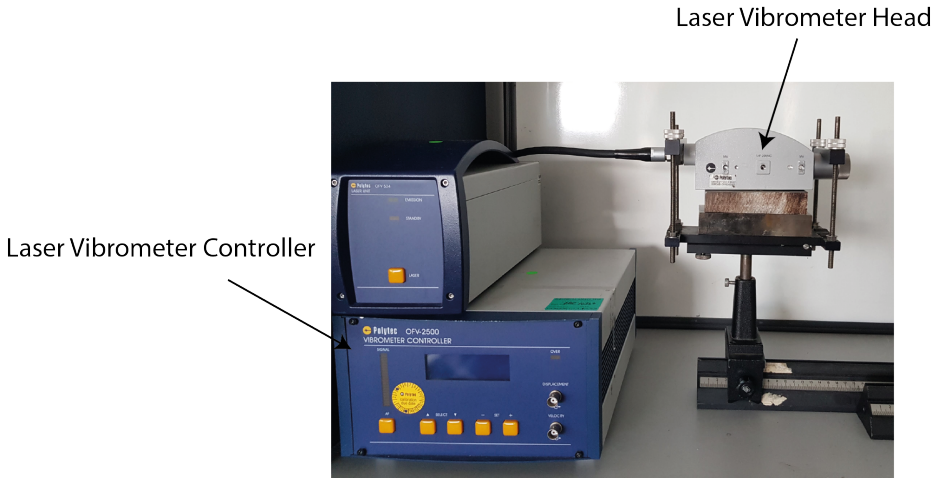

(b) Laser vibrometer.

Figure 8.4: Photo of test apparatus used to measure the surface velocity of an elastic plate.

8.2.3 Results

The one thousand stacked signals and averaged A-scan signal are shown in Figure 8.5a and Figure 8.5b, respectively. The stacked signals show a large amount of variance between captures due to a small sound to noise ratio. To reduce this amount of variance the author recommends that in future experiments this is completed in an environment where external vibrations cannot affect the measurements, such as a laser laboratory. When averaged a much clearer signal is displayed, showing the necessity of completing a large number of captures.

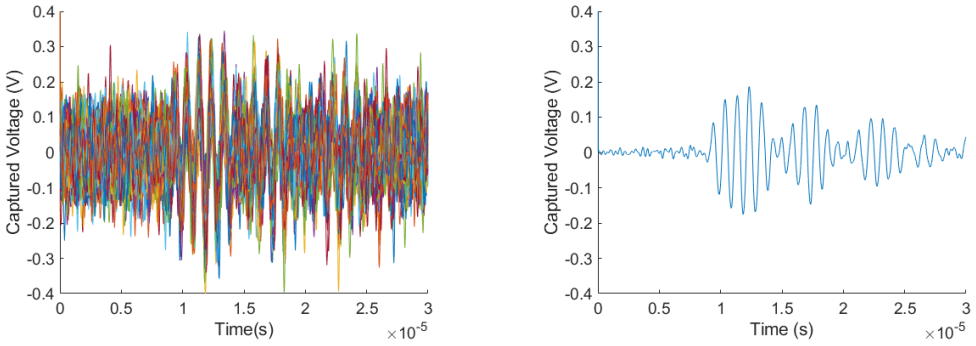

(a) Stacked signals. (b) Averaged signal.

Figure 8.5: Time domain captures of the velocity information received from the laser vibrometer.

To verify that the laser vibrometer was correctly measuring the signal produced by the ultrasonic transducer, the excitation frequency of the 1MHz transducer was varied, and the frequency of the plate was inspected using the laser vibrometer. The results are presented in Figure 8.6 and show a good correlation between the measured and excitation frequency, verifying the laser vibrometers response rate.

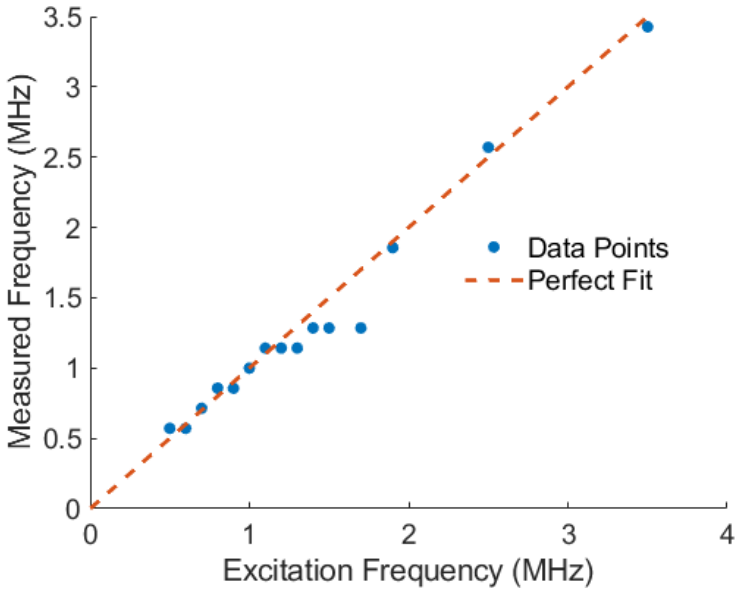

Figure 8.6: Excitation frequency of 1MHz transducer compared against measured frequency using the laser vibrometer.

For both transducers, with frequencies of 1MHz and 2MHz, the velocity at the surface of the aluminium component is shown in Figure 8.7. Both transducers show a similar trend; an increase in excitation voltage increases the velocity of the aluminium surface.

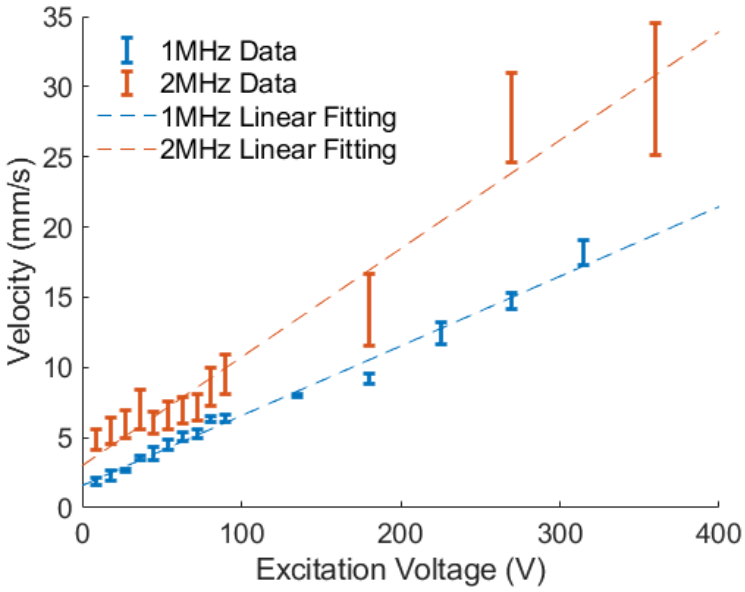

Figure 8.7: Velocity of the surface of an aluminium plate when excited by shear waves produced by a piezoelectric transducer where the excitation voltage is varied.

The displacement was calculated by integrating the velocity results using the MATLAB function *cumtrapz*, which calculates the cumulative integral. It was found to vary

from $1 - 6nm$ for the 1MHz transducer. As the excitation voltage was increased, the displacement became larger.

The velocity and displacement measurements are comparable to previously investigations (Rabani et al., 2016), where the viscosity of an ultrasonic oscillating rod viscosity probe was measured using a laser vibrometer. These results illustrate the large difference between ultrasonic and conventional viscometers, with regards to the magnitude of displacement and velocity. The velocity of the 2MHz transducer is greater than the 1MHz transducer, a result that has also previously been noted (Rabani et al., 2016), however further investigations with a greater number of frequency transducers needs to be completed before this relationship is confirmed.

When using the velocity, it is unclear which velocity to use for the shear rate calculation. Figure 8.8 shows a sketch of the velocity profile, where as the distance into the fluid increases, the velocity of the shear wave decreases. For this investigation it has been decided to use the root mean square value of the maximum velocity. The maximum velocity has been chosen as measurements are taken at the interface, and this location corresponds to the maximum velocity. For the shear rate calculation the difference between the maximum and RMS velocity does not significantly change the value of the shear rate. This transformation of the velocity will be completed for all future shear rate measurements in this chapter.

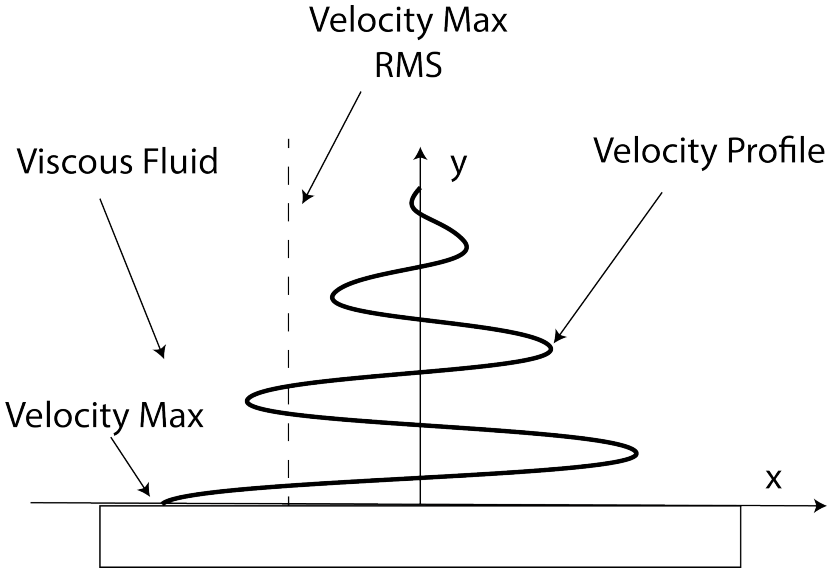

Figure 8.8: A sketch of the velocity profile for a solid-liquid system.

Figure 8.9 shows the maximum shear rate against the excitation voltage. The velocity of the fluid is calculated using Equation 8.5, and the maximum shear rate is calculated using Equation 6.34. In the calculations, the inputs are a hypothetical fluid with a viscosity of 18.6µPas and a density of 1.225kgm^{-3}, the properties of air.

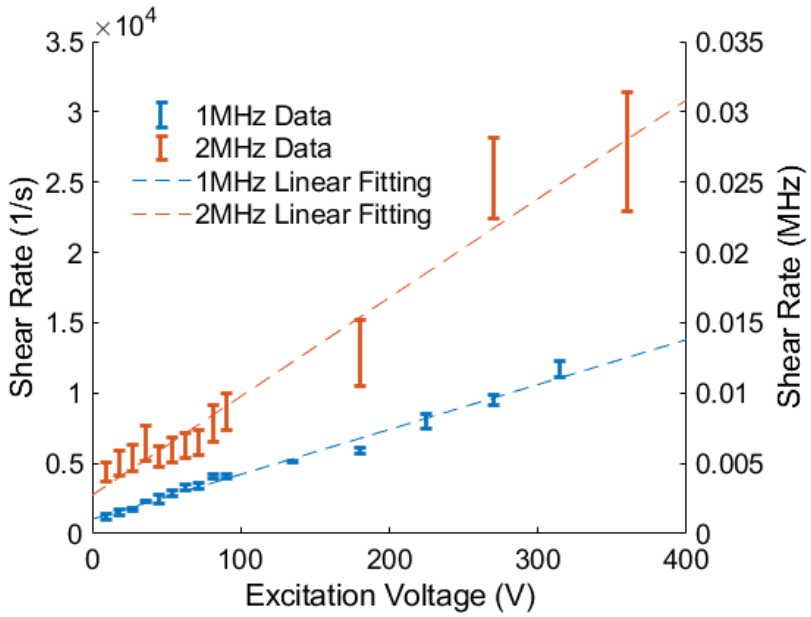

Figure 8.9: Shear rate calculation for air where the velocity information corresponding to Figure 8.7.

This figure shows the amplitude of the excitation voltage affects the velocity - allowing for one transducer to complete viscosity measurements at different shear rates. For example, the 1MHz transducer would be able to measure the viscosity of a fluid that has similar properties to air over the shear rate range $1,200s^{-1} - 12,000s^{-1}$.

8.3 Measurement of Reflection Coefficient When Varying the Excitation Voltage

As shown in the previous section, when using the shear ultrasound viscometer, a change in excitation voltage caused a change in the velocity of the fluid. From Equation 6.34, this will relate to a change in shear rate. This investigation monitors the reflection coefficient, and therefore viscosity as the input voltage is varied. It is hypothesised that as the voltage is increased, the shear rate exerted on the fluid will increase, which will either; lead to a decrease in viscosity and therefore increase in refection coefficient for a shear-thinning fluid, or the viscosity will remain constant and therefore so will the reflection coefficient for a Newtonian fluid. This investigation studies the reflection coefficient when the excitation voltage is varied.

There has been very little literature published that uses the excitation voltage to vary the shear rate exerted on a fluid sample. The exception to this was a study completed by Izumo (2013), who claimed to develop the first tuning-fork vibration rheometer by altering the displacement of a tuning-fork oscillator to control the shear rate. The theoretical model used to describe the relationship between the applied force, F, and the viscosity, η, was developed using the mechanical impedance, R_z, that

the oscillators measure from the fluid. The equation is reprinted below, Equation 8.7, where A is the surface of both sides of the oscillator plate and V is the applied voltage.

$$R_z = \frac{F}{Ve^{i\omega t}} = A\sqrt{\pi f \eta \rho} \tag{8.7}$$

In the report, no equation was provided that related the velocity, displacement, force and shear rate. Instead, a shear rate conversion was used; however, the details were not provided. When changing the driving current, which in turn altered the displacement of the tuning fork from $0.2 - 1.2mm$, measurements were completed on a range of Newtonian and non-Newtonian fluids. As expected, the viscosity of the Newtonian fluids remained constant regardless of the driving current. The viscosity of the non-Newtonian fluids showed a change when the driving current was altered, Figure 8.10.

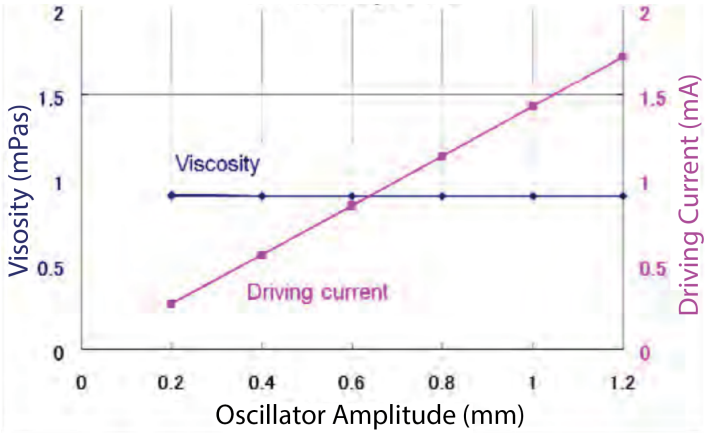

(a) Newtonian sample; water.

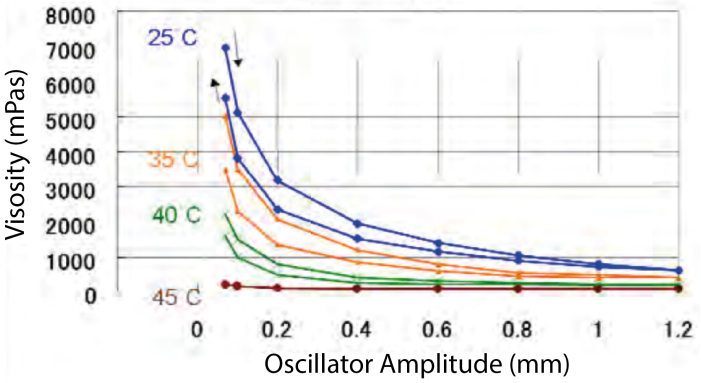

(b) Non-Newtonian sample; hand cream.

Figure 8.10: Izumo (2013). Viscosity measurements for a tuning fork viscometer where the amplitude of the oscillating fork is varied.

8.3.1 Apparatus and Method

The multiple frequency matching layer viscometer described in Chapter 7 was selected to measure the reflection coefficient from the test fluids. This ultrasonic viscometer

was chosen over the viscometer used in the previous velocity investigation, Section 8.2, as the matching layer greatly increases the sensitivity of the measurements. A thermocouple was attached next to the piezoelectric transducer, and a second thermocouple was attached to the surface of the matching layer to constantly monitor temperature.

The multiple frequency matching layer viscometer was connected to an amplifier where the excitation voltage was adjusted, which was connected to an arbitrary function generator where the signal settings were controlled. Two different amplifiers were used for this investigation, a RITEC RAM 5000 and an AIM-TTI Instruments TG5011. Both amplifiers had built-in arbitrary function generators, and details of the two amplifiers are shown in Table 8.1. The received signal was captured on a Picoscope and transferred to a PC, where it was stored and analysed. A schematic of this configuration is shown in Figure 8.11.

Parameter	RITEC RAM 5000	AIM-TTI Instruments TG5011
Waveform	Sine	Sine
Number of Cycles	8	8
Transmission	Burst	Burst
Maximum Voltage	110V	10V
Voltage Resolution	9V	1V

Table 8.1: Summary of the amplifier apparatus.

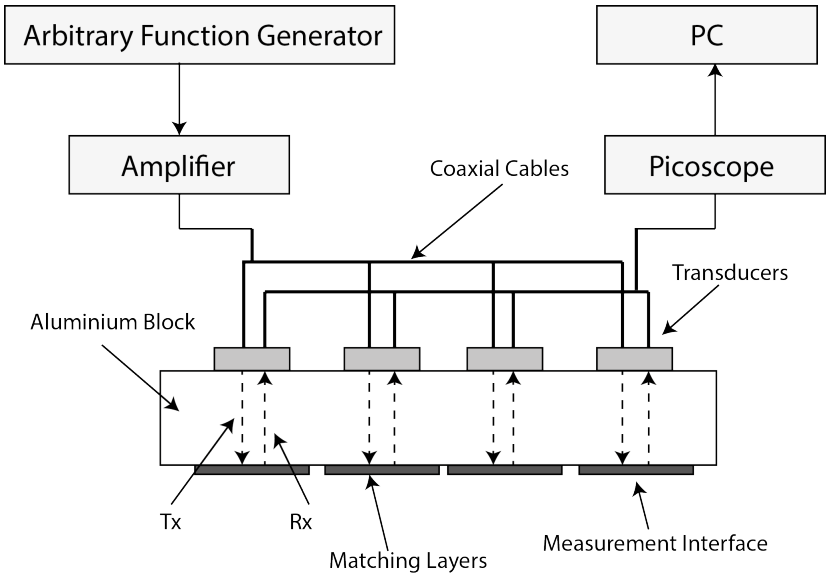

Figure 8.11: A schematic of the experimental configuration for ultrasonic viscosity measurements with a varying excitation voltage.

As with previous matching layer viscometer measurements, a reference measurement was recorded at a matching layer-air boundary. This reference measurement was captured for each excitation voltage and each frequency transducer. A small sample of test fluid, 5ml, was deposited on each of the matching layers, and the returned signal

was captured and processed. Using this amount of oil ensures that the thickness of the oil layer is much larger than the penetration depth, and the surface area of the sample is much larger than the ultrasound focus area, allowing for the assumption of a semi-infinite problem.

Details of the test samples and the corresponding experimental parameters are collated in Table 8.2.

Test Sample	Description	Rheological Properties	Frequency (MHz)	Voltage (V)
PAO 40	Newtonian calibration base oil.	Newtonian	1, 2, 10	0 - 10
DMA Blend	Mixture of equal parts of PAO40	Non-Newtonian	2	0 - 10
	and Isodecyl Methacrylate.		1,2,10	0 - 180
EAL Sample 5	Environmentally acceptable lubricant.	Non-Newtonian	1,2,10	0 - 10
Ketchup	Common shear thinning sample.	Non-Newtonian	2	0 - 10
Hand Cream	Common shear thinning sample.	Non-Newtonian	2	0 - 10

Table 8.2: Oil samples used in voltage increase investigation, with corresponding test parameters.

8.3.2 Results

8.3.2.1 RITEC RAM 5000 Amplifier

Figure 8.12a is an example of the received A-scan, and shows a voltage offset. The voltage offset is a common phenomenon and can be caused by a mismatch of the input transistors and components during fabrication (Palmer, 2001). This offset in voltage was removed when analysing the signal using the MATLAB function *detrend*, Figure 8.12b.

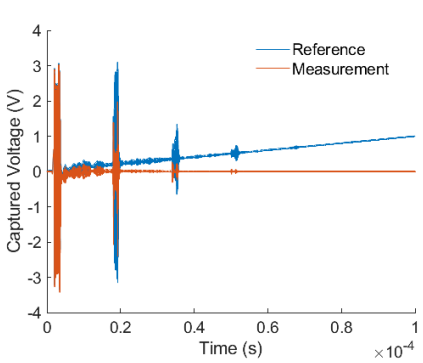

(a) A-scan illustrating voltage offset.

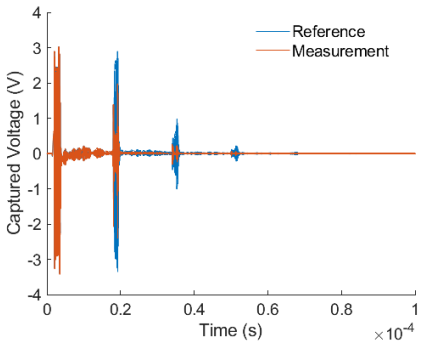

(b) A-scan after applying function *detrend*.

Figure 8.12: A-scan's when using the RITEC RAM 5000.

Figure 8.13 shows the A-scan from the 2MHz sensor when excited with different voltages. This plot shows, as expected, an increase in excitation voltage returns an ultrasound signal with a greater amplitude.

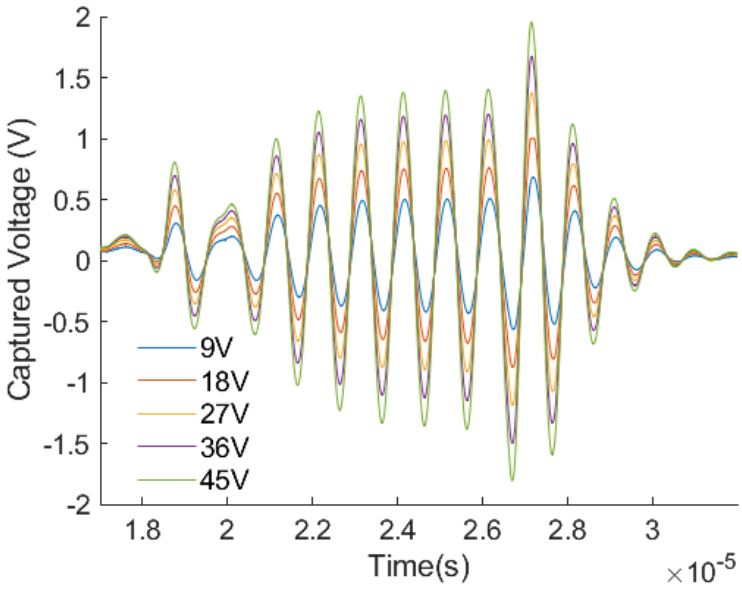

Figure 8.13: Stacked A-scan response for an ultrasonic matching layer that has been excited with varying voltages.

The first set of experiments monitored the reflection coefficient of a Newtonian and non-Newtonian solution over a large excitation voltage range, $0 - 180V$ and frequency range $1 - 10MHz$, Figure 8.14 and Figure 8.15, respectively. Details of these oils are shown in Table 7.5 and Table 7.6.

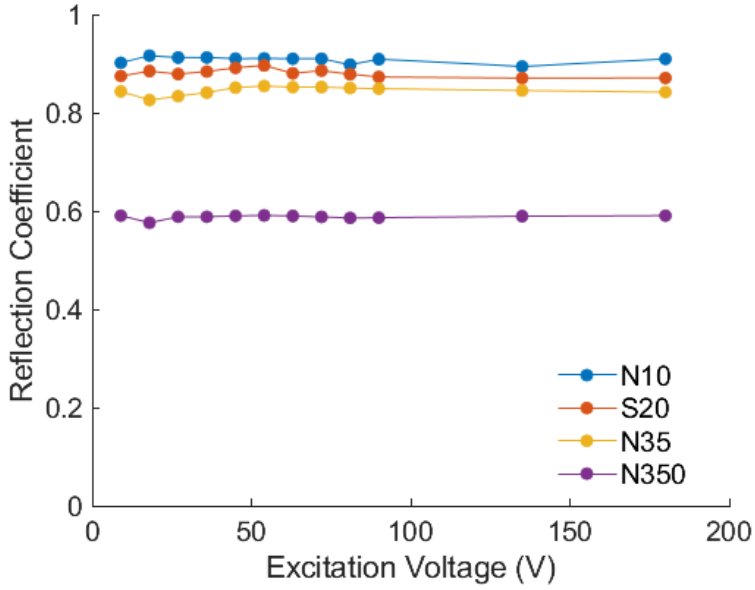

Figure 8.14: Reflection coefficient response of Newtonian samples for a 2MHz matching layer ultrasonic matching layer where the excitation voltage was varied from 0-180V.

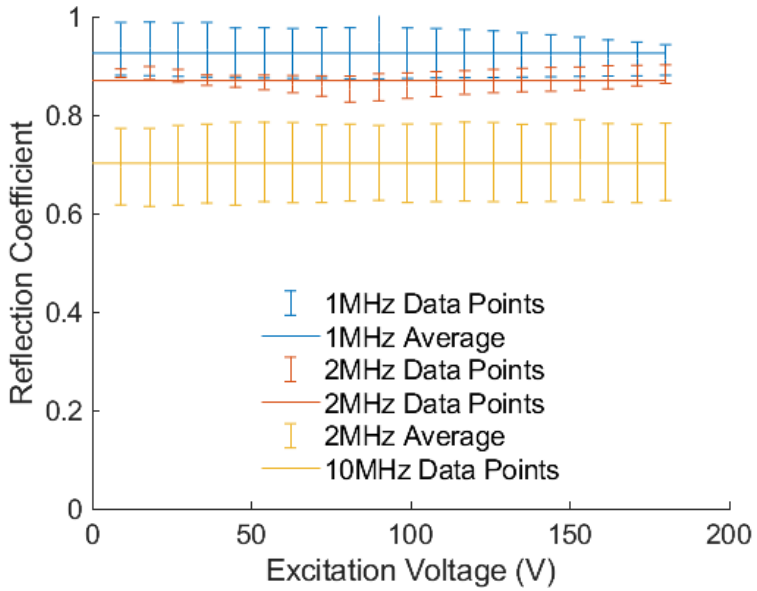

Figure 8.15: Reflection coefficient response of a non-Newtonian fluid (DMA blend), for a matching layer ultrasonic viscometer where the excitation voltage was varied from 0-180V.

For both Newtonian and non-Newtonian samples a change in excitation voltage does not alter the reflection coefficient. This result is expected for the Newtonian samples, as the viscosity and therefore reflection coefficient is independent of shear rate, but is unexpected for the non-Newtonian samples, where a shear-thinning behaviour has been measured in previous investigations. This lack of variation in the reflection coefficient could be caused by the shear variation not being large enough. Using this experimental set-up it is expected that there will be an increase in shear rate from 2.48×10^5 - $9.53 \times 10^5 s^{-1}$.

The temperature was monitored throughout each test, and it remained constant.

8.3.2.2 AIM-TTI TG5011 Amplifier

To verify the results obtained when using the RITEC RAM 5000 amplifier, measurements were completed using the amplifier, AIM-TTI Instruments TG5011, which had a lower maximum excitation voltage of $10V$ but did not produce a voltage offset.

The first plot shows the reflection coefficient of the non-Newtonian sample tested using the RITEC amplifier that produced Figure 8.15, and another non-Newtonian sample that is detailed in Table 8.3. Measurements were completed over 1200 seconds, where a reading was taken every 20 seconds, and the voltage was changed every 60 seconds, Figure 8.16.

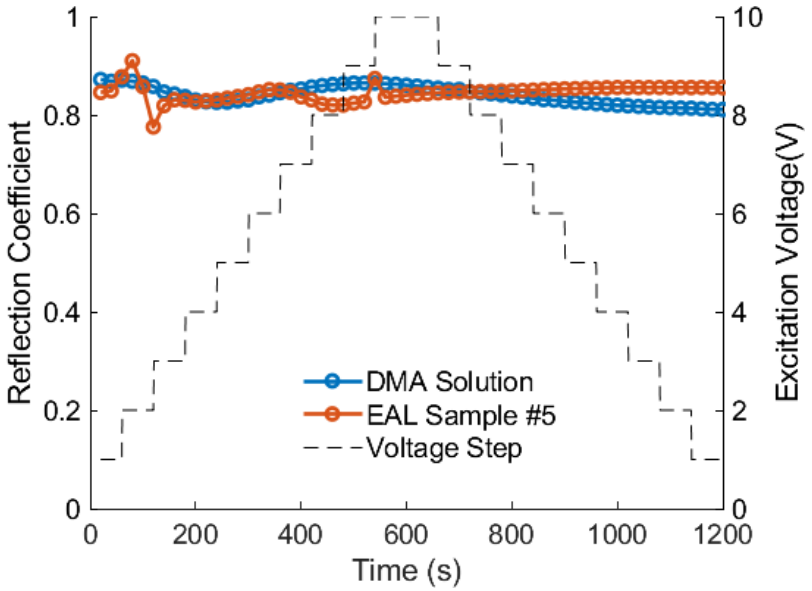

Figure 8.16: Reflection coefficient response of a non-Newtonian sample for a $1MHz$ matching layer ultrasonic matching layer where the excitation voltage was varied from $0 - 10V$.

For completeness, a Newtonian sample, Avantor mineral oil 85071, was measured across the frequencies 1MHz, 2MHz and 10MHz, and the results are shown in Figure 8.17.

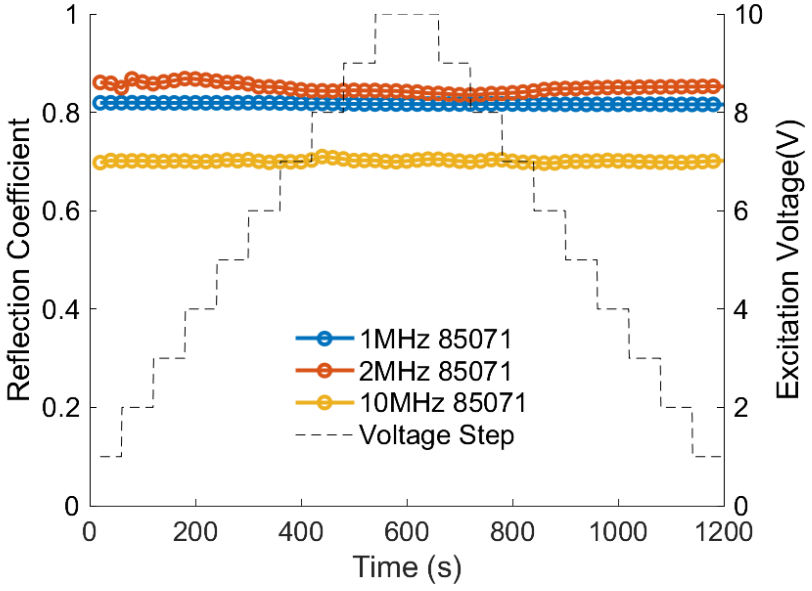

Figure 8.17: Reflection coefficient response of a Newtonian sample for a matching layer ultrasonic matching layer where the excitation voltage was varied from 0-10V.

The results again show a lack of variation in the reflection coefficient. This is expected as the voltage range, and therefore the shear rate range is smaller than in the previous experiments when using the RITEC amplifier.

As discussed in the introduction, an investigation completed by Izumo (2013) found that as the excitation voltage was increased for a tuning fork viscometer, the viscosity of highly shear-thinning samples, ketchup and hand cream, decreased. Two similar non-Newtonian household samples were measured using the matching layer ultrasound viscometer, and it was hoped that a similar change in viscosity would be captured. The results of this experiment are presented in Figure 8.18.

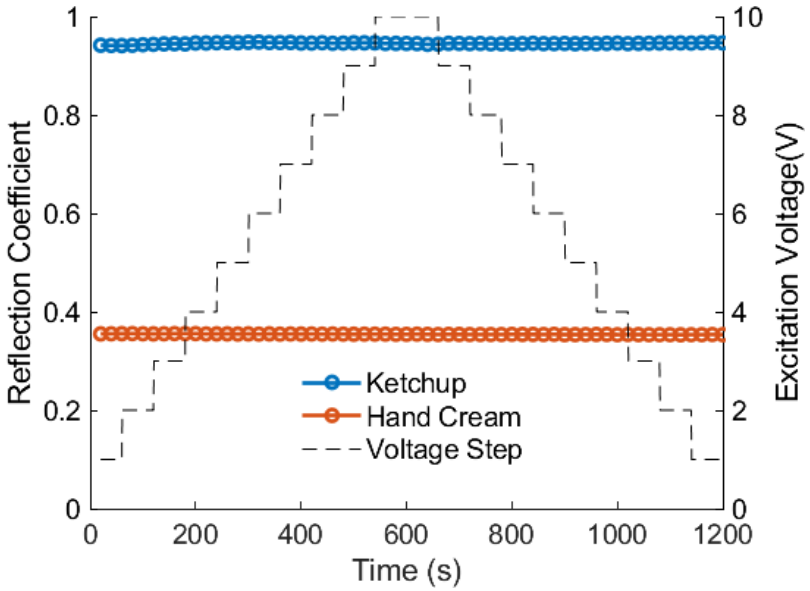

Figure 8.18: Reflection coefficient response of two household non-Newtonian samples for a 1MHz matching layer ultrasonic matching layer where the excitation voltage was varied from 0-10V.

Any small variation in the reflection coefficient value is not synchronous with the voltage steps and is not mirrored at $Time = 600s$. Therefore, any variation is more likely to be due to external factors, such as electrical noise.

Again, the constant reflection coefficient may be explained by the voltage increase having a negligible effect on the shear rate. Figure 8.7 shows an increase in a voltage of 10V would lead to a velocity increase from 2.7 to 3.3 mm/s. For the non-Newtonian sample $EAL\#5$, using Equation 6.34 , the shear rate will increase from 2.84×10^5 to $3.48 \times 10^5 s^{-1}$. This increase in shear rate will cause the viscosity to decrease by approximately 5cP which may not be large enough to observe a change in the reflection coefficient.

Although a change in reflection coefficient was not captured for a change in excitation voltage, this does not mean that the velocity does not have to be considered when calculating the shear rate.

8.4 Experimental Comparison of Oscillatory and Steady Shear Measurements at High Shear Rates

In this investigation, the viscosity of two non-Newtonian EAL samples was measured using a multiple frequency matching layer viscometer and compared with viscosity measurements using a high shear rotational viscometer.

8.4.1 Test Samples

In open literature there is very limited viscosity information of non-Newtonian oil samples that have been tested using a steady shear viscometer at shear rates comparable to the high shear rates produced by the matching layer ultrasonic viscometer.

An exception to this is two non-Newtonian samples that have been characterised by Borras et al. (2018) over a range of shear rates using a steady shear viscometer. These two samples are EALs, Environmentally Acceptable Lubricants, which are lubricants that are less toxic than their counterparts, making them a more viable option in applications where the lubricant is released into the environment. For consistency, the naming notation is carried through from previous report by Borras et al. (2018), where they are identified as $EAL\#4$ and $EAL\#5$. Information regarding these non-Newtonian samples is presented in Table 8.3 and was supplied by Borras et al. (2018).

Lubricant Sample	Classification	Base Oil	Viscosity @ $40°C (mm^2/s)$	VI
$EAL\#4$	EAL	PAO	68	205
$EAL\#5$	EAL	PAO	100	225

Table 8.3: Samples tested. Details from Borras et al. (2018).

Borras measured the density of the samples using a Stabinger viscometer SVM 3000 and found that the density varies linearly with temperature and can therefore be calculated using Equation 8.8. The variables for this equation are presented in Table 8.4. It is assumed that the density of a sample is independent of shear rate.

$$\rho_T = \rho_{T0} + k(T - T_0) \tag{8.8}$$

Lubricant	k	$\rho_{T0} = 0°C$	R^2
$EAL\#4$	-0.649	874.02	0.99
$EAL\#5$	-0.645	872.95	0.99

Table 8.4: Coefficient from linear fitting density and temperature. (Borras et al., 2018)

8.4.2 Multiple Frequency Matching Layer Viscometer Apparatus and Method

A multiple frequency ultrasonic matching layer viscometer was connected to an arbitrary function generator, an amplifier, a Picoscope and a PC in the configuration shown in Figure 8.11. An amplifier was selected over the Picoscope for signal generation as it allowed for greater control of the excitation voltage. The amplifier used was an AIM-TTI Instruments TG5011, chosen, as in previous experiments, it did not produce a voltage offset. The viscosity of the two EAL samples was measured at $25°C$, using the input excitation settings detailed in Table 8.5, and the measurement technique and signal processing were completed using the methodology detailed in Chapter 7.

Frequency	1MHz	2MHz	5MHz	10MHz
Number of Caputures	100	100	100	100
Timestep (ns)	2	2	2	2
Excitation Type	Sine	Sine	Sine	Sine
Number of Cycles	8	10	10	10
Excitation Voltage (V)	10	10	10	10

Table 8.5: Excitation signal settings.

8.4.3 Multiple Frequency Matching Layer Viscometer Results

The results for this investigation are presented in Figure 8.19, and as expected for a shear-thinning fluid, the viscosity decreases with increasing frequency. It should be noted that in all future viscosity measurements the units are cP, and is chosen due to its widespread use in industry.

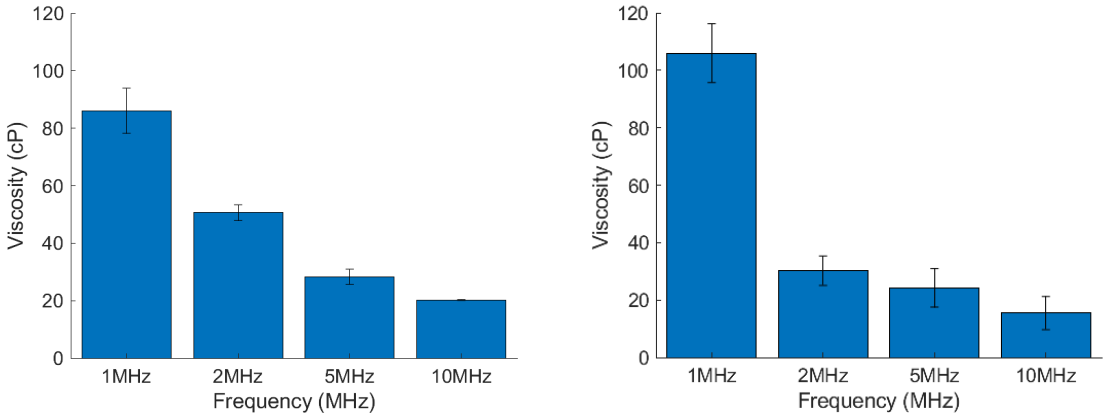

(a) $EAL\#4$ (b) $EAL\#5$

Figure 8.19: EAL viscosity measurements completed over a range of frequencies using the multiple frequency matching layer viscometer.

The reflection coefficient and velocity information was manipulated using the viscosity model, Equation 5.30, velocity model, Equation 8.5, and shear rate model, Equation

6.34 to obtain the viscosity and shear rate information, Figure 8.20. This figure shows that by experimentally obtaining the reflection coefficient and velocity information, the shear rate viscosity information for a fluid can be found using the models listed. The relaxation time was presumed to be shorter than 2×10^{-8}s as has previously been measured for base oils and viscosity modifiers (Schirru, 2016).

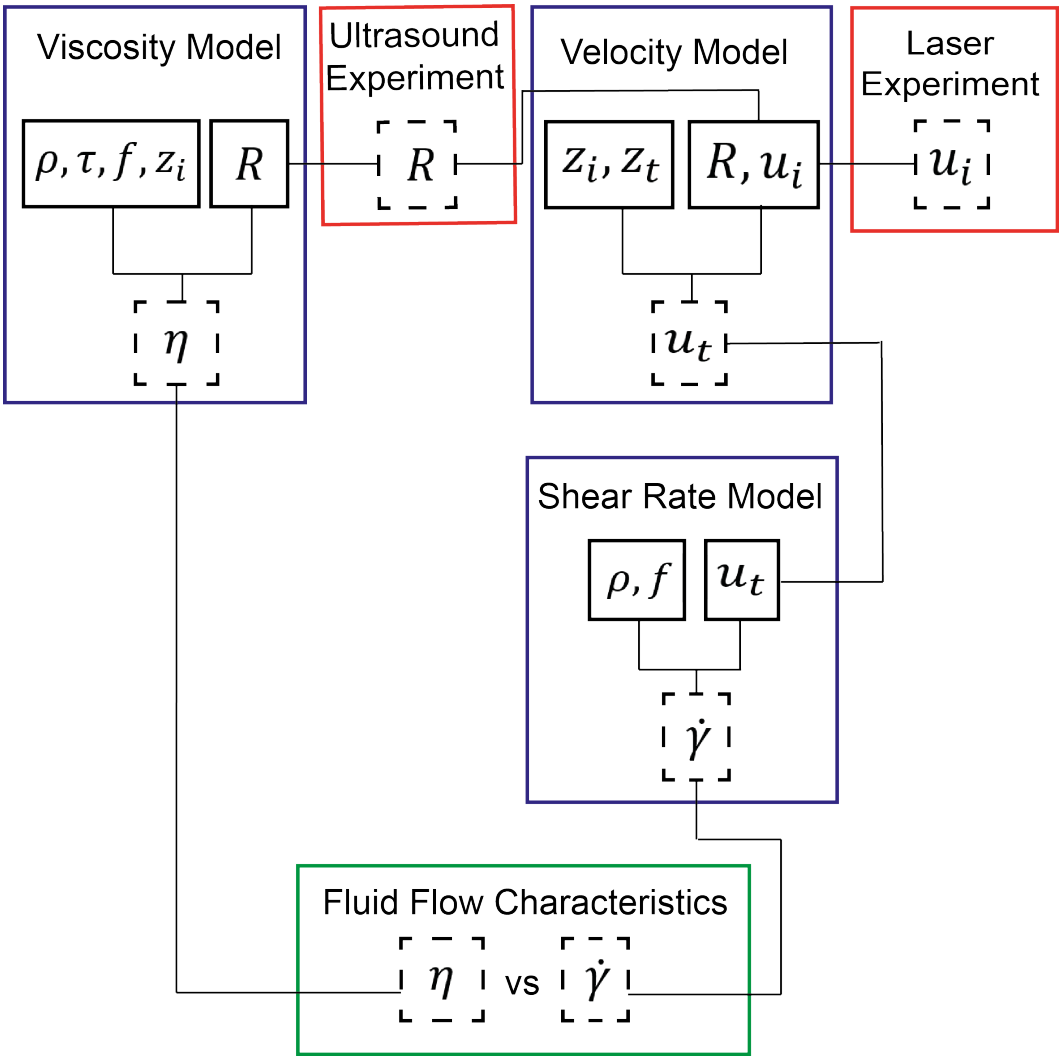

Figure 8.20: Relationship between the viscosity model, Equation 5.30, velocity model, Equation 8.5, and shear rate model, Equation 6.34.

The density value at $25°C$ was calculated and used to find the shear rate using Equation 6.34, and this is presented in Table 8.6. In this calculation, it is assumed that the velocity of the aluminium block is constant regardless of the fluid placed on top, with any damping effects negligible.

Lubricant Sample	Frequency (MHz)	Kinematic Viscosity	Velocity (mm/s)	Shear Rate (1/s)
EAL#4	1	100.4	2.1	521.4
EAL#4	2	59	3.8	1741.3
EAL#5	1	123.7	2.1	469.7
EAL#5	2	35.3	3.8	2252.5

Table 8.6: Shear rates exerted on test samples from the ultrasonic viscometer, calculated using Equation 6.34.

8.4.4 Steady Shear Viscometer Results

Borras et al. (2018) completed oscillatory shear measurements over a broad range of shear rates, using a Brookfield viscometer for low shear measurements and a PCS Ultra Shear Viscometer, USV, for high shear measurements. Figure 8.21 shows the steady shear viscosity measurements of the two EAL samples. The torque limitation of the USV means that high shear rate measurements are carried out at a greater temperature.

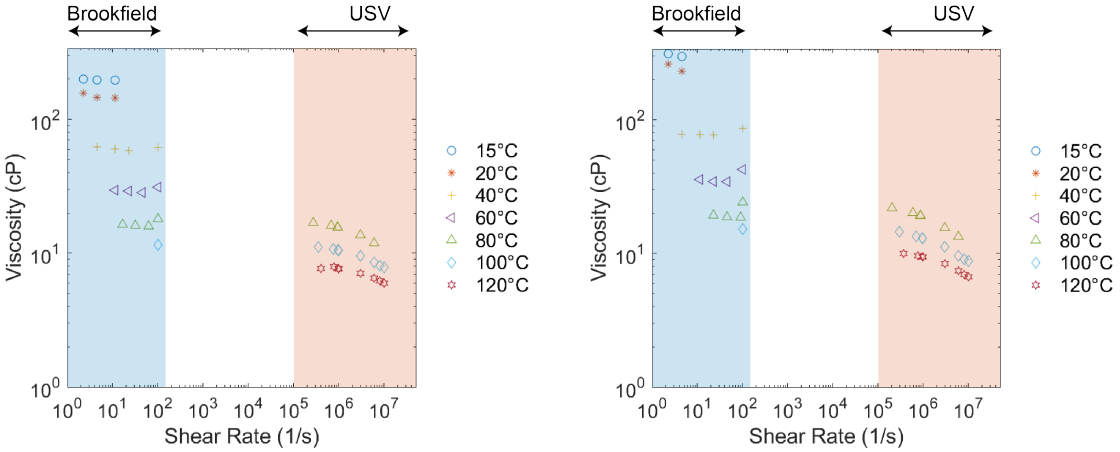

(a) *EAL#4* (b) *EAL#5*

Figure 8.21: Steady shear viscosity measurements completed using the Brookfield and USV (Borras et al., 2018).

For a shear-thinning fluid, the viscosity shear rate relationship can be fitted using the Carreau-Yasuda model (Yasuda et al., 1981), Equation 2.13. This fit requires the viscosity measurements at different shear rates to be known at a single temperature. Using ASTM D341, the low shear rate measurements were calculated at 80°C, 100°C and 120°C - the temperature at which the high shear rate measurements were completed. Figure 8.22 shows the viscosity of two non-Newtonian samples plotted against shear rate for three temperatures. The constants of these fits were generated by using the MATLAB *Curve Fitting* application and are noted in Table 8.7. The constant, η_∞, suggests that both test samples have the same base oil, as the viscosity of the second Newtonian plateau is the same across all temperatures.

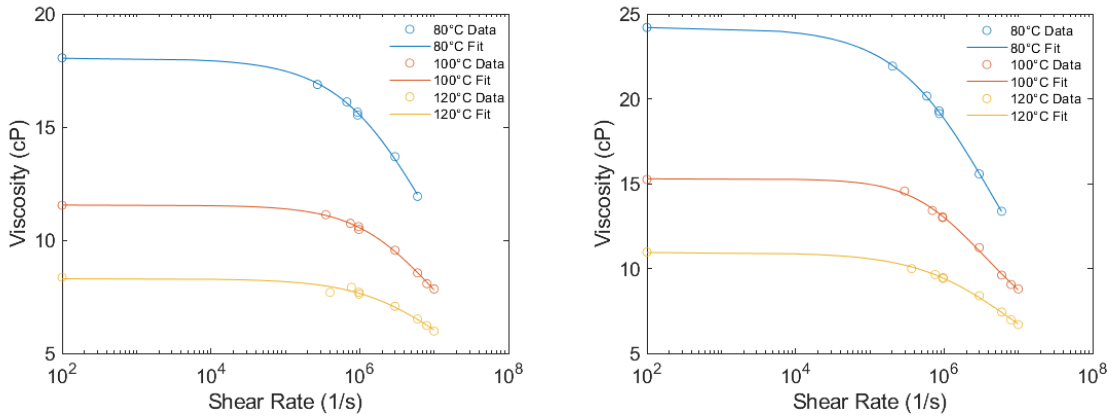

(a) *EAL#4* (b) *EAL#5*

Figure 8.22: Steady shear viscosity measurements where the low temperature measurements have been transformed to temperatures at which the high shear measurements were completed.

	EAL#4			*EAL#5*		
	80°C	100°C	120°C	80°C	100°C	120°C
a	0.721	0.842	0.7525	0.681	1.01	0.7018
λ	1.89E-07	1.80E-07	1.14E-07	3.50E-07	8.59E-07	2.01E-07
n	0.5	0.525	0.5	0.5	0.6761	0.5
η_∞	3	2.66	2.5	2.974	2.66	2.5
η_0	18.04	11.55	8.3	24.21	15.28	10.94
R	0.9987	0.9987	0.98	0.9998	0.998	0.9973

Table 8.7: Fitting parameters for the Carreau-Yasuda fit for the viscosity shear rate relationship.

In previous studies (Vladescu et al., 2018)(Marx et al., 2018), the Carreau-Yasuda fit has successfully been reduced to a single curve across different temperatures, where the shear stability index, Equation 8.9 replaces the viscosity, and the reduced shear rate replaces the shear rate, Equation 8.10 . Figure 8.23 shows the viscosity data in Figure 8.22 transformed using this approach.

$$SSI = \frac{\eta - \eta_\infty}{\eta_0 - \eta_\infty} \tag{8.9}$$

$$a_T = \frac{[\eta_0 - \eta_\infty]_T}{[\eta_0 - \eta_\infty]_{T_R}} \times \frac{T_R}{T} \tag{8.10}$$

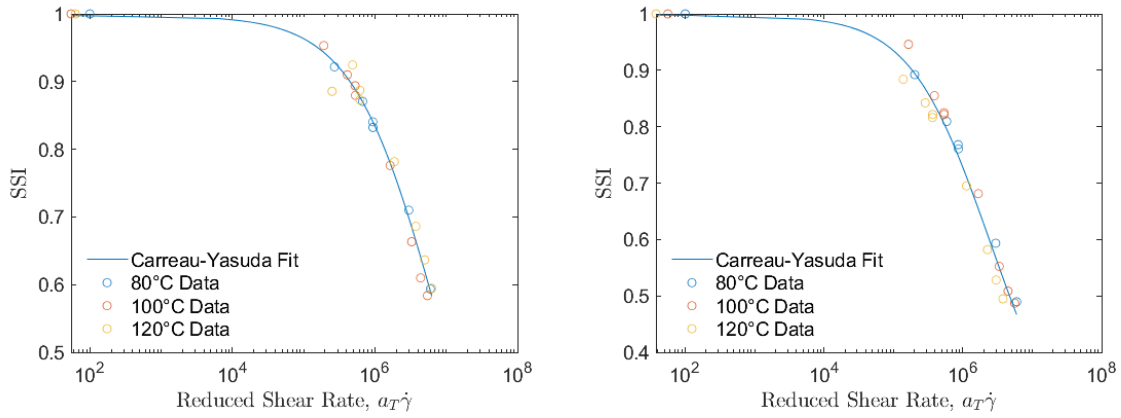

(a) *EAL#4* (b) *EAL#5*

Figure 8.23: Reduced shear rate viscosity plot for EAL#4 and EAL#5 measured using steady shear viscometers.

As the data points all lie on the Carreau-Yasua fit it can be assumed that the samples are thermally stable across the temperature range $80°C$ - $120°C$. This transformation allows for the determination of the viscosity at any temperature and shear rate when the low shear rate viscosity, η_0, and high shear rate viscosity, η_∞, at the temperature of interest, T, and reference temperature, T_R, is known. The fitting parameters of this plot are shown in Table 8.8.

	EAL#4	*EAL#5*
a	0.761	0.7291
λ	2.172e-7	4.762e-7
n	0.5005	0.5004
η_∞	0.0001	0.01
η_0	0.9981	0.9978
R	0.99	0.98

Table 8.8: Fitting parameters for the Carreau-Yasuda fit for the reduced shear rate curve.

8.4.5 Experimental Comparison of Viscosity Measurements for the Ultrasound Viscometer and USV

By finding the viscosity of the samples at $25°C$ using Figure 8.19, a plot is produced that combines the viscosity measurements completed by the steady shear viscometers and the multiple frequency matching layer viscometer, Figure 8.24. The viscosity from the ultrasonic viscometer was plotted against the shear rate using Stokes's second problem, which relates the shear rate with the excitation frequency, velocity and viscosity of the test fluid, and the Cox-Merz rule, which relates the shear rate solely with the excitation frequency.

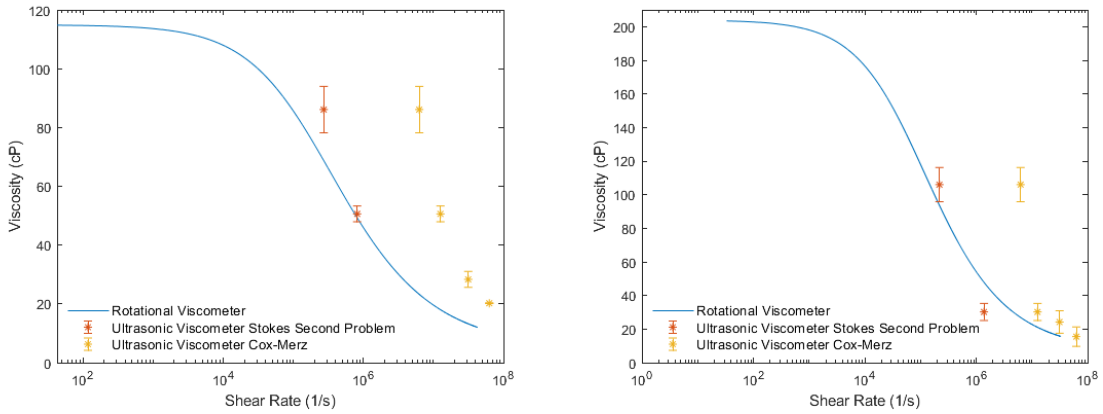

(a) *EAL#4* (b) *EAL#5*

Figure 8.24: Viscosity measurements of EAL samples measured using steady shear and oscillatory viscometers.

For EAL#4, the viscosity when using the shear rate from Stokes' second problem is slightly greater than the results obtained using the conventional viscometer. For EAL#5, the shear rate for the viscosity measurements using the 1MHz sensor is slightly greater than the measurements from the rotational viscometer, but the viscosity measured using the 2MHz transducer is lower. For both non-Newtonian samples, the viscosity measurements are more similar to the steady shear viscosity measurements when using the shear rate from Stokes' second problem compared to the Cox-Merz model.

The main factors which may lead to disparities between the steady shear results and the oscillatory results can be split into three sections; viscosity measurements when using the multiple frequency matching layer viscometer, conversion to different temperatures and shear rates using the Carreau-Yasuda equation, the shear rate calculation when using Stokes' second problem.

The main uncertainties in viscosity measurements using the multiple frequency matching layer viscometer arise when assuming the relaxation time of the non-Newtonian samples. For this investigation, it has been assumed that the relaxation time is very short and therefore does not affect the viscosity measurements. If the relaxation time increases, the viscosity measurements will decrease, Figure 5.14b. This assumption will have a greater importance when completing viscosity measurements at higher frequencies, where the relaxation time has a greater effect.

Another area of uncertainty is when applying Stokes' second problem to calculate the shear rate, as it is a Newtonian model. For both these oil samples, we know that they are shear-thinning non-Newtonian oils. The derivation of Cox-Merz to analyse Stokes' second problem for a non-Newtonian fluid has previously been investigated and has been found that the magnitude of the shear rate is affected by the fluid models chosen and is mathematically complex (Ai and Vafai, 2005).

A further assumption made is that the oil samples behave in the same way at $25°C$ and therefore the Cox-Merz rule can be used at all temperatures. This assumption may by untrue and if so it is possible that as the temperature reduces, the viscosity shear thins at an increased rate. In future investigations, as it is impossible to reduce the temperature of the oils when testing using the Couette viscometers to remain within the allowable torque range, viscosity measurements should be completed at higher temperatures using the multiple frequency matching layer viscometer.

To fully understand the measurement using the ultrasound matching layer viscometer, it is necessary to discuss the relationship between the shear displacement amplitude and the molecule size. For oils that contain polymer molecules, these molecules may be equal to or even larger than the size of the displacement from the ultrasound shear wave. This is unlike conventional viscometers, where the displacement is orders of magnitude greater than the size of the molecules. Therefore, for the ultrasound shear viscometer, the displacement may cause the polymers only partially to shear, as shown in Figure 8.25. This may lead to a value for the viscosity measurements that is greater than is expected for the high shear rate, as the molecule has not been fully untangled. This relationship between shear and displacement is not well understood, and further research is required to understand this relationship.

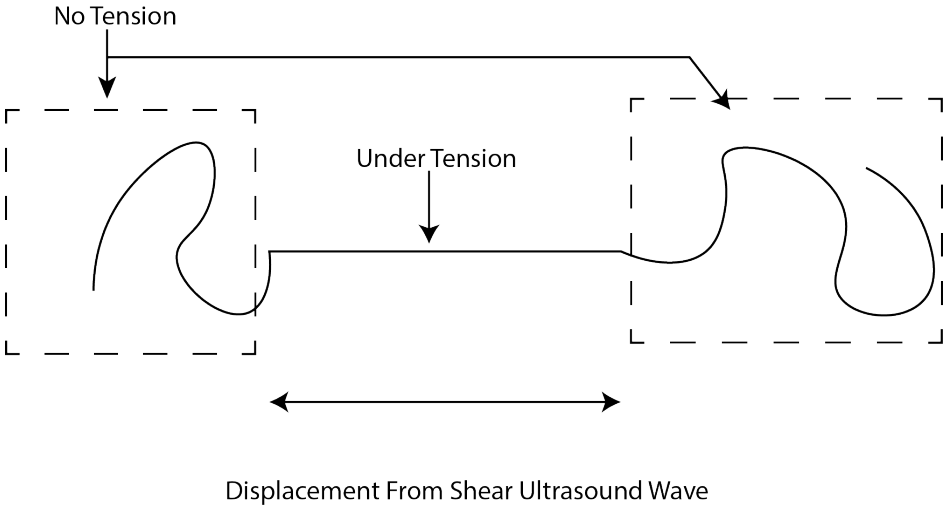

Figure 8.25: Small amplitude shear mechanism sketch for a polymer molecule.

Further work needs to be completed to verify this relationship, including measurements of the velocity at higher shear rates and comparison of shear and oscillatory measurements for a greater number of oil samples.

	Non-Newtonian #1	Non-Newtonian #2	Non-Newtonian #3	Non-Newtonian #4
a	0.3255	0.2065	0.2	0.3063
λ	1e-8	1e-8	1e-8	1e-8
n	0.3	0.2	0.2	0.1
η_∞	20.94	24.09	11.95	3.16
η_0	111	45.72	12.6	93.11

Table 8.10: Non-Newtonian Carreau-Yasuda fit parameters.

8.5 Non-Newtonian Shear Rate Measurements Using Steady Shear and Oscillatory Viscometers

Through understanding the shear rate of the multiple frequency matching layer viscometer, the non-Newtonian oil solutions plotted in Figure 7.19, can be plotted in a scatter plot rather than a box plot, Figure 8.26. The information regarding these non-Newtonian oil samples has been reprinted in Table 8.9 and the fit parameters are shown in Table 8.10.

Non-Newtonian Solution ID	Base Oil	Base Oil (%)	DMA (%)
#1	PAO40	70	30
#2	PAO40	50	50
#3	PAO40	30	70
#4	PAO100	50	50

Table 8.9: Non-Newtonian oil sample information.

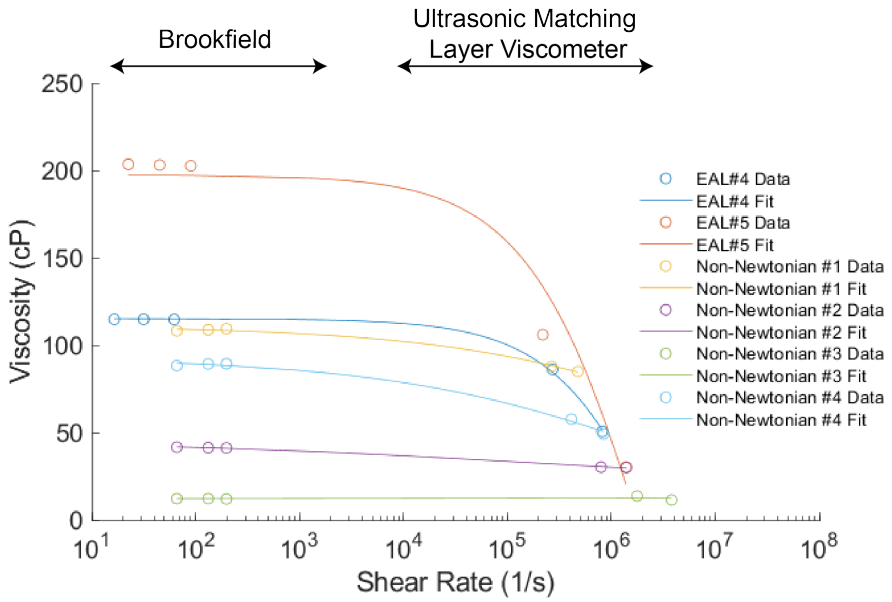

Figure 8.26: Reflection coefficient response for several Newtonian and non-Newtonian solutions, measured using the multiple frequency matching layer viscometer.

Using the *Curve Fitting* application from MATLAB allows the Carreau-Yasuda model constants to be determined. For oils with different concentrations and different

base oils, the shear rate at which the first Newtonian plateau ends and the transition zone begins varies, as does the gradient of the transition zone.

Figure 8.26 illustrates that as the viscosity decreases, the shear rate at which the oil is subjected to increases. This shear rate variation demonstrates the difficulty of using an ultrasonic viscometer at a specified shear rate; it is impossible to complete measurements at a selected shear rate without full knowledge of the kinematic viscosity of the oil, the velocity that the transducer will force the oil to move, and the frequency. However, the shear rate can be tuned by varying the frequency, as shown by Figure 7.17, when the bandwidth of the transducer is suitably large.

The plot further shows an extensive shear rate range between the Brookfield viscosity measurements and the ultrasonic shear rate measurements, where no viscosity measurements are completed. In future work, investigations should be completed to use the ultrasonic viscometer at lower frequencies to allow for viscosity measurements at lower shear rates.

This shear rate relationship allows for viscosity measurements of steady and oscillatory measurements completed by the ultrasonic viscometer to be plotted on a common axis, which illustrates the importance of this work.

8.6 Summary

The shear rate of an ultrasonic matching layer viscometer was experimentally determined by measuring the input parameters of the shear rate equation derived from Stokes' second layer.

The first set of experiments determined the velocity of the oil sample. It was not possible to directly measure the velocity of the fluid. Therefore, to determine this parameter, the velocity of the plate, which the oil was in contact with, was measured. By manipulating the reflection coefficient equation, and the acoustic impedance equation, the velocity of the fluid was indirectly calculated. The velocity of the fluid changes depending upon the viscosity of the fluid, the acoustic impedance, and the excitation voltage. For the two EAL samples, it was found to measure 1.6mm/s – 27mm/s when the excitation voltage was increased from 9V - 320V.

The second investigations monitored the reflection coefficient as the excitation voltage varied from 0-180V. This experiment was repeated using two amplifiers to validate the measurements. For all oil samples, Newtonian and non-Newtonian, the reflection coefficient was independent of the viscosity over the excitation voltage range applied. This result was expected as the large increase in excitation voltage caused a small change to the magnitude of the shear rate.

Finding the input parameters allowed for the shear rate to be determined for the ultrasonic matching layer viscometer. This shear rate was then compared to the viscosity measurements from steady shear viscometers after the measurements had been processed using a series of temperature conversions, Carreau-Yasuda fits and normalisation.

8.7 Conclusion

The viscosity measurements from the ultrasonic matching layer viscometers are similar to the viscosity measurements completed by the steady shear viscometers, validating the application of Stokes' second problem to determine the shear rate.

Chapter 9

Conclusions

This chapter provides a brief outline of the work that has been completed in this thesis and key findings. The chapter has been split up into three sections; the instrumentation and optimisation of a multiple frequency matching layer viscometer, the development and evaluation of a three-layered model that enables the viscosity of a lubricating oil to be found and the development and evaluation of a model to determine the shear rate subjected to the lubricating oil from the matching layer viscometer. Finally, the possible future directions of this research is discussed.

9.1 Novelty Statement

It is essential to understand the viscosity of lubricating over a range of high shear rates, to understand how the oils perform in-situ. This can either be completed using ex-situ viscometers where the harsh operating conditions from an engine are replicated or by completing measurements using an in-situ viscometer. This thesis adapted an in-situ ultrasound viscometer to complete measurements as it allows for sensitive measurements over a broad range of shear rates. A novel ultrasonic viscometer was built using varying frequency transducers and multiple thickness matching layers to allow for sensitive measurements to be completed over 1-10MHz. Furthermore, a novel mathematical model has been developed using the Newtonian and Maxwell model for Newtonian and non-Newtonian fluids to retrieve the viscosity information from the ultrasound shear wave. In addition to this, a second novel mathematical model has been adapted from Stokes' second problem to understand the shear rate exerted on the lubricating oil. By combining these novel aspects, viscosity shear rate measurements were successfully acquired for Newtonian and non-Newtonian lubricating oils using a novel viscometer.

9.2 Hardware and Method Advancements

9.2.1 Instrumentation and Optimisation of a Multiple Frequency Matching Layer Viscometer

To obtain the reflection coefficient at different shear rates it was necessary to instrument a multiple frequency matching layer viscometer. This viscometer was instrumented with four different frequency transducers, 1MHz, 2MHz, 5MHz and 10MHz, and four corresponding thickness matching layers. In future work this frequency range should be expanded, where it is expected that the limiting factor will either be the thickness of the transducer, or the thickness of the matching layer.

This viscometer was then optimised by inspecting the reflection coefficient of calibration oils with a range of viscosities, $16 - 1300cP$, as different input signal settings were varied. The main findings of these investigations were: increasing the cycle number reduced the measurement error, whether a chirp or sine wave was chosen did not have an affect on the reflection coefficient, and if exciting across a frequency range close to the central frequency of the transducer, the reflection coefficient remained constant.

Using this multiple frequency matching layer viscometer Newtonian and non-Newtonian samples that had a low shear viscosity, between $12 - 108cP$, were measured. The results were compared with measurements completed on a low shear Couette viscometer. The Newtonian fluid had a consistent viscosity across both measurement techniques as was expected, and the non-Newtonian fluid decreased in viscosity as the frequency increased, which again was expected.

9.3 Mathematical Model Advancements

9.3.1 Development and Evaluation of a Three-Layered Ultrasonic Model for non-Newtonian Fluids

To complete viscosity measurements it is necessary to correlate the measured reflection coefficient with the viscosity of the fluid.

The models were developed by defining the relationship between a materials acoustic impedance and the shear wave reflection coefficient. The acoustic impedance was then related to the fluids Newtonian and non-Newtonian viscosity by using a Newtonian and Maxwell model, respectively.

This model also aided in understanding the influence that different parameters pose on the measurement technique. The notable findings included: the system had maximum sensitivity when the matching layer thickness was $\lambda/4$, and identifying potential difficulties when completing measurements at low frequencies due to low sensitivity. It was also shown that at short relaxation times the non-Newtonian rheological model

reduced to the Newtonian model. To increase the accuracy of the mathematical model and ore accurately describe lubricating oils, more complex non-Newtonian fluid models could be used that allow for multiple relaxation times.

Using the multiple frequency matching layer viscometer, viscosity measurements were completed at room temperature on Newtonian calibration oils that ranged in viscosity from $16 - 710cP$. By comparing the measurements with the low shear Couette viscosity results the models were validated for all frequencies. It was found that any variation between the measurement and the model was dependant on the sensor. To eliminate this the input parameters of the model were tuned, which increased the coefficient of determination value, for example the 2MHz sensor R^2 value increased from 0.92 to 0.99.

9.3.2 Development of a Shear Rate Model for a Matching Layer Shear Ultrasound Viscometer

To use the matching layer viscometer for measurements of non-Newtonian fluids, it is vital to understand the shear rate that the viscometer exerts on the lubricating oil. From previous work, the Cox-Merz rule was not able to accurately relate the shear rate for oscillatory and steady shear measurements, especially at high shear rates. Using Stokes' second problem, a model was developed to find the shear rate for an oscillatory system and was further modified to include the velocity when the oil was subjected to an oscillating shear wave. A sensitivity analysis was completed to compare different input parameters with the velocity profile, shear rate profile and maximum shear rate. This model proposed that the maximum shear rate was dependent on the viscosity of the oil and the velocity and frequency that it was oscillating. In contrast, the Cox-Merz rule states that the shear rate is only dependant on the frequency.

9.4 Evaluation of Hardware and Model Advancements

9.4.1 Evaluation of a Shear Rate Model for a Matching Layer Shear Ultrasound Viscometer

To evaluate the shear rate from Stokes' second problem, it was necessary to know the viscosity of the oil and the frequency and velocity that it was oscillating.

The first parameter inspected was the velocity of the fluid. This was completed indirectly by measuring the velocity of a reflective elastic surface subjected to the shear wave and then finding the velocity of the fluid by using the relationship between pressure, velocity, and acoustic impedance. When completing this investigation, there was a direct positive correlation between the excitation voltage and velocity. This

was further examined by increasing the excitation voltage and completing viscosity measurements using the matching layer viscometer on Newtonian and non-Newtonian fluids. It was observed that there was no change in the reflection coefficient which was thought to be due to the increase in excitation voltage not causing a significant enough change in the shear rate, 2.84×10^5 - $3.48 \times 10^5 s^{-1}$ for sample EAL # 5 measured from 1 - $10V$.

The viscosity of two EAL samples was measured using the multiple frequency matching layer viscometer, and the results were compared to viscosity results completed on an ultra-shear Couette viscometer. To allow for comparison, the results obtained by the ultra-shear Couette viscometer were manipulated to find the viscosity at a range of temperatures and shear rates. When comparing the viscosity measurements obtained with the ultrasonic viscometer, the results were plotted using the shear rate from Stokes' second problem and the Cox-Merz rule. It was found that the shear rate measurements from Stokes' second problem provided a better correlation. This was completed for a limited number of lubricating oils and therefore to confidently conclude that the shear rate from Stokes' second problem is accurate further samples need to be tested over a greater frequency range.

9.5 Future Directions

The following list shows potential directions for future work and has been split into the two sections hardware and methods, modelling, and further work required to analyse models.

9.5.1 Hardware and Methods

- Complete measurements over a greater range of shear rates. This could be completed by either increasing the frequency range or a more significant change in velocity by further increasing the excitation voltage.

- Investigate the use of transducers that have an extensive bandwidth. This would allow for sensitive viscosity measurements to be completed at various shear rates, with a single transducer and matching layer. This would miniaturise the technology, making it more suitable for in-situ applications.

- Installation in-situ. A matching layer viscometer has previously been installed in a journal bearing (Schirru and Dwyer-Joyce, 2016) and a lubricant line (Manfredi et al., 2019), however further investigations are required to understand how the viscometer performance when subjected to the harsh environment of an engine.

9.5.2 Modelling

- Development of a shear rate model for non-Newtonian fluids. In this thesis, the model developed derives the shear rate from Stokes's second problem, which is applicable for Newtonian fluids. A non-Newtonian model is much more mathematically complex but would allow for a better representation of the measured shear rate.

9.5.3 Evaluation of Models

- Measure the velocity of transducers that pulse with a frequency greater than 3MHz. The laser vibrometer encoder determines this limiting factor. Using different hardware would allow for velocity measurement at a higher frequency, and the viscosity shear rate curve could be extended, further verifying the shear rate model.

- Further validation of the velocity measurement could be obtained by directly measuring the velocity of the fluid, which would remove the need for conversion from the reflective surface using the acoustic impedance relationship. This could be achieved by using a laser vibrometer where the emitter and receiver can be separated.

- To further verify the shear rate model, a greater number of lubricating oils tested using the multiple frequency matching layer viscometer needs to be compared to viscosity results obtained using a steady shear viscometer. This would also aid in further verification of the three-layered non-Newtonian model.

- Complete ultrasound measurements at elevated temperatures. This would allow a direct comparison between the viscosity measurements completed using the ultra-shear Couette viscometer, removing error when completing a temperature conversion.

References

A&D Company (2009). Sine-Wave Vibro Viscometer User's Handbook. Technical report, A&D, Tokyo.

Ai, L. and Vafai, K. (2005). An investigation of stokes' second problem for non-Newtonian fluids. *Numerical Heat Transfer; Part A: Applications*, 47(10):955–980.

Al-Hadithi, T. S., Barnes, H. A., and Walters, K. (1992). The relationship between the linear (oscillatory) and nonlinear (steady-state) flow properties of a series of polymer and colloidal systems. *Colloid & Polymer Science*, 270(1):40–46.

Alig, I., Lellinger, D., Sulimma, J., and Tadjbakhsch, S. (1997). Ultrasonic shear wave reflection method for measurements of the viscoelastic properties of polymer films. *Review of Scientific Instruments*, 68(3):1536–1542.

API (2015). API Base Oil Interchangeability Guidelines For Passenger Car Motor Oils And Diesel Engine Oils. Technical report, API.

Ash, D. C., Joyce, M. J., Barnes, C., Booth, C. J., and Jefferies, A. C. (2003). Viscosity measurement of industrial oils using the droplet quartz crystal microbalance. *Measurement Science and Technology*, 14(11):1955–1962.

ASTM (2014). E1065/E1065M: Standard Practice for Evaluating Characteristics of Ultrasonic Search Units. Technical report, ASTM.

ASTM (2017). ASTM D341-17 Standard Practice for Viscosity-Temperature Charts for Liquid Petroleum Products. Technical Report July, ASTM.

ASTM (2018). ASTM D2196-18e1 Standard Test Methods for Rheological Properties of Non-Newtonian Materials by Rotational Viscometer. Technical Report June, ASTM.

ATC Europe (2016). Lubricant Additives Use and Benefits. Technical report, ATC, Brussels.

Bair, S. (2015). The First Normal Stress Difference in a Shear-Thinning Motor Oil at Elevated Pressure. *Tribology Transactions*, 58(4):654–659.

Bair, S., Yamaguchi, T., Brouwer, L., Schwarze, H., Vergne, P., and Poll, G. (2014). Oscillatory and steady shear viscosity: The Cox-Merz rule, superposition, and application to EHL friction. *Tribology International*, 79:126–131.

Barlow, A. J. and Lamb, J. (1959). The Visco-Elastic Behaviour of Lubricating Oils under Cyclic Shearing Stress. *Proceedings of the Royal Society A: Mathematical, Physical and Engineering Sciences*, 253(1272):52–69.

Barlow, A. J. and Subramaniam, S. (1966). Experimental technique for the determination of the viscoelastic properties of liquids in the frequency range 5-75 Mc/s. *Brit. J. Appl. Phys.*, 17:1201–1214.

Bartz, W. J. (1976). About the influence of viscosity index improvers on the cold flow properties of engine oils. *Tribology International*, 9(1):13–20.

Barus, C. (1893). Isothermals, isopiestics and isometrics relative to viscosity. *American Journal Science*, 45:87–96.

Belmiloud, N., Dufour, I., Colin, A., and Nicu, L. (2008). Rheological behavior probed by vibrating microcantilevers. *Applied Physics Letters*, 92(4).

Blaauwgeers, R., Blazkova, M., Človevčko, M., Eltsov, V. B., de Graaf, R., Hosio, J., Krusius, M., Schmoranzer, D., Schoepe, W., Skrbek, L., Skyba, P., Solntsev, R. E., and Zmeev, D. E. (2007). Quartz tuning fork: Thermometer, pressure- and viscometer for helium liquids. *Journal of Low Temperature Physics*, 146(5-6):537–562.

Borras, F. X., de Rooij, M. B., and Schipper, D. J. (2018). Rheological and wetting properties of Environmentally Acceptable Lubricants (EALs) for application in stern tube seals. *Lubricants*, 6(4).

Bradley, D. I., Človečko, M., Gažo, E., and Skyba, P. (2008). Probing Andreev reflection in superfluid 3He-B using a quartz tuning fork. *Journal of Low Temperature Physics*, 152(5-6):147–155.

Brekhovskikh, L. (1980). *Waves In Layered Media*. Elsevier Science, 2nd edition.

Brookfield Engineering (2019). DVNext Cone/Plate Rheometer.

Buiochi, F., Franco, E. E., Higuti, R. T., and Adamowski, J. C. (2006). Viscosity measuring cell using ultrasonic wave mode conversion. *Ferroelectrics*, 333(1):139–149.

Cheeke, J. D. N. (2017). *Fundamentals and applications of ultrasonic waves, second edition*. CRC Press.

Cheng, D. C. and Davis, J. B. (1969). An automatic on-line viscometer for the measurement of non-Newtonian viscosity for process control applications. *Rheologica Acta*, 8(2):161–173.

Chung, P. L. (1973). A linear oscillatory viscometer. *Review of Scientific Instruments*, 44(11):1669–1670.

Clubb, D. O., Buu, O. V., Bowley, R. M., Nyman, R., and Owers-Bradley, J. R. (2004). Quartz tuning fork viscometers for helium liquids. *Journal of Low Temperature Physics*, 136(1-2):1–13.

Cohen-Tenoudji, F., Pardee, W. J., Tittmann, B. R., Ahlberg, L. A., and Elsley, R. K. (1987). A Shear Wave Rheology Sensor. *IEEE Transactions on Ultrasonics, Ferroelectrics, and Frequency Control*, 34(2):263–269.

Connelly, R. W. and Greener, J. (1985). High-Shear Viscometry with a Rotational Parallel-Disk Device. *Journal of Rheology*, 29(2):209–226.

Costley, R. D., Balasubramaniam, K., Ingham, W. M., Simpson, J. A., and Shah, V. (1998). Torsional Waveguide Sensor for Molten Materials. In *Review of Progress in Quantitative Nondestructive Evaluation*, pages 859–866. Springer US.

Cox, W. P. and Merz, E. H. (1958). Correlation of dynamic and steady flow viscosities. *Journal of Polymer Science*, 28(118):619–622.

Curie, J. (1880). Developpement par compression de l'electricite polaire dans les cristaux hemiedres 'a faces inclinees. *Bulletin de la societe mineralogique de France*, 1(3):90–93.

Desilets, C. S., Fraser, J. D., and Kino, G. S. (1978). The Design of Efficient Broad-Band Piezoelectric Transducers. *IEEE Transactions on Sonics and Ultrasonics*, 25(3):115–125.

Divišová, H., Lang, J., Rotter, M., and Schmoranzer, D. (2012). Measurement of viscosity in small volumes of fluids by tuning fork oscillators. In *EPJ Web of Conferences*, volume 25.

Dontula, P., Macosko, C. W., and Scriven, L. E. (1999). Does the viscosity of glycerin fall at high shear rates? *Industrial and Engineering Chemistry Research*, 38(4):1729–1735.

Doraiswamy, D., Mujumdar, A. N., Tsao, I., Beris, A. N., Danforth, S. C., and Metzner, A. B. (1991). The Cox–Merz rule extended: A rheological model for concentrated suspensions and other materials with a yield stress. *Journal of Rheology*, 35(4):647–685.

Duda, J. L., Klaus, E. E., and Lin, S. C. (1988). Capillary viscometry study of non-newtonian fluids: Influence of viscous heating. *Industrial and Engineering Chemistry Research*, 27(2):352–361.

Eernisse, E. P., Ward, R. W., and Wiggins, R. B. (1988). Survey of Quartz Bulk Resonator Sensor Technologies. *IEEE Transactions on Ultrasonics, Ferroelectrics, and Frequency Control*, 35(3):323–330.

Emerson (2020). Micro Motion™ Fork Viscosity Meters. Technical report, Emerson.

Erickson, D., Lu, F., Li, D., White, T., and Gao, J. (2002). An experimental investigation into the dimension-sensitive viscosity of polymer containing lubricant oils in microchannels. *Experimental Thermal and Fluid Science*, 25(8):623–630.

Ferriss, D. and Quested, P. (2000). Some Comparisons of the Roscoe and Bechwith-Newell Analyses for the Determination of Viscosity of Liquid Metals using the Oscillating Cup Viscometer. Technical report, NPL.

Franco, E. E. and Buiochi, F. (2019). Ultrasonic measurement of viscosity: Signal processing methodologies. *Ultrasonics*, 91(September 2017):213–219.

Fujitsu, T. and Griffiths, J. (2006). Lubricating Oil Composition.

Galvin, G. D., Hutton, J. F., and Jones, B. (1981). Development of a high-pressure, high-shear-rate capillary viscometer. *Journal of Non-Newtonian Fluid Mechanics*, 8(1-2):11–28.

Giessibl, F. J. (1997). Forces and frequency shifts in atomic-resolution dynamic-force microscopy. *Physical Review B - Condensed Matter and Materials Physics*, 56(24):16010–16015.

Gleissle, W. and Hochstein, B. (2003). Validity of the Cox-Merz rule for concentrated suspensions. *Citation: Journal of Rheology*, 47:897.

Greenwood, M. S. and Bamberger, J. A. (2002). Measurement of viscosity and shear wave velocity of a liquid or slurry for on-line process control. *Ultrasonics*, 39(9):623–630.

Gupta, S. V. (2014). *Viscometry for Liquids*, volume 194. Springer, 1 edition.

Hadimioglu, B. and Khuri-Yakub, B. T. (1990). Polymer films as acoustic matching layers. In *Ultrasonics Symposium Proceedings*, volume 3, pages 1337–1340. Publ by IEEE.

Haller, M. I. and Khuri-Yakub, B. T. (1992). Composites for ultrasonic air transducers. In *Proceedings - IEEE Ultrasonics Symposium*, volume 1992-Octob, pages 937–939.

Hirayama, T., Shibata, S., Harada, T., Hashimoto, Y., and Yamashita, N. (2020). Shear property of oil film containing oiliness additive in narrow gap measured with newly-developed parallel-disk viscometer supported by aerostatic bearing. *Lubrication Science*, 32(2):46–57.

Infineum International Limited (2009). Infineum Insight | Moving to even lower viscosities.

ISO (2017). ISO 5577:2017: Non-destructive testing Ultrasonic testing Vocabulary. Technical report, ISO.

Izumo, N. (2013). Vibration Rheometer RV-10000. Technical report, A&D Company Ltd, Kitamoto City.

Jakoby, B., Beigelbeck, R., Keplinger, F., Lucklum, F., Niedermayer, A., Reichel, E. K., Riesch, C., Voglhuber-Brunnmaier, T., and Weiss, B. (2010). Miniaturized sensors for the viscosity and density of liquids - Performance and issues. *IEEE Transactions on Ultrasonics, Ferroelectrics, and Frequency Control*, 57(1):111–120.

Jung, H. and Gweon, D. G. (2000). Creep characteristics of piezoelectric actuators. *Review of Scientific Instruments*, 71(4):1896–1900.

Kalotay, P. (1999). Density and viscosity monitoring systems using Coriolis flow meters. *ISA Transactions*.

Kang, K., Lee, L. J., and Koelling, K. W. (2005). High shear microfluidics and its application in rheological measurement. *Experiments in Fluids*, 38(2):222–232.

Kawatra, S. K. and Bakshi, A. K. (1998). On-line measurement of slurry rheology in a thickener at a copper concentrator. *Minerals and Metallurgical Processing*, 15(4):37–40.

Keiji Kanazawa, K. and Gordon, J. G. (1985). The oscillation frequency of a quartz resonator in contact with liquid. *Analytica Chimica Acta*, 175(C):99–105.

Kim, J. O. and Bau, H. H. (1989). Instrument for simultaneous measurement of density and viscosity. *Review of Scientific Instruments*, 60.

Kinsler, L. and Frey, A. (1962). *Fundamentals of Acoustics*. New York:Wiley, 6th edition.

Kramer, J., Uhl, J. T., and Prud'Homme, R. K. (1987). Measurement of the viscosity of guar gum solutions to 50,000 1/s using a parallel plate rheometer. *Polymer Engineering and Science*, 27(8):598–602.

Kulmyrzaev, A. and Mcclements, D. J. (2000). High frequency dynamic shear rheology of honey. *Journal of Food Engineering*, 45(4):219–224.

Kumar, S., Mishra, N. M., and Mukherjee, P. S. (2005). Additives depletion and engine oil condition - A case study. *Industrial Lubrication and Tribology*, 57(2):69–72.

Li, X. (2018). *Measuring friction at an interface using ultrasonic response*. PhD thesis, University of Sheffield.

Liu, P., Lu, J., Yu, H., Ren, N., Lockwood, F. E., and Wang, Q. J. (2017). Lubricant shear thinning behavior correlated with variation of radius of gyration via molecular dynamics simulations. *Journal of Chemical Physics*, 147(8):84904.

Manfredi, O. F., Mills, R. S., Schirru, M. M., and Dwyer-Joyce, R. S. (2019). Non-invasive measurement of lubricating oil viscosity using an ultrasonic continuously repeated chirp shear wave. *Ultrasonics*, 94:332–339.

Marx, N., Fernández, L., Barceló, F., and Spikes, H. (2018). Shear Thinning and Hydrodynamic Friction of Viscosity Modifier-Containing Oils. Part II: Impact of Shear Thinning on Journal Bearing Friction. *Tribology Letters*, 66(3):1–11.

Marx, N., Ponjavic, A., Taylor, R. I., and Spikes, H. A. (2017). Study of Permanent Shear Thinning of VM Polymer Solutions. *Tribology Letters*, 65(3):106.

Mason, W. P., Baker, W. O., Mcskimin, H. J., and Heiss, J. H. (1949). Measurement of shear elasticity and viscosity of liquids at ultrasonic frequencies. *Physical Review*, 75(6):936–946.

Mason, W. P. and Mcskimin, H. J. (1947). Ultrasonic Attenuation Caused by Scattering in Polycrystalline Metals. *Citation: The Journal of the Acoustical Society of America*, 19:711.

Maxwell, J. C. (1865). A Dynamical Theory of the Electromagnetic Field Author (s): J . Clerk Maxwell Source : Philosophical Transactions of the Royal Society of London , Vol . 155 (1865), pp . 459- Published by : Royal Society Stable URL : http://www.jstor.org/stable/108892. *Transactions of the Royal Society of London*, 155(1865):459–512.

Merrill, E. W. (1954). A coaxial cylinder viscometer for the study of fluids under high velocity gradients. *Journal of Colloid Science*, 9(1):7–19.

Mriziq, K. S., Dai, H. J., Dadmun, M. D., Jellison, G. E., and Cochran, H. D. (2004). High-shear-rate optical rheometer. *Review of Scientific Instruments*, 75(6):2171–2176.

Nayfeh, A. H. (1988). Surface wave characteristics of fluid-loaded multilayered media. *Journal of the Acoustical Society of America*, 84(6):2187–2191.

Newman, P. G. and Rozycki, G. S. (1998). The history of ultrasound. *Surgical Clinics of North America*, 78(2):179–195.

Nguele, R., Al-Salim, H. S., and Mohammad, K. (2014). Modeling and forecasting of depletion of additives in car engine oils using attenuated total reflectance fast transform infrared spectroscopy. *Lubricants*, 2(4):206–222.

Nishizawa, O., Satoh, T., and Lei, X. (1998). Detection of shear wave in ultrasonic range by using a laser Doppler vibrometer. *Review of Scientific Instruments*, 69(6):2572–2573.

Palmer, R. (2001). DC Parameters: Input Offset Voltage. Technical report, Texas Instruments.

PCS Instruments (2018). USV Ultra Shear Viscometer. Technical report, PCS.

Peng and Hsu (2008). Analysis and measurement of stokes layer flows in an oscillating narrow channel. *Journal of Hydrodynamics*, 20(6):770–775.

Pollak, S., Hüttemann, S., Quiñones-Cisneros, S. E., and Weidner, E. (2017). Development and calibration of a high pressure high shear rate capillary rheometer. *Journal of Petroleum Science and Engineering*, 157:581–587.

Rabani, A., Pinfield, V. J., and Challis, R. E. (2016). Rate of shear of an ultrasonic oscillating rod viscosity probe. *Ultrasonics*, 65:18–22.

Ram, A. (1968). High Shear Viscometry. In F.R. Eirich, A. P., editor, *Rheology*, chapter High Shear. Academic Press, 4 edition.

Rao, S. S. (2018). Basic Equations of Fluid Mechanics. In *The Finite Element Method in Engineering*, pages 589–610. Elsevier.

RhenSense Inc. (2020). m-VROC Viscometer. Technical report, RheoSense.

Roth, W. and Rich, S. R. (1953). A new method for continuous viscosity measurement. General theory of the ultra-viscoson. *Journal of Applied Physics*, 24:940.

Rudnick, L. R. (2009). *Lubricant Additives : Chemistry and Applications*. CRC Press, 2nd edition.

SAE International (2015). Engine Oil Viscosity Classification J300. Technical report, SAE.

Saggin, R. and Coupland, J. N. (2001). Oil viscosity measurement by ultrasonic reflectance. *JAOCS, Journal of the American Oil Chemists' Society*, 78(5):509–511.

Saggin, R. and Coupland, J. N. (2004). Rheology of xanthan/sucrose mixtures at ultrasonic frequencies. *Journal of Food Engineering*, 65(1):49–53.

Schaschke, C. J. (2010). High Pressure Viscosity Measurement with Falling Body Type Viscometers. *International Review of Chemical Engineering (I.RE.CH.E.)*, 2(5).

Schirru, M. (2016). *Development of an Ultrasonic Sensing Technique to Measure Lubricant Viscosity in Engine Journal Bearing In-Situ*. PhD thesis, University of Sheffield.

Schirru, M., Li, X., Cadeddu, M., and Dwyer-Joyce, R. S. (2018). Development of a shear ultrasonic spectroscopy technique for the evaluation of viscoelastic fluid properties: Theory and experimental validation. *Ultrasonics*, 94(July).

Schirru, M., Mills, R., Dwyer-Joyce, R., Smith, O., and Sutton, M. (2015). Viscosity Measurement in a Lubricant Film Using an Ultrasonically Resonating Matching Layer. *Tribology Letters*, 60(3):42.

Schirru, M. M. and Dwyer-Joyce, R. S. (2016). A model for the reflection of shear ultrasonic waves at a thin liquid film and its application to viscometry in a journal bearing. *Proceedings of the Institution of Mechanical Engineers, Part J: Journal of Engineering Tribology*, 230(6):667–679.

Schitter, G., Stark, R. W., and Stemmer, A. (2002). Sensors for closed-loop piezo control: strain gauges versus optical sensors. *Measurement Science and Technology*, 13(4):N47.

Steiner, G., Gautsch, J., Breidler, R., and Plank, F. (2010). A novel fluid dynamic inline viscometer suitable for harsh process conditions. In *Procedia Engineering*, volume 5, pages 1470–1473.

Strutt, J. W. (1877). *The Theory of Sound*. Cambridge University Press, Cambridge.

TA Instruments (2020). Discovery Hybrid Rheometer. Technical report, TA Instruments.

Talbot, A. F. (1974). High shear viscometry of concentrated solutions of poly (alkylmethacrylate) in a petroleum lubricating oil. *Rheologica Acta*, 13(2):305–317.

Tang, Z. and Li, S. (2014). A Review of Recent Developments of Friction Modifiers for Liquid Lubricants (2007–present). *Current Opinion in Solid State and Materials Science*, 18(3):119–139.

Taylor, R. I., De Kraker, B. R., Morina, A., Neville, A., and Liskiewicz, T. (2017). Shear rates in engines and implications for lubricant design. *Proceedings of the Institution of Mechanical Engineers, Part J: Journal of Engineering Tribology*, 231(9):1106–1116.

Thompson, M. T. L. (2009). Multilayer acoustic impedance converter for ultrasonic transducers.

Vieira, S. (1986). The behavior and calibration of some piezoelectric ceramics used in the STM. *IBM Journal of Research and Development*, 30(5):553–556.

Viswanath, D. S., Ghosh, T. K., Prasad, D. H. L., Dutt, N. V. K., and Rani, K. Y. (2007). *Viscosity of Liquids*. Springer.

Vladescu, S. C., Marx, N., Fernández, L., Barceló, F., and Spikes, H. (2018). Hydrodynamic Friction of Viscosity-Modified Oils in a Journal Bearing Machine. *Tribology Letters*, 66(4):0.

Vogel, H. (1921). The law of the relationship between viscosity of liquids and the temperature. *Physikalische Zeitschrift*, 22:645–646.

Walters, K. and Barnes, H. A. (1980). *Anomalous Extensional-Flow Effects in the Use of Commercial Viscometers*, pages 45–62. Springer US, Boston, MA.

Wen, Y. H., Lin, H. C., Li, C. H., and Hua, C. C. (2004). An experimental appraisal of the Cox-Merz rule and Laun's rule based on bidisperse entangled polystyrene solutions. *Polymer*, 45(25):8551–8559.

White, D. (1988). Neurosonology Pioneers. *Ultrasound Med. Biol.*, 14:541–561.

Whorlow, R. W. (1992). *Rheological techniques.* Ellis Horwood Limited, second edition.

Yasuda, K., Armstrong, R. C., and Cohen, R. E. (1981). Shear flow properties of concentrated solutions of linear and star branched polystyrenes. *Rheologica Acta*, 20(2):163–178.

Zahirovic, S., Lubansky, A. S., Leong, Y., David, Y. · ., Boger, V., Zahirovic, S., Ventures, M., Lubansky, A. S., Boger, · . D. V., and Yeow, Y. L. (2009). Obtaining the steady shear rheological properties and apparent wall slip velocity data of a water-in-oil emulsion from gap-dependent parallel plate viscometry data. *Rheol Acta*, 48:221–229.

Završnik, M. and Joseph-Strasser, M. (2013). Inline viscometery for non-Newtonian viscosity characterization. *AMA Conferences 2013*, pages 587–591.

Appendix A

Newtonian Model

```
%% Newtonian Mathematical Model
% Calculating RC at multiple frequencies and viscosities.

%% Initialising Equation
Frequency = (0:100:10e6);
Viscosity = (0.1:0.1:0.4);

%% Constants For All Models
RhoM = 1420; %Density Matching Layer
RhoS = 2700; %Density of Solid Layer
RhoL = 831.9; %Density of Liquid

CM = 780; %Speed of Sound of Matching Layer
CS= 3100; %Speed of Sound of Solid Layer

zm = RhoM * CM; %Matching Layer Acoustic Impedance
zs = RhoS * CS; %Solid Layer Acoustic Impedance

%% For Loop Initialisation
SizeFrequency = size (Frequency);
LengthFrequency = SizeFrequency (1,2);

SizeViscosity = size (Viscosity);
LengthViscosity = SizeViscosity (1,2);

%% Calculating RC from Newtonian Model
for a = 1: LengthFrequency
    for b = 1: LengthViscosity

        AngularVelocity  =2 * pi * Frequency(1,a) ;
        G = abs(1i*AngularVelocity * Viscosity(1,b));
        zl_Newtonian = sqrt(RhoL * G);

        % RC for a three layered perfectly matched system.
        R_ml(b,a) = (zm^2 - (zs*zl_Newtonian))/(zm^2 + (zs*
   zl_Newtonian));

        % RC for a two layered system.
        R_2Layered(b,a) =(zs - zl_Newtonian) / (zs+zl_Newtonian);
    end
end


```

```
%% Figure settings.
figure('color','white','Renderer', 'painters')
hold all
set(gca,'Fontsize',14,'fontname','arial')
box off
dataselectleg =legend('1MHz Experimental','2MHz Experimental', '5MHz
    Experimental','10MHz Experimental');
set(dataselectleg,'Location','Best','Box','Off','Color','None','
    Fontsize',14,'fontname','arial');

%% Plotting Three Layered System
Frequency = Frequency ./ 10^6; %Changing frequency from Hz to MHz

plot (Frequency, R_ml,'linewidth',2,'linestyle','- ','Marker','.')
xlabel ('Frequency (MHz)');ylabel ('Reflection Coefficient_{res}')
legend ('0.1 Pas', '0.2 Pas', '0.3 Pas', '0.4 Pas', '0.5 Pas')

%% Figure settings.
figure('color','white','Renderer', 'painters')
hold all
set(gca,'Fontsize',14,'fontname','arial')
box off
dataselectleg =legend('1MHz Experimental','2MHz Experimental', '5MHz
    Experimental','10MHz Experimental');
set(dataselectleg,'Location','Best','Box','Off','Color','None','
    Fontsize',14,'fontname','arial');

%% Plotting Two Layered System
plot (Frequency, R_2Layered,'linewidth',2,'linestyle','- ','Marker','.
    ')
xlabel ('Frequency (MHz)');ylabel ('Reflection Coefficient')
legend ('0.1 Pas', '0.2 Pas', '0.3 Pas', '0.4 Pas', '0.5 Pas')
```

Appendix B

Maxwell Model

```
%% Maxwell Mathematical Model
% Calculating RC at multiple frequencies and viscosities.

%% Initialising Equation
Frequency = (0:100:10e6);
Viscosity = (0.1:0.1:0.4);

%% Constants For All Models
RhoM = 1420;%Density Matching Layer
RhoS = 2700;%Density of Solid Layer
RhoL = 831.9; %Density of Liquid

CM = 780; %Speed of Sound of Matching Layer
CS= 3100; %Speed of Sound of Solid Layer

zm = RhoM * CM; %Matching Layer Acoustic Impedance
zs = RhoS * CS; %Solid Layer Acoustic Impedance

RelaxationTime1 = 1*10e-8; % Relaxation Time of Liquid(s)

%% For Loop Initialisation
SizeFrequency = size (Frequency);
LengthFrequency = SizeFrequency (1,2);

SizeViscosity = size (Viscosity);
LengthViscosity = SizeViscosity (1,2);


%% Calculating RC from Maxwell Model
for a = 1: LengthFrequency
    for b = 1: LengthViscosity

        AngularVelocity  =2 * pi * Frequency(1,a) ;


        G1 = (AngularVelocity^2 * Viscosity(1,b) * RelaxationTime1)/(1
    + (AngularVelocity^2 * RelaxationTime1^2));
        G2 = (AngularVelocity * Viscosity(1,b))/ (1 + (AngularVelocity
   ^2 * RelaxationTime1^2));
        G = G1 + (1i*G2);
        zl_MaxwellMod1 = sqrt(RhoL * G);

        % RC for a three layered perfectly matched system.
```

```
42          R_ml(b,a) = (zm^2 - (zs*zl_MaxwellMod1))/(zm^2 + (zs*
    zl_MaxwellMod1));
43
44          % RC for a two layered system.
45          R_2 (b,a) = (zs-zl_MaxwellMod1) / (zs+zl_MaxwellMod1);
46      end
47  end
48
49  R_Maxwell_mod = abs(R_ml); %Determining the modulus.
50
51  %% Figure settings.
52  Frequency = Frequency ./ 10^6; %Changing frequency from Hz to MHz
53  figure('color','white','Renderer', 'painters')
54  hold all
55  set(gca,'Fontsize',14,'fontname','arial')
56  box off
57  dataselectleg =legend('1MHz Experimental','2MHz Experimental', '5MHz
    Experimental','10MHz Experimental');
58  set(dataselectleg,'Location','Best','Box','Off','Color','None','
    Fontsize',14,'fontname','arial');
59
60  %% Plotting Three Layered System
61  plot(Frequency, R_Maxwell_mod,'linewidth',2,'linestyle','-')
62  xlabel ('Frequency (MHz)');ylabel ('Reflection Coefficient_{res}')
63  legend ('0.1 Pas', '0.2 Pas', '0.3 Pas', '0.4 Pas', '0.5 Pas')
64
65
66  %% Figure settings.
67  figure('color','white','Renderer', 'painters')
68  hold all
69  set(gca,'Fontsize',14,'fontname','arial')
70  box off
71  dataselectleg =legend('1MHz Experimental','2MHz Experimental', '5MHz
    Experimental','10MHz Experimental');
72  set(dataselectleg,'Location','Best','Box','Off','Color','None','
    Fontsize',14,'fontname','arial');
73
74  %% Plotting Two Layered System
75  plot(Frequency, R_2,'linewidth',2,'linestyle','-')
76  xlabel ('Frequency (MHz)');ylabel ('Reflection Coefficient')
77  legend ('0.1 Pas', '0.2 Pas', '0.3 Pas', '0.4 Pas', '0.5 Pas')
```

Appendix C

Stokes' Second Problem Model

```
%% Stokes Second Layer Problem - Velocity and Shear Rate
% Basic second layer equation where the velocity profile and shear
    rate is
%modelled for changing viscosity oils.

%% Equation Initialisation
UBar = 10; % Initial Velocity
Freq = 1e6; % Frequency
DynVisc = (0.2:0.2:1); %Dynamic Viscosity Values
Density = 860; % Density of S20 @25C
t = 1; %Length of time.

%% Preliminary Calculations
T = 1/Freq; %Time period.
AngularFreq = 2 * pi * Freq; %Angular frequency.

%% For Loop Initialisation
SizeDynamicViscosity = size(DynVisc);
LengthDynamicViscosity = SizeDynamicViscosity(1,2);

%% Calculating Velocity Profile
for b = 1:LengthDynamicViscosity

    KinVisc = DynVisc(1,b) / Density;

    % Thickness of Stokes Layer
    Delta99 = 4.6 * ((2*KinVisc)/AngularFreq)^0.5;

    % Second For Loop Initialisation
    y = (0:1e-9:Delta99);
    Sizey = size(y);
    Lengthy = Sizey (1,2);

    SizeFreq = size(Freq);
    LengthFreq = SizeFreq(1,2);

    % Velocity and shear rate.
    for a = 1:Lengthy
        U(b,a) = (UBar * exp(-sqrt(pi/(T*KinVisc))*y(1,a)))*cos((
    AngularFreq*t)-sqrt(pi/(T*KinVisc))*y(1,a));
        ShearRate(b,a) = -U(b,a) * (((2*pi)/(T*KinVisc))^0.5) * cos ((
    AngularFreq *t)+(pi/4));
    end
```

```
end

x =repelem( 0, Lengthy); %For plotting purposes

%% Figure settings.
Colour1 = [0, 0.4470, 0.7410];
Colour2 = [0.8500, 0.3250, 0.0980];
Colour3 = [0.9290,0.6940,0.1250];
Colour4 = [0.4940,0.1840,0.5560];
Colour5 = [0.4660,0.6740,0.1880];
Colour6 = [0.3010,0.7450,0.9330];
Colour7 = [0.6350,0.0780,0.1840];

figure('color','white','Renderer', 'painters')
hold all
set(gca,'Fontsize',14,'fontname','arial')
box off
dataselectleg =legend('1MHz Experimental','2MHz Experimental', '5MHz
    Experimental','10MHz Experimental');
set(dataselectleg,'Location','Best','Box','Off','Color','None','
    Fontsize',14,'fontname','arial');
sz = 100;

%% Plotting Velocity Profile
y = y*10^6; %Changing length from m to \mu m
plot (U, y,'LineWidth',2)
xlim([-10 10])
xlabel('Velocity (m/s)'); ylabel('\delta (\mu m)')
hold on
plot(x, y, 'LineWidth',2, 'LineStyle','--', 'Color','k')
legend ('0.2 Pas','0.4 Pas', '0.6 Pas', '0.8 Pas', '1 Pas')

%% Figure Settings
figure('color','white','Renderer', 'painters')
hold all
set(gca,'Fontsize',14,'fontname','arial')
box off
dataselectleg =legend('1MHz Experimental','2MHz Experimental', '5MHz
    Experimental','10MHz Experimental');
set(dataselectleg,'Location','Best','Box','Off','Color','None','
    Fontsize',14,'fontname','arial');
sz = 100;


%% Plotting Shear Rate
ShearRatePlot = ShearRate .* 10e-6; %Changing shear rate from s^-1 to
    Ms^-1
plot (ShearRatePlot, y,'LineWidth',2)
xlim([-12 12])
xlabel('Shear Rate (Ms^{-1})'); ylabel('\delta (\mu m)')
hold on
plot(x, y, 'LineWidth',2, 'LineStyle','--', 'Color','k')
legend ('0.2 Pas','0.4 Pas', '0.6 Pas', '0.8 Pas', '1 Pas')
```

Appendix D

Raw Data To Reflection Coefficient

```
%% Reflection Coefficient from Raw Data

% List of samples to call from folders.
SampleID = {'85070.260.180291','85082.260.190031','85098.260.180327','
    85083.260.19012','N10', 'S20','85099.260.180250','85093.260.190107
    ','PAO4','PAO8','PAO40','PAO100','17092020_EAL\Lubricant4','
    17092020_EAL\Lubricant5','06032020\UOT5'};

%% For Loop Initialisation
Number_Samples = (length(SampleID));

Number_Repeats = 3;
for a = 1: Number_Samples
    for b = 1:Number_Repeats
        % Load Files
        Directory = "E:\16122019\Viscosity Measurements\Measurements\5
    MHz\";
        IDSelect = SampleID {1,a};
        IDSelectIndex = num2str(IDSelect);
        Meas= "\Meas\";
        Ref= "\Ref\";
        Repeat_Iteration = num2str(b);
        DirectoryEnd = " Step 48 Time.csv "

        RefDirectory = strcat (Directory, IDSelectIndex, Ref,
    Repeat_Iteration, DirectoryEnd);
        RefDirectory = char(RefDirectory);
        RefOpen = csvread(RefDirectory, 0 , 1);

        OilDirectory = strcat (Directory, IDSelectIndex, Meas,
    Repeat_Iteration, DirectoryEnd);
        OilDirectory = char(OilDirectory);
        OilOpen = csvread(OilDirectory, 0 , 1);

        %Averaging Data
        MeanRef = mean(RefOpen');
        MeanOil = mean(OilOpen');

        FileSize = size (OilOpen);
        NoCaptures = FileSize(1,2);
        timebase=2E-9;
        N=FileSize(1,1);
        time=(0:N-1)*timebase;
```

```
fs=1/timebase;

% Plotting Averaged A-Scan
figure
subplot (4,1,1)
plot (time, MeanRef)
hold on
plot (time, MeanOil)

% Trim Averaged Time Domain Data
StartTime = 1.65e-5;
EndTime = 2e-5;
IndexTimeLow = max(find((time)<StartTime));
IndexTimeHigh = max(find((time)<EndTime));

IndexedTime = time(IndexTimeLow:IndexTimeHigh);
MeanRef = MeanRef(IndexTimeLow:IndexTimeHigh);
MeanOil = MeanOil(IndexTimeLow:IndexTimeHigh);

% Plot Trimmed Averaged A-Scan
subplot (4,1,2)
plot (IndexedTime , MeanRef)
hold on
plot (IndexedTime , MeanOil)
xlabel ('Time (s)')
ylabel ('Amplitude (V)')

% Zero Pad Settings
padsize = 1000;  % Set the size of zero padding.
zeropad = zeros(padsize, 1);
zero_pad_signal_ref = [MeanRef zeropad'];
zero_pad_signal_oil = [MeanOil zeropad'];
zero_pad_length = length (zero_pad_signal_ref);

% FFT Settings
Nfft=zero_pad_length;
w=hann(Nfft,'periodic');
freq=fs*(0:Nfft-1)'/Nfft;
Freq=freq(1:Nfft/2)/1E6;

% FFT Reference Measurement
clear OIL Oil
AverTimeMeasRef=fft(zero_pad_signal_ref'.*w); % fft complex
AVERTIMEMEASREF =abs(AverTimeMeasRef(1:Nfft/2,:)*2/N);

% FFT Oil Measurement
AverTimeMeasOil=fft(zero_pad_signal_oil'.*w); % fft complex
AVERTIMEMEASOIL =abs(AverTimeMeasOil(1:Nfft/2,:)*2/N);

%Plotting FFT
subplot (4,1,3)
plot (Freq, AVERTIMEMEASREF)
hold on
plot (Freq, AVERTIMEMEASOIL)
xlim ([1 3])

RC = AVERTIMEMEASOIL ./ AVERTIMEMEASREF; % Calculating RC

```

```
96          % Plotting RC
97          subplot (4,1,4)
98          plot (Freq, RC)
99          xlim ([1 3])
100         hold on
101         plot (Freq, RC)
102
103         % Calculating RC from Single Frequency Index
104         FrequencyTarget = 4.3;
105         IndexFrequencyIndex = max(find((FrequencyTarget)>Freq));
106         RCM1 = RC(IndexFrequencyIndex, 1);
107     end
108 end
```